# Analysis of damage mechanisms in composite structures reinforced by tufting

Alan Martins

Par **Alan MARTINS**

# *Analysis of damage mechanisms in composite structures reinforced by tufting*

Thèse présentée
pour l'obtention du grade
de Docteur de l'UTC

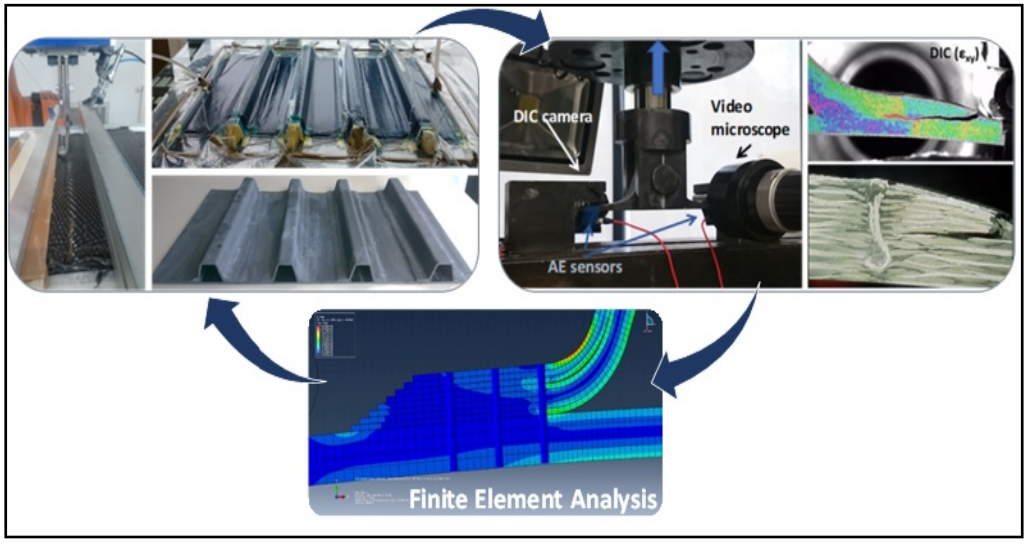


Soutenue le 15 novembre 2018
**Spécialité :** Mécanique et Matériaux : Unité de recherche en Mécanique - Laboratoire Roberval (UMR-7337)
D2443

Thèse présentée par **Alan MARTINS**

Pour l'obtention du grade de **Docteur de l'Université de Technologie de Compiègne**

Spécialité : **Mécanique et matériaux**

# Analysis of damage mechanisms in composite structures reinforced by tufting

Soutenance le 15 novembre 2018

Devant la commission d'examen composée de :

| | | |
|---|---|---|
| **C. Binetruy** | **Professeur, Ecole Centrale de Nantes** | **Rapporteur** |
| **R. Zitoune** | **Maître de conférences (HDR), Institut Clément Ader, Toulouse** | **Rapporteur** |
| **A. Ancelotti Jr** | **Professeur, UNIFEI- Brésil** | **Examinateur** |
| **B. Lascoup** | **Expert mécanique et CND, IRT Jules Vernes** | **Examinateur** |
| **M. Risbet** | **Professeur, UTC** | **Examinateur** |
| **W. Harizi** | **Maître de conférences** | **Examinateur** |
| **A. Laksimi** | **Professeur, UTC** | **Co-directeur de thèse** |
| **Z. Aboura** | **Professeur, UTC** | **Directeur de thèse** |

# ACKNOWLEDGEMENTS

This work of thesis which was carried out during three years does not only concern my effort but that of a whole team. I am proud to have worked with Zoheir Aboura and Abdel Laksimi, my thesis supervisors. They were always supportive, sharing with me interesting ideas and scientific knowledge which developed me through this period. From supervisors, they also became great friends. Also, I would like to acknowledge Walid Harizi and Kamel Khellil for all the time spent to give me advises to develop my work and those of joy.

To all collaborators in Roberval laboratory, I would like to express my sincere gratitude to the support that made my life simpler during that time, in especial to Valérie Duquene.

I also would like to thank my friends Khalil Hamdi, Céline, Sitou, Augustin, Corentin, Jing, Ivan, Tea, Adela and Benjamin for the funny moments that we spent together on the coffee time, at PIC or elsewhere. You were part of my family in France and became my stay easier.

It is also worth to acknowledge professor Antonio Ancelotti Jr for every advice and teaching about composite materials since Master. I owe so much for every accomplishment since there. Thank you for the friendship.

Additionally, I render thanks to the Ph.D. scholarship awarded by *Conselho Nacional de Desenvolvimento* Científico e *Tecnológico* (*CNPq*) – Brazil.

Last but not least, my sincere gratitude for my girlfriend Luciana, who has been my life partner through the years. Thank you for always encouraging me and for the unconditional love.

# ABSTRACT

This study focused mainly on the assessment of the mechanical performance and the failure mechanisms of tufted composites under divers loading conditions. Laminated plates and stiffened panels reinforced by tufting was manufactured with different tufting parameters to evaluate their effect in the properties of the composites. Multi-instrumented characterization carried out during the tests assisted the investigation. The tufted plates subjected to short-beam shear tests aided especially in the behavior analysis of tufting density and angle in mode II loading condition, while impact and compression after impact (CAI) tests on the damage tolerance. Open-hole fatigue tests were also performed to evaluate the tufts response, especially regarding their position to the center hole, to the strain concentration factor generated by the hole.

The following part of this work consisted of the mechanical tests on omega stiffened panel reinforced by tufting. The procedure optimized the tufting parameters employed for reinforcing the structures from the previous batch of specimens until reaching an optimal point that the main properties, primarily found in pull-off tests, are equal or superior to those of the control specimens. This improvement also considered the modifications in the shape of the stiffeners. Furthermore, a novel approach based on the piezoresistive effect of carbon tufts under loading of the composite specimens is performed. This may support the monitoring of the health status on the tufted threads and therefore of the composite because of the structural nature of the tufts.

The results showed that tufting reinforcements are capable of increasing the interlaminar fracture toughness and damage tolerance of the composites considerably owing mainly to their crack bridging phenomena. The tufting parameters are decisive factors for achieving the best mechanical properties. However, this work reported that tuft threads are also responsible for generating cracks due to the strain concentration and defects caused by their insertion and consequently, can decrease the strength of the composites. The investigation concludes that the random insertion of the tufts is not ideal for the performance of the material and thus must be avoided. The development of the tufting insertion in the omega stiffeners was supported by the multi-instrumented characterization that led to optimizing reinforcement in the structure.

Although the study achieved the goal of obtaining mechanical properties significantly superior to the omega panels reinforced by tufting, it is noticeable that the procedure employed is not optimal. The present work also proposes a preliminary finite element model to overcome the

costly and time consuming of the experimental tests. It intends primarily optimizing the tufting parameters in the structure. The model developed was capable of predicting the same damage events as observed experimentally, but it still distant from the quantitative predictions of the results. The structural health monitoring of the tufted composite laminates by the carbon threads seems promising and could help in the future for supplying data about the tufts health status under loading that are not achieved by the conventional characterization methods employed in this work.

# TABLE OF CONTENTS

# LIST OF FIGURES

# LIST OF TABLES

# INTRODUCTION

Composite materials have been increasingly applied to structural and semi-structural components in the aerospace, transportation, defense, energy and civil sectors. This is mainly due to their considerable strength and stiffness to weight ratios comparing to metallic alloys, which reduces the structure weight and increases the fuel efficiency in the most applications [1]. The composites present superior fatigue life which possibilities the reduction in the maintenance frequency and structure lifespan. They also allow manufacturing of complex shapes, reducing part counts and consequently saving weight by diminishing the number of fasteners.

Conventional composite laminates are one of the most applied composite materials in the manufacturing of structural parts due to their capability to bear high in-plane loadings. They consist of multiple fabric layers stacked and embedded in a typically brittle matrix. A 2D arrangement of reinforcement fibers makes each layer free from the adjacent ply and consequently, causes the connection between the layers given by the matrix only. The interlaminar region (between fabric plies and matrix) is, therefore, subjected to damages due to the lower fracture toughness of the matrix. Delamination is one of the significant damages in conventional composite laminates which can considerably reduce the load-bearing capacity of a structure and may be induced by out-of-plane loading (static and impact loading) and typically combined with stress concentrations (related with structure geometry) or discontinuities such as manufacturing defects , ply drops or free edges [2].

Improving the resistance to crack initiation and propagation throughout fabric plies can enhance the interlaminar fracture toughness considerably. Therefore, several methods have been developed to counteract the susceptibility of the composite laminates to delamination and can be mainly classified into matrix toughening or 3D fiber architecture.

Through-thickness reinforcement (TTR) seems to be promising to improve the out-of-plane properties with various works reporting its advantages in the literature. However, some results are controversial and indicate that transversal reinforcements can reduce the in-plane properties of the laminated composites. The reality is definitely between these two affirmations. The performance of the laminated composites reinforced through-thickness will necessarily depend on the type of structure, the loading condition, the nature of the 2D plies and the reinforcing threads, and others. Due to the various parameters necessary to adapt and control according to

the case of structure considered, it is not reasonable, for example, to create a complete reinforcement along the whole structure. This will only result in reducing its in-plane properties, and the out-of-plane contribution will be negligible.

It is therefore essential to introduce the concept of "think stitching" or "think 3D reinforcement" by analogy with the "think composites" introduced at the beginning of the evolution of these materials.

Transversal reinforcements should only be inserted in the zones of significant weakness. It must allow a local increase of through-thickness properties such as to mitigate any delamination, stress concentration, possible impacted area., and thus increase the scope of composite structures. For this reason, it is necessary to manage this technology in the whole process. It starts from the reinforcement process and its specificities, the understanding of the damage mechanisms in the structures reinforced by tufting, the development of means for in-situ inspection until the analytical and/or numerical models. This thesis does not claim to deal exhaustively with all of these points. However, in the study of some instances, it is necessary to investigate, as much as possible, the entire described chain.

The present work aims to investigate the mechanical properties of laminated composites reinforced through-thickness by tufting. The manufacturing of various composite specimens molded by the VARTM process aided to evaluate the tufting parameters in the mechanical properties of the composites. They were subjected to different loading conditions (in and out-of-plane loading) to understanding the function of the tufts in their interlaminar fracture toughness and damage tolerance, as well as on the in-plane properties. Multi-instrumented characterization employed under mechanical tests such as Digital Image Correlation (DIC), acoustic emission (AE) and in-situ microscopy aided the investigation of failure mechanisms in the tufted composites. Moreover, a new approach for monitoring structural health is proposed in this work by taking advantage of the piezoresistive behavior of the tufted carbon threads. This may be further employed complementary to others techniques to detect major damages in the composites under loading. This thesis also presents an initial development of a finite element model for the tufted composites. The data obtained during the mechanical tests will contribute to the numerical modeling and consequently optimizing the tufting parameters to enhance the mechanical performance of the structures.

The current manufacturing technologies investigated in the literature, some already employed in the industry, are reviewed in Chapter 1 as potential methods to improve the out-of-plane properties and damage tolerance of laminated composites. This chapter discusses the main methods, presenting significant advantages and drawbacks, with the focus mainly on the 3D textile preforming techniques.

Chapter 2 gives a detailed summary of the materials and manufacturing process utilized in this work. It also describes the methodologies employed in the mechanical characterization of the composites.

The in-plane and through-thickness mechanical properties of the tufted composite plates are investigated in Chapter 3. The mechanical tests performed with multi-instrumented techniques provided a better understanding of the damage scenario. Short beam shear tests allowed examining the behavior of the tufting angle in the interlaminar shear strength and stiffness of the carbon/epoxy laminates in the principal directions. Impact and CAI tests investigated the effect of the tufting parameters, angle and tufting density, in the damage tolerance of the composites. Moreover, open hole fatigue tests allowed studying the tufts role in the fatigue strength and their behavior in the strain concentration factor of the laminated composites. The in-plane properties were also evaluated and compared with the control specimens for the specimens subjected to compression tests and open hole fatigue tests.

Chapter 4 concerns the investigation of omega stiffened composite panels reinforced by tufting. The multiple characterization techniques employed during pull-off tests contributed to establishing the damage scenario and consequently, enhancing the tufting position and specimen geometry for the next batch of specimens. 3-point bending tests subjected the structures to a complex loading, which is supposed to be more realistic, and provided supplementary comprehension of the tufts in the structure.

The structural health monitoring of the composites by the piezoresistive effect of the tuft carbon threads is studied in Chapter 5. The manufacturing of different structures such as laminated and sandwich plates and, omega stiffeners as well as their characterization under various loading conditions permitted a better evaluation of this approach. Supplementary characterization techniques used during and after tests aided in the validation of this novel technique.

The thesis terminates with an overview of the main conclusions obtained for each covered subject and, the perspectives for the future works.

# CHAPTER 1 LITERATURE REVIEW ON INTERLAMINAR TOUGHENING TECHNIQUES FOR COMPOSITES

## 1.1 Introduction

The present section concerns the literature review of different techniques employed throughout the years for improving the interlaminar fracture toughness and damage tolerance of laminated composites. It consists of the studies carried out for the continuous fiber-reinforced polymeric composites and overviews the particularities of each method, emphasizing the 3D textile preforming techniques.

## 1.2 Matrix toughening

Composite laminates can be toughened by incorporation of rubbers [3]–[7], thermoplastic polymers [8]–[10], rigid particles [11]–[14] or hybrid insertion of elastomeric and inorganic fillers [15]–[17] into the polymeric matrix. Matrix-fiber interactions have a strong influence on the mechanical behavior of composite materials and play an essential role in delamination events. For this reason, different methods have been proposed to increase the interaction between the fiber/matrix. Although this technique seems interesting, it is not addressed in this thesis and therefore this chapter will not discuss the matter.

Enhancing the toughness of epoxy resins by addition of a second polymer such as an elastomeric or a thermoplastic modifier has been widely reported in the last two decades [18]. It consists of dissolving the second polymer in the polymer matrix, which subsequently will separate phase during the cure cycle to form a toughened dispersed phase capable of shielding crack tip and therefore improve the fracture toughness [18], [19].

The epoxy resins modified with rubber has been reported since the 1960s. The primary toughening mechanisms involving rubber reinforcements are particle debonding/cavitation, localized shear banding of the matrix as well as rubber particle bridging [20]. The fracture toughness increases considerably with the insertion of rubber particles in composite laminates [6], [7], [21]–[23] and can achieve improvements up to 10 times about the control specimens in mode I [22]. The crack propagation is contained by adding rubber particles, which results in the smaller damaged area under impact loading [4] and may lead increase damage tolerance on

Compression After Impact (CAI) [7]. However, composite laminates toughened with rubber particles have been reported to decrease the glass transition temperature, failure strength and tensile modulus significantly [4], [5], [24]–[26].

The insertion of thermoplastic particles as a toughening phase for epoxy resins may avoid the issues on the mechanical properties related to rubber modifiers. These new materials disclosed an outstanding advantage over the elastomeric modified systems [18]. The toughening of composites by thermoplastic particles has shown its efficiency on improving fracture toughness with insertion of polyamide(PA) [27], poly(bisphenol A-co-epichlorohydrin) (PBAE) [28], polyetherimide (PEI)[29], polysulfone(PSU) [30], poly (aryl ether ketone)(PAEK)[31], and polyhydroxy ether bisphenol A (phenoxy) [32] particles, and depends on different parameters such as particle morphology and compatibility with matrix. The composites with matrix reinforced by thermoplastic particles exhibited a considerable decrease in the damaged area under impact tests, which consequently improved CAI strength [30], [33], [34].

Rigid (inorganic) particles also became a solution to the drawbacks caused by the addition of rubber particles into thermoset polymers and can increase tensile modulus, hardness and failure strength [11], [35] when compared with the neat matrix. Diverse rigid fillers have been studied to reinforce the matrix, such as glass beads, silica, carbon nanotubes, and nanofillers, graphene, black carbon, calcium carbonate, and titania. However, significant improvement of the fracture toughness, as seen for rubber toughening, is not reported to the inorganic particles with the same volume fraction of fillers [36]. Further, toughening mechanisms of the epoxy resins reinforced by particles differ considerably according to aspect ratio and size as well material type, which difficult the understanding of damage mechanisms to optimize the filler insertion in the composite [14], [37].

Hybrid toughening has also been investigated to overcome the issues presented by soft particles, such as rubber, by incorporating with them rigid fillers, which consequently combine the best properties of each modifier. The specific toughening mechanisms related to each type of particle should interact positively so that for a given volume fraction of modifiers, the toughness of the hybrid composite would be higher than the additive contribution of the two modifiers [17]. The hybrid reinforcement with rubber and glass particles in the epoxy resin reported a considerable improvement on fracture toughness comparing with the neat specimens, where rigid glass particles increased the crack resistance mainly through a crack-pinning mechanism while the rubbery particles enhanced the extent of localized plastic shear deformations around the crack

tip [38]. The fatigue life was also improved up to ten times by a hybrid toughening with nanosilica/rubber microparticles in glass fiber reinforced polymer [15].

The methods above have difficulties in distributing the particles appropriately in the matrix which may lead to stress concentration. Furthermore, a significant number of particles is necessary to achieve significant toughness. This generally increases the resin viscosity, that is usually unacceptable for liquid composite molding (LCM) processes [39]. Interleaving method has been proposed in the literature to avoid this problem.

Interleaving is an old concept used in the aircraft industry to enhance acoustic damping and interrupt fatigue crack propagation in metallic structures. The inclusion of discrete layers of a second material in the form of particles, film, and fibers between the plies can describe the interlayer toughening [40]. This approach has been used to improve the penetration resistance and damage tolerance of carbon/epoxy composites by increasing their fracture toughness [41]–[47]. Different toughening mechanisms are involved, such as plastic deformation and crack bridging, depending on the interleaf form [48]. However, the toughened resin layers have relatively lower stiffness and strength, and therefore their application has to be limited in order not to alter the overall composite performance [49], [50]. Besides, this may cause a great weight penalty to the laminate and potentially decrease of glass transition (Tg) [42], [45], [46].

## 1.3 3D textile preforms

3D preforms have been exhibiting a tremendous potential to improve the out-of-plane mechanical properties of the composite structures, such as damage tolerance and fracture toughness. A variety of techniques are used to interlace through-thickness fibers in dry and prepreg preforms as shown in Figure 1.1. Manufacturing techniques as 3D weaving, 3D knitting, or 3D braiding are known to be an integral process performing near-net-shape 3D preforms, while stitching, Z-pinning or Z-anchoring consists of an initial preform layup followed by insertion of Z-reinforcements. This chapter highlights the main process to manufacture 3D preforms, discussing their advantages, drawbacks and some industrial applications.

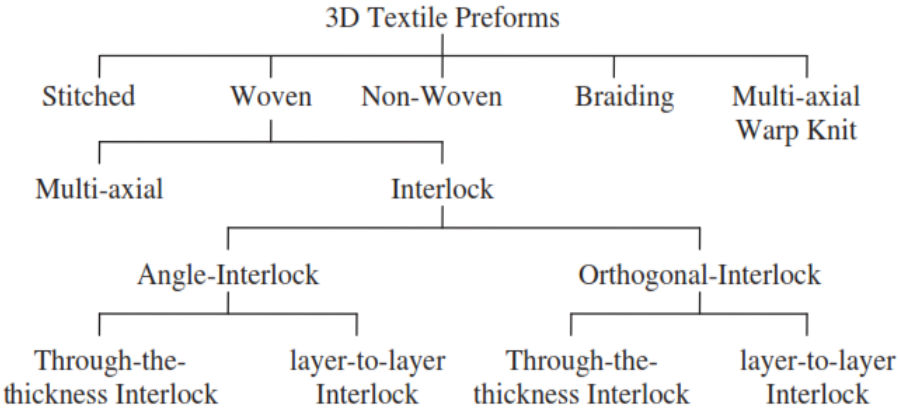


**Figure 1.1 - 3D textile preform** [51]**.**

### 1.3.1 Weaving, braiding, and knitting

3D woven composites were first performed by Avco Corporation in 1972 with C/C material in an attempt to replace high-temperature metal alloys on aircraft brakes. Specially designed automated looms which interlace three sets of fiber tows, in-plane orthogonal tows (warp and weft) with through-thickness tows (binder), in the weaving machine are responsible for manufacturing 3D woven preforms [51], [52]. This process allows obtaining near-net-shape preforms with a complicated geometry for a composite component. One of the main benefits of the 3D weaving process is the wide variety of fiber architectures that can be used to create different fabrics with a controlled amount of binder yarns [51]. Based on the typical fabric architectures, they are commonly subdivided into three main categories as 3D orthogonal weave, 3D layer-to-layer interlock weave, and 3D through-thickness angle interlock (as illustrated in Figure 1.2).

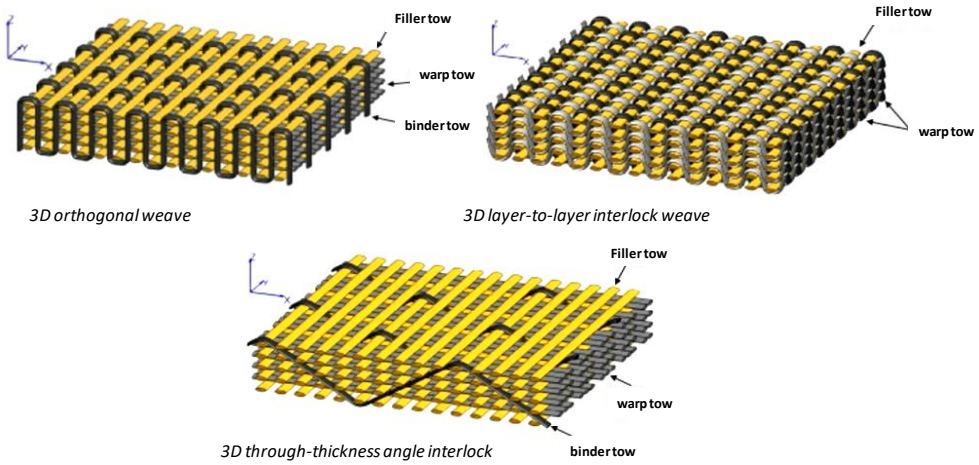


**Figure 1.2 - Examples of 3D woven architectures** [53]**.**

The literature reports improvements on fracture toughness for 3D woven composites in the main modes of loading condition (open and shear mode)[54]–[56] and impact resistance [57], [58], which are directly dependent of the preforming parameters, as z-binder density and angle. However, the preform architecture must optimize to diminish the in-plane fiber waviness created by the binder insertion that can consequently decrease the in-plane properties of the composite structure. This fact was reported by Brand et al. [55] which improved more than three times the compressive strength of 3D woven composites in comparison with 2D laminates. Some composites parts manufactured with 3D woven are present in Figure 1.3, which highlights the manufacturing ability to perform complex parts.


**Figure 1.3- a) complex 3D woven preform geometry and composite stiffener** [59] **and, b) 3D woven preform applied to manufacture LEAP fan blade (Safran Aircraft Engines - Safran Group)** [60].

3D braiding was the first textile process employed to manufacture 3D preform for composite materials. The technique developed in the 1960s, produced C/C composites to save weight by replacing high-temperature metallic alloys used in the rocket motor components [52]. Figure 1.4 exemplifies 3D braiding manufacturing and feasible preforms achieved with the technique. Unfortunately, there are little publications on literature about 3D braided composites, making it difficult to report general conclusions. 3D braiding technology is an extension of 2D braiding in which the fabric is constructed by intertwining or orthogonal interlacing of three or more yarns to form an integral structure through position displacement [61]. This process can be used to produce complex near net-shaped preforms. The manufacturing process is reported to be low cost and does not require an intensive workforce. However, large structures may be unfeasible due to the position of the yarn carriers [62]. 3D braided composites increase the interlaminar

fracture toughness and therefore improve delamination resistance considerably compared to laminate counterparts with the same fiber volume content [63]. This behavior provides more significant impact and notch resistance due to the interlaced strand of the preforms. T-stiffeners manufactured with 3D braided preforms presented lower stress concentration in the noodle region comparing with 2D tape laminate stiffener bonded onto a skin [64]. The capability of the braiding process in varying the interlaced pattern becomes the mechanical properties of 3D braided composites widely adaptable [65], [66]. Otherwise, in-plane properties of 3D braided composites are importantly decreased comparing to the 2D composite laminates due to the lack of straight yarns in the principal directions and also to the fiber crimp [65].

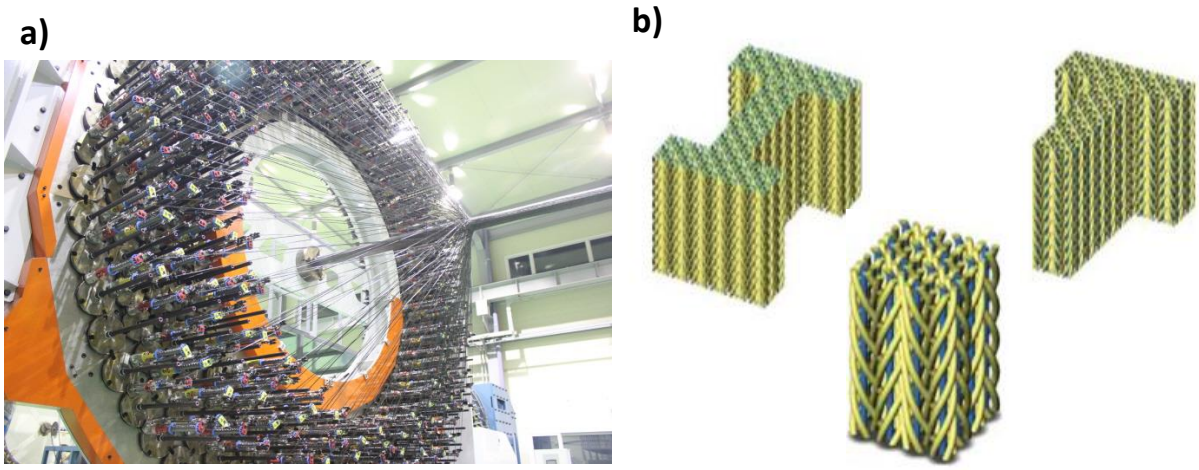


**Figure 1.4- a) Circular 3D Interlock Braiding Machine** [67]**, b) Example of 3D braided preforms** [68] **.**

Little information is reported in the literature about mechanical properties and applications of 3D knitted composites, making this technique the least investigated among those already mentioned in this topic. Three-dimensional knitted preforms present great drapability and consequently can produce complex shapes composites such as spheres, cones, ellipsoids and T-pipe junctions with better formability. However, the major issues of this process such as the fiber breakages, lower fiber fraction and concentrated stress caused by the loops, reduce the in-plane properties of composites considerably when compared with alternative techniques. Multilayer multiaxial warp-knitted (MMWK) is a class of knitted 3D preforms capable of overcoming these issues by employing together non-crimp fabrics (NCFs). The use of warp knitting techniques in conjunction with fiber placement concepts can produce multilayer fabrics containing the fibers straight and relatively uncrimped [69] (Figure 1.5). Multiaxial knitted composites have exhibited higher open mode fracture toughness [56], [70], superior impact and compression after impact strength [71], [72] and fatigue life [73] compared to conventional composite laminates.

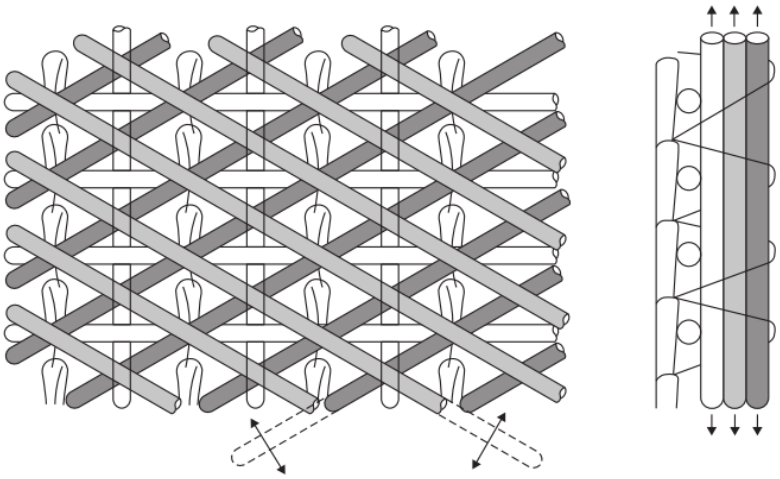

**Figure 1.5 - Illustration of multiaxial warp-knitted fabric** [74].

### 1.3.2 Through-Thickness Reinforcement (TTR)

#### a) *Z-pinning*

Z-pinning is the only practical technique capable of reinforcing through-thickness of prepreg preforms in large commercial quantities. Aztex Inc. (Waltham, USA) developed in the early 1990s the Ultrasonic Assisted Z-Fibre$^{TM}$ (UAZ$^{(R)}$) technology which is the most common process utilized nowadays to reinforce large quantities. It consists of the insertion through a preform (as an uncured pre-impregnate, dry fabric or foam core) of short, thin pins (diameter range between 0.2-1.0 mm) made of high stiffness and strength material such as a metal wire (e.g., titanium alloy and steel) or pultruded composite using an ultrasonic hammer. Figure 1.6 schematizes the UAZ manufacturing process. A foam sandwich is utilized as Z-pins carrier and discarded after the insertion process. The sandwich consists of two types of foam: a dense foam, such as 51IG Rohacell, used to locate the pins accurately, and a low-density polystyrene foam, which collapses down to almost zero thickness when the pins are inserted into the part to be reinforced [75]. The process consists on place the carrier under the prepreg preform on the desired region, and drives the pins from the foam into the plies by using an ultrasonic device, displaced manually or numerically controlled. The ultrasonic device generates high-frequency compressive waves (~20 kHz) which squash the carrier foam and thereby drive the Z-pins into the uncured composite [76]. Some pressure applied to the hammer and the heating created by the ultrasonic vibration in the device tip during the process also helps to insert the pins. The excess length of the pins comprised on the surface of the foam carrier is sheared away

subsequently to the complete inclusion of Z-pins into the uncured preform. Then, the reinforced preform is ready for curing methods.

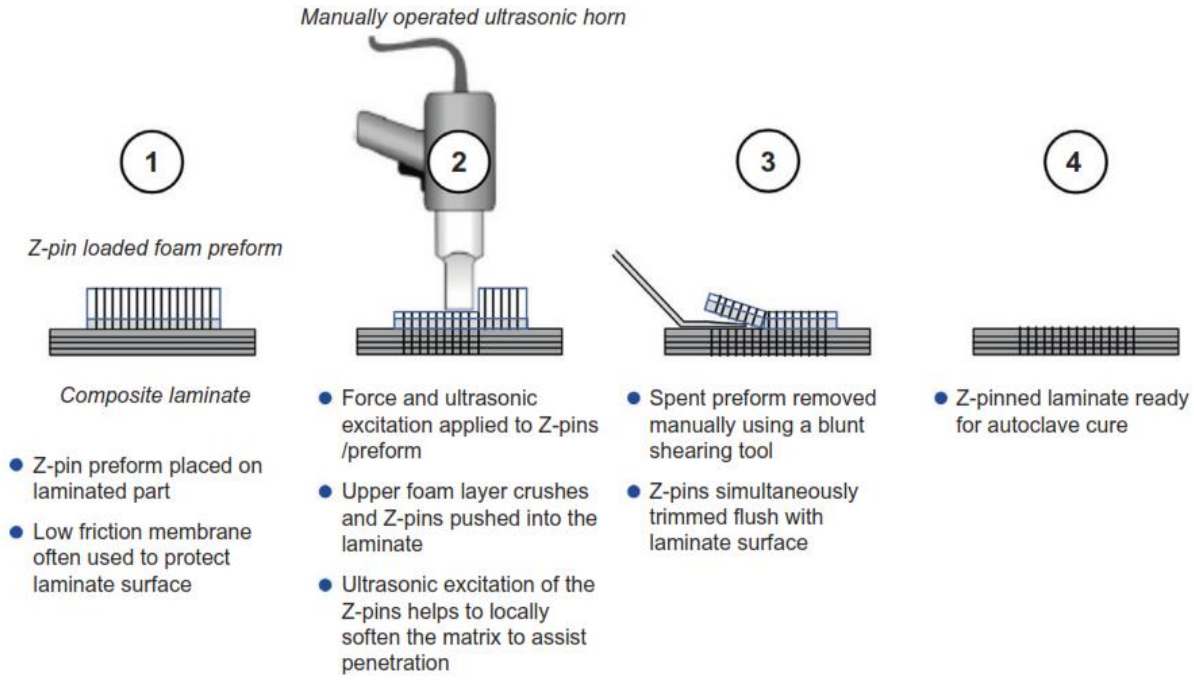


**Figure 1.6 - Typical procedure for Z-pin insertions** [77]**.**

'Caul plate' insertion is also a Z-pinning technique used to reinforce prepreg laminates through their thickness. However, the literature provides little information about this process mainly due to its rare use. The process primarily consists of placing a carrier foam, which contains the Z-pins, onto a laid-up prepreg laminate. The system is vacuum bagged with a rigid caul plate placed on the top of the carrier and submitted to autoclave cure. During the cure cycle, the resin is softened by heating, which drives the Z-pins into the prepreg preform with the applied pressure [78]. Figure 1.7 exhibits a schema of the process.

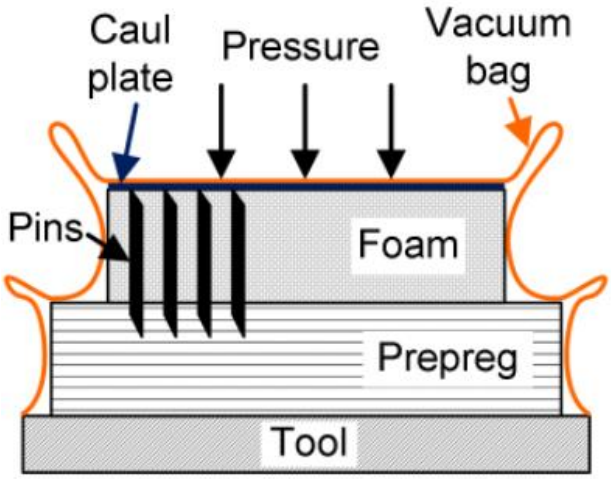


**Figure 1.7-Schema of the caul plate Z-pinning method** [79].

EADS Innovation Works developed a new Z-pinning method recently. The manufacturing process uses a vibrating hollow needle from where composite pins made from twisted carbon fibers are inserted into a dry-preform[80]. Then, the material can be injected using a liquid composite molding process.

Applications of Z-pinning technology concentrate mainly on high-performance segments of the automotive and aerospace industry, which are the largest markets for prepreg materials. This avoids the insertion of fasteners or rivets to join the stiffeners to the panel and consequently reduces stress concentration in the reinforced area as well as saves considerable weight. The front fuselage region of the Boeing-Sikorsky RAH-66 Comanche helicopter utilized the mentioned technology due to its superior damage tolerance over the previous honeycomb structure [81]. F/A-18E/F Super Hornet fighter aircraft has also used Z-pins to reinforce inlet duct skin panels and to fasten hat stiffeners to composite panels, saving 17 kg on the aircraft gross weight by replacing 4600 titanium fasteners and approximately US$ 83000 per aircraft [82], [83].

Several studies have reported a significant increase for Z-pinned laminates on the fracture toughness under mode I, mode II and mixed mode I/II loading conditions [84]–[87]. The considerable improvement of the interlaminar fracture toughness is mainly due to the crack bridging behavior provided by the Z-pins. The sequence of damage processes caused in the z-pinned composites under mode I loading consist mainly of the elastic stretching, debonding from the surrounding zone, and frictional pull-out from host laminate [76]. The crack bridging effect is also reported under mode II loading. The effect of the crack passing through the rows of Z-pins submits them to increase bending and internal shear, resulting in the elastic shear

deformation, debonding, subbing, and pull-out of the pins [76], [86]. Mode I and II fracture toughness depend on the Z-pinning parameters as density and pin diameter. The increase on Z-pin content improves the delamination toughness on both mode conditions [88]–[90] and has reported improvements up to 20 and 10 times in mode I and II fracture toughness respectively when compared to control laminates [89]. Cartié et al.[88] investigated the influence of Z-pin diameter on the laminate properties and found a significant increase in the mode I fracture toughness and a slight improvement on mode II loading condition with the reduction in the diameter. Z-pinned composite structures also proved effective in arresting crack growth when subjected to mixed mode loading [91]. Experimental tests with T-joints [92]–[94] and L-shaped joints [95], [96] has exhibited improvements in the ultimate strength of joint structures reinforced by Z-pins.

Impact damage resistance and CAI strength report significant improvements for z-pinned laminates, especially when they are submitted to high impact energies [75], [85], [89], [90]. Impact damaged area is importantly reduced when inserting Z-pins and may achieve a decrease up to 64%, depending on the impact energy level and laminate thickness [97]–[100]. Despite the remarkable out-of-plane properties obtained by the Z-pinned laminates, the majority of the works in the literature have reported degradation of the in-plane properties [101]. These properties, such as elastic modulus and strength, reduce gradually with increasing the diameter of the pins as well as reinforcement density [97]. The reduction in the elastic properties is due to microstructural damage caused by z-pinning process, particularly in-plane fiber waviness, out-of-plane fiber crimp, and swelling that reduces the fiber volume content, while a decrease in the composite strength is attributed mainly to the fiber breakage during insertion of the Z-pins [102]. Figure 1.8 presents the change in the microstructure caused by Z-pin insertion. A preliminary study should be done before reinforcement in order to optimize the parameters (e.g., pins diameter and volume content) and consequently diminish the issues related to the Z-pins insertion on the in-plane properties.

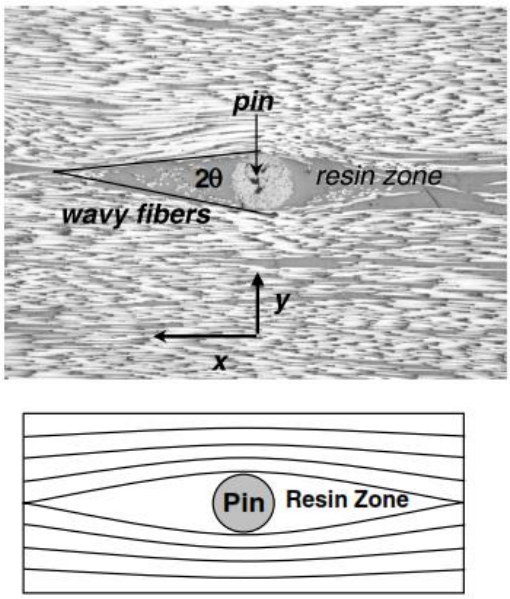


**Figure 1.8 - Waviness and resin pocket zone at a Z-pin** [99].

### b) *Z-anchoring*

Z-anchor® is a relatively through-thickness new method to reinforce dry preform, developed and patented by Mitsubishi Heavy Industries and Shikibo [103]. It consists of pushing a variable amount of continuous in-plane fibers through the preform thickness using a set of specially designed needles [104]. The deformed fibers typically form a conical shape (Figure 1.9), named as EFB (entangled fiber bundles), playing an essential role in the improvement of the interlaminar strength.

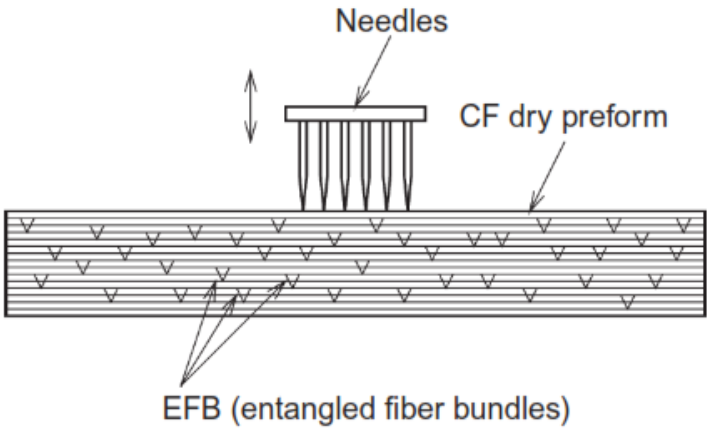


**Figure 1.9 - Schematic illustration of the Z-anchor process** [104].

Kusaka et al.[105] reported a continuing improvement of the mode I fracture toughness at increasing the Z-anchor density, achieving values up to 5-fold higher when compared to the control laminates. Kusaka et al. [106] also studied mode II fracture toughness, resulting in an almost linear improvement when increasing Z-anchor density, reaching up to 7-fold increase. The fatigue life of the Z-anchored specimens under mode I delamination propagation tests was investigated by Hojo et al. [107] which found fatigue threshold values 3.4-5.0 times higher than those without Z-anchor reinforcement. Compression after impact strength is also claimed to increase 35% with Z-anchor technology without reducing the in-plane properties significantly [108]. This method is expected to create significant damages in the fibers and therefore reducing considerably the in-plane properties. However, there is a lack of study available in the literature about the damage extent and its effect on the in-plane properties.

**c) *Stitching***

Stitching process mainly consists of the through-thickness reinforcement of dry preforms via a needle which inserts thread materials of high tensile strength, such as aramid, kevlar, glass, and carbon. The stitching reinforcement of prepreg materials has also been investigated during the 1980s in order to improve the damage tolerance and mechanical strength [108][109]. However, it presents significant issues considering the needle introduction into viscous prepreg layers [110].

The development of the stitching machines occurred over the three past decades driven principally by the aerospace industry to improve the quality and reproducibility of composites structures. NASA and Boeing developed in the 1990s a 28-meter long stitching machine for reinforcing laminated composite wing, in order to reduce weight and costs when compared with an equivalent aluminum wing [111]. The computer numerically controlled stitching machine performed a stitch rate of 3200 stitches/minute and could reinforce panels up to 13 m by 2.5 m, and 35 mm thick [81].

Various stitching methods have been developed during the last decades to improve the interlaminar toughness of laminated composites. The most common are lock stitching, modified lock stitching and, chain stitching. Lock stitching consists of a needle on the upper side which inserts a thread through the dry-preform, caught by a rotation hook on the bottom side and then interlocked with the other thread feed by the bobbin (Figure 1.10a). This method enables

working with two different thread materials. However, the two threads interlocked in the laminate center (seen in Figure 1.10b-c) create stress concentration points [112].

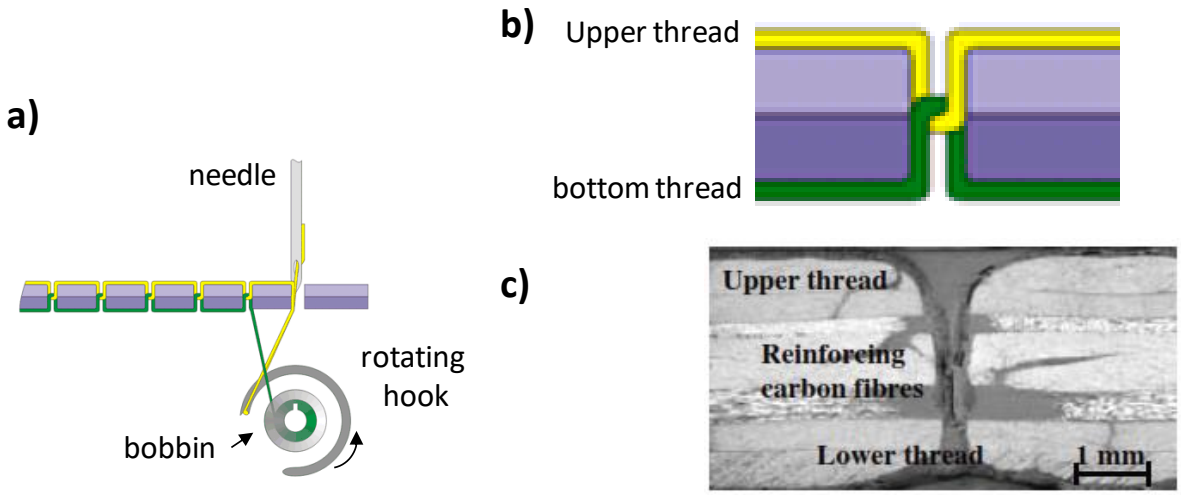


**Figure 1.10 - a) Lock stitching technique, b) schematic of the through-thickness stitched threads pattern and c) stitched laminate** [113].

Modified lock stitching has been developed from the lock stitching method. This process involves interlocking the threads on the lower side by controlling the tension of the needle and bobbin threads (Figure 1.11). It reduces the issues concerning the knot formation in the center of the laminate as seen to the lock stitching technique, but instead, it can increase fiber crimping in the outer surface due to the knot [114].

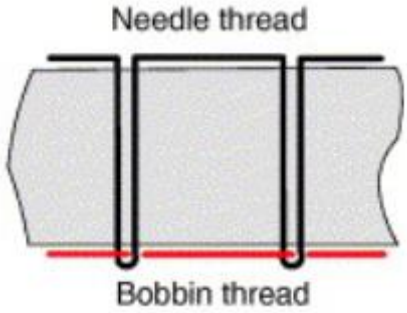


**Figure 1.11- Modified lock stitch pattern**[115].

Chain stitching technique enables creating a through-thickness reinforcement with a single thread differently from the techniques above. It consists of the insertion of the thread through the dry-preform by a needle, subsequently caught on the bottom surface via a catcher (Figure 1.12). The tension of sewing threads is relatively low which leads to reduced fiber spreading [116]. However, the fiber crimp created by the interlock knot on the bottom surface may also affect the in-plane properties [113].

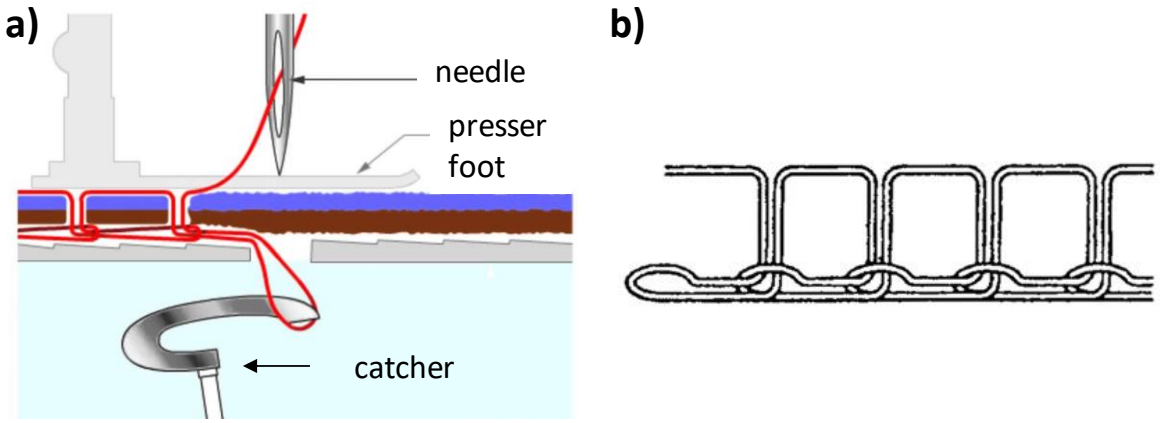


**Figure 1.12- Chain stitching a) schematic of the stitching process b) stitch pattern** [112]**.**

Fracture toughness of stitched composite is described to increase up to 45 times [117] in mode I [56], [109], [117]–[123] and up to 15 times [124] in mode II [110], [125]–[128] compared to unstitched laminates. The resistance to crack propagation improves at increasing on stitching density [110], [119], [124], [126], [129], mainly due to the rise on the number of stitches arresting its propagation. Thread diameter also improves the fracture toughness due to the enhancement on tensile strength and stiffness by the thicker threads by maintaining the same stitch pitch or stitch areal density [119], [124], [126]. Stitched composites has improved the impact resistance under low energy [115], [127], [130]–[132], high energy [133], [134] and ballistic [135]–[138]. As a result, compression after impact (CAI) strength is significantly increased [110], [137], [139], [140] until 400% [141] relatively to unstitched specimens. However, in-plane properties usually report a decrease in tensile strength [127], [142]–[144], achieving more than 80% [112]. The extent of damage during stitching reinforcement increases with the stitching density and the thread diameter, leading to reductions in tensile properties [144]. On the other hand, compressive strength can present slight improvement [139], not affect significantly the strength [108], [145] or be reduced [109], [128], [137], [146] up to 50% [137].

The laminate properties of stitched composites depend on several parameters, such as thread tension, fabric compaction by stitching tools and thread, type of needles (size and shape), thread type (size, stiffness and strength), preform fabric material, fiber orientation, stitching process speed, preform thickness, stitching density and stitching pattern [147]. These parameters can alter significantly the degree of defects and damages which lead mainly to a reduction in the in-plane properties.

The needle penetration into fabrics causes fiber breakage, and the extent of this damage is mainly related to needle diameter, thread diameter as well as fabric density. Stitching insertion

also causes fiber misalignment around the reinforcement and consequently resin pocket zone (Figure 1.13a). Thread diameter is the primary parameter associated with these defects due to the increase in the fabric waviness. The stitching reinforcement generates fiber crimp on the surface of the preform mainly caused by the shear stress, and strain applied, as well as by pressing the reinforced preform in a pressurized mold during the molding process, which generates the local bending effect (Figure 1.13b-c). The adjusting of the tension applied to the stitched yarn can diminish this issue. Moreover, compaction may also create stitches crimp effect during a liquid composite molding process (Figure 1.13d).

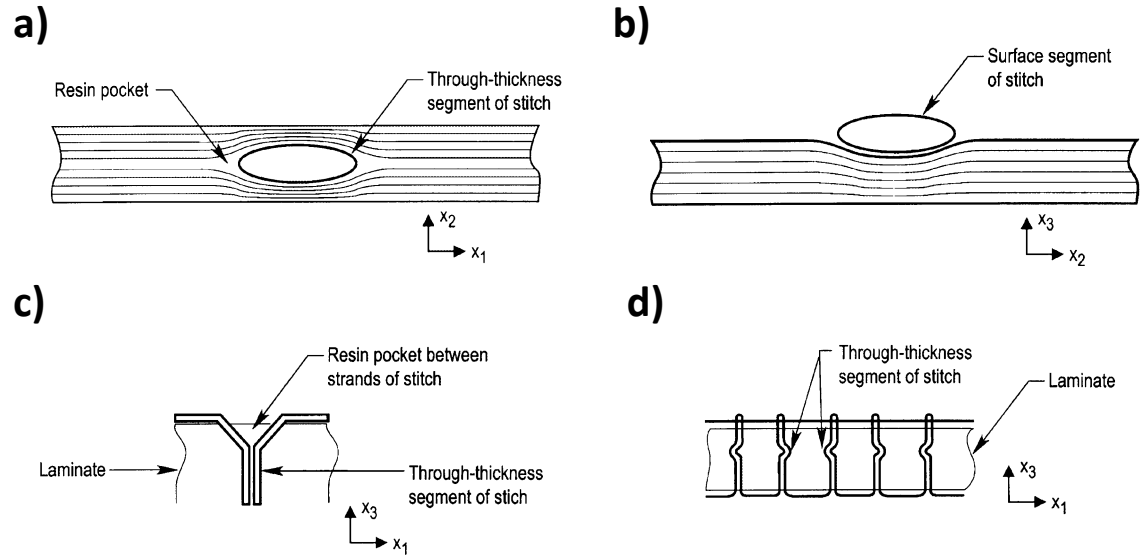


**Figure 1.13- Schematic of the main stitching defects** [114] **a) in-plane fibers misalignment, b) through-thickness fibers crimp, c) resin pocket created on the laminate surface between the stitched threads and d) stitched threads misalignment.**

### d) *Single-sided stitching techniques*

Single-sided stitching technologies are proposed for replacing the conventional stitching processes to overcome the drawbacks associated with the access on the dry preforms from the bottom side. Single-sided stitching that comprises two-needle ITA stitching, One Side Stitching®, blind stitching, and tufting are borrowed technologies from the textile industry and adapted for composite applications [81]. Different from the conventional techniques, these single-sided methods enable manufacturing large composite structures with complex geometries which can only be accessed by one side. In the last decades, single-sided stitching process has been developed in Germany [148], [149] to provide new ways of through-thickness

reinforcement using stitching heads mounted on a multi-axis robot. This increases the precision, flexibility, and agility for the manufacturing process of composite structures.

**Two-needle ITA**

The one-sided stitching technology developed by the Institute for textiles (ITA) of the university RWTH Aachen consists of two needles inclined by 45° on the top of the dry preform. Each needle introduces the thread through the preform, forming a loop on the underside when moving upward, which is subsequently caught by the other stitching needle and interlocked on the top of the preform (Figure 1.14). Due to both inclined stitching needle, this process is limited to preforms thickness up to 8 mm. A little information is found in the literature concerning this technique and the mechanical properties of the stitched composites, making any discussion impracticable.

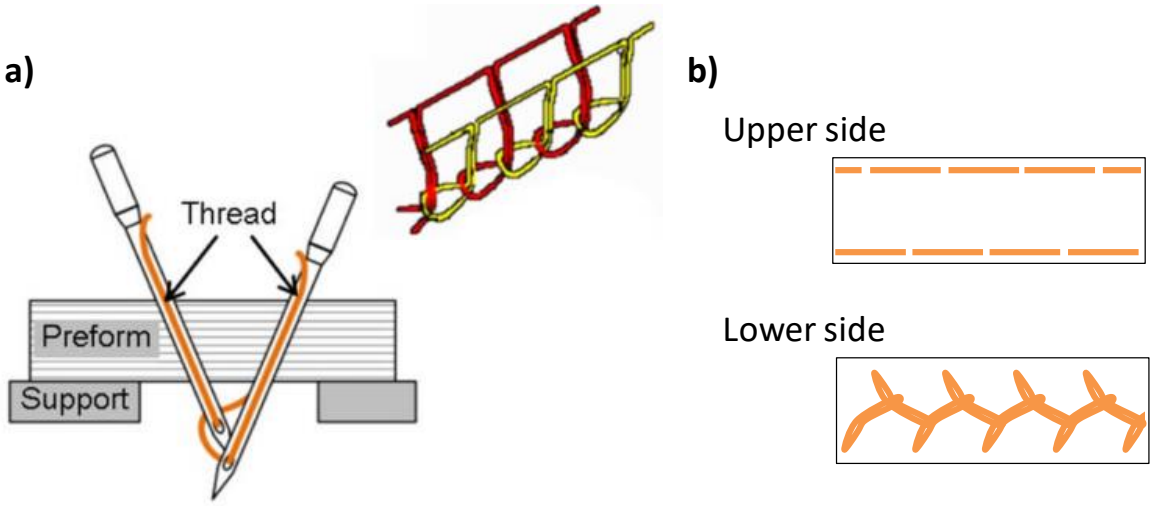


**Figure 1.14- ITA stitching technique: a) needle configuration and stitch pattern**[79]**, b) stitch pattern for upper and lower views adapted from** [150]**.**

**One-side stitching (OSS®)**

The company Altin-Naehtechnik (Germany) developed the OSS® technique that is based on the single-side reinforcement using two needles disposed on the upper side of the dry preform [113]. The stitching architecture is similar to that presented by chain stitching method. The process uses two needles, one oriented vertical and other inclined by 45° (catcher needle), and free space under preform for the penetration of the needles must be considered to perform the reinforcement. The vertical needle inserts the thread through the preform thickness and achieves

the bottom side, where it forms a thread loop after an upward motion of the needle. The inclined needle catches the loop and carries it to the top side of the preform, interlocking the loop with the previous stitched loop [151] (Figure 1.15). The composites reinforced with OSS® process may enhance the fracture toughness about 4 times in mode I and 76% in mode II loading condition [152]. The ultimate strength of the stitched composites was not significantly modified under open hole compression (OHC) and CAI tests when compared to the unstitched specimens [153]. The investigations of T-joints reinforced by OSS [151], [154] reported an increase in failure strength under pull-off tests by up to 25% [155].

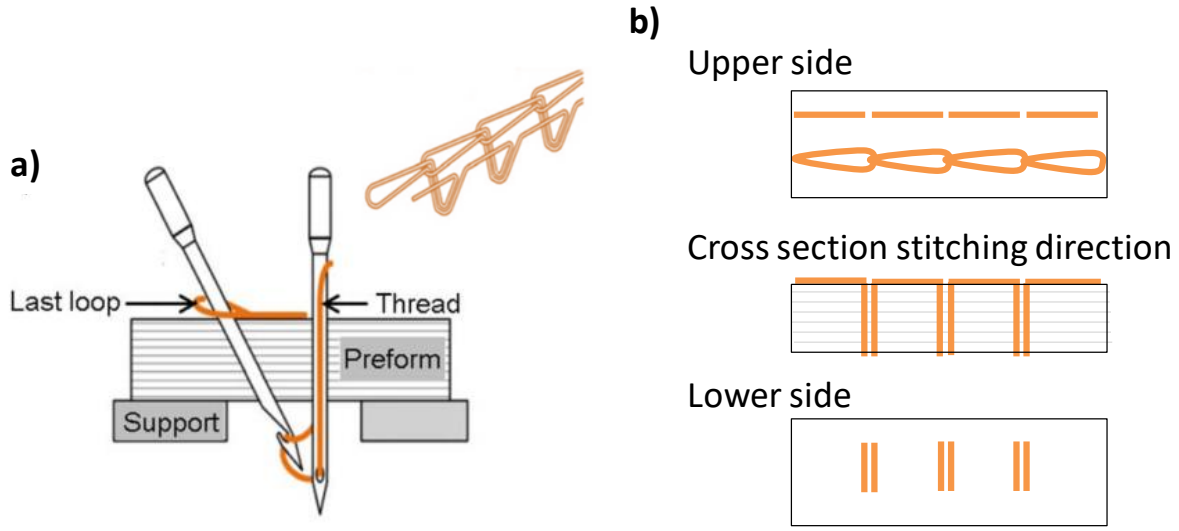


**Figure 1.15- OSS® technique: a) needle configuration and stitch formation adapted from** [79]**, b) stitch pattern views adapted from** [150].

Latécoère developed a Type A aircraft door for the COMDOR project, applying OSS® technology to reinforce the composite through-thickness as well as maintaining the position of the dry-preforms during manufacturing. The stitched composite door (Figure 1.16) avoided the insertion of about 800 titanium fasteners, which may increase weight and cost in the structure, currently employed on Type A composite doors to attach the molded stringers, beams, and frame to the skin of the door [156].

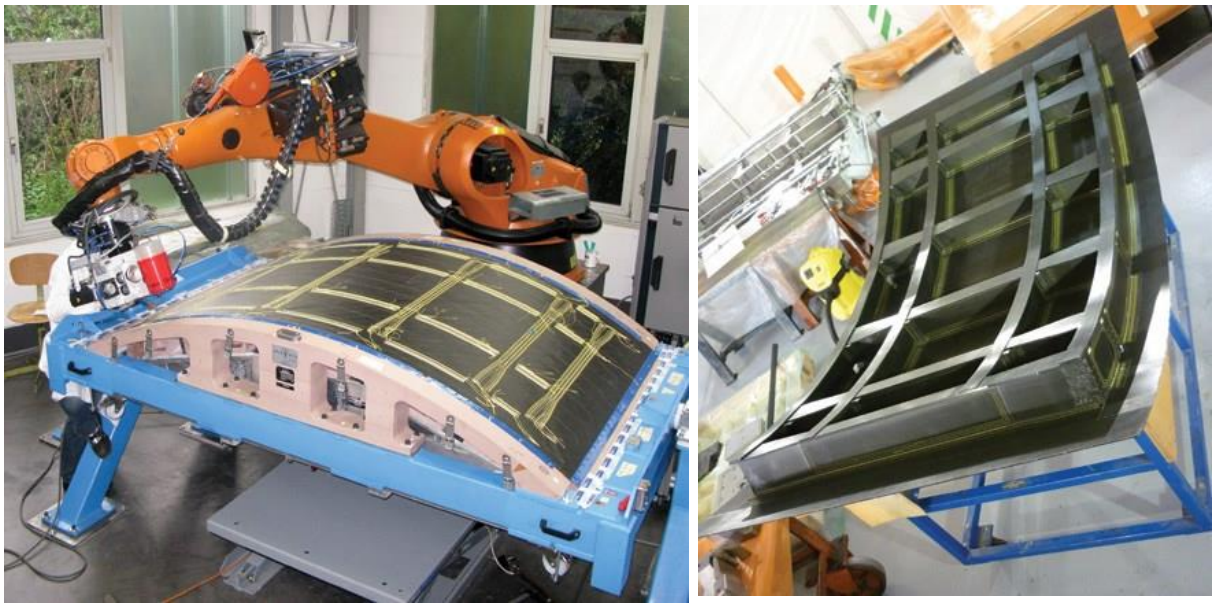

**Figure 1.16- Aircraft door reinforced via OSS® technology (developed by Latécoère).**

### Blind stitching

In the blind stitching technique developed by Keilmann Sondermaschinenbau GmbH (KSL), dry preforms are reinforced through-thickness by a curved needle of 50 mm from its top side. The inserted single thread forms a curved trajectory which leaves from the same surface and is caught from the loop created at the end of the stitch by a separate hook. Then, it interlocks with the previous thread loop on the preform surface (Figure 1.17) [157]. This method is capable of improving the debonding resistance of skin-stringer, increasing the maximum load of about 38% as well as the ductility under 3-point bending[157].

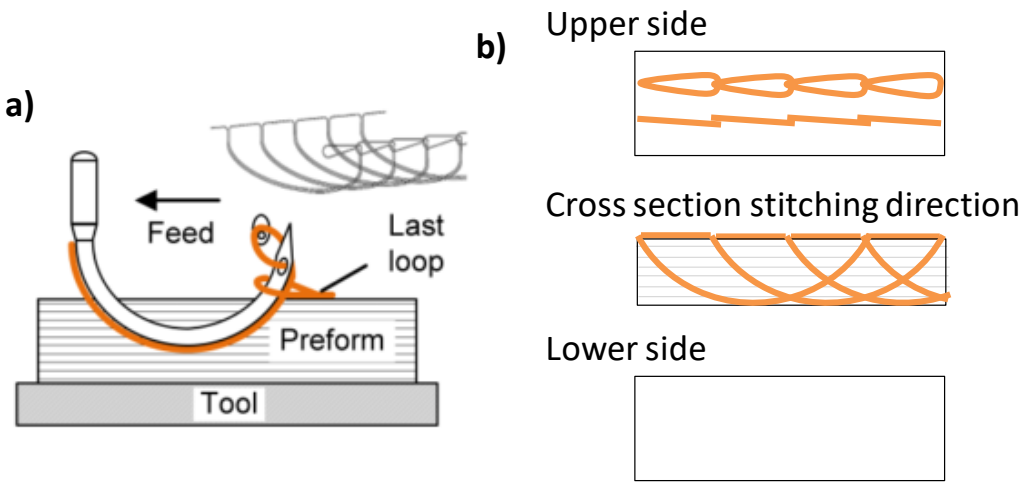


**Figure 1.17– Blind stitching technique a) needle configuration and stitch formation** [79] **and b) stitch pattern views adapted from** [150].

Blind stitching technology has been already applied on an industrial scale to manufacture the rear pressure bulkhead of the Airbus A380 jet airliner. Six widths of carbon dry-preforms were stitched together to obtain the appropriate dimensions of the rear pressure bulkhead measuring 5.5 m x 6.2 m (Figure 1.18) [158].

**Figure 1.18- Dry-preforms joined together by blind stitching technique and laid on mold [159].**

### Tufting

Tufting is a single thread method that differs from the other mentioned single-side techniques for not interlocking the threads during the process. A hollow needle pushes the thread into the dry-preform and during the upward motion to the top of the surface creates a loop due to the friction between the preform and thread. A presser foot maintains in place the already inserted tuft until the subsequent needle penetration (Figure 1.19a) [79]. The stitched loops typically become visible in the bottom of the preform, but tuft depth can be controlled to ending the loop inside of the material as a blind stitch (seen on step 2 in Figure 1.19a). The advantage of this process is the low tension introduced during the insertion of the thread [160]. It diminishes the stitching effect on the in-plane properties of composite laminates [161]. However, due to the non-interlocked stitches, tufted fabrics must be carefully handled until a liquid molding process to avoiding tuft loosening (Figure 1.19b).

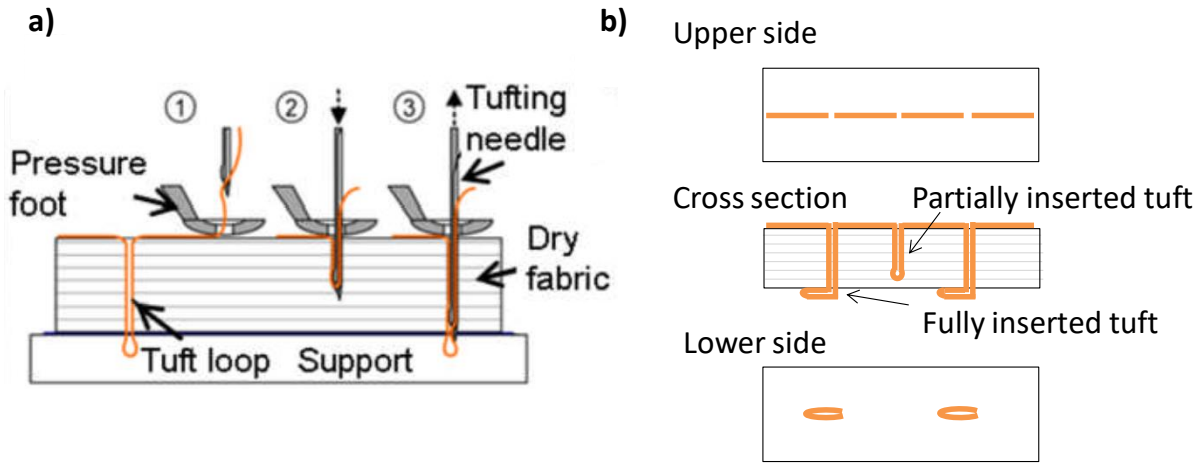


**Figure 1.19- Tufting technique a) different stitching steps** [79]**, b) stitch pattern views.**

Tufting process allows a maximum variability of its parameters as stitch spacing, seam radius, insertion angle (45°-135°) and preform thickness thanks to its simple mechanism and compact tufting head design in comparison with the others single-sided stitching technologies [79]. Figure 1.20 presents manufacturing of a tail cone using the tufting process to reinforce the dry-preforms [116].

**Figure 1.20 - Tail cone made of carbon composite reinforced by tufting technique** [116].

Table 1.1 outlines the main characteristics of each single-sided stitching process.

**Table 1.1 – Stitching methods and their main characteristics ( adapted from**[150][79]**).**

| | ITA | OSS | Blind | Tufting |
|---|---|---|---|---|
| **Speed ($min^{-1}$)** | 2 x 700 | 500 | 500 | 500 |
| **Max laminate thickness (mm)** | 5 (-8) | 20 | 10 | 40 |
| **Stitch spacing (mm)** | 3-7 | 2-10 | 5-10 | ≥ 2 |
| **Thread consumption** | -High fiber consumption | -High fiber consumption | -Large thread demand<br>-Low efficiency | -Very high efficiency with optimal placement in the laminate |
| **Handling** | -Easy handling due to the interlock of the threads | -Easy handling due to the interlock of the threads | -Possible stitching in a rigid tool<br>-Lower layers are not stitched | -No interlacing, thus no joining between the single layers<br>-Possible stitching in a rigid tool |
| **Fiber disorientation** | -Material penetration with 2 needles: great misalignment | -Material penetration with 2 needles<br>-Different orientation of 3D-reinforcement | -The stitching process does not influence lower single layers<br>-Local thread concentration; therefore, high shear | -Low thread tensioning<br>-Thick needle necessary, thus misalignment and fiber breakage on fabric tows of the preform |
| **Compaction** | -High compaction due to the interlocking of the stitches | - Seam width influences the material in a larger area | -Compaction of the layers are adjustable<br>-Due to the pre-compaction slight deviation of needle possible | -Thread strength (joining) insufficient for insertion of compaction<br>-Low fiber material in the laminate |

The following section focuses on the tufting technique and the mechanical properties of tufted composites.

### 1.3.3 Mechanical properties of tufted composite laminates

#### a) *In-plane properties*

Through-thickness reinforcements can improve the out-of-plane mechanical properties of composite laminates while in-plane properties report a significant decrease [77], [144], [162]. Tufting reinforcements have shown controversial findings in the literature, with negative results[140], [161], [163]–[165], negligible[166], [167] as well as positive effect [161], [165], [168] on the in-plane stiffness and strength. The laminate layup and several tufting parameters such as density, the angle of insertion, thread type (e.g., material and diameter), needle diameter, speed, and pattern can alter the in-plane behavior as described in others stitching techniques [114], [144], [168]. As any other stitching technique, the tufting process may create defects in the dry preforms during insertion and consequently reduce the in-plane properties.

Dhanapal et al. [161] reported a 30% decrease in the tensile strength of the unidirectional carbon composites reinforced by tufting in comparison with the control specimens. On the other hand, tufted composites with quasi-isotropic layup increased 3.5% the tensile strength. The same behavior was described by M. Colin de Verdiere et al. [164] when studying tufted NCF laminates with two different layups ($[0/90]_{3S}$ and $[\pm45]_{3S}$) under tensile tests. NCF composites with $[0/90]_{3S}$ layup reduced 13% the tensile modulus and strength compared to untufted laminates. Otherwise, $[\pm45]_{3S}$ tufted laminates improved tensile modulus by 12% and kept the tensile strength very similar to the control specimens. Treiber et al. [169] investigated the tufting density (0, 0.5 and 2% of the areal density of the laminate) effect on the in-plane properties of carbon composite laminates, describing a decrease of the tensile strength by 19% with 0.5% of tufting density. However, when increasing the tufting density to 2.0%, the difference is no longer evidenced in comparison with the 0.5%. Carvelli et al. [166] also reported improvements in the tensile strength up to 22% at increasing tufting density of NCF laminate composites while tufting insertion did not affect the tensile modulus.

#### b) *Out-of-plane properties*

Tufting reinforcement has been shown to improve the fracture toughness under both loading modes I and II. In general, for mode I loading condition, the interlaminar tufting increases the

delamination resistance by reducing the crack opening displacement, while in mode II, it increases the delamination resistance by resisting crack sliding displacement [23]. Karuppannan et al. [161] compared unidirectional and quasi-isotropic tufted carbon fiber composites, obtaining values more than 16 times higher for the mode I fracture toughness when compared to control specimens. Plain et al. [170] investigated the mode I fracture toughness of tufted composite laminates reinforced at three different angles (0º,22.5º, and 45º) and, presented results 2.35 times superior to the 0º tufted laminates than to the control composites. A 2.5-fold increase on opening mode has also been reported to tufted composites against untufted samples by Lombetti et al. [116]. Pappas et al. [171] evaluated the mode I fracture toughness of tufted composites at different densities and tuft loops. The maximum value was six times higher, achieved for the higher tuft density of the composite laminates without tuft loops. However, there is a lack of works on the literature reporting the fracture behavior of tufted laminates under mode II loading. It should be related to difficult to apply pure mode II loading due to the opening mechanism acting in the delamination crack [172]. Bigaud [173] described a 5-fold increase of the total fracture toughness on shear loading for the tufted specimens. Verdiere et al.[174] studied the tufting effect on mode II fracture toughness of the carbon non-crimp fabric composites and found values two times higher than the untufted samples.

Deconinck et al. [175] studied the behavior of high-velocity impact in tufted carbon fiber composites. The delamination area was decreased up to 24% in comparison to untufted specimens while increasing the tufting density. Dell'Anno et al. [163] investigated the CAI strength on carbon fiber composites reinforced by tufting with carbon and glass threads. The authors reported an increase of CAI strength by 25% and 27% for carbon and glass threads respectively. Scarponi et al. [140] also presented the improvements in CAI strength by employing tufted aramid fibers reinforcements. They studied the techniques of low and high tensioned lock stitch, tufting and z-pinning to reinforce trough-the-thickness carbon fiber preforms. The tufted laminates showed CAI strength superior to the others techniques and especially 16% higher than the control specimens.

Table 1.2 summarizes some results reported in the literature for tufted composites under different loading conditions, emphasizing the higher and lower values when compared to the control specimens. The values presented consist of studies with different stacking sequence and preform material as well as tufting parameters (e.g., tuft density, thread material, tuft diameter and angle of insertion).

**Table 1.2 - Tufted composites results in comparison to unstitched specimens under different loading conditions.**

| | Higher value | Lower value |
|---|---|---|
| **Compressive strength** | 15% [176] | -19% [161] |
| **Compressive modulus** | 2% [79] | -11% [176] |
| **Tensile strength** | 22% [166] | -30% [161] |
| **Tensile modulus** | 2%[169] | -13% [176] |
| **Interlaminar shear strength** | -17% [177] | -38% [177] |
| **Mode I** | 16 times [161] | 2.5 times [170] |
| **Mode II** | 5 times [173] | 2 times [174] |
| **CAI** | 27% [163] | 16% [140] |

The enhancements of out-of-plane properties are also reported for tufted sandwich structures. Lascoup et al. [178] obtained improvements of bending module (278%) and maximum stress (9 times greater) under 4-point bending tests in comparison to the untufted specimens. Moreover, a 14-fold increase of the stiffness and the ultimate stress 8 times superior were achieved under transversal flatwise compression tests. The impact resistance was also enhanced and described by different authors[179]–[182].In general, the stitched sandwich composites were capable of bearing greater impact loading, absorb more the impact energy, reduce the damaged area and penetration depth. Lascoup et al. [179] reported a 2.5-fold increase on the load of the first significant damage and a reduction of 30% in the maximum penetration under impact loading compared to untufted structures. They achieved the values when reducing the tufting density from 50 to 12.5 mm stitching space with a reinforcement inclined by 45°. Samlal et al.[180] studied sandwich plates reinforced by tuft threads at 45°, reporting considerable improvements on the load carrying capacity and ballistic limit. Taylor et al. [181] also investigated tufted sandwich structures and, observed an increase of the absorbed energy under impact loading at increasing the tufting density. Fan and Xiao-qing[182] described a decrease of the damaged width and penetration depth of the tufted structures impacted at 25J of 67% and 4% respectively, for the core sandwich composites transversely tufted.

In general, as reported above, tufting finds its full interest in laminated plates and specimens scale when subjected to out-of-plane loading. Thus, the discussion follows with the investigation of the contribution of this technique in structure scale and stiffened pieces reported in the open literature.

Composites stiffened panels are widely in many parts of the aircraft to increase efficiency regarding stiffness, strength, and weight-optimization [1]. This type of structure is composed

of a thin-walled composite plate braced by a certain number of shaped stiffeners (e.g., Ω, I, T, L, C, Z, and J) in one direction [183]. Because their efficiency to carry loading when compared with unstiffened plates, they are widely adopted in aircraft wings, vertical/horizontal tails, and structural configuration for the fuselages [184], [185]. However, these parts, mostly manufactured by 2D laminated composites, exhibit low out-of-plane properties. This response can be due to a weak interaction in the junction between two-parts (skin/stiffener) assembled via bonding manufacturing, but mainly owing to the reduced mechanical properties of the polymers. Besides, a poor interface produced during the molding process can also reduce the out-of-plane properties. The mentioned issues can lead to the initiation and propagation of delamination, especially during the structure loading in the mentioned regions, which reduces the load-bearing capacity of the composites expressively.

Tufting method has been used to reinforce the stiffeners in order to enhance their performance and damage tolerance. Cartié et al. [92] investigated composite T-joints reinforced with tufts (Figure 1.21a) under quasi-static and fatigue pull-off loading. The delamination between the skin and the stiffener stopped entirely and the samples failed in bending. It increased the load carrying capability and energy dissipation during quasi-static tests (Figure 1.21b) as well as the lifespan on fatigue loading by 12.5 times.

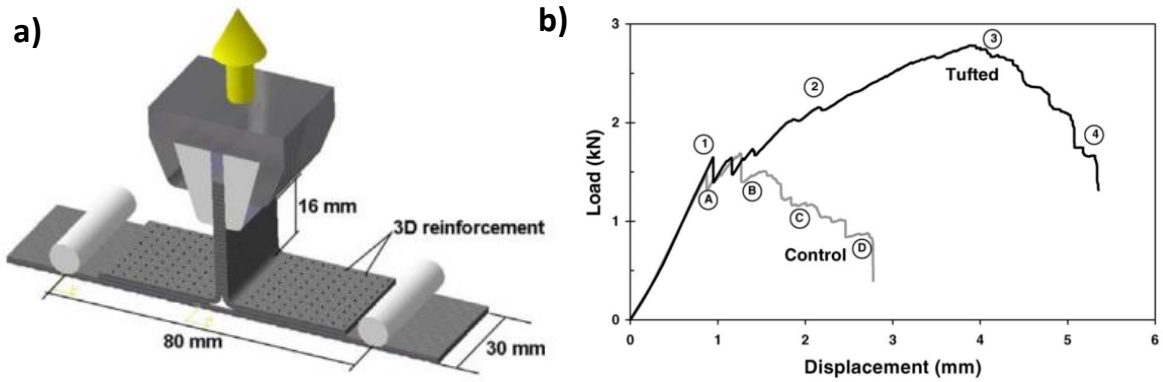


**Figure 1.21 - a)schematic of T-stiffener reinforced by tufting technique under pull-off tests and b) Typical load displacement plots for the tufted and control T-stiffeners under pull-off tests** [92].

Kratz et al.[186] studied glass fiber T-stiffeners reinforced with carbon tufts. The specimens were submitted to 4-point bending, presenting an increase of the failure initiation load (up to 16%), and slight improvement of the stiffness and absorbed energy (force *times* displacement) for the tufted structures in comparison with the control specimens. Clegg et al. [187] reported an improvement up to 39.5% of the absorbed energy under 4-point bending by varying the tufting position in the carbon fiber T-joints (Figure 1.22b). The considerable improvement

compared to Kratz et al.[186] is mainly due to the tufting reinforcement in the noodle region (Figure 1.22a).

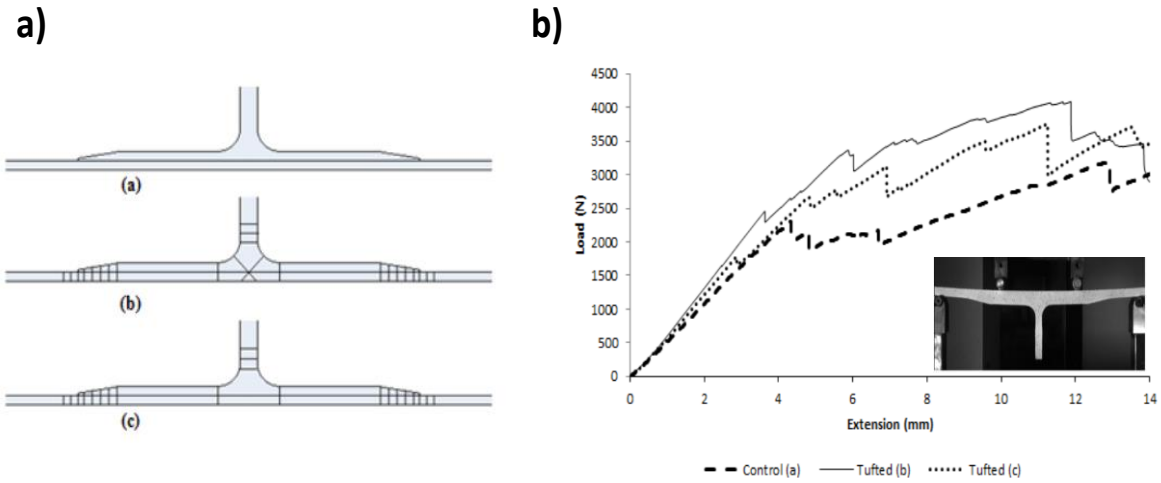


**Figure 1.22 - a) Untufted specimen and specimens configurations based on the tufting position in the T-stiffeners and, b) Typical load-displacement for the control and tufted variants submitted to bending tests**

Stickler et al. [188]–[190] utilized a different approach to manufacture T-joints stiffeners. It consists of linking vertical web and skin preforms using tufting reinforcements (Figure 1.23). A variety of mechanical tests were performed comparing a range of tufting density. However, an investigation between the tufted and control specimens are not possible, which leads only a discussion of the different tufting parameters and their mechanical behaviors.

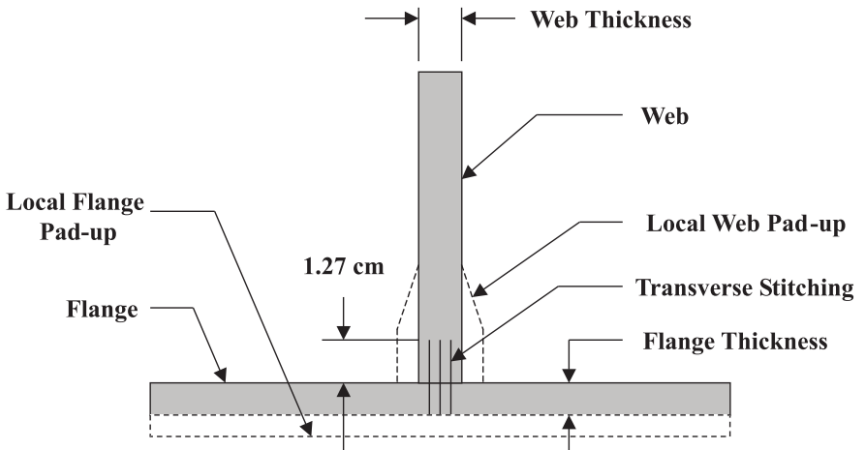


**Figure 1.23 - Illustration of the tufted T-stringer and its variations (dashed lines) investigated by Stickler et al.** [189].

Mills et al. [191] investigated the tufting density and thread material effect on carbon fibers T-stiffeners. The manufacturing of the structures utilized a pre-infused and cured web plate, positioned between the two flanges of dry-preforms. The flanges were tufted with the skin, and subsequently, the infusion process molded of the whole structure. Figure 1.24 presents the

molded T-stiffener plate with the two different regions reinforced by glass and carbon fiber threads. The pull-off tests carried out in the specimens showed a considerable enhancement of the absorbed energy, especially for the densest tufting specimens, 309% and 215% for carbon and glass fiber threads respectively. Maximum load was also improved up to 54% and 62%, for carbon and glass fiber threads respectively when compared to the control structures.

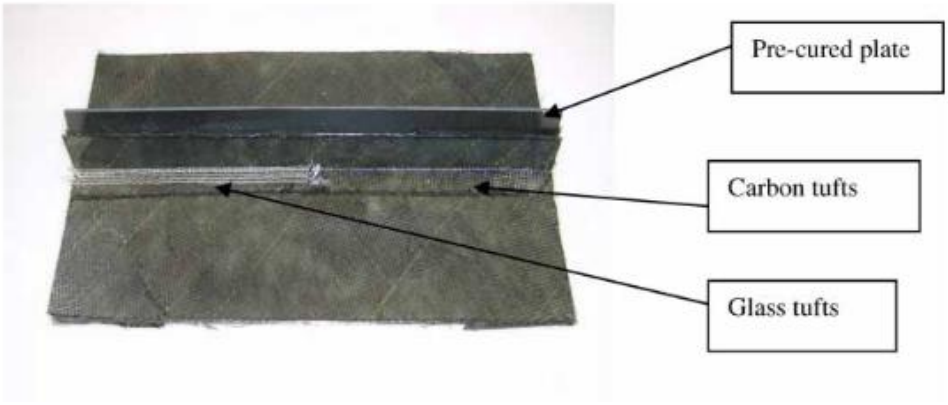


**Figure 1.24 - Carbon T-stiffener plate tufted on the flange region with carbon and glass fibers thread**[191].

Omega stiffeners reinforced through-thickness with tufts were investigated by Préau et al.[192]. Pull-off (Figure 1.25) and 4-point bending loading tests aided to evaluate the effect of the tufting depth (partial and full insertion) in the laminated composites. Tufted specimens with partial insertion presented great improvements of the absorbed energy (10 times superior on 4-point bending) and maximum load (more than 45% on pull-off loading) to both loading conditions over untufted specimens. The stiffener and skin parts maintained connected due to the crack bridging properties of the tufts, differently from the control specimens that presented a sudden failure. Additionally, the partial insertion avoided the issues regarding the tufting reinforcement in the initiation failure threshold as seen in the fully tufted specimens.

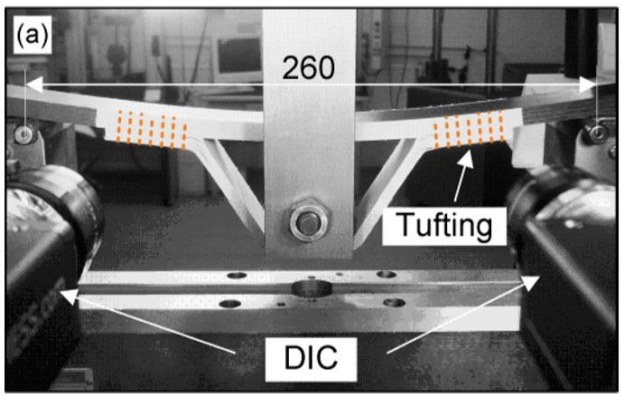


**Figure 1.25 - Tufted omega stiffener submitted to pull-off test** [192]**.**

## 1.4 Conclusions

Several works have been reporting the improvements on the out-of-plane properties and damage tolerance under different loading conditions of laminate composites reinforced by tufting. The tufting process has shown advantages as a single side stitching method for controlling the reinforcement parameters such as tuft density and angle of insertion, mainly thanks to its single needle. These parameters contribute significantly to improve the interlaminar strength of laminated composites, as already reported in this chapter. However, tufted composites have reported a significant decrease of the in-plane properties due to the damages generated when inserting tufts into the preforms, and present the damage extent related to the tufting parameters (e.g., tuft density and thread diameter).

Through this bibliographic review, the works that accurately describe the mechanisms of damage initiation and propagation in the presence of tufting are rare. They report only a quantitative evaluation of the composite performance without locally analyzing the effect of tufting. It is believed in this thesis that the understanding of the damage mechanisms is essential for optimizing the reinforcements in the structure as well as to perform upcoming models capable of simulating and then predicting the damage behavior of such structures.

The traditional insertion of tufts in the entire laminated composite has to be avoided, because of the significant damage amount created. It is important to understand "why" and "how" the mechanisms involved in the presence of tufts behaves. This may help to enhance the insertion of tufts in order to diminish the mentioned issues.

The analysis of the mechanical behavior of untufted composites submitted to various loading conditions and characterized by multi- instrumented techniques as well as by post-mortem analysis helps to design the tufts insertion in the structure and may decrease the negative impact of these reinforcement embedded in the laminated composites. The present work utilized the mentioned approach to improving the mechanical response of stiffened structures reinforced by tufting and also investigated the tufts parameters in the in-plane properties and damage tolerance of composite plates.

Finally, this literature review did not find works regarding the health monitoring of the structures reinforced by tufting. However, if tufts can improve the strength of structures, they also become a key element in the composite and consequently, their state of health must be

constantly monitored. This thesis proposes a novel approach based on the inspection of the tufts that seems interesting and promising.

# CHAPTER 2 MATERIALS AND METHODS

## 2.1 Introduction

The present chapter summarizes the materials and process (Section 2.2) employed for the manufacturing of the tufted and control composites, as well as the mechanical test methods (Section 2.3), used to investigate their mechanical behavior in this study. Essential information about the tufting process parameters and the infusion process are described in section 2.2.1 and 2.2.2 respectively. The sections 2.2.3-2.2.5 present the manufacturing steps, from tufting reinforcement to composite molding, in order to obtain the laminate and sandwich plates, and omega-shaped stiffeners respectively.

The study was divided into three main topics based on the specimen format, as laminated plates, sandwich plates, and omega stiffened composite panels as seen in Figure 2.1. Three main categories subdivided the different laminate panels (Panel I, II and III), distinguishing for their different fabric preforms and tufting parameters employed. Panel I aided in the investigation of the tufting parameters, tufting density an angle of insertion, under different loading conditions as shown in the flowchart. Plate II varied the material of the preform (carbon and glass fiber fabrics) as well the tuft threads to evaluate the feasibility of the tufted yarns in monitoring the damage evolution (generate by successive impact loadings). The fatigue tests were carried out using the Plate III, which were reinforced by tufting and drilled after the molding process.

The sandwich plates were manufactured specifically to investigate the electrical resistance response of the tufted threads into the structures. This aimed to monitor the strain evolution in quasi-static and dynamic loading using the piezoresistive effect.

The omega stiffeners presented three batches of specimens that correspond to the developments from the batch I until the batch III. Batch II concerns the improvements on the structure geometry as means for enhancing the mechanical properties after mechanical characterization of the Batch I. This set of specimens were manufactured on glass fiber fabrics to evaluate the new mold and also for the in-situ electrical measurements from the tufted yarns. The mechanical response under pull-off tests aided to design the tufting parameters of the last batch (Batch III). The following sections present more details about the materials and the manufacturing process.

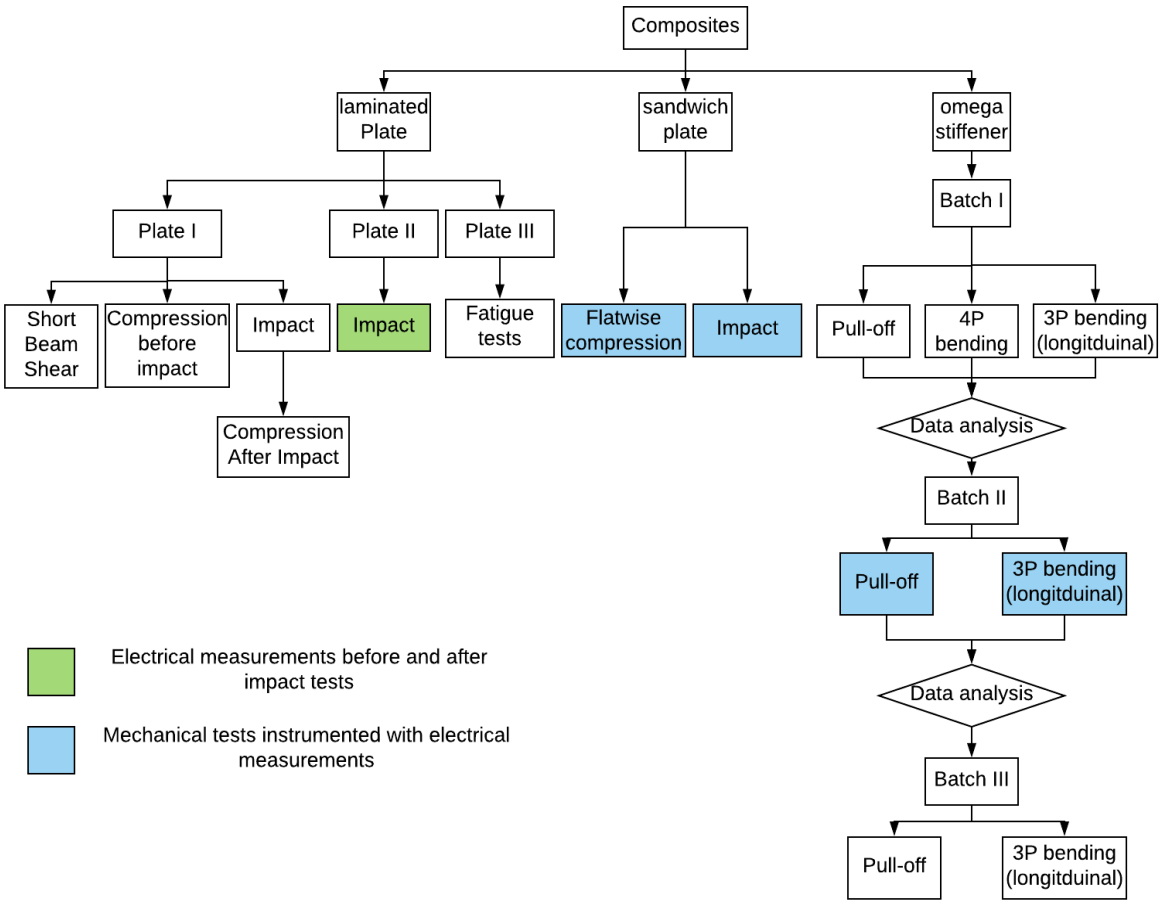


**Figure 2.1 - Flowchart of the different composites manufactured in this work and their associated mechanical tests.**

## 2.2 Materials and processing

### 2.2.1 Tufting process

The present thesis studied the mechanical behavior of laminated composites reinforced by the tufting process. This stitching method differs from the others due to the thread reinforcement inserted via a single needle which creates through-thickness reinforcement without interlocking the threads. The single needle allows great variation of the stitching density as well as the angle of insertion (Figure 2.2). Tufting areal density is composed of the stitch pitch in the tuft row direction (Sx) and the space between two adjacent rows (Sy). Tufting pattern uses mainly two basic configurations based on the alignment between two adjacent tufted rows that consist of the square and triangular pattern (Figure 2.3). This study employed only the square pattern to reinforce the composites. Tufting depth through the preform (Figure 2.2) is also controlled and

reported to change the mechanical behavior of the composites [192], [193]. The process can use foam under the dry-preform to hold the tuft loops when performing a complete insertion.

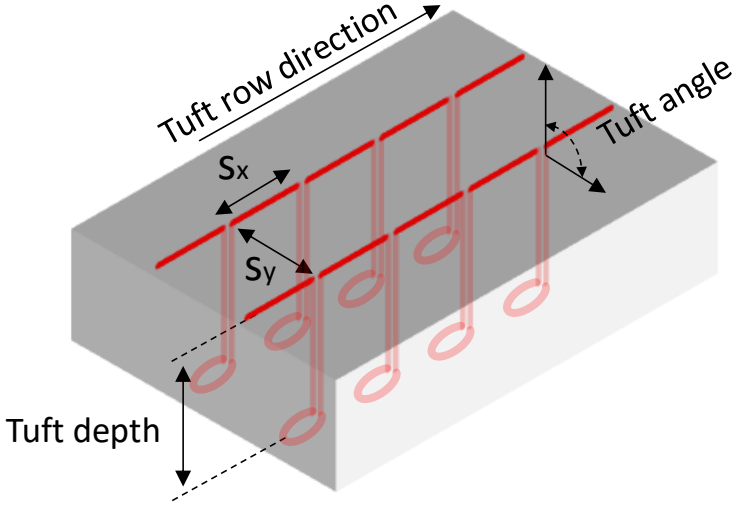


**Figure 2.2 - Tufting parameters.**

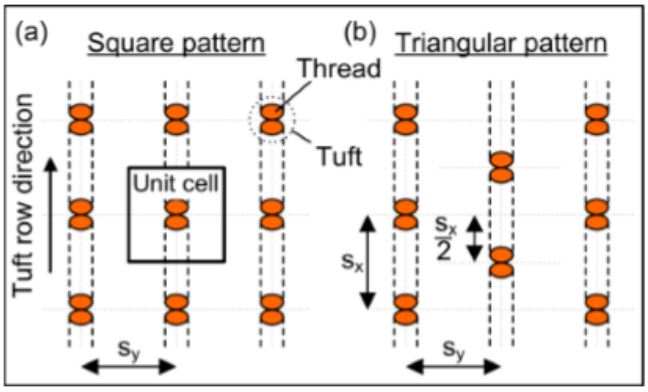


**Figure 2.3 - Typical tuft patterns** [79].

The tufting reinforcements carried out in this study utilized a tufting head (KSL RS 522) mounted on KUKA 6-axis robot arm (KR 100-2 HA 2000) as seen in Figure 2.4a. The software supplied by MasterCam® helped in the simulation of the tufting path reinforcements and the set-up of the tufting parameters (Figure 2.4b).

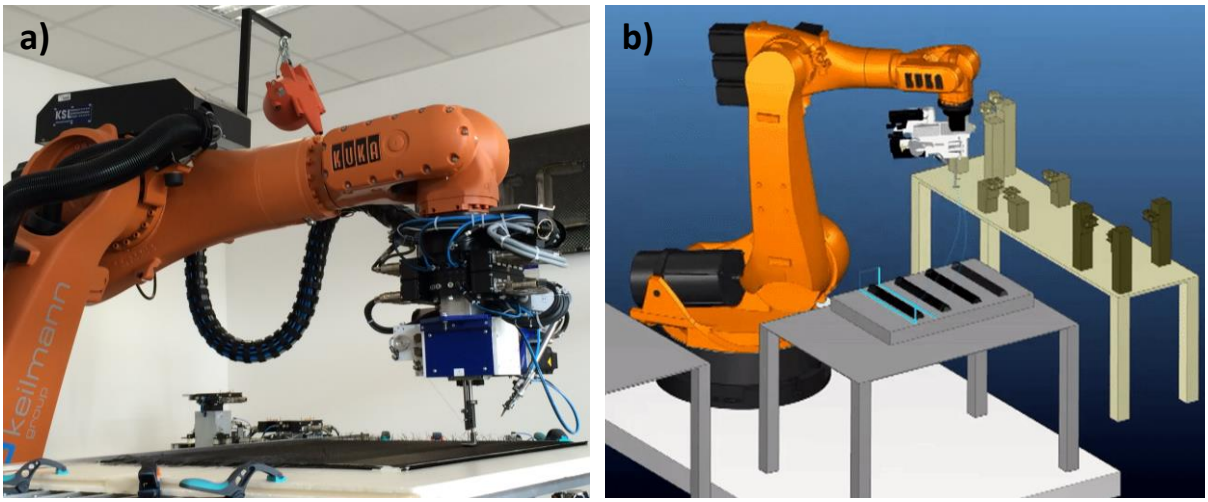


**Figure 2.4 - a) Tufting head mounted on 6-axis robot arm, b) Software of simulation employed to generate and evaluate the tufting path.**

The reinforcements used the same needle type (supplier KSL, model EP 11 Nm 230) for manufacturing the tufted dry-preforms. The presser feet applied in the tufting process were developed and made by a 3D printing method with a flat surface to avoid misalignments on fabric tows caused by locally-concentrated force. Figure 2.5a presents the former presser foot with curved surface utilized in the previous works. Additive manufacturing made the feet employed in the present work for transversal tufting (Figure 2.5b), inclined insertion of 60º (Figure 2.5c) and insertion in the corner of omega structures (Figure 2.5d).

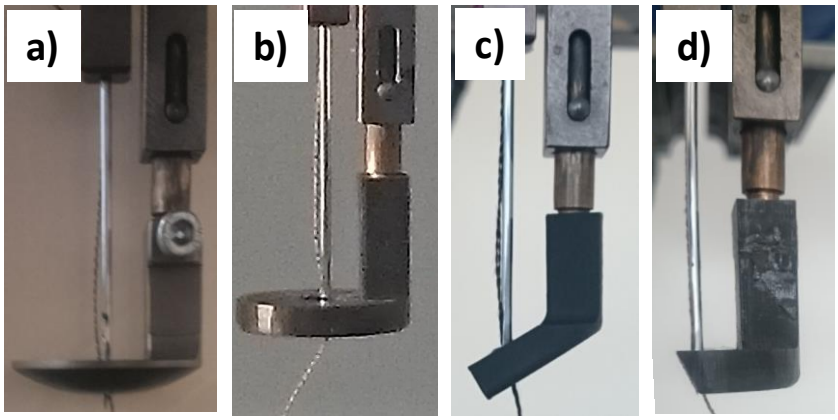


**Figure 2.5 - a) The former presser foot used on previous tufting process and, the 3D printed presser feet with plane bottom surface used for b) general reinforcements, c) inclined insertion of 60° and d) corner reinforcements of the omega stiffeners.**

A unique thread type was mostly used to reinforce the composites in this research. The carbon/PBO thread (2K Tenax-J HTA 40 carbon thread wrapped by two PBO yarns) is reported by Bigaud in her Ph.D. thesis [173] to present additional resistance, mainly due to its protection with PBO yarns, to the friction caused during the thread path from the heel until the insertion into the preform. This material diminishes the issues with broken fibers, described to reduce

the thread strength, as well as improves the flexibility when forming the loops. The PBO yarns also enhance the attachment of the tufted yarns with the dry-preforms, reducing loosening of loops during the handle of the reinforced preform.

### 2.2.2 Vacuum Assisted Resin Transfer Molding (VARTM)

VARTM consists of a vacuum infusion process which utilizes a rigid mold to provide part geometry while a thin flexible membrane over the dry preform is responsible for compress the fabrics against the rigid mold by atmospheric pressure. The flexible membrane aided by tapes seals the whole system and places it under vacuum. Then, resin impregnates the dry preform due to a pressure gradient imposed by negative pressure on the flow front. Figure 2.6 shows a schematic of the VARTM process. Generally, the process employs consumable materials such as infusion mesh and peel ply to improve the process performance.

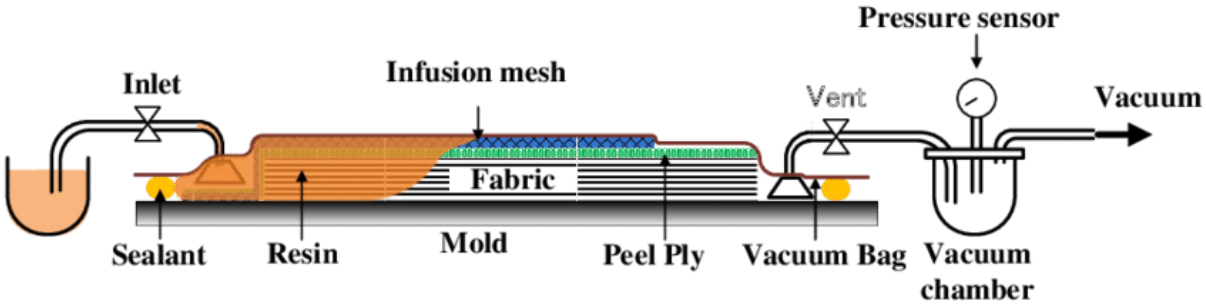


**Figure 2.6 - Typical VARTM process** [194].

### 2.2.3 Manufacturing of the composite laminated plates

#### a) *Tufting reinforcement*

**Plate I**

Woven carbon fabric/epoxy composites were manufactured using a 6K 5HS woven fabrics with 364 g/m$^2$ areal density. The tufting process utilized carbon/PBO threads to reinforce the laminates. Two laminates with a $[0]_{12}$ layup were made according to the angle of the inserted tufts. The transversal tufting introduced reinforcements parallel to the normal plane of the preform with tuft rows in the same direction of the warp tows (Figure 2.7), while angular tufting inserted threads at ±30° to the normal plane with the rows perpendicular to the warp direction (Figure 2.8). The choice of the insertion at ±30° consisted of the maximum angle possible due

to the machine limits. The preforms were divided into zones for the control specimens (untufted) and, for the 5×5 mm and 10×10 mm tufting density.

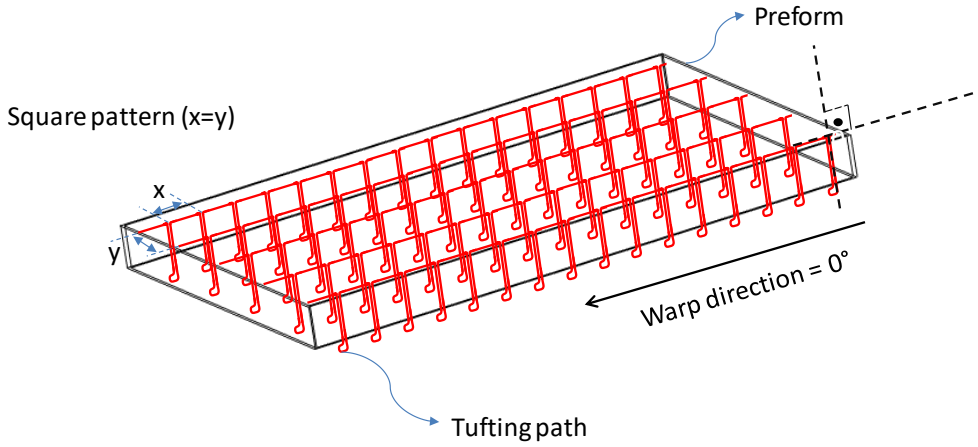


**Figure 2.7 - Schematic of the transversal tufted specimens.**

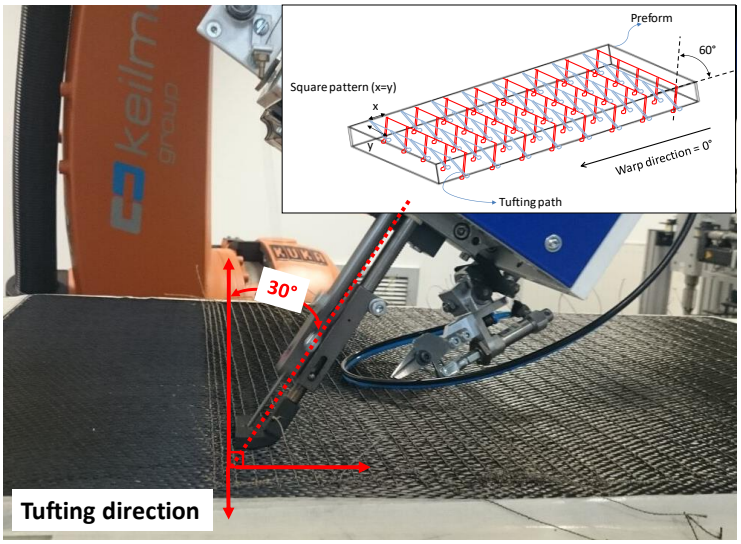


**Figure 2.8 - The insertion of inclined tufts of 30° and the schematic of the reinforced composites.**

Previous works developed in the laboratory concluded that the foam applied under the carbon fabrics was not sufficient to hold the tuft loops, which led to the insertion of a PA film between the foam and dry preform (Figure 2.9). This film aided to handle the material without loosening their loops, from the foam release until the molding process.

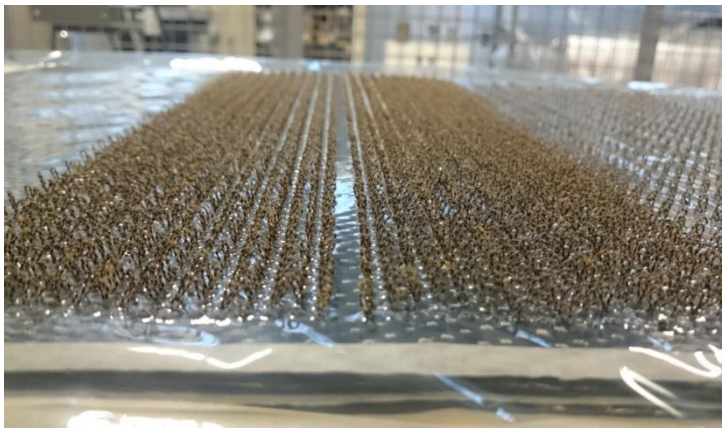

**Figure 2.9 - The inclined tufts exhibited from the bottom surface with their loops maintained by the film.**

### Open Hole specimens for the tensile and fatigue tests (Plate II)

The samples utilized for the open hole tensile and fatigue tests used a 2x2 twill woven fabric with an areal density of 200 g/m$^2$**.** Two specimen configurations with the same $[0]_{16}$ layup based on the distance of the tuft rows from the center width (Δx), equal to 7mm and 10mm, as seen in Figure 2.10a. The tuft density of 5x5 mm was performed for both configurations of specimens and followed the 0° direction of the stacking direction. Figure 2.10 presents the reinforced dry preform with the two tuft configurations as well as the unreinforced zone at the top of the image, left for manufacturing the control specimens.

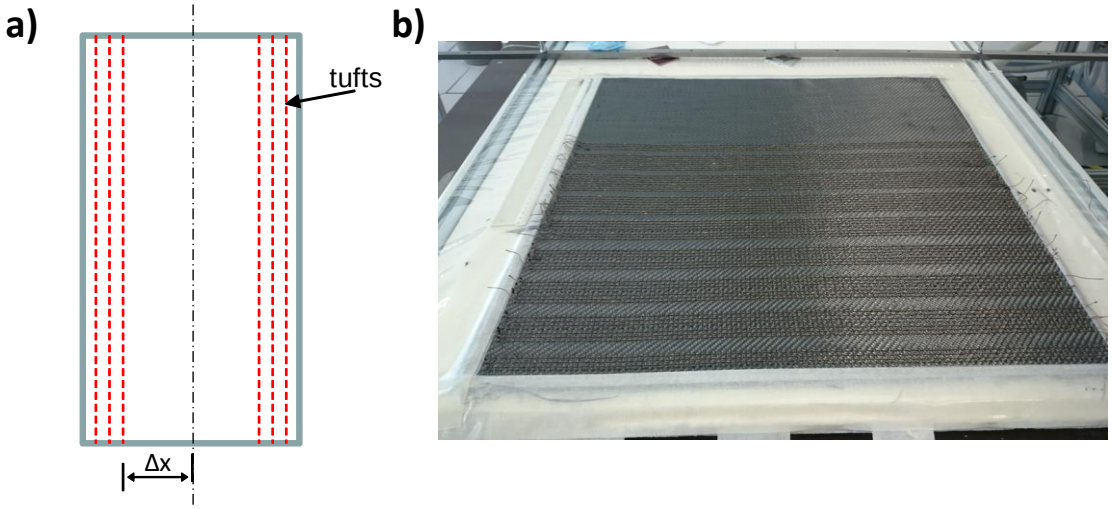


**Figure 2.10 - a) Schematic illustration of the tuft rows distance from the center of the specimens, b) Tufted preform with the upper side left intentionally unreinforced to produce the control specimens.**

**Composite laminates for the feasibility tests of the electrical resistance (Plate III)**

It was manufactured two laminate composites with the same layup $[0]_6$ in carbon and glass fibers 2x2 twill weave fabrics with an areal density of 200 g/m² and 280 g/m$^2$ respectively. Tufting performed reinforcements with both carbon/PBO threads and neat carbon threads (two twisted carbon fiber strands made of Tenax-J HTA 40 F15 1K 67 TEX). The tuft rows followed the width direction of the dry preforms (size of 150x500 mm). The tuft loops were adjusted as small as possible to avoid their contact that could change the electrical measurements by percolation.

Similarly, the tufting performed a square pattern reinforcement with 10x10 mm density to avoid this concern. Due to the short length of the loops, which could unfasten the tufting pattern during manipulation of the preform, PTFE film was used between the dry preform and PU foam to maintain the threads. The film releasing occured before the molding process.

**b)** ***VARTM process***

VARTM process utilized an EPOLAM 5015 epoxy resin system to mold the composite plates. Figure 2.11a exhibits similar process employed in the manufacturing of the laminates for impact and fatigue tests, while Figure 2.11b presents the two dry preforms (glass fibers and carbon fibers) infused on the same vacuum bag. During the infusion process, the vacuum pressure was about -1000 mBar at room temperature. The cure cycle was carried out at room temperature for 24 hours and post-cured at 80ºC for 16 hours.

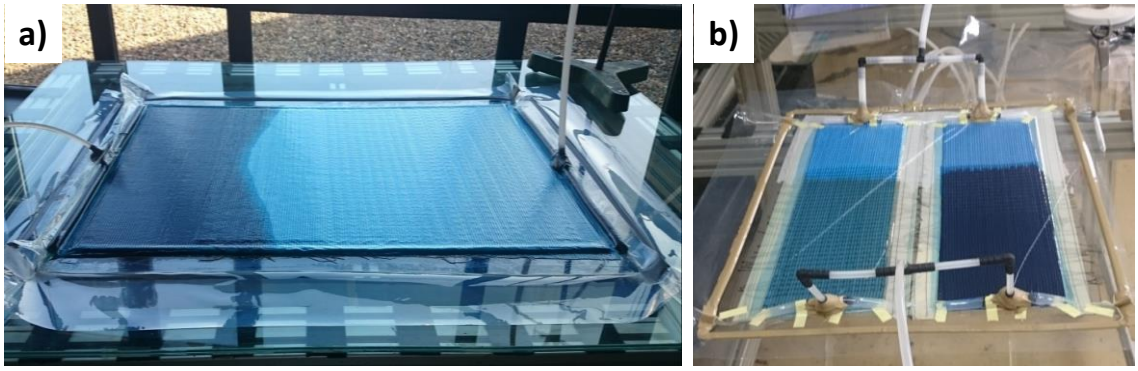


**Figure 2.11 - The infusion procedure employed to manufacture a) the Plate I and III, and b) Plate II.**

### c) *Specimens preparation*

Specimens with dimensions of 100×150 mm were prepared for the impact and CAI tests according to ASTM D7136-15 [195], with the warp direction aligned along the longitudinal side. Table 2.1 presents their designations according to the tufting density and angle of insertion utilized in the manufacturing of each set of the specimen.

**Table 2.1 - Specimens designation for Plate I**

| specimen | Tufting angle | Tufting density* (mm x mm) |
|---|---|---|
| **REF** | - | - |
| **T10** | transversal | 10x10 |
| **T5** | transversal | 5x5 |
| **A10** | Angular (±30°) | 10x10 |
| **A5** | Angular (±30°) | 5x5 |

The drilling procedures of the laminated composites specimens for the open hole tensile and fatigue tests were made thanks to Redouane Zitoune at *Université de Toulouse - Clement Ader Institute*. It applied two types of drilling tools, three lips twist (Figure 2.12a) and core drill (Figure 2.12b), to bore a hole of 8 mm diameter in the center of the specimens. The primary goal consisted of comparing the drill effect in the mechanical behavior of the laminates. More information concerning the drilling process does not pertain to the subject of this thesis. Figure 2.13 shows the schematic illustration of the specimens, regarding the tufts distance from the center, and their final dimensions. They are designated OH1_L, and OH1_C for the specimens tufted 7 mm from the central axis drilled by three lips twist and core drill respectively, while OH2_L and OH2_C correspond to the samples with tuft row 10 mm distant from the middle and bored hole by three lips twist and core drill respectively. Moreover, the identification of the control specimens consisted in CNT_L and CNT_C, based on to the holes performed by three lips and core drill in that order.

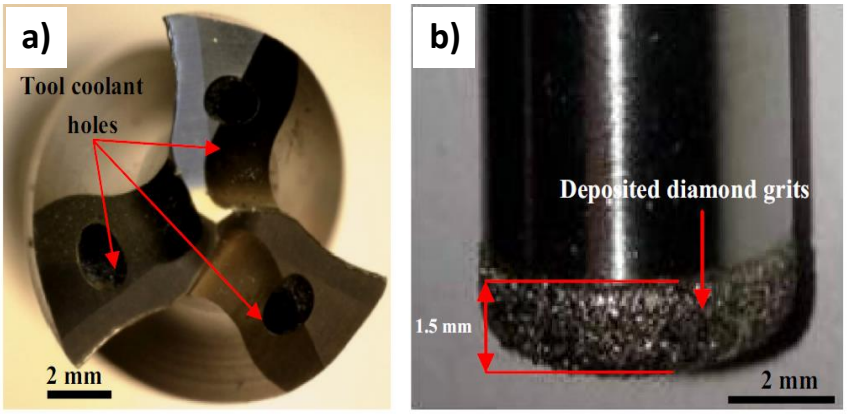


**Figure 2.12 - Drills utilized for boring the holes on the stitched specimens: a) Three lips twist drill and, b) core drill.**

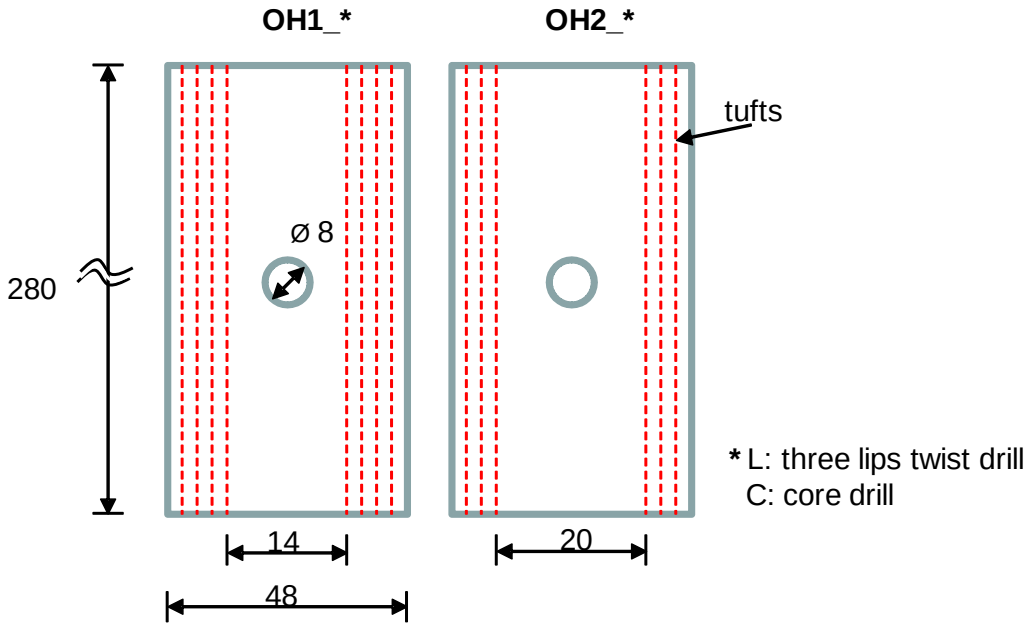


**Figure 2.13 - Schematic illustration of the tufted open-hole samples.**

### 2.2.4 Sandwich plates manufacturing

The sandwich structures studied in the present work consisted of polystyrene foam,18 mm thick, and two parallel face sheets with a $[0]_8$ layup for each face of glass 2/2 twill woven (280 g/m$^2$). Tufting process utilized carbon/PBO threads and tufting density of 10x10 mm and 15x15 mm for the manufacturing of the composites subjected to flatwise compression and impact tests respectively. Additionally, the insertion employed a support foam to hold the tuft yarns as exhibited in Figure 2.14.

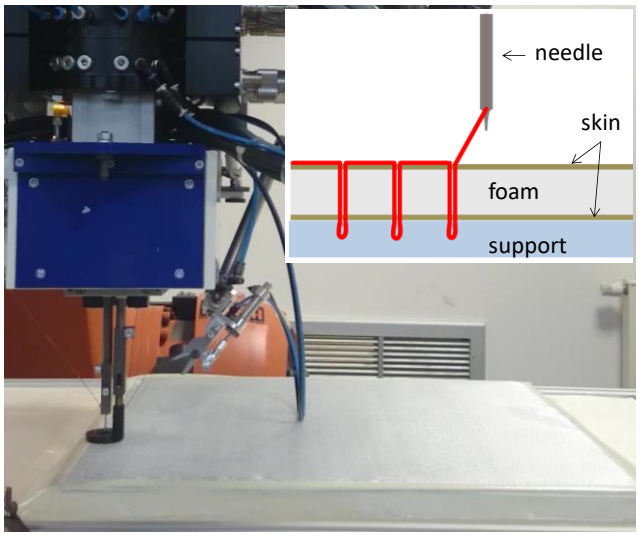


**Figure 2.14- Tufting reinforcement in the sandwich preform.**

The molding of the sandwich preforms by infusion process utilized an EPOLAM 5015 epoxy resin at about -1 bar of vacuum pressure (Figure 2.15). Further, the cure cycle occurred for 24 h at room temperature, followed by 16 h of post-cure at 80°C. The nominal final thickness of the sandwich plate was 22 mm.

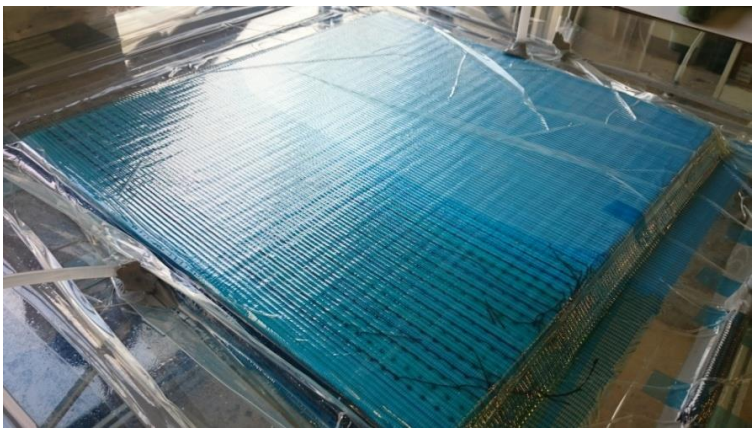

**Figure 2.15 - Vacuum infusion process of the tufted sandwich preform.**

### 2.2.5 Manufacturing of the omega-shaped stiffeners

The present section exhibits the manufacturing process to obtain the composite omega stiffeners. The mechanical behaviors analyzed in the first batch during and after mechanical tests permitted to develop the second and third batch of specimens based on the drawbacks found in the previous set. In order to manufacture the two later set of specimens, a new inner mold was developed with different dimensions to enhance the mechanical properties of the omega stiffened structures. The second batch of omega structures was fabricated especially to

test the new mold and to improve the manufacturing procedures from the tufting to the molding process before pass by the carbon fiber structures (third set of specimens). This configuration aided in the evaluation of the electrical response of the carbon tufts during pull-off tests. Moreover, the investigation of this batch of specimens during tests help to improve mechanically the new set of samples, designated as Batch III, mainly by enhancing the tufting parameters.

**a)** ***Batch I***

**Tufting reinforcement**

The laminated composite structures were manufactured using 5-harness satin carbon fibers woven (5HS) with an areal density of 500 g/m$^2$. The layup sequence was $[0]_8$ to both parts of the panel (skin and omega stiffener). Figure 2.16 presents a schematic of the skin and stiffeners preforms employed for manufacturing the control and tufted omega stringers, as well as the process to obtain the reinforced structures by tufting. A single stiffened panel containing four stiffeners, two for control specimens and two for tufted specimens, was performed. The stiffener and skin fabrics for both control and tufted samples were tufted in their border to help the handling during the manufacturing process and consequently to avoid fabrics misalignment before the reinforce of both parts by tufting. Additionally, a PTFE film laid up on the foam aided to hold the tuft loops under tufting and the handling of the stitched fabrics.

Figure 2.16 presents the manufacturing steps utilized to fabricate the two stringers reinforced with tuft carbon/PBO threads. The process initiates by maintaining the stiffener fabrics on the skin preforms with two frames supports to avoid misalignments during tufting. Three rows of tufts with a tufting density of 5x5 mm and following the 0° fabric direction joined the skin and stiffener preforms, both aligned parallel to the width (warp direction). A trimming removed the exceeding part of fabrics from the stiffener preform and subsequently, the metallic inner mold, covered with a release film, was placed between the main preforms. Thus, the metallic supports were applied to hold the preforms to avoid the misalignment of the fabrics. The tufting reinforcement utilized the same parameters as described to the other side of the stiffener and their excess trimmed off in sequence.

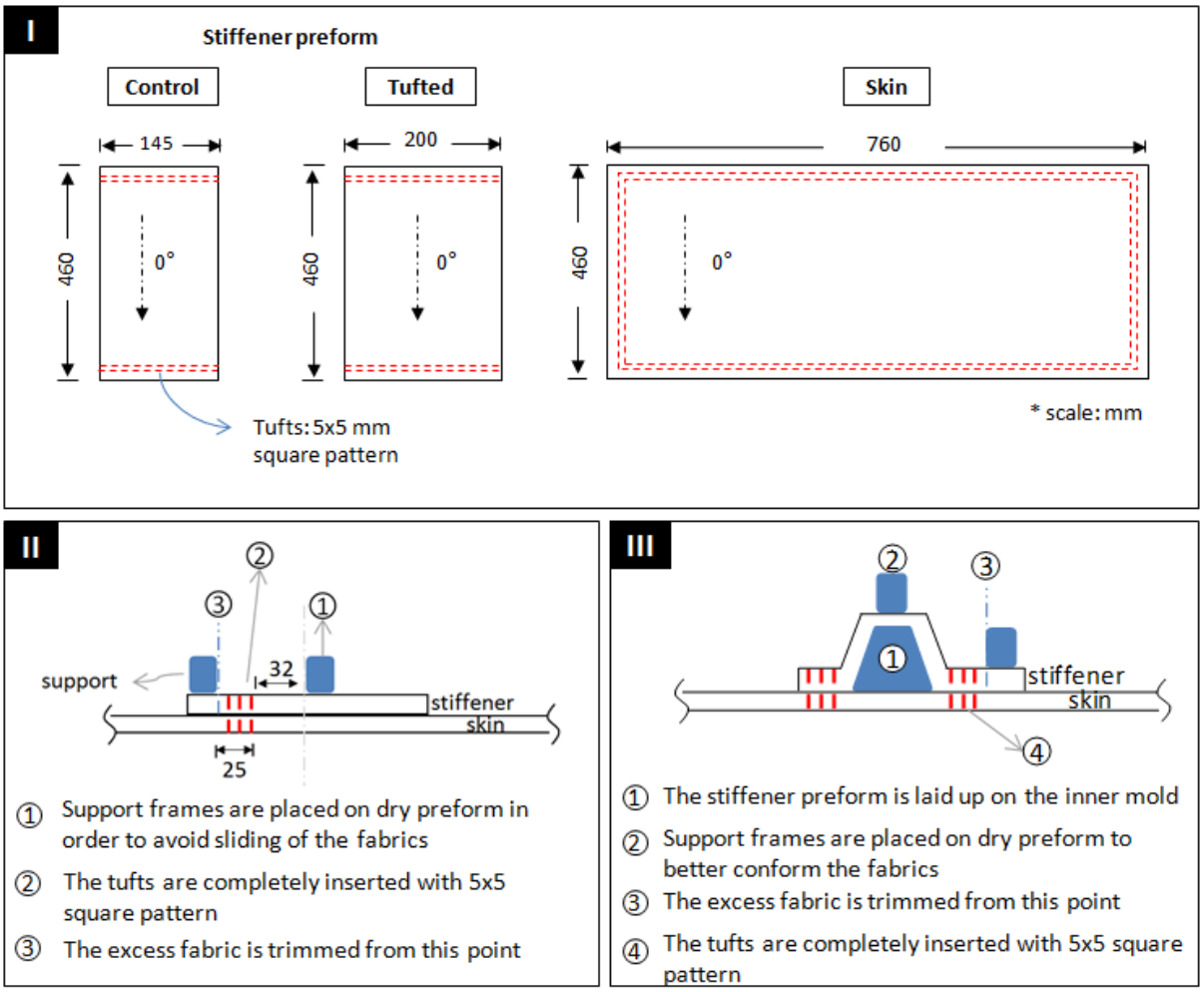


**Figure 2.16 - Schematic of the manufacturing steps to produce the omega stiffeners.**

Figure 2.17 shows the through-thickness reinforcement of the carbon fabrics, detailing the frame supports used to maintain the fabrics in place during tufting as well as to the trimming procedure. The stitched fabrics were carefully released from the foam after the through-thickness reinforcement, followed by the releasing of the PTFE film from the tuft loops (Figure 2.18).

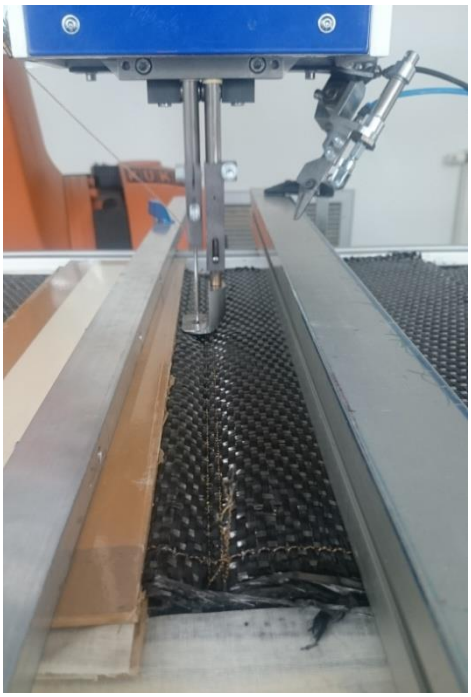

**Figure 2.17 - The reinforcement between the stiffener and skin preforms for the manufacturing of the omega stringer.**

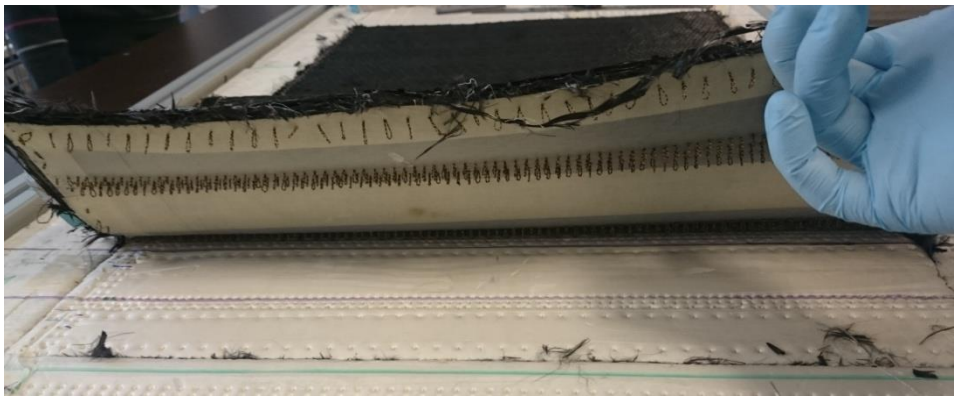

**Figure 2.18 - The releasing of the stitched dry-preforms.**

## VARTM process

Adhesive tapes aided to keep in place the stiffener preforms employed for manufacturing the control specimens (Figure 2.19a). This configuration presented a considerable extent of loosening fiber tows from its fabrics as well as poor compaction of the preforms over the mold, differently from the tufted stringers. The fabrics were infused with EPOLAM 5015 epoxy resin system by VARTM process at room temperature (Figure 2.19b). The cure cycle was carried out at room temperature for 24 hours and post-cured at 80ºC for 16 hours. The inner molds were therefore released from the laminated stiffened panel as seen in Figure 2.20.

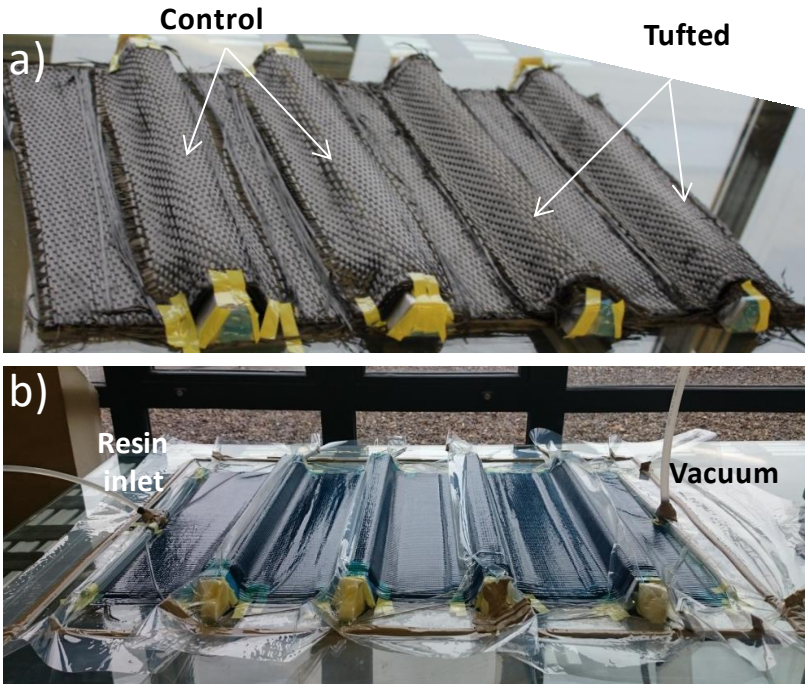


**Figure 2.19 - a) The preparation of the preforms before the VARTM process and, b) infusion process.**

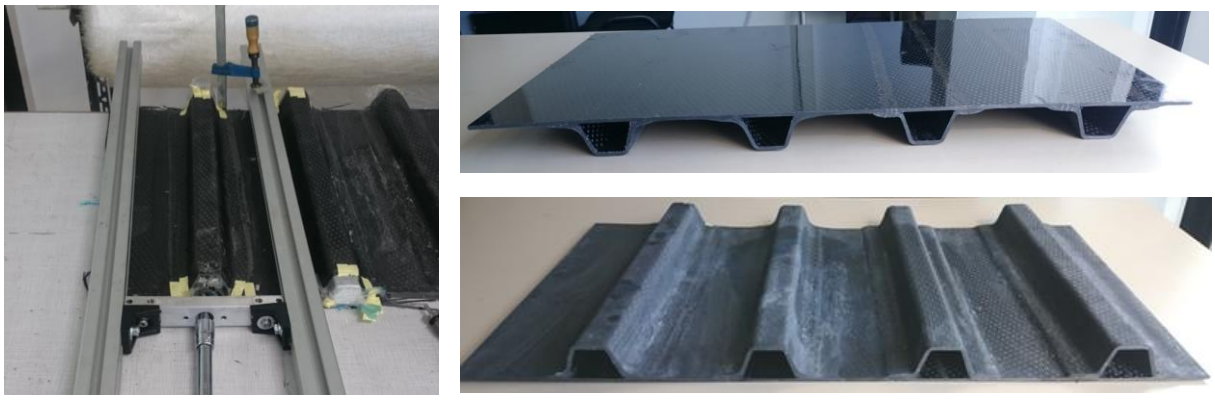

**Figure 2.20 - Mold releasing and final stiffened plate with the tufted and control stringers.**

Figure 2.21a exhibits the geometry of the control and tufted specimens with their final dimensions described by the schema of the tufted structure (Figure 2.21b). It is observed better compaction on the radius zone of the stitched specimens when compared to the control specimens mainly due to the compression of the fabrics during tufting.

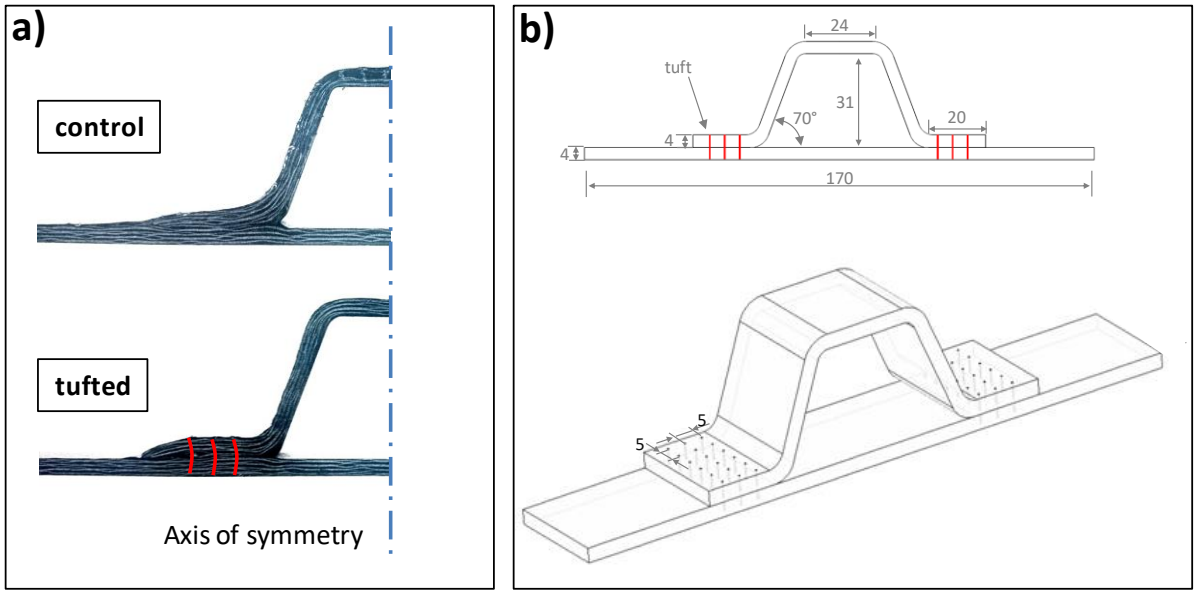


**Figure 2.21 - a) Control and tufted omega stiffened composite stringers and, b) the dimensions of the specimens and tufts position into the structure.**

### b) *Batch II (Glass fiber composites)*

#### Tufting reinforcement

Non-crimp fabrics (NCF) made with unidirectional layers of glass fiber tows (0/90), and areal density of 600 g/m$^2$ were employed to manufacture the omega stringers. The structure layup consisted of $[0]_{10}$ to the stiffener and $[0]_{12}$ to the skin part. Tuft carbon/PBO threads reinforced the dry preforms. The primary goals to apply the carbon/PBO threads are due to the excellent electrical properties of the carbon fibers and especially to their protection by the PBO yarns as shown in Figure 2.22a. Furthermore, from the previous works in the laboratory, it is noticed that the PBO protect two parallel yarns to have contact (Figure 2.22). It means that after a tuft failure, PBO yarns avoid the percolation and consequently the misunderstanding of the electrical response and its relation to the damage events.

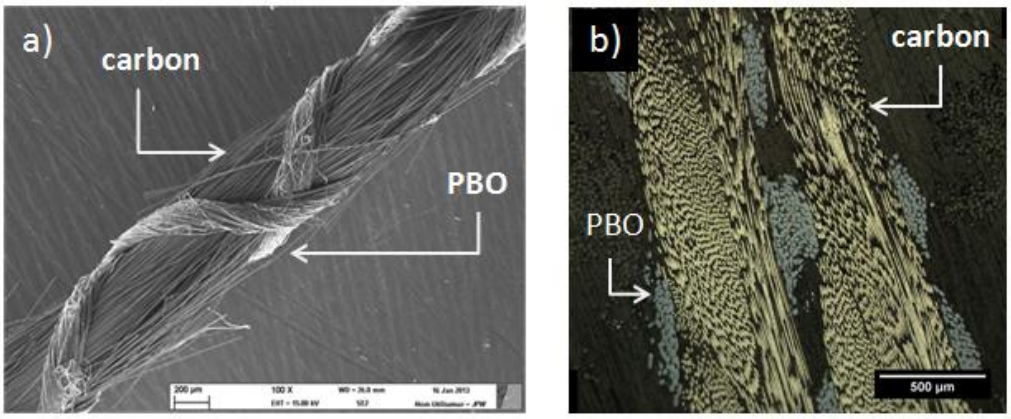


**Figure 2.22 - SEM image of a carbon fiber/PBO yarn employed by the tufting process, b) Light microscope image of the tufted carbon/PBO yarn in the laminate composite.**

The skin was tufted throughout the edge into the foam in order to avoid the fabrics misalignments. The fabrics were laid upon the new inner mold, and subsequently, a film placed over the whole system compacted the preforms against the mold/table when applied vacuum at the table. The reinforcements were inserted in the flange/skin contact along the width direction while maintaining the vacuum (Figure 2.23). The three set of tufted specimens manufactured in this study consisted of the combination of parameters such as the distance between the tuft rows, number of rows and tufting depth. The tufting reinforcement maintained the stitching step of 7 mm along the row for the three configurations. Table 2.2 presents the parameters employed for each set of specimens and their designation.

**Table 2.2 - Tufting parameters employed for each set of specimens.**

| specimen | Number of rows/stiffener side | Tuft depth | The distance between tuft rows (mm) |
|---|---|---|---|
| **VR** | Control specimen | - | - |
| **V2T** | 2 rows | Partial | 15 |
| **V3TC** | 3 rows | Partial | 10 |
| **V3TL** | 3 rows | Complete | 10 |

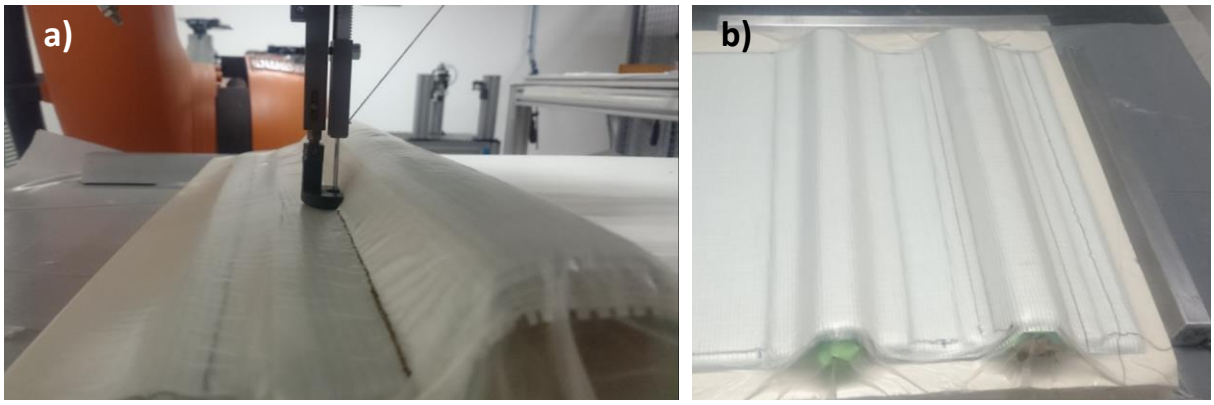


**Figure 2.23 - a) Tufting reinforcement between stiffener and skin preforms under vacuum pressure and, b) a top view of the second stringer prepared to be stitched (left side) and the stitched preforms on the right side of the image.**

## VARTM process

The composite omega stiffeners were infused by VARTM using EPOLAM 5015 epoxy resin system at about -1 bar of vacuum pressure. Then, the cure cycle occurred for about 24 h at room temperature and post-cured at 80 °C for 16 h. The three set of specimens, as well as the dimensions of the latest mold used, are shown in Figure 2.24. The stiffener and skin thickness of the molded samples were approximately 5 and 6 mm respectively.

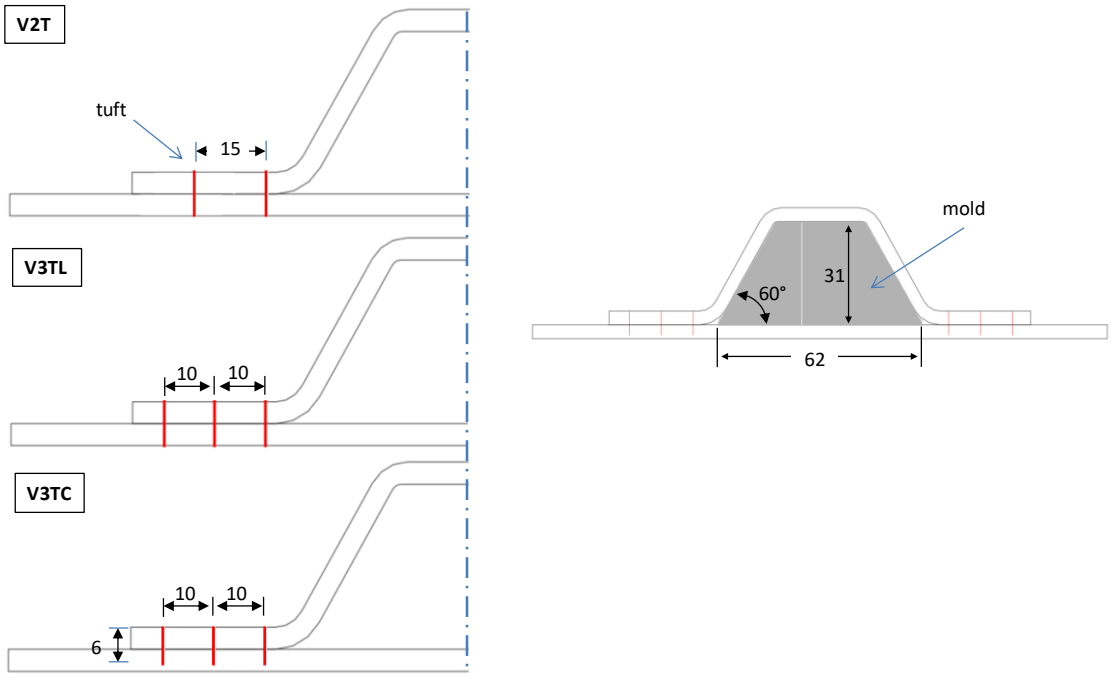


**Figure 2.24 - Schematic illustration of the three specimen configurations and the inner dimensions based on the mold.**

### c) *Batch III (Carbon fiber composites)*

**Tufting reinforcement**

Some enhancements were made to the tufting process for the manufacturing of this batch of omega stiffeners in comparison with the last procedures for Batch I and II. Figure 2.25 schematically illustrates the new steps employed. This new batch of specimens applied the same materials utilized in the manufacturing of the Batch I. Both stiffener and skin had $[0]_8$ symmetric layup with the warp direction along the plate width. The trimming of the stiffener preform was no longer performed, which led to the same dimensions for the control and tufted fabrics (Figure 2.25-I). As seen in the manufacturing process of the Batch I, the fabrics plies were also tufted on the edge to avoid sliding between them. The preforms were laid up over the new inner molds and fixed by a support frame as better exhibited in Figure 2.26. Then, the insertion of partial tufts on both sides occurred without supports due to the short space left, and finally, the tufted preform was released from the foam support and molded on the infusion process. The two set of tufted specimens fabricated for the present batch are related to the number of tuft rows inserted along the panel width. The set of samples consisted of a single tuft row (TUF1) and two tuft rows (TUF2) on each side of the stiffener.

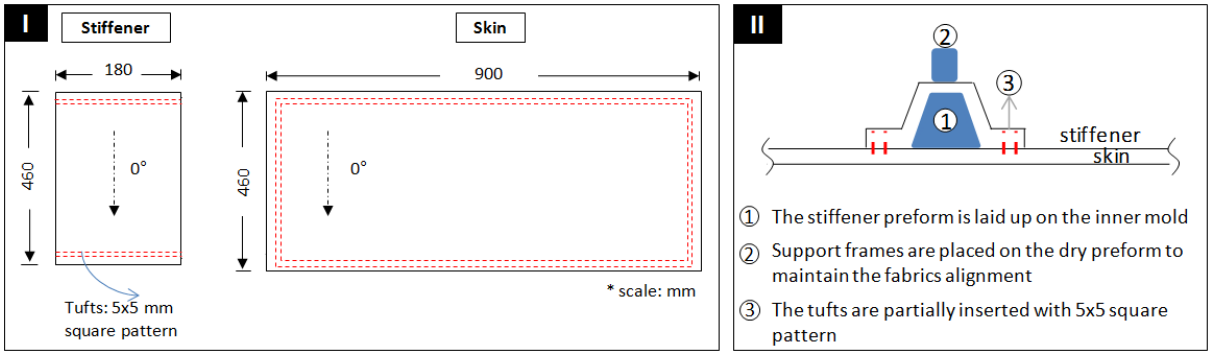


**Figure 2.25 - Manufacturing steps to produce the stiffened composite panels.**

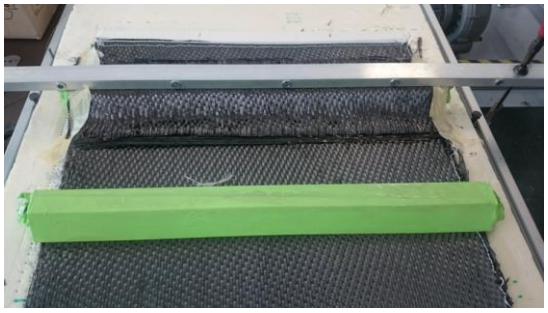

**Figure 2.26 - Support frame for maintaining the dry preforms during the tufting process.**

### VARTM process

The same epoxy resin system and cure cycle were employed to mold this new set of specimens. The preforms for the control specimens were placed before infusion process and also presented loosen of the carbon fibers tows as seen especially in Batch I. Figure 2.27 shows the infusion process of the stiffened panel containing the three set of specimens (control, TUF2, and TUF1).

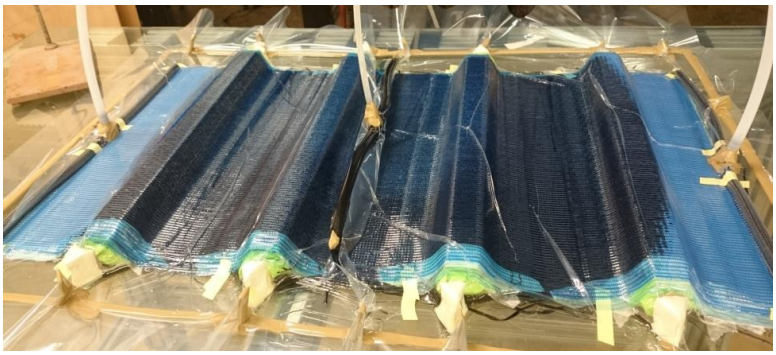

**Figure 2.27 - VARTM process of the stiffened panel (Batch III).**

The new inner mold, which is composed of two parts, presented remarkable easiness for releasing from the laminated parts (Figure 2.28a). Figure 2.28b shows the schema of the final dimensions obtained for the specimens exhibited in Figure 2.28c.

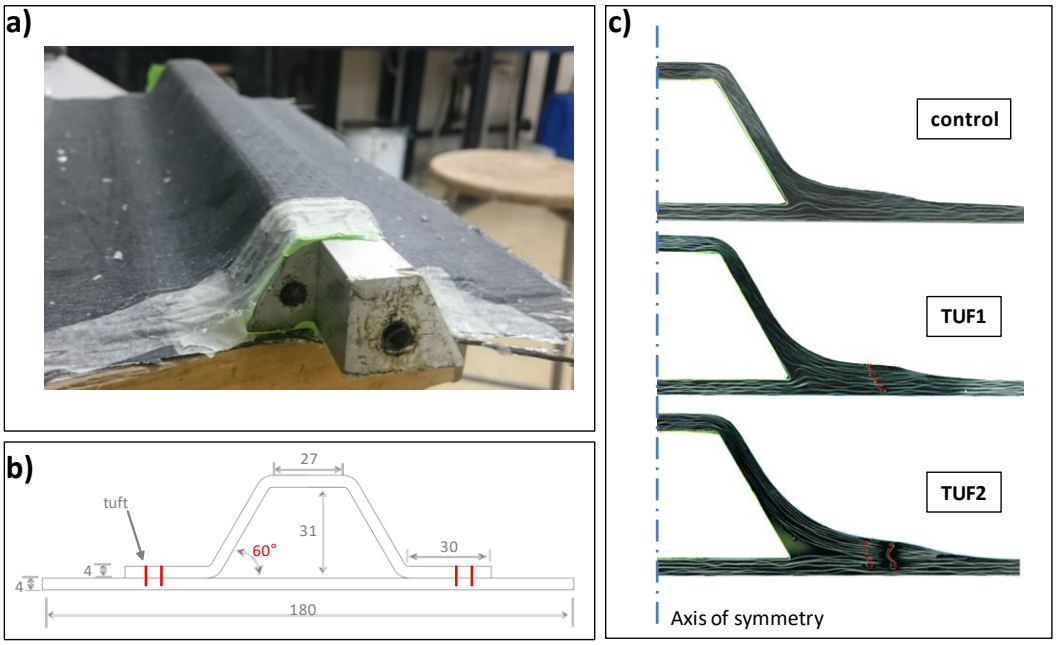


**Figure 2.28 - a) Mold releasing of the bi-parts mold from the specimens, b) final dimensions of the samples and, c) the laminated composites specimens.**

## 2.3 Test methods

### 2.3.1 Digital image correlation (DIC)

DIC is a full-field image analysis method, which provides reliable measurements for characterizing complex mechanical response at various scales. It consists of compare digital photographs of a specimen surface at different stages of deformation. The digital pictures must have blocks of pixels randomly distributed on the specimen surface with significant contrast and intensity levels. This stochastic speckle pattern provides the grey scale necessary for generating a matrix of positions (pixels) from every image taken at different times. These speckles can be provided naturally from the texture of the specimen or applied on the surface to create a satisfactory pattern for obtaining a correlation with optimal resolution. The correlation is carried out by tracking the displacement of these patterns and consequently, allows the generation of 2D and 3D deformation vector fields and strain maps [196] (Figure 2.29). The full-field measures can obtain significant information about local and global strain distribution, crack growth, and used for the determination of essential fracture mechanics parameters [197].

The 2D digital image correlation (2D-DIC) allows the measurements of the in-plane displacements/deformation fields. This technique is simple to apply due to the use of a single camera to capture the images (one for each specific time). The main issue concerns the need for a precise set-up between the camera and the specimen, which must be perpendicular in order to avoid problems in the correlation. The use of a telecentric lens may prevent this issue owed to its capability to increase the detection field while reducing the error in a tiny range.

Stereo-digital image correlation (or 3D-DIC) is able for acquiring the out-of-plane displacement/deformation fields. Moreover, this technique allows obtaining precisely surface geometry information such as specimens shape as well as out-of-plane defects and damages, which may be related to the manufacturing process or former mechanical loading respectively. In-plane measurements can also be performed by this method which avoids the issues of proper alignment between the camera and specimen surface, seen in 2D-DIC. In the stereo-DIC method, a series of image pairs captured from two different views of the object are used to locate and track a given set of surface points during motion and/or deformation [198]. These images can be captured by a pair of "twin" cameras or acquired with a single camera and optical devices to generate both views. Calibrating the system is necessary in the 3D-DIC method to

obtain the intrinsic (e.g., effective focal length, principal point, and lens distortion coefficient) and extrinsic (3D position and orientation between the two cameras to a world coordinate system) parameters of the cameras by triangulating their positions. The accuracy of the correlated images depends heavily on the calibration parameters, which is consequently related to the calibration of the cameras.

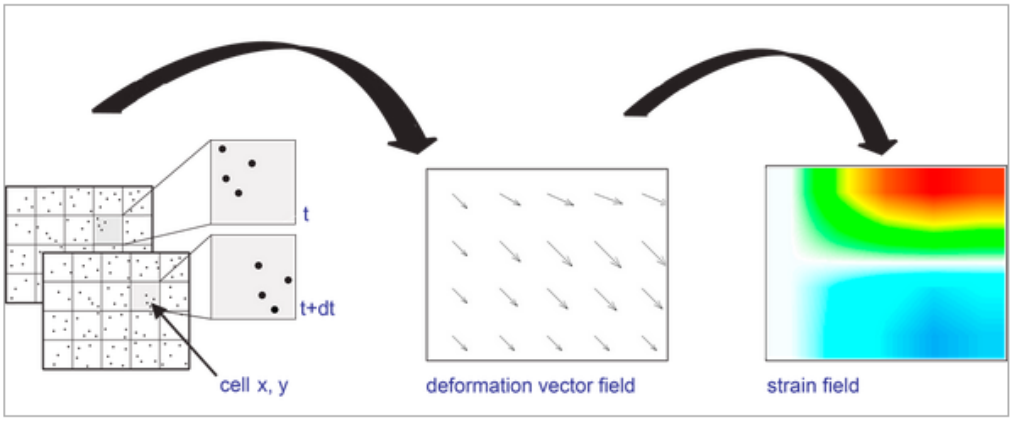


**Figure 2.29 - Basic concept of Digital image correlation** [199].

### 2.3.2 Acoustic emission (AE)

It is a nondestructive testing method capable of detecting crack initiation and development. When subjected to stress by mechanical, pressure or thermal means, the structures may propagate cracks, resulting in a sudden release of energy which will convert partially to transient elastic waves. The piezoelectric transducers detect the elastic waves that propagate on the material surface and convert to electric signals that are subsequently magnified, processed and recorded. A typical AE system setup and the AE signal parameters are represented in Figure 2.30a and Figure 2.30b respectively.

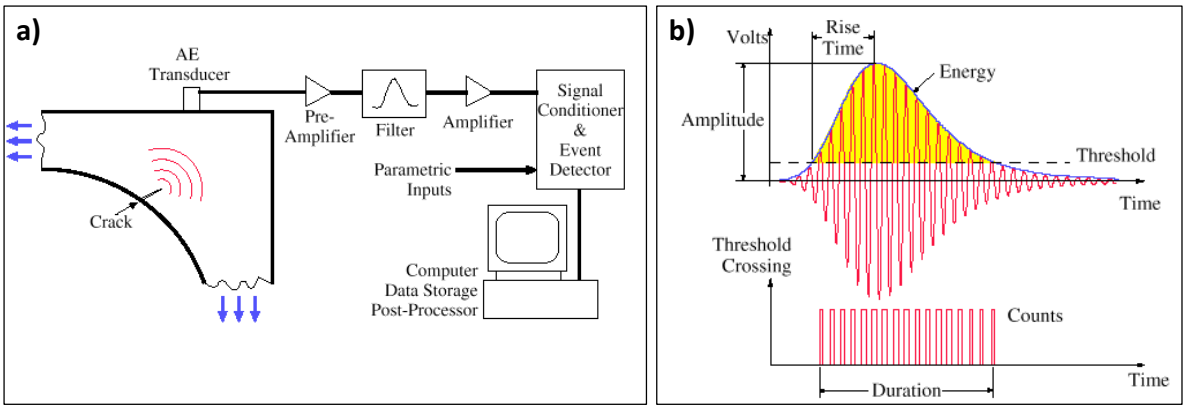


**Figure 2.30 - a) Basic principle of the acoustic emission technique and, b) Typical AE signal feature** [200]

This technique was firstly investigated on 1950's by Kaiser [201] and has been increasingly applied to investigate structures under loading, intending to characterize damage initiation and development, as well as their extent, nature, and position, for example. Several materials have been investigated by the acoustic emission method when subjected to mechanical tests. For the composite materials, the technique is applied to detect and differentiate the damage events, such as matrix cracking, fiber debonding, delamination and fiber breakage under different loading conditions [202]–[208]. The signal waves change their parameter characteristics (Figure 2.30b) from a type of damage mechanism to another and consequently allow to clustering in different classes these events occurred under loading tests. Figure 2.31 presents the typical AE wave signals for the primary damage mechanisms on laminated composites.

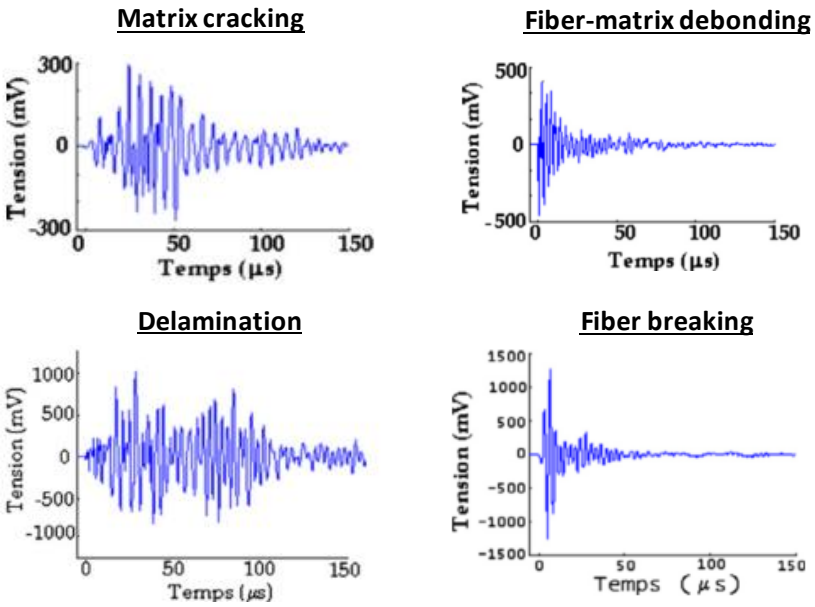


**Figure 2.31 - Typical wave signals of the primary damage mechanisms on laminated composites.**

This thesis employed the AE technique during mechanical tests by using wideband sensors (Micro80 - 200-900 kHz) to obtain the acoustic events. The acquired signals were preamplified with a selected gain of 40 dB and bandwidth from 20 kHz to 1.2 MHz. The data acquisition was carried out with the channel supplied by Mistras Group and controlled by AEwin® software. Figure 2.31 lists the signal threshold and timing parameters values used in the data acquisition.

**Table 2.3 - Parameter values employed on AE acquisition.**

| Threshold (dB) | PDT (µs) | HDT(µs) | HLT(µs) |
|---|---|---|---|
| 40 | 30 | 150 | 300 |

### 2.3.3 Ultrasonic C-scan

Ultrasonic is nondestructive testing widely used in engineering applications for detecting and evaluating flaw, dimensional measurements, and material characterization (e.g., cracks, voids, porosity, and other internal discontinuities). It consists of pulsing very short ultrasonic waves with high frequencies that typically vary between 0.1-15 MHz and can occasionally achieve up to 50MHz, throughout the material. The mechanical waves travel through the material with some loss of energy and deflect at interfaces and/or defects [209]. In general, the analysis of materials utilizes mostly two ultrasonic approaches. Through-transmission method consists of using two transducers, one on each side of the material, for its characterization. The main issue of this approach concerns the difficult at some testing to access both sides of the structures. For this reason, the use of both-transducers positioned on the same side or a single transmitter-receiver transducer to acquire the data by the pulse-echo method may avoid the mentioned issue (Figure 2.32).

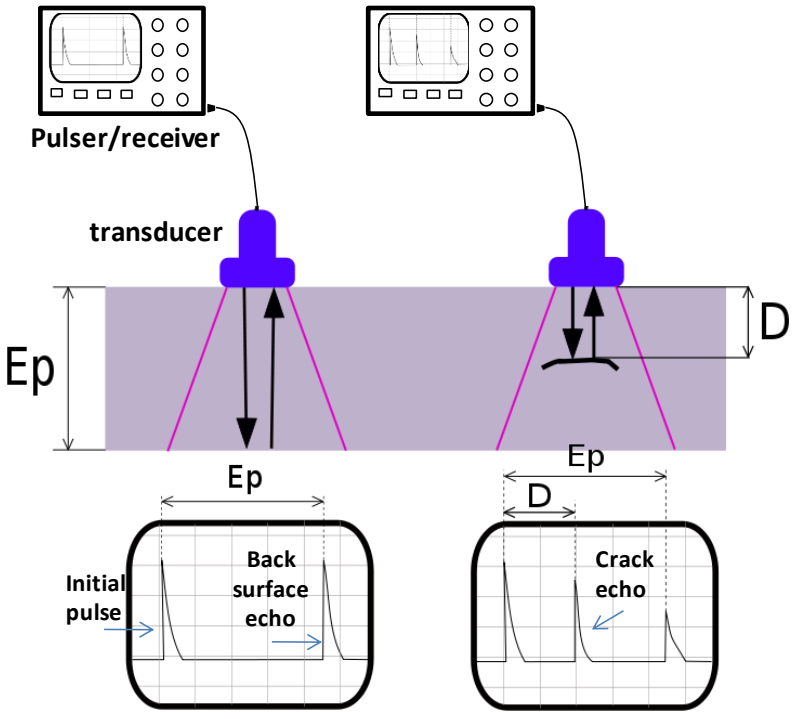


**Figure 2.32 - Basic concept of ultrasonic testing.**

C-Scan is a two-dimensional representation of the scanned structure displayed as a top or planar view. The colors shown in the images represent the gated signal amplitude or signal depth at each point of the mapped piece [210]. This approach has been widely applied to check laminated composites after the molding process, intended to characterize the distribution, size, and shape of voids [211]–[213]. Additionally, the C-Scan characterization of laminated

composites subjected previously to mechanical tests enables measuring the extent of damage from the scanned area [176], such as those submitted to impact loading [98], [214]–[216].

The present work characterized the specimens by C-Scan mapping merged in a water tank to provide ultrasonic coupling (Figure 2.33). The transducer coordinates are tracked via mechanical scanner with encoders based on the desired index resolution. The measurements by the pulse-echo technique employed a 10 MHz focused transducer with a diameter of 12.7 mm and a focal distance of 63.5 mm.

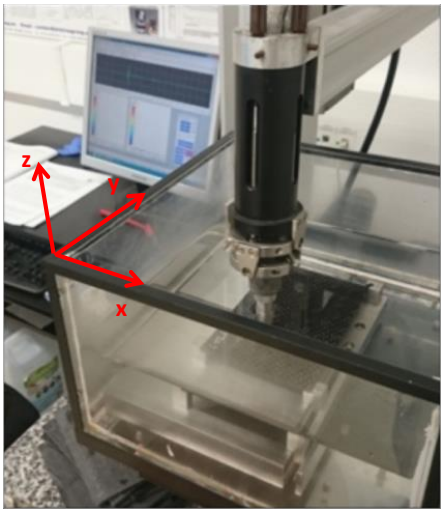


**Figure 2.33 - The ultrasonic pulse-echo immersion technique.**

### 2.3.4 Electrical measurements

The electrical measurements carried out in this thesis intended to evaluate the piezoresistive response of the tufts in the laminates. This approach based on Ohm's law for monitoring electrical resistance values either under or before/after mechanical tests. The measuring of the corresponding voltage response to an injected current (or the opposite) enables to determine the resistance by using the relation (1).

$$R = \frac{\Delta U}{\Delta I} \quad \textbf{(1)}$$

Where R is the electrical resistance (Ω), U the voltage (V) and I the current (A). The electrical resistance of a uniform conductor can be given by the following equation (2) regarding resistivity.

$$R = \rho \frac{\mathrm{L}}{A} \quad \textbf{(2)}$$

where $L$ is the length of the conductor ($m$), $A$ is the cross-sectional area of the conductor ($m^2$), and $\rho$ is the electrical resistivity of the material ($\Omega.m$).

Two types of approach can be employed to perform the electrical measurements. The two-wire method is the most straightforward technique and consists of the difference in electric potential energy acquired by a voltmeter that injects an electrical current according to the resistance range. This procedure may present significant error values, especially under 100Ω due to the total lead resistance added to the measurements. On the other hand, the four-wire method offers a solution more stable, especially at lower resistance range. This method consists of the current injection by the two external contact points and the measuring of the difference in electric potential by the two internal wires. This procedure enables controlling the current applied to the system and consequently diminishes the problems related with the total lead current.

The electrical measurements carried out in this work utilized both measurements methods. The in-situ monitoring of the specimens under mechanical tests employed mainly the two-wire method, due to the issues concerning the insertion of additional probes which consequently precluded the four-wire analysis. The analyses before and after tests used the four-wire technique for the measurements. Both methods acquired the results via a precision source/measure unit Keysight B2901A from electrical cables soldered at a same tufted row. The contact between the wires and tufted yarns was improved by polishing the resin around the reinforcements, applying a thin conductive silver paint and welding with tin-lead solder.

### 2.3.5 Infrared thermography (IRT)

An infrared camera detects radiation in the infrared range emitted from the surface of an object, converts it on temperature and consequently generates an image of the temperature distribution. The temperature is directly related to the extent of radiation emitted by an object, which means that temperature increase when increasing the radiation. This technique can measure the temperatures without contact with the object and has been exploited for quality assurance of manufacturing process and non-destructive evaluation of the structures under service. IRT can use passive and active approaches to the investigation of structural monitoring and damage evaluation. A passive method is the most straightforward technique that captures the radiation emitted directly from the physical event in the structure. Otherwise, the active approach uses

an external source to excite the specimen (e.g., impulse thermal-wave or ultrasonic thermal-wave). In case of the presence of defects in the structure, IRT can distinguish them using the thermal conductivity difference between the defect and the material transmitted at the specimen surface. Infrared thermography has been used to evaluate bonded repair in laminated composites [217]–[219] as well as monitoring damages under fatigue tests [218], [220]–[222], impact loading [223], [224] and static tests [225], [226].

The investigation in this thesis employed an IR camera produced by FLIR model 320, which detects a temperature range of -20°C to 120°C with ± 0.05 °C of accuracy, resolution of 320×240 pixels and data capture rate of 50Hz.

### 2.3.6 Test methods for the laminated plates (Plate I)

#### a) *Short beam shear test*

The dimensions of the samples followed the ASTM D2344-16 [227] standard with the specimen length of 6 and width of 2 times the thickness respectively. Three specimens in the longitudinal as well as in the transversal direction of the laminate layup were prepared from the specimens REF, A5, and T5. The crosshead speed was 1 mm/ min. The span length was 20 mm and, support cylinder and loading nose diameter of 3 mm and 6 mm respectively. A DIC camera placed in one side captured the images during tests, subsequently correlated with VIC2D®, while the video microscopy monitored the opposite side.

#### b) *Impact test*

Three specimens of each configuration were submitted to impact energies of 25 J and 60 J on the Instron Dynatup 9250HV drop-weight impact machine, using a hemispherical indentor of 50.8 mm diameter and weight impactor adjusted to 14.2 kg. Preliminary tests validated the capability of the low-velocity impact of 25 J for creating barely visible impact damage (BVID) in the composites. Differently, the medium velocity impact of 60J is meant to create visible damages in the specimens. The primary goal was to evaluate the tufted composites behavior in the two classes of impact velocity (low and medium) which are intended to create different damages levels, under impact and compression after impact. The control of the impact energy consisted of varying the velocity while maintaining the same mass in the tests. Also, a laser sensor installed on the bottom side of the samples, from the middle of the laminate, measured the out-of-plane displacement during impact loading.

Ultrasound C-Scan method using a pulse-echo immersion mode with a 10 MHz focal transducer characterized the damaged area generated under impact tests. The area of scanning was of 80x80 mm from the center of the impacted surface. The images of the damaged area were built with the ultrasound wave that rebound from the back surface. The ImageJ software aided in the measure of damage extent by calculating the damaged area after conversion on binary images.

**c)** ***Compression before impact***

Compression Before Impact (CBI) tests employed three samples of each one of the REF, A5, and T5 configurations. The tests followed the standard test method ASTM D6641/D6641M-01 [228].

**d)** ***Compression After Impact test***

Compression After Impact (CAI) tests employed a support frame according to the specified in ASTM D7137-12 [229] to avoid buckling. Digital Image Correlation (DIC) monitored a single side surface (impacted surface) taking a series of digital photographs from a stereo-system with two cameras (camera CC-0003 by ALLIED Vision Technologies) throughout the loading history. It mainly consisted of the investigation of the out-of-plane displacements (w) from the images correlated by the software VIC 3D® of the specimens subjected to compressive loading. The parameters of the subset and step size used for the correlation were 29 and 7 respectively. The area chosen to analyze the mean out-of-plane displacement (w) was 30x30 mm centralized in the impacted zone. Moreover, a characterization by stereo-DIC from both surfaces for some specimen configurations (REF, A5, and T5) allowed the investigation of the out-of-plane behavior from the two sides. The acquisition and correlation parameters were kept the same as already described to the one side stereo-DIC during CAI tests.

Also, the dent depth generated during impact tests was compared among the sample configurations by analysis of DIC image acquired before CAI tests (Figure 2.34). The dent depth measured by DIC has been used by different authors [230]–[232]. This method allows measuring with precision, especially the small dent depth that is frequently formed by low-velocity impacts.

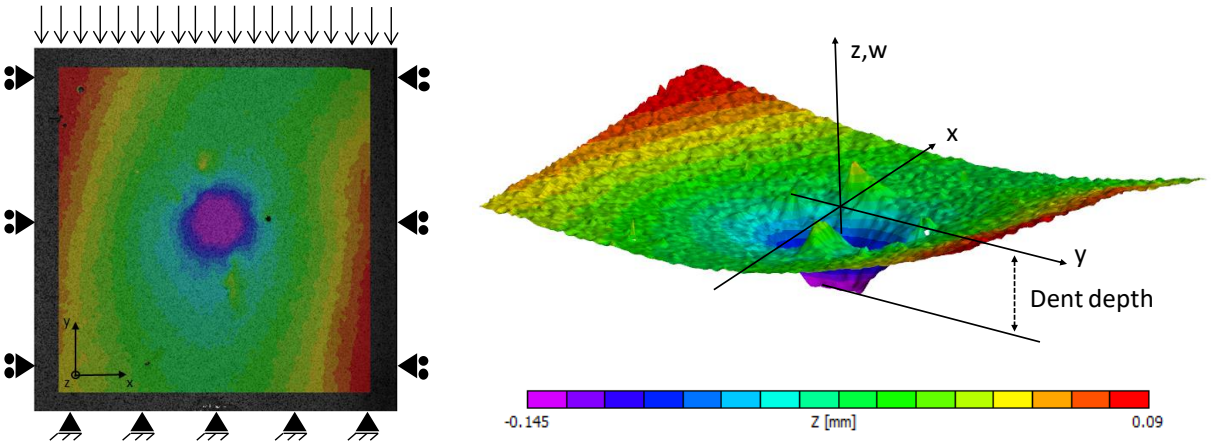


**Figure 2.34- The contour plot and the corresponding 3D image of the impacted specimen on the Z field.**

Additionally, two wideband sensors (Micro80 - 200-900 kHz) were longitudinally placed 45 mm from the center of the sample, one on each side of the transversal axis, for the AE monitoring. Figure 2.35a exhibits the multi-instrumented CAI test with DIC cameras and AE sensors after sample failure. The two couples of stereo-DIC cameras mounted for CAI tests on the specific configuration of specimens, as mentioned, are presented in Figure 2.35b.

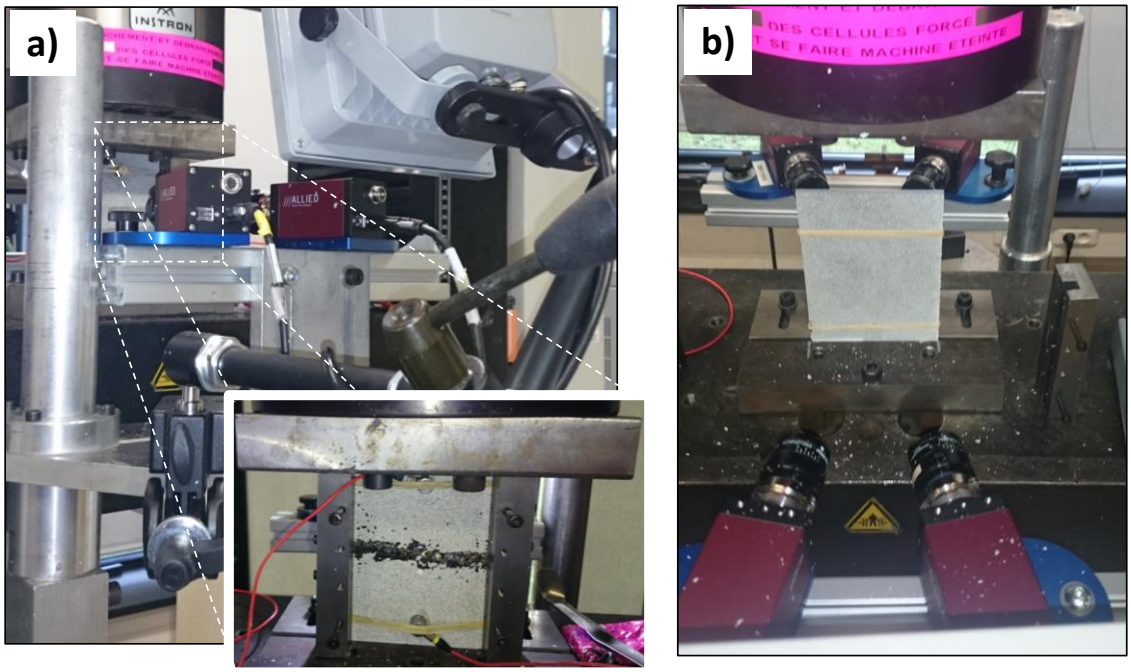


**Figure 2.35 - a) Multi-instrumented CAI test with AE sensors and DIC cameras and, b) stereo-DIC cameras mounted on both sides of the specimens.**

### 2.3.7 Test methods for the laminated plates (Plate II)

Chapter 5 details the testing methods utilized for the characterization of this batch of specimens.

### 2.3.8 Test methods for the laminated plates (Plate III)

#### a) *Fatigue test*

The fatigue tests consisted of three main blocks as seen in Figure 2.36. The specimens were first submitted to the load/unload tensile tests by incrementing the load of 10,20,30,35,40,45,50 and 55 kN. Subsequently, tensile fatigue tests were carried out under constant stress amplitude, a sinusoidal waveform with a frequency of 2 Hz and stress ratio R=0.1. The selection of the maximum force (55 kN) considered the results obtained from preliminary fatigue tests as well as the ultimate tensile strength. The third block consisted of subjecting the specimens previously tested at $1x10^6$ cycles on fatigue to tensile tests until their failure. This part aided in the evaluation of the stiffness and strength of the specimens in comparison with the previous blocks of tests.

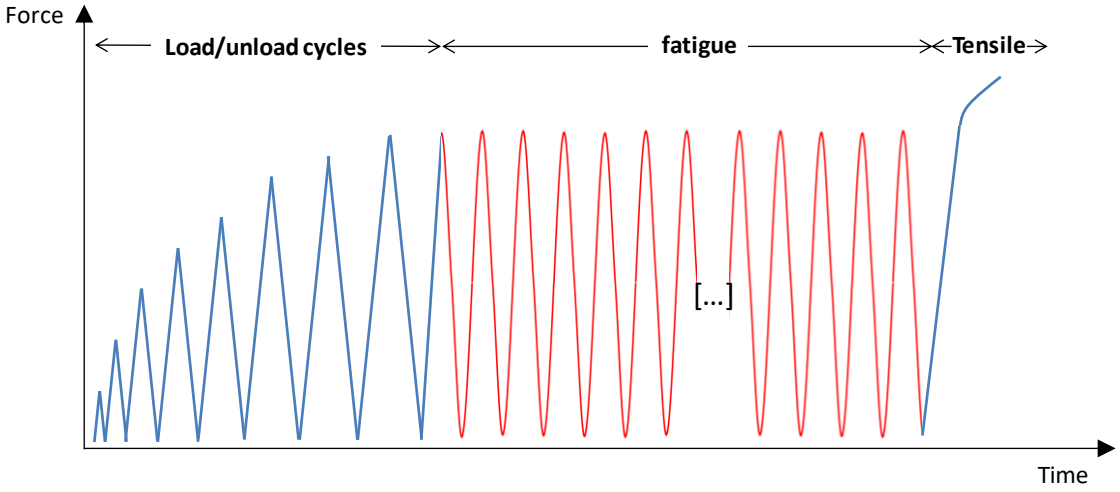


**Figure 2.36 - Schematic illustration of the testing procedure consisted of loading/unloading cycles, fatigue ($1x10^6$ cycles) and tensile loading until specimen failure**

The tests were carried out on a servo-hydraulic fatigue testing machine (Instron 1343) with a crosshead speed of 1 mm/min and the distance between the jaws of 190 mm. Two cameras (camera CC-0003 by ALLIED Vision Technologies) utilized the stereo-DIC method to perform the acquisition of images throughout the three blocks of the mechanical tests and consequently correlate them by VIC 3D®. The cameras acquired one image at every $1x10^5$ cycles in the maximum stress point during the fatigue tests. The correlation applied the subset and step size values of 21 and 3 respectively. The tests also counted with two wideband AE sensors (Micro80 - 200-900 kHz), each one at 40 mm from the specimen centerline, and an extensometer with a gauge length of 10 mm located 50 mm from the specimen centerline. Figure 2.37 presents the instruments employed for characterization of the composites.

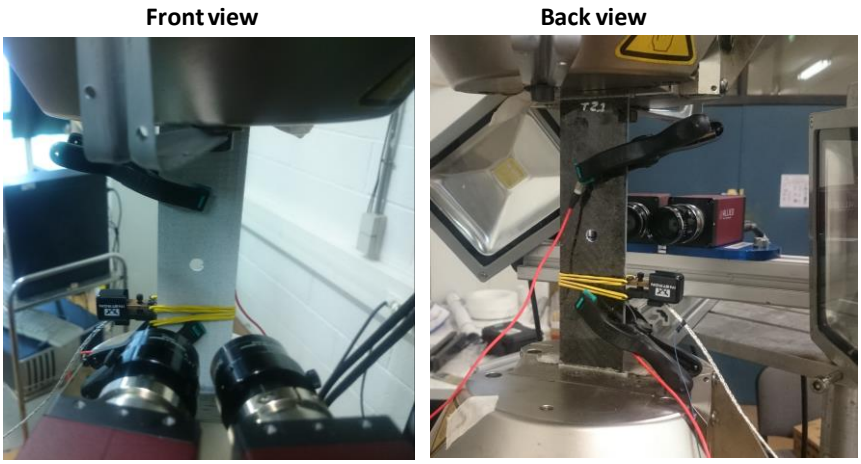


**Figure 2.37 - Experimental test apparatus used for investigation of the opened hole specimens behavior under fatigue testing.**

### 2.3.9 Test methods for the sandwich plates

Chapter 5 details the testing methods utilized for the characterization of these specimens.

### 2.3.10 Test methods for the omega stiffeners

#### a) *Pull-off tests (Batch I)*

The pull-off tests executed in this thesis intended especially for creating failure by opening mode (mode I fracture). The quasi-static tests were carried out at a constant cross-head speed of 1 mm/min. Two lower fixed rollers (5 mm diameter) were 70 mm equidistant from the center, and the middle roller (10 mm diameter) was responsible for loading the structure from the stiffener part (Figure 2.38). They were monitored by DIC to evaluate the in-plane strain fields from a single side of the sample, focusing mainly on the critical zone of the omega structure (intersection of the stiffener and the skin). The series of digital photographs (camera CC-0003 by ALLIED Vision Technologies) were taken throughout the loading history and correlated with the software VIC 2D®. The parameters of the subset and step size were 25 and 5 respectively. Video microscope was settled up in the opposite face of the DIC camera for investigating the damage development during tests. The AE analysis monitored the acoustic activity during tests through of two wideband sensors (Micro80 - 200-900 kHz) longitudinally placed on the bottom side of the skin from 45 mm to the center, one on each side of the transversal axis.

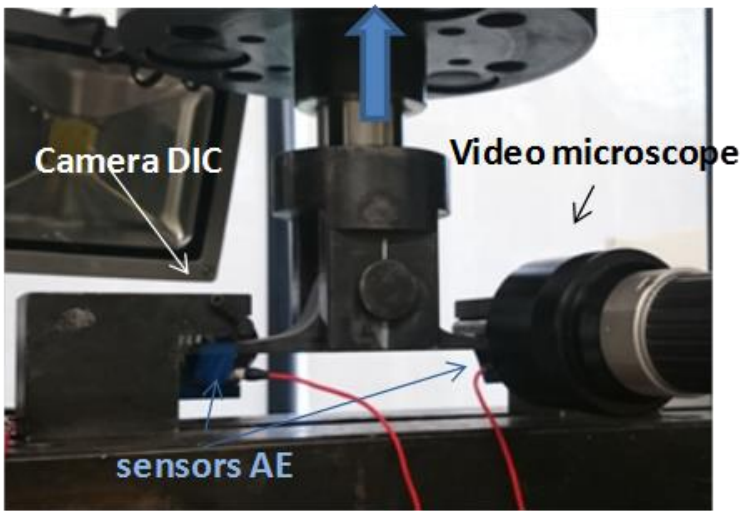


**Figure 2.38- Pull-off test apparatus.**

**b)** ***Pull-off tests (Batch II)***

Chapter 5 details the testing methods utilized for the characterization of this batch of specimens.

**c)** ***Pull-off tests (Batch III)***

The carbon fiber panels stiffened with omega stringers employed the same test parameters as utilized for the glass fiber specimens (Batch II of samples), however with no electrical measurements. Video microscope was also added to a single side of the sample.

**d)** ***4-point bending test (Batch I)***

4-point bending tests evaluated the behavior of the samples (Batch I) by generating localized shearing in the stiffener/skin contact. The support and the load nose rolls measured 20 mm and 12 mm of diameter respectively. The lower span (support) was 120 mm, the upper span (load nose) was 53 mm, and the crosshead speed was 1 mm/min. The instruments employed in the present tests were adjusted in the same manner as described for the pull-off tests of the Batch I, with two AE sensors placed 73.5 mm longitudinally from the middle of the specimens.

**e)** ***3-point bending test (Structure)***

The three batches of omega structures manufactured for this work were subjected to 3-Point bending tests to evaluate their behavior in mixed loading conditions. It differentiates from the pull-off and 4-point bending tests that envisaged mainly to assess the interface region, between

stiffener flange and skin, in mode I and mode II loading conditions respectively. The present testing method seems more realistic to investigate the tufting behavior by loading the composite panels. The test apparatus consists of two parallel supports with a diameter of 20 mm and loading noses of 25 mm located in both transverse sides of the stiffener. Figure 2.39 shows the longitudinal and transverse view of the test setup. As seen in the transverse view, the joining of tabs to the surface of the structure intended to flatten the surface and consequently better distribute the loading. Two wideband acoustic emission sensors (Micro80 - 200-900 kHz) and an LVDT extensometer were utilized to characterize the structures during tests as seen in Figure 2.39.

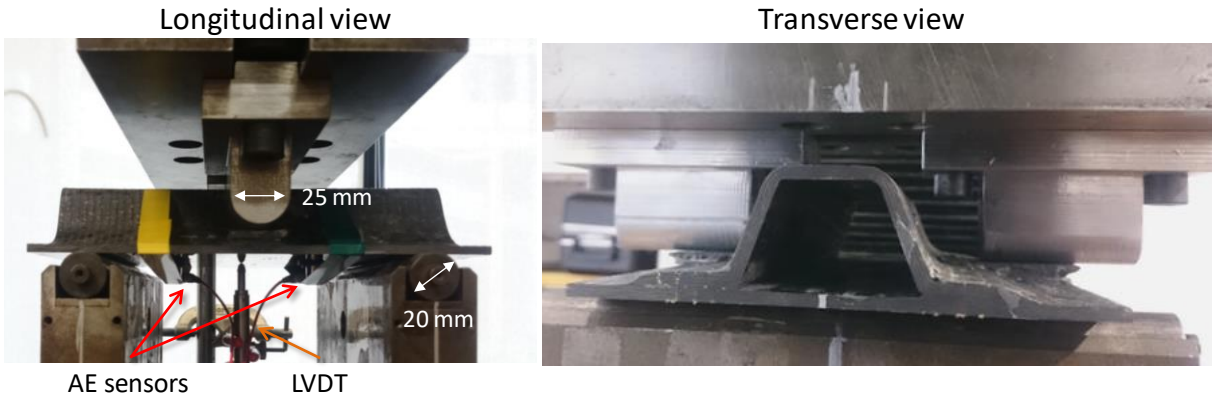


**Figure 2.39 - 3-point bending test setup.**

The support span (X) and the distance between the loading noses (Y), as exhibited in Figure 2.40, were adjusted according to the batch of the structure. It was carried out because of the difference of the stiffener width from Batch I to Batch II and III as well as the length of the specimens. Moreover, the distance between the AE sensors was according to each batch of the structure. Table 2.4 presents the parameters.

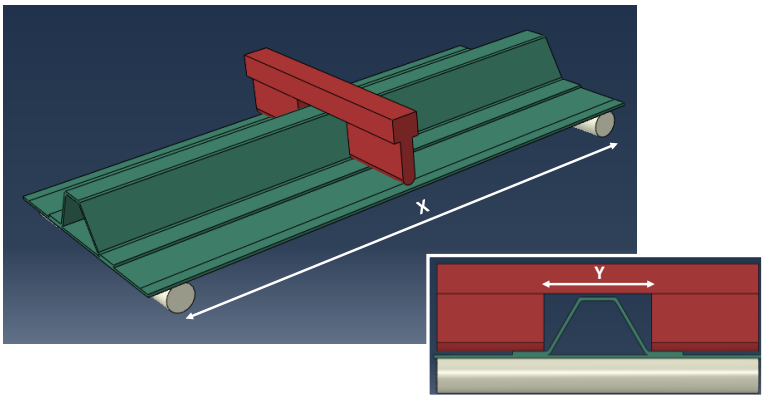


**Figure 2.40 - Schematic of the 3-point bending test setup for omega stiffeners.**

**Table 2.4 - Parameters employed for the test apparatus according to the specimens batch**

| | Support span (X) | Distance between loading noses (Y) | Distance between AE sensors |
|---|---|---|---|
| **Batch I** | 144 mm | 78 mm | 80 mm |
| **Batch II** | 240 mm | 105 mm | 160 mm |
| **Batch III** | 240 mm | 105 mm | 160 mm |

Besides the acoustic emission and LVDT measurements, electrical resistance was obtained for Batch II stiffeners during tests. Chapter 5 details the testing methods utilized for the characterization of this batch of specimens under 3-point bending tests.

# CHAPTER 3 INVESTIGATION OF THE MECHANICAL BEHAVIOR OF LAMINATED COMPOSITE PLATES REINFORCED BY TUFTING

## 3.1 Introduction

This chapter investigates the in-plane and out-of-plane mechanical properties as well as the damage tolerance of the laminated composites reinforced by tufting. The first part consists of the study of the specimens submitted to short beam shear tests. They were multi-instrumented with a 2D-DIC camera and in-situ microscope to better understanding the damage development and the contribution of the tuft threads in the out-of-plane properties. Afterward, drop-weight impact tests were carried out to investigate the damage tolerance of the tufted composites and their behavior in comparison with the control specimens. Compression before and after impact tests (CBI and CAI respectively) aided to obtain the residual strength of the samples and evaluate the different set of specimens according to the tufting parameters (density and angle of tufting). Finally, the last part of the present chapter regards to the mechanical behavior of the open-hole specimens subjected to tensile fatigue tests. It reported the investigations concerning the effect of the type of drill, utilized for performing the holes, and the tuft rows position in the mechanical properties of the composites. The approach consisted of the load-unload cycles, fatigue loading, and quasi-static tests until failure. Further, an investigation of the strain concentration factor was executed using the strain fields acquired by DIC during the mentioned tests.

## 3.2 Results

### 3.2.1 Laminate composite plates (Plate I)

The present section concerns the results for the tufted composites subjected to different mechanical tests. The details about the manufacturing process of the specimens are described in section 2.2.3. Table 3.1 reminds the designations of the samples investigated.

**Table 3.1– Specimens description**

| specimen | Description | Tufting density (mm x mm) |
|---|---|---|
| **REF** | Control specimens | ---- |
| **T10** | Transversal tufting | 10x10 |
| **T5** | Transversal tufting | 5x5 |
| **A10** | Angular tufting (±30°) | 10x10 |
| **A5** | Angular tufting (±30°) | 5x5 |

**a)** ***Short beam shear test***

The investigations of tufting behavior on the shear loading condition utilized specimens prepared from the transversal (weft) and longitudinal (warp) direction to the $[0]_8$ layup for the configurations REF, T5, and A5. The tuft rows are aligned along the longitudinal direction of the specimens. Figure 3.1 exhibits a schematic of the samples obtained from the plate I and the axis direction employed in this study.

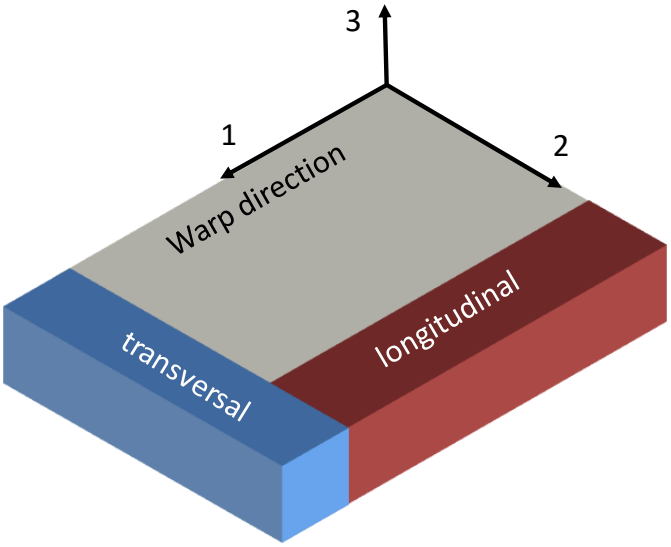


**Figure 3.1 - Schematic illustration of the specimens obtained about its laminate direction.**

The results can help the understanding of the damage mechanisms and are comparable to the specimens subjected to low-velocity impact loading in the next section, once that loading conditions on low-velocity impact consist mainly of the mode II shear loading. The short-beam shear tests followed the standard ASTM D2344-16 [227] to the test methods and specimens preparation. The interlaminar shear strength ($\tau_{xz}$) of the composites consists of the maximum shear stress that occurs at the neutral axis, as reported in the standard mentioned above and described in equation (3):

$$\tau_{xz} = 0.75 \frac{P}{b.h} \quad \textbf{(3)}$$

where *P* is the load (*N*), *b* and *h* the width and thickness of the specimen respectively.

Figure 3.2 shows the maximum shear stress obtained for the control, A5 and T5 specimens in both longitudinal ($\tau_{13max}$) and transversal ($\tau_{23max}$) direction. The results evidence that tufting reinforcements do not increase the shear strength and moreover, the transversal tufted specimens presented lower values than untufted composites. However, in comparison to the decrease range of 17-38% reported in the literature [177], tufting effect seems negligible in the longitudinal direction and presents a slight decrease of 8% and 10 % transversal specimens T5 and A5 respectively. One of the main reasons to the tufted specimens does not enhance interlaminar shear strength is due to the layer created on the surface of the specimen owed to the tuft loops. It increases the specimen thickness when compared to control specimens, which consequently reduces the strength. However, this thickness growth does not bring anyone mechanical benefit to the composite, because it contains in the majority polymeric resin. A future study may be performed in specimens with a partial insertion of tufts or with the surface machined to diminish the effect related to the increase of thickness that is generated by the loops. This procedure could lead to a better investigation of the interlaminar shear strength of the tufted composites.

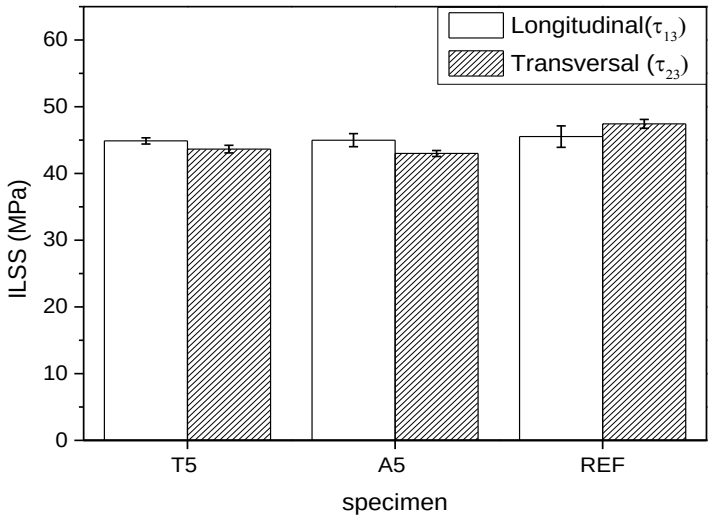


**Figure 3.2 - Interlaminar shear strength for the samples longitudinal and transversal from REF, T5, and A5.**

Considering that short-beam tests generate principally mode II loading, DIC performed during tests were utilized to calculate the mean shear strain ($\gamma_{xz}$) and consecutively the interlaminar

shear modulus ($G_{xz}$). It is assumed that shear stress presents parabolic distribution through beam thickness and reaches its maximum on the neutral plane as seen in Figure 3.3a. A small zone was selected (red dashed rectangle in Figure 3.3b) centered in the neutral plane (Z=0) to obtain the shear strain values. Moreover, the longitudinal position based especially on finding a region that exhibits negligible principal strains ($\varepsilon_{xx}$ and $\varepsilon_{zz} \approx 0$) and less affected by the strain concentration due to the rolls loading. This approach has shown its efficiency to achieve the interlaminar shear strain as reported by Song [233]. In this research work, the author divided the transversal area of the DIC images on small parts to study the strain fields acquired during short-beam shear tests. The primary goal was locating a zone which presents negligible mean principal strains by virtual strain gage via DIC method and associating with the maximum shear stress location.

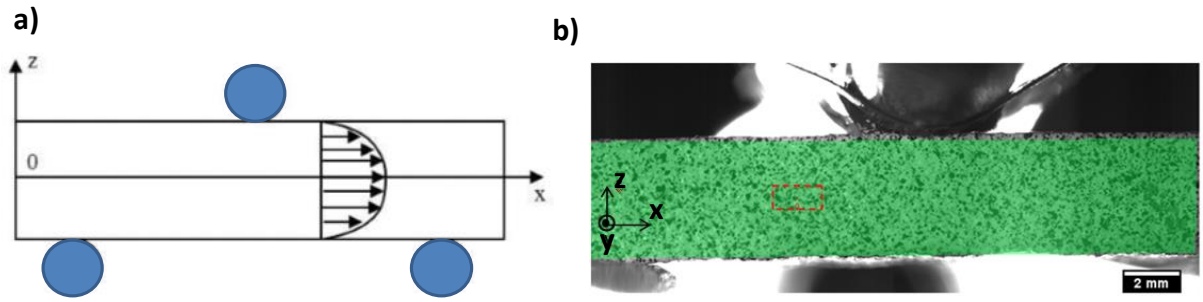


**Figure 3.3 - a) Schematic of the shear stress distribution through-thickness of a specimen under short beam strength tests and, b) Virtual gage applied on DIC strain field to calculate the mean strain**

The position of the virtual gage was not the same to every specimen. Song [233] reported in her thesis that the mean shear strain found in tufted specimens differs significantly from a region containing tuft thread to another not including. Thus, the choice of a gage position including tufting thread and fabric preform is fundamental to homogenize the properties of the structure. Figure 3.4 and Figure 3.5 presents a typical response of the shear stress in function of the out-of-plane strain ($\varepsilon_{zz}$), longitudinal strain ($\varepsilon_{xx}$) and interlaminar shear strain ($\varepsilon_{xz}$), obtained by DIC analysis for the longitudinal and transversal specimens respectively.

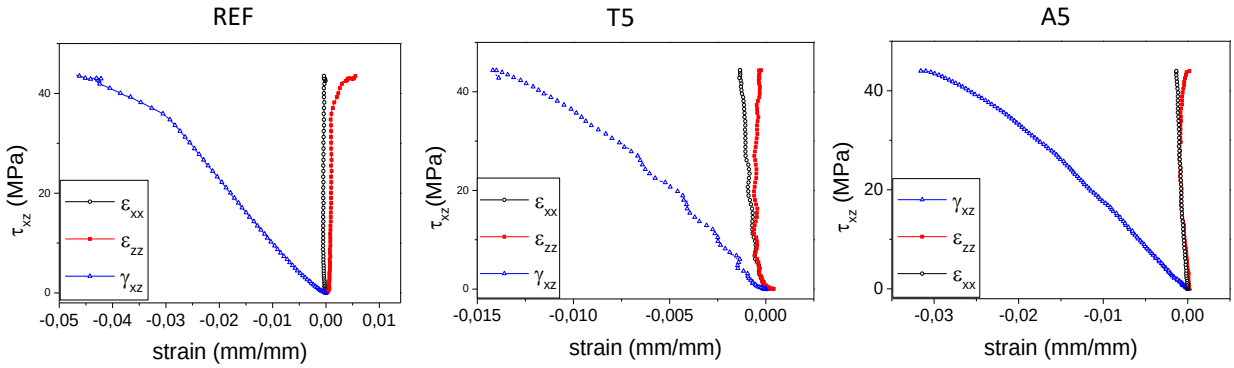


**Figure 3.4 - Mean strains ($\varepsilon_{xx}$, $\varepsilon_{zz}$, and $\gamma_{xz}$) obtained by DIC images from REF, T5 and A5 longitudinal specimens.**

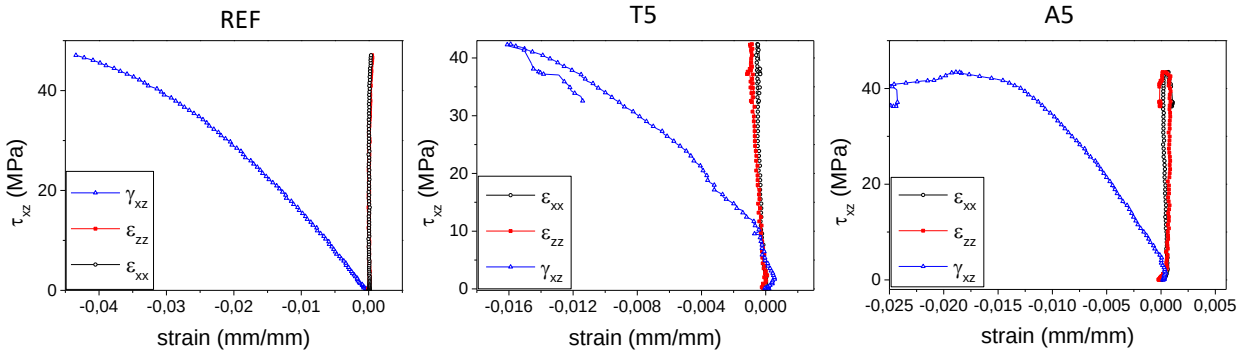


**Figure 3.5 - Mean strains ($\varepsilon_{xx}$, $\varepsilon_{zz}$, and $\gamma_{xz}$) obtained by DIC images from REF, T5 and A5 transversal specimens.**

Figure 3.6 shows the interlaminar shear moduli for the longitudinal ($G_{13}$) and transversal ($G_{23}$) samples obtained from the interlaminar shear stress-strain curves in the linear response. Compared to the untufted composites, $G_{13}$ presented a 3.37-fold and 1.9-fold increase for T5 and A5 respectively, while $G_{23}$ presented enhancements of 13% and 38% for T5 and A5 respectively. In general, the tuft threads create a through-thickness interlocking which difficult shearing between the fabric plies. Furthermore, the significant difference of the $G_{13}$ values found for T5, and A5 specimens are supposed to be related to the significant distance into two pairs of crossed threads left in A5 when comparing to T5, which can enable the shearing between the plies. Otherwise, the higher values of $G_{23}$ obtained for the A5 specimens against T5 are mainly due to the complex geometry of the tufted threads that increase the reinforcement amount in this direction and reduce the interlaminar shearing process.

The results presented for the untufted specimens in both directions are different from expected to an orthogonal stacking sequence of fabrics. Despite orthogonal woven fabrics as plain weave, twill weave and satin weave are assumed to have the same mechanical properties on warp and weft direction; the mechanical properties may change regarding the principal directions in the

composites. This behavior can be related to the weaving manufacturing mode and composite layup as reported to different authors [234], [235]. According to Alif et al. [234], the delamination resistance and the difference in fracture toughness between the warp and weft directions increase with increasing the weave index. They described that for the twill and satin weaves, crack propagation in the 90° direction, i.e., along with the weft yarns, requires significantly larger loads than propagation in the 0° direction. These researches corroborate with the results found in the present work for the control composites, where the transversal and longitudinal direction is aligned with weft and warp directions of the fabrics respectively. However, this behavior is no longer significant for the tufted composites owed to the considerable contribution of the tufts to the mechanical response of the composites.

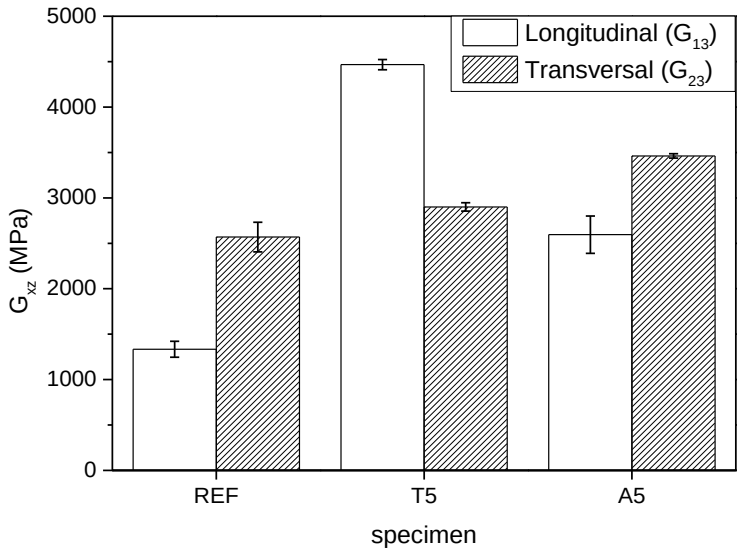


**Figure 3.6-. Interlaminar shear modulus ($G_{xz}$) for REF, T5, and A5 specimens.**

Figure 3.7a and b exhibit the typical behavior of the specimens from the longitudinal and transversal direction respectively subjected to the short beam shear tests. The events i and ii marked in the curves are presented in Figure 3.8 and Figure 3.9 by the DIC shear strain fields ($\varepsilon_{xz}$) before and after a significant load drop correspondingly.

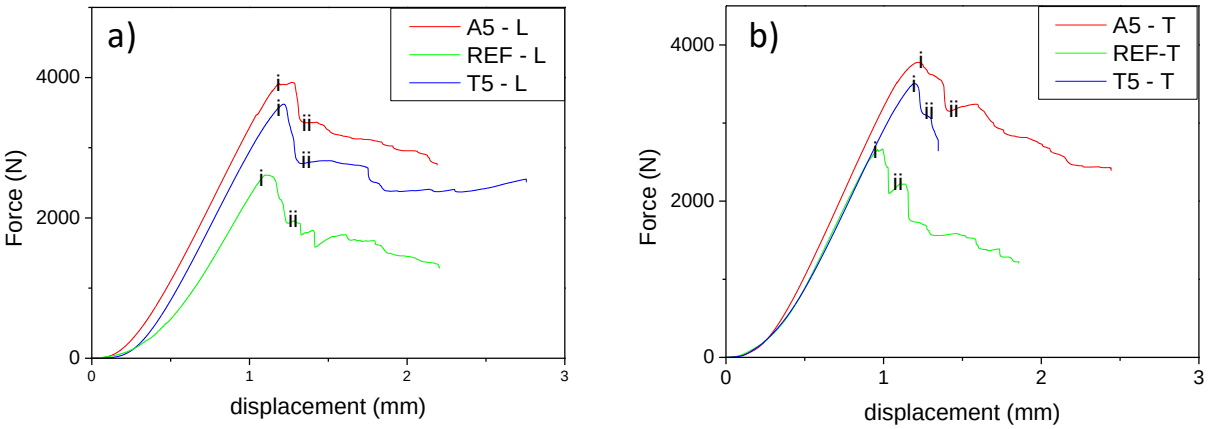


**Figure 3.7 - Typical load-displacement curves for REF, A5 and T5 in a) longitudinal and, b) transversal direction.**

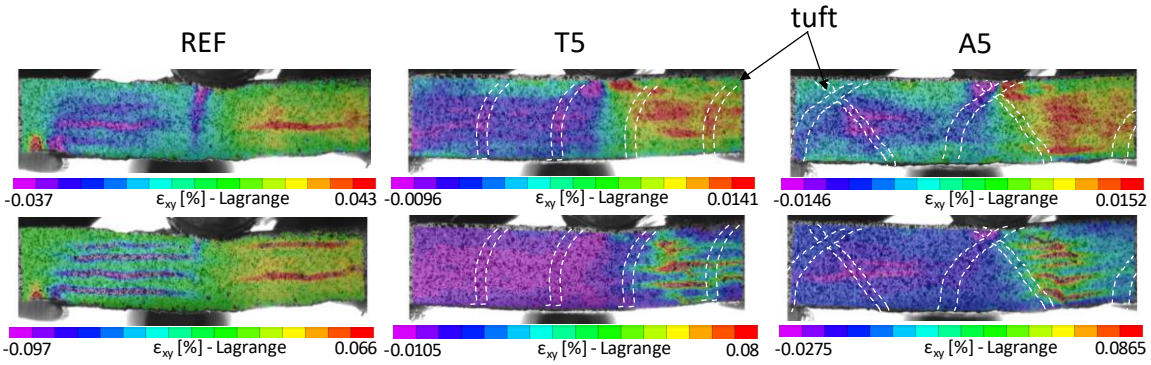


**Figure 3.8 – DIC strain field for the longitudinal specimens before and after the sudden load drop due to crack growth.**

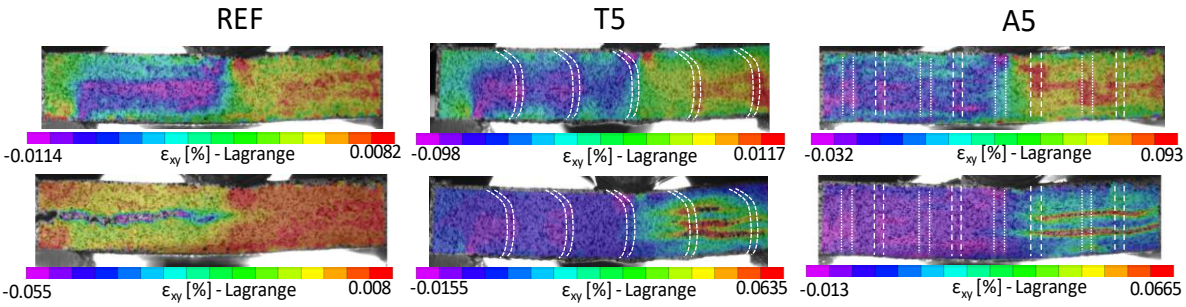


**Figure 3.9 - DIC strain field for the transversal specimens before and after the sudden load drop due to crack growth.**

The region between the tufts presents a considerable concentration of shear strain before the initiation of delamination and, after the load drop, the same tuft threads contain the development of delamination. However, when analyzing the video micrographics (Figure 3.10 and Figure 3.11), it is visible that cracks initiate from tuft threads and propagate into the plies due to the strain concentrated around the threads. This behavior may be responsible for the inferior shear strength of the tufted specimens and counteracts the improvements on shear strain resistance.

On the other hand, once that cracks initiate and propagate as delamination, they are arrested by the next tuft row disposed longitudinally to the specimens. It avoids sudden failure and enhances the mode II interlaminar fracture toughness of the laminated composites.

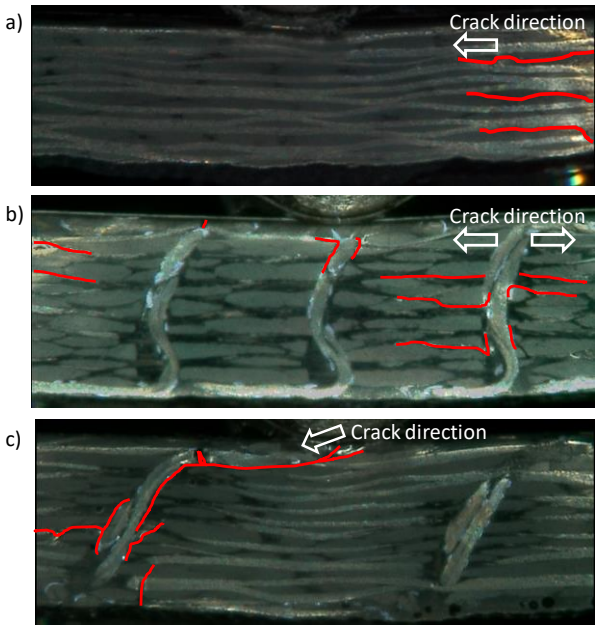


**Figure 3.10 - Micrograph acquired after crack initiation by video microscope under tests for a) control, b) T5 and c) A5 longitudinal specimens.**

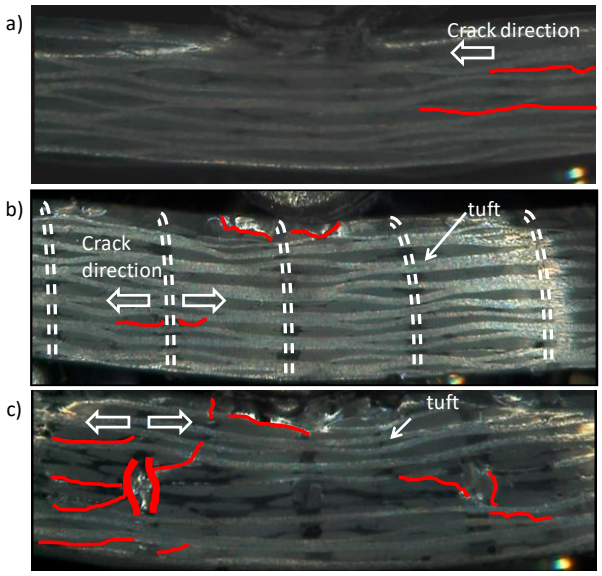


**Figure 3.11 – Micrograph acquired after crack initiation by video microscope under tests for a) control, b) T5 and c) A5 transversal specimens.**

Table 3.2 summarizes the values obtained for interlaminar shear strength ($\tau_{xzmax}$) and shear modulus ($G_{xz}$) in the principal directions.

**Table 3.2 - Mean values of shear strength and shear modulus for the specimens tested in the principal directions under short beam shear tests.**

| specimen | $\tau_{xzmax}$ (MPa) | | $G_{xz}$ (GPa) | |
|---|---|---|---|---|
| | $\tau_{13}$ | $\tau_{23}$ | $G_{13}$ | $G_{23}$ |
| **REF** | 45.5 ± 1.6 | 47.4 ± 0,7 | 1334 ± 87 | 2569 ± 163 |
| **A5** | 45.0 ± 1.0 | 43.0 ± 0,4 | 2595 ± 205 | 2900 ± 46 |
| **T5** | 44,9 ± 0,5 | 43.7 ± 0,6 | 4467 ± 56 | 3462 ± 24 |

**b)** ***Impact tests***

The present section consists of the results obtained from the compression before impact, drop-weight impact, and compression after impact tests, respectively.

**Compression before impact (CBI)**

CBI tests were mainly performed to evaluate the residual strength with the composites submitted to compression after impact tests. The results of CBI strength were also compared to investigate the tufting effect on the in-plane properties. The compressive tests followed the ASTM D6641−14 standard [228], instead of using the same specimens dimensions employed on CAI tests, due to issues on achieving the material failure in the preliminary tests. Three samples of the sets REF, A5 and T5 were subjected to CBI loading, and their ultimate strength results exhibited in Table 3.3. The values of the tufted composites are significantly decreased when compared to the control specimens (REF) and validate the drawbacks already reported in the literature for the through-thickness reinforcements. Fiber rupture of the fabrics and misalignments are one of the issues that decrease the in-plane properties of the laminate composites. Moreover, the rise of thickness caused by a thin layer formed on the specimens surface of the tufted composites may make difficult this evaluation, once that the deposited layer is mainly composed of resin and tuft loops, which is not seen to improve the in-plane properties but increases the material cross-section and consequently, reduces the sample strength.

**Table 3.3 - Ultimate strength for REF, A5, and T5 obtained on CBI tests.**

| specimen | Ultimate strength (MPa) |
|---|---|
| REF | 453,1 ± 40,9 |
| T5 | 323,9 ± 28,9 |
| A5 | 271,9 ± 19.7 |

Figure 3.12 shows the micrographs of the post-mortem specimens. The control specimens (Figure 3.12a) presents significant catastrophic failure in comparison to the tufted specimens. The compressive loading induces the out-of-plane swelling of the untufted laminates due to their poor interlaminar fracture toughness, which consequently generates delamination. Otherwise, interlaminar failure is less perceptible for the tufted laminates thanks to the enhancement of the out-of-plane properties, opposing the through-thickness opening force generated during compressive tests. However, it is supposed from the images for T5 and A5 specimens, Figure 3.12b, and c respectively, that failure is initiated on the surface of the tufted region. This behavior can also be related to the decrease in the ultimate strength of the tufted composites.

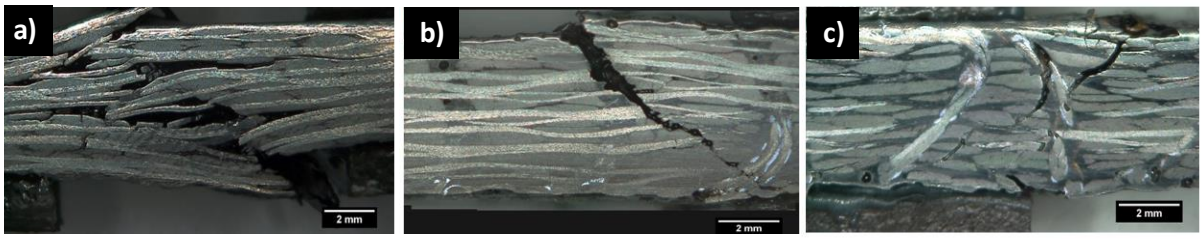


**Figure 3.12 - Post-mortem micrographs of a) REF, b) T5 and, c) A5 specimens subjected to CBI tests.**

The behavior of specimens under short beam shear tests shows that tufting improves shear stiffness, but degrades the ultimate shear stress. This degradation lies in the over-thickness of resin, due to the tufting process, which causes the stress to decrease without a significant mechanical contribution.

The damage scenario presents that the damage takes place around the tufts, but the tufts allow arresting the crack development during the ruin procedure. These observations and understanding of the specimens at a local level provides a basis for further tests, including impact tests upon which the major damage mechanism consists of successive delamination due to the shearing through the plies.

**Drop-weight Impact**

The curves load vs. deflection were plotted in Figure 3.13 and Figure 3.14 to the 25 and 60 J impact energies respectively. The tuft rows are aligned along and perpendicular to the longitudinal direction of the specimens for the transversal and angular tufting (see section 2.2.3a). Initially, they show a linear part followed by a first load drop. Then, a stiffness loss before the maximum load characterizes the second part. The general behavior under tests

confirmed the enhancement of composite toughness by the tufting reinforcements, showing a maximum deflection to the untufted (REF) when compared to the tufted specimens.

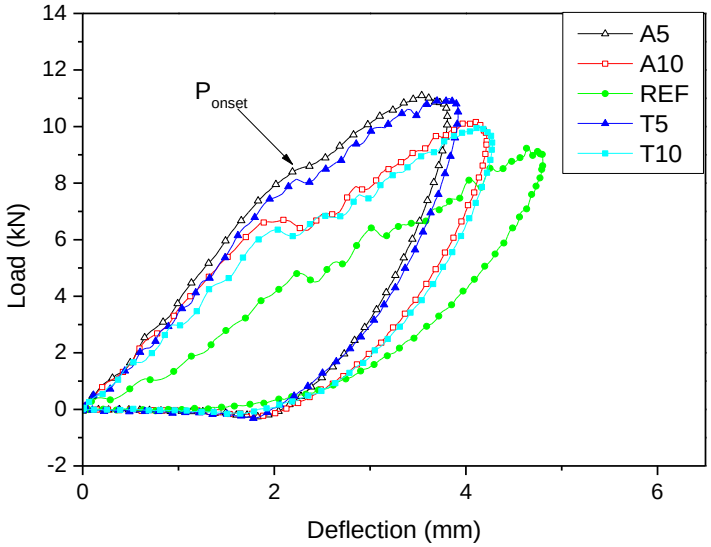


**Figure 3.13 - Typical load-deflection curves during impact at 25 J.**

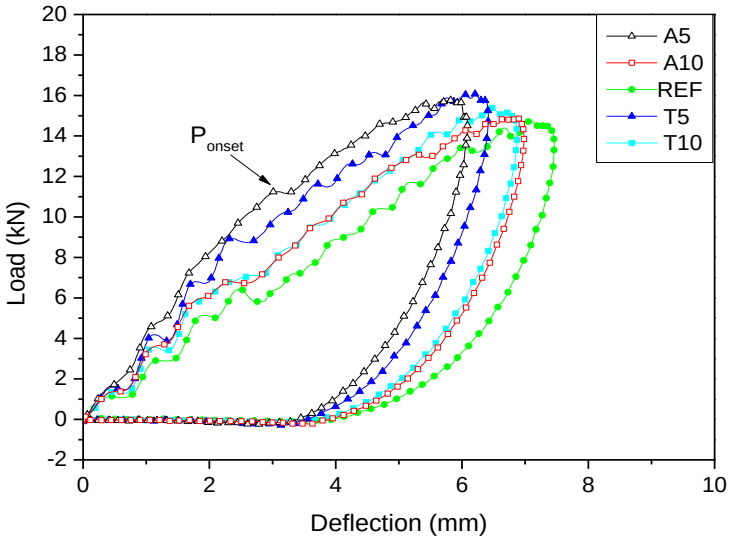


**Figure 3.14 - Typical load-deflection curves during impact at 60 J.**

The force needed for the delamination onset ($P_{onset}$) was higher in the angular tufting samples than in the transversal for both impact energies, especially to the densest samples as summarized in Table 3.4. This point concerns the first significant damages which result in stiffness loss. It means that the inclined tufts increase the delamination resistance by resisting crack sliding displacement. Moreover, for all set of specimens, the $P_{onset}$ is not considerably changed by tufting reinforcements from 25J to 60J tests, except in the case of the angular configuration where a significant increase is found. This indicates a greater capacity of this configuration to absorb impact loading.

The deflection on the bottom side of the samples was measured during impact tests by a laser system. Table 3.4 compares the results of maximum deflection for both impact energies. Transversal tufts presented a little improvement in comparison to angular reinforcement for resisting the transversal deflection. This response can be attributed to the tuft carbon threads aligned in the transversal direction which enhance the through-thickness stiffness. Also, as expected, the maximum deflection was inversely proportional to the tufting density as a result of the enhancement of the transversal stiffness. These results corroborate with the analysis of the interlaminar shear moduli obtained from the short beam shear tests, which found an increase of the shear modulus for the tufted specimens in comparison to the control and especially, a significant response for the T5 configuration.

**Table 3.4 - $P_{onset}$ values and maximum deflection at both impacted energies.**

| specimen | $P_{onset}$ (N±SD) | | Max. deflection (mm±SD) | |
|---|---|---|---|---|
| | 25J | 60J | 25J | 60J |
| **REF** | 6,31 ± 0,08 | 6,52 ± 0,08 | 4,78 ± 0.24 | 7,03 ± 0,15 |
| **T10** | 7,00 ± 0,07 | 7,15 ± 0,01 | 3,66 ± 0.06 | 6,39 ± 0,22 |
| **T5** | 7,98 ± 0,09 | 8,99 ± 0,01 | 3,47 ± 0,16 | 5,59 ± 0,11 |
| **A10** | 6,85 ± 0,62 | 6,71 ± 0,22 | 3,84 ± 0,13 | 6,61 ± 0,14 |
| **A5** | 8,18 ± 0,74 | 11,30 ± 0,01 | 3,33 ± 0,13 | 6,02 ± 0,07 |

Figure 3.15 shows the typical damaged area of the different sample configurations concerning the two impact energies studied. The images obtained by the ultrasonic C-Scan method from a scanned zone of 80x80 mm were processed and analyzed on software ImageJ. The results evidence that tufting reinforcements change the damaged area, which behavior depends directly to the tufting parameters (angle and density).

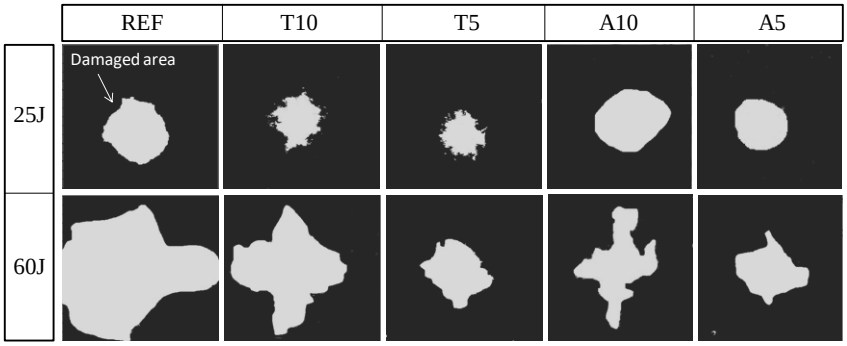


**Figure 3.15 - C-Scan images from the impacted samples analyzed on ImageJ.**

Figure 3.16 presents the percentage of the damaged area for each specimen set. The results describe that the damaged area is inversely proportional to the tufting density. The transversal

tufted samples impacted at 25J were the most efficient to arrest the delamination progress. However, the T10 configuration had larger damaged area than A10 for the samples impacted at 60J, which did not follow the behavior as in the lower energy. Additionally, the inclined tufts become more efficient to restrain fissures development at 60J, which is reported by the lower increase in the damaged area from 25 to 60J when compared to transversal tufted specimens. It can be concluded that tufting reinforcement reduces the delamination by concentrating the damage in a small area and, the angular tufting is not seen to alter the damaged area response significantly in comparison to the transversal specimens.

It is noticeable that the damaged area is directly proportional to the deflection when comparing the maximum deflection at the bottom side of the impact (Table 3.4) with the damaged area (Figure 3.16). For example, the control specimen deflects the most among the configurations under impact loading because of their lower out-of-plane toughness, which generates and propagates more the delamination when compared to the other sample configurations. Further, the T10 and, A10 configurations decrease the deflection under impact in comparison to the control specimens, causing the reduction in the damaged area consequently. Based on this analysis, the densest tufted specimens achieved the optimal results.

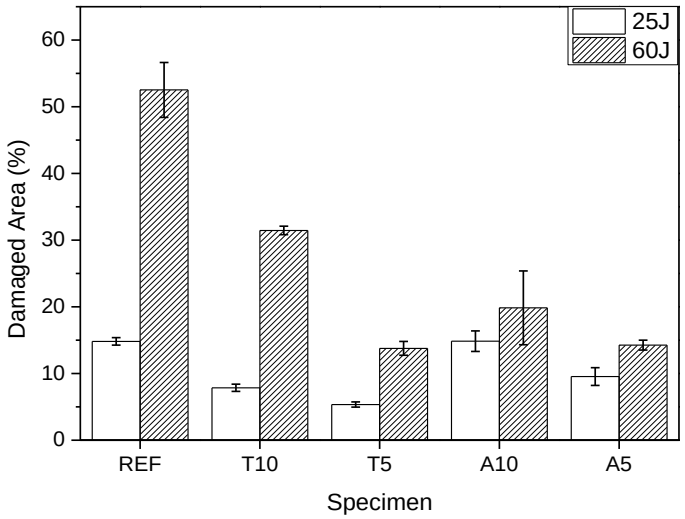


**Figure 3.16 - Average of damaged area for REF; T10; T5; A10 and A5 samples at 25 J and 60 J.**

Figure 3.17a-c shows optical micrographs from REF, T5 and A5 specimens impacted at 25 J, respectively with their significant cracks highlighted in the figures. Figure 3.17a presents the through-thickness crack evolution for the untufted sample. The cracks propagate in the matrix at approximately 45º, due to transverse shear stress, and develop until reaching the fabric interface where they continue as delamination. The damages on the bottom layer are due to high

tensile stress induced by the bending on impact loading. The sample behaves as reported in the literature for laminated composites subject to drop-weight impact.

Figure 3.17b shows the crack development for the laminate reinforced transversally, T5. Differently, from the behavior seen in the untufted specimen, delamination is no longer evident, and the cracks are in the majority in the matrix at 45º. The tuft threads inhibit the crack development by displacing the crack tips to along them, therefore decreasing the damage energy. Also, improving the through-thickness stiffness means lower tensile stress response owed to the bending caused by the impact loading. This behavior can be verified by the decrease of damage extent in the bottom layer when compared with the control specimens.

By analyzing the Figure 3.17c, it is seen that delamination is more critical than in the transversal samples but less than in the untufted specimens. The tuft threads act diverting the cracks and especially arresting the delamination progress. Significant cracks also appear through the thread length for the A5 composite, supposedly from the surface to inside along the threads. Additionally, due to the angle of tufting equal to ±30º employed to the normal of the surface, the threads do not cross near the middle plane of the thickness. The angular tufting process also presented a substantial concentration of porosities near to the threads in comparison to the others specimens.

Furthermore, the threads were not as straight as expected to both tufting configurations investigated. The compaction of the preform causes this behavior during the VARTM process. This fact must be taken into account especially in future finite element analysis. Also, the resin layer created on the surface of the laminate by the tuft loops helps crack initiation and propagation as seen in Figure 3.17b and c.

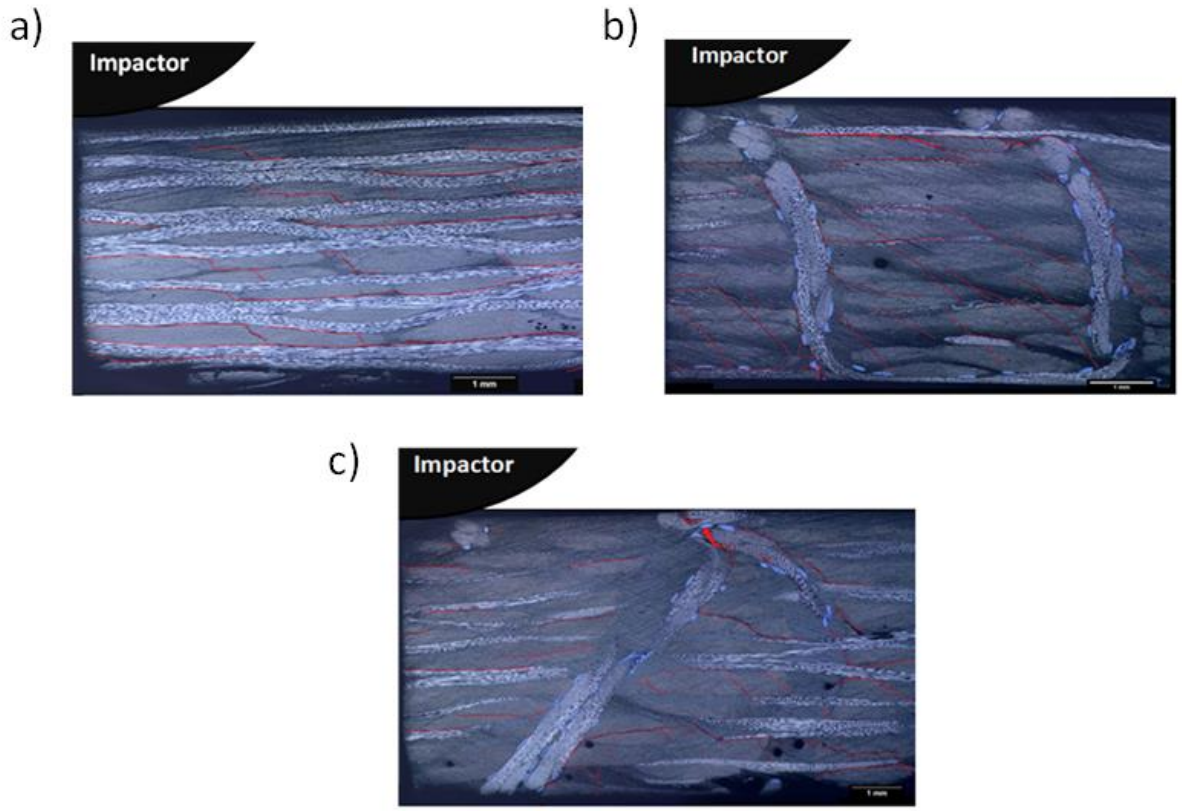


**Figure 3.17 - Optical micrographs for a) control; b) T5 and c) A5 specimens impacted at 25 J.**

From the microscopy observations, a typical damage scenario is schematized for each set of samples and shown in Figure 3.18. For the untufted samples (Figure 3.18e), the damage develops from the impacted point to the distal face in a conical shape as described in the literature, while for the tufted composite laminates this study concludes that:

- The dent depth generated during impact loading increases at increasing of tufting density, regardless of the tufting angle. Figure 3.19 and Figure 3.20 shows the measures of the dent depth performed by DIC.
- The damages are mainly developed at 45° (matrix cracks) to the transversal tufted laminates (T5 and T10 in Figure 3.18c and d respectively) while they are in the majority at 0° (delamination) to the laminates with inclined tufts (A5 and A10 in Figure 3.18a and b respectively).
- The damaged area diminishes with increasing tufting density.
- The angular tufted laminates show impact damages more considerable than the composites reinforced with transversal tufts. These damages on angular tufted

specimens mainly concern the delamination, which may weaken the structure on compression unless that the tufting density helps to reduce this phenomenon.

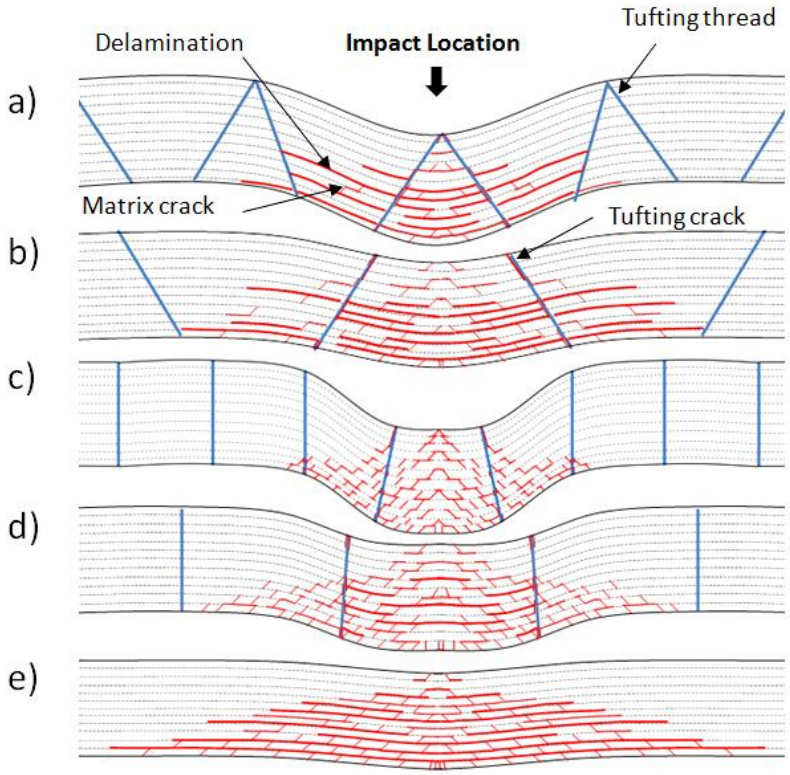


**Figure 3.18 - A schematic representation of the impact damages for the sets of specimens: a) A5; b) A10; c) T5; d) T10 and e) control specimen.**

### Compression after impact

The images took before CAI tests by the 3D-DIC method, helped in the analysis of the Z displacement field for measuring the impact dent depth. Figure 3.19 and Figure 3.20 exhibit the dent depth obtained from the impacted surfaces at 25 and 60 J respectively, and compare to the damaged area values previously analyzed by C-Scan. They indicate that the increase of the impact energy also amplifies the dent depth. Additionally, the tufting reinforcements increase the dent depth by improving the through-thickness stiffness. This response is also associated with the maximum deflection under impact already discussed. In comparison to the damaged area, the dent depth shows inversely proportional, especially to the 60J results.

The tufting threads prevent the failure development in the laminates when impacted, mainly caused by delamination. The interlaminar cracks are enclosed in a smaller zone in comparison to the control specimens due to the concentration of the impacted energy by the threads, which creates a more considerable dent depth with a reduced damaged area in the tufted samples. Otherwise, untufted samples dissipate the impact energy through the failure mechanisms as delamination and therefore presents the larger damaged area and the smaller dent depth among the specimens.

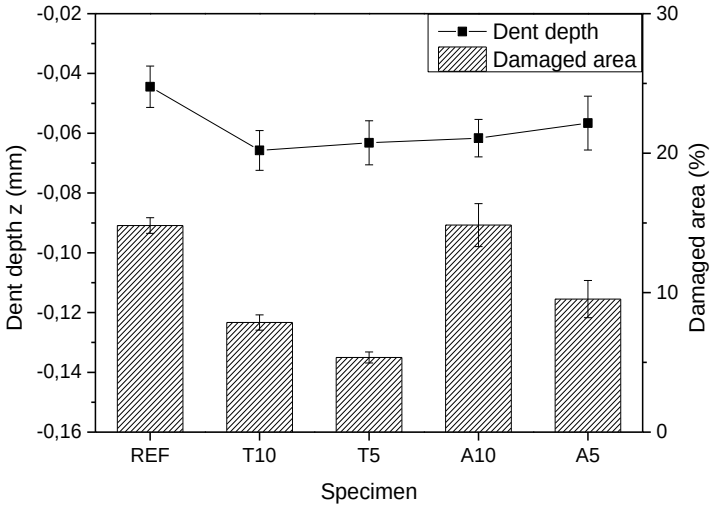


**Figure 3.19 - Dent depth from the impacted surface and its comparison to the damaged area at 25J.**

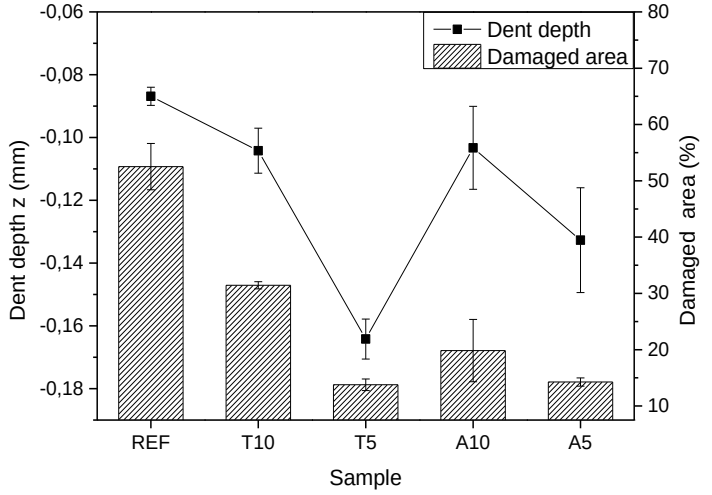


**Figure 3.20 - Dent depth from the impacted surface and its comparison to the damaged area at 60 J.**

A specific investigation from both surfaces of the REF, T10, and T5 specimens occurred by investigating the out-of-plane displacements obtained from the 3D-DIC method. Figure 3.21 presents a typical behavior of the tufted specimens from the out-of-plane-positions (Z) acquired by 3D-DIC in the beginning and end (just before significant failure) of CAI tests. The images

show the two face maps, face 2 and face 1 designated for the bottom and top surface respectively, utilized to acquire a virtual gage and consequently to calculate the out-of-plane displacements.

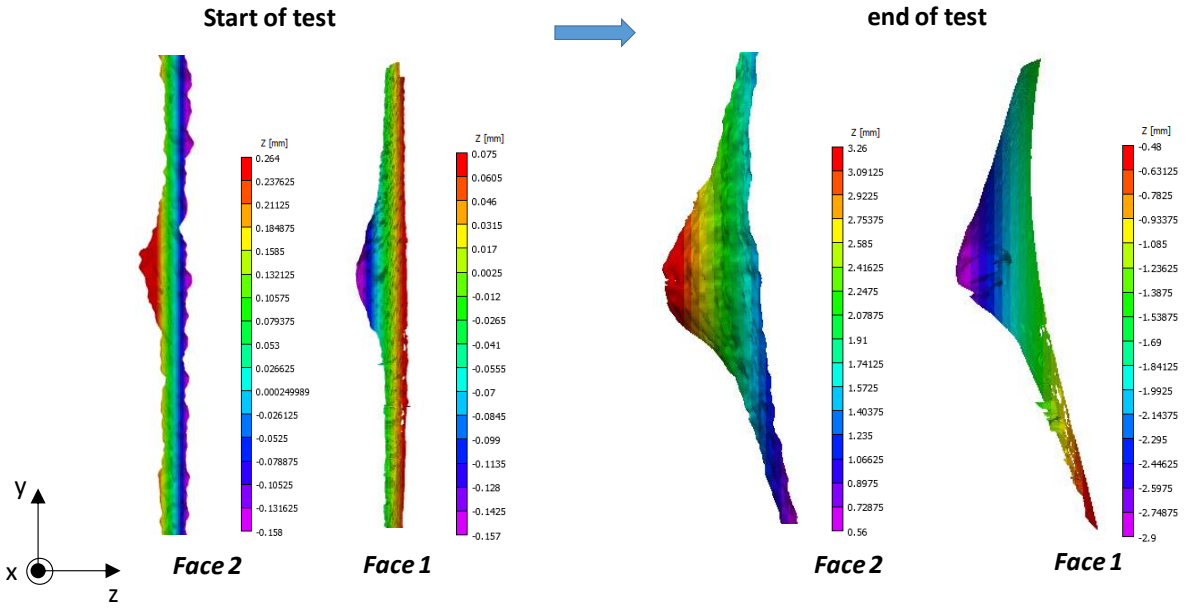


**Figure 3.21 - Example of a tufted specimen from the side view (zy-plane) of the out-of-plane geometry (Z) acquired for the two faces, from the bottom (Face 2) and top (Face 1) of the impacted zone.**

Figure 3.22a, c, and e present a typical behavior of the out-of-plane displacements for the REF, T10 and T5 specimens submitted to 25 J of impact energy respectively. Figure 3.22b, d and f exhibit the specimens REF, T10, and T5 subjected to 60 J respectively. The curves presented concern the mean values obtained from a virtual gage on the middle of the impacted zone (face 1 and face 2) of the images correlated by VIC-3D. Positive values correspond to out-of-plane displacements in the same direction and sense of the cameras, while an opposite sense leads to negative displacements. The difference between the two curves, designated as Dif(f2,f1) curves, results on a significant parameter to investigate the resistance to the out-of-plane opening forces generated under compressive loading. This behavior is significantly reduced for the tufted specimens T5 in both impact energies, with the resultant curve nearly to zero until the end of the test. It is mainly due to the crack bridging response of the tufts, which avoids the plies opening throughout compressive loading. These responses also validate the micrographs obtained for post-mortem specimens on CBI tests (Figure 3.12), where interlaminar damages were less pronounced to the tufted laminates. However, the T10 specimens subjected to 60 J, presented values higher than the others specimens, which is probably due to the significant dent depth formed during impact tests.

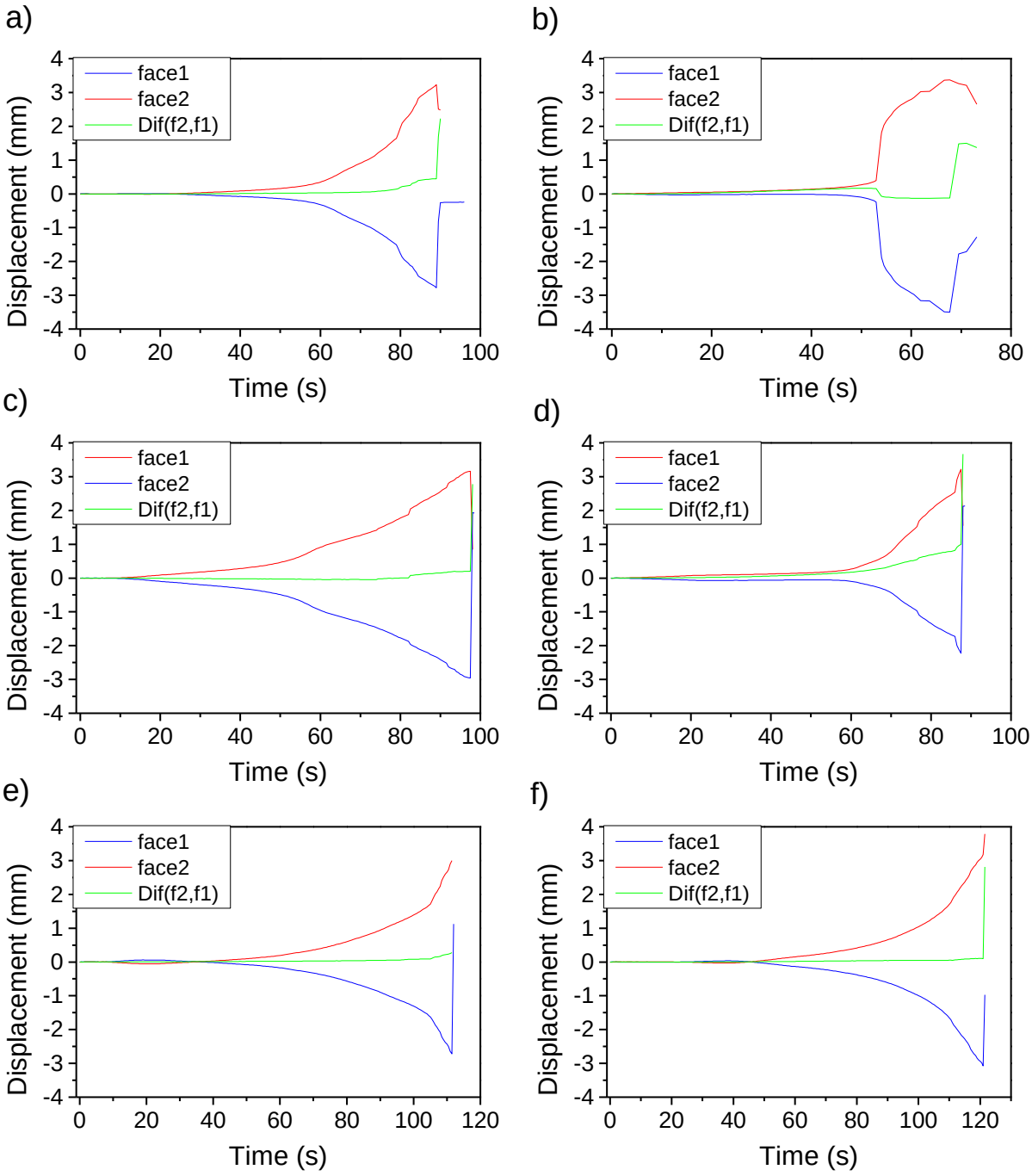


**Figure 3.22 - Out-of-plane displacement (w) on both sample sides and its differential for a) REF, c) T10 and e) T5 at 25J CAI; b) REF, d) T10 and f) T5 at 60J CAI.**

Figure 3.23 and Figure 3.24 show the typical behavior of the samples under CAI tests submitted at 25 and 60J impact energies respectively. In both energies, the curves of the untufted samples distinguish from the others with a noticeable load drop near to the ultimate strength. Delamination generated during impact weakens the samples under compressive loading. They cause a deflection reverse at the impact side and reduces the load carrying capacity of the delaminated plates [39]. This failure is reduced for the tufted specimens, especially increasing

the tufting density. Additionally, the transversal tufted laminates were more capable of containing the buckling in comparison to the angular tufted composites. The specimens impacted at 25J evidence better the difference of behavior between the control and the tufted composites. This response is related to the lower amount of damaged tuft threads caused in this impact energy, which makes them more able to restrain the opening mechanism and unstable compression than the samples impacted at 60J.

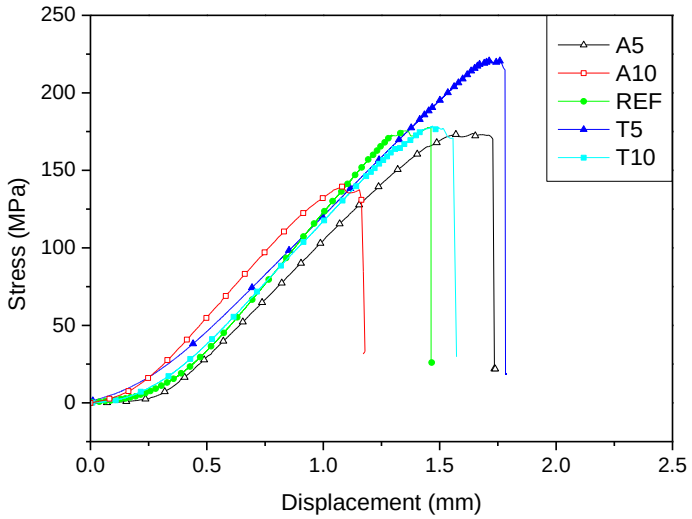


**Figure 3.23 - Typical behavior on CAI tests to the samples impacted at 25 J.**

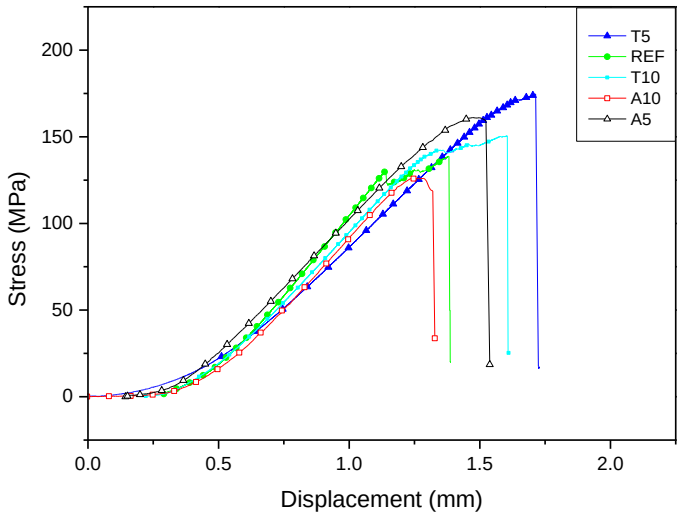


**Figure 3.24 - Typical behavior on CAI tests to the samples impacted at 60 J.**

Figure 3.25 summarizes the average ultimate strength for the samples under CAI tests. A10 is the only configuration that presents ultimate strength values lower than the control specimens. In general, the tufting reinforcement plays a role in increasing the transversal strength of the

samples. The interlaminar opening is considered the principal factor in the buckling of the specimens that consequently leads to premature failure. The CAI strength achieved improvements of 6% (T10), 27% (T5) and 2% (A5) when impacted at 25J in comparison to the control specimens. To the samples impacted at 60J, the improvements were 19% (T10), 25% (T5) and 15% (A5). Unfortunately, the A10 configuration decreased the CAI strength of about 21% and 10% (25 and 60J respectively).

It is remarkable that for the angular reinforcements the significant damage created on impact tests is mainly concentrated around the tufting threads as exemplified in Figure 3.18a and b for A5 and A10 configuration respectively. The cracks in this region are initiated on impact loading and advance on CAI tests as schematized in Figure 3.26. It can be due to the maximum shear stress produced during CAI tests at 45° which is closer to the inclination of the tufts. This behavior becomes very critical for the A10 configuration (Fig.15.a) where it will generate an early failure when compared to T10.

The results of the damaged area scanned by C-Scan image consist of a planar view of the through-thickness damages, which impede distinguishing the cracks around the threads that are small when visualizing in the same plan of the image. However, these cracks can decrease the compressive strength significantly on CAI. A10 samples impacted at 60J evidence best this issue due to their damaged area be lower than the T10 configuration, and despite this, they obtained values of CAI strength lower than T10. These cracks also appear for the A5 configuration, but due to the crossing of the threads near to the surface, the cracks do not propagate in this region. Also, the fissures that propagate from the bottom side of the samples (opposite to the impacted surface) along to the tufted threads are deflected and bridged by the threads which avoid the loss of resistance when compared with the A10 configuration, as shown in Figure 3.26b. It will be essential in the future to analyze this kind of damage by X-ray microtomography technique.

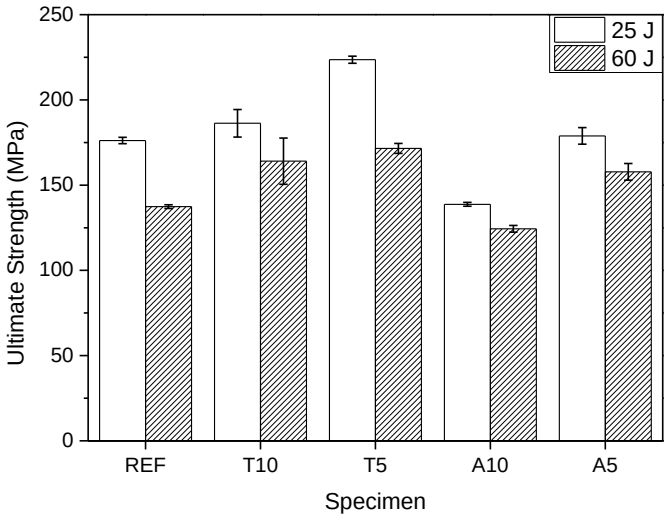


**Figure 3.25 - Ultimate compressive strength comparison for the different sample configurations.**

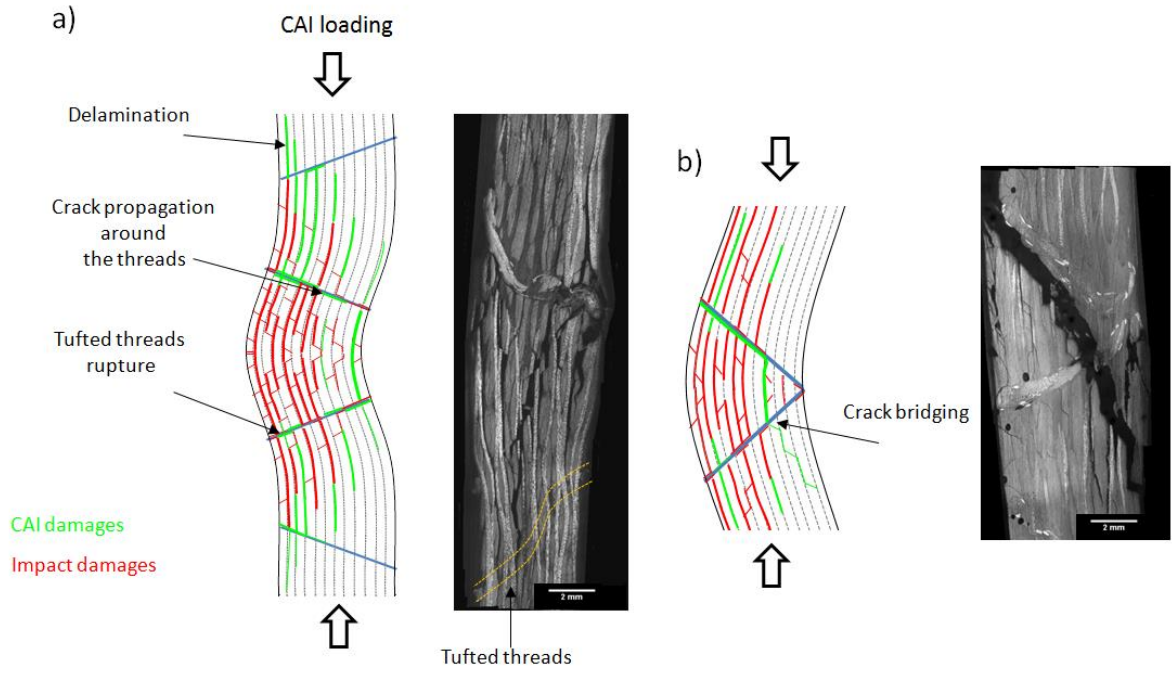


**Figure 3.26 - Schematization of the damage on CAI of the composite laminates: a) A10 and b) A5.**

Figure 3.27 exhibits post-mortem micrographs of specimens subjected to CAI, previously impacted at 60 J. Tuft reinforcements bridge the plies together as already mentioned for the images of specimens submitted to CBI tests. It precludes the laminate swelling and consequently contains the opening force in the cross-sectional direction of the plies that leads to interlaminar cracks. These damages are responsible for the unstable failure of the plies by micro-buckling, and their great extent may importantly reduce the CAI strength. Besides, the damages generated during impact loading, which is more extensive to the untufted specimens,

aid in developing delamination during compressive tests and therefore, decrease the ultimate strength. The delamination extent is superior to control specimens and decreases inversely with tufting density. The mentioned behavior can explain the lower values to A10 and REF obtained for CAI strength.

Figure 3.28a presents the bridging phenomena observed by Scanning Electronic Microscopy (SEM) for a tufted specimen subjected to CAI test. Despite the arresting of the crack growth, tufts create a weak region in the laminate surface from the insertion points, which are responsible for generating major cracks that will lead the structure to the failure (Figure 3.28b).

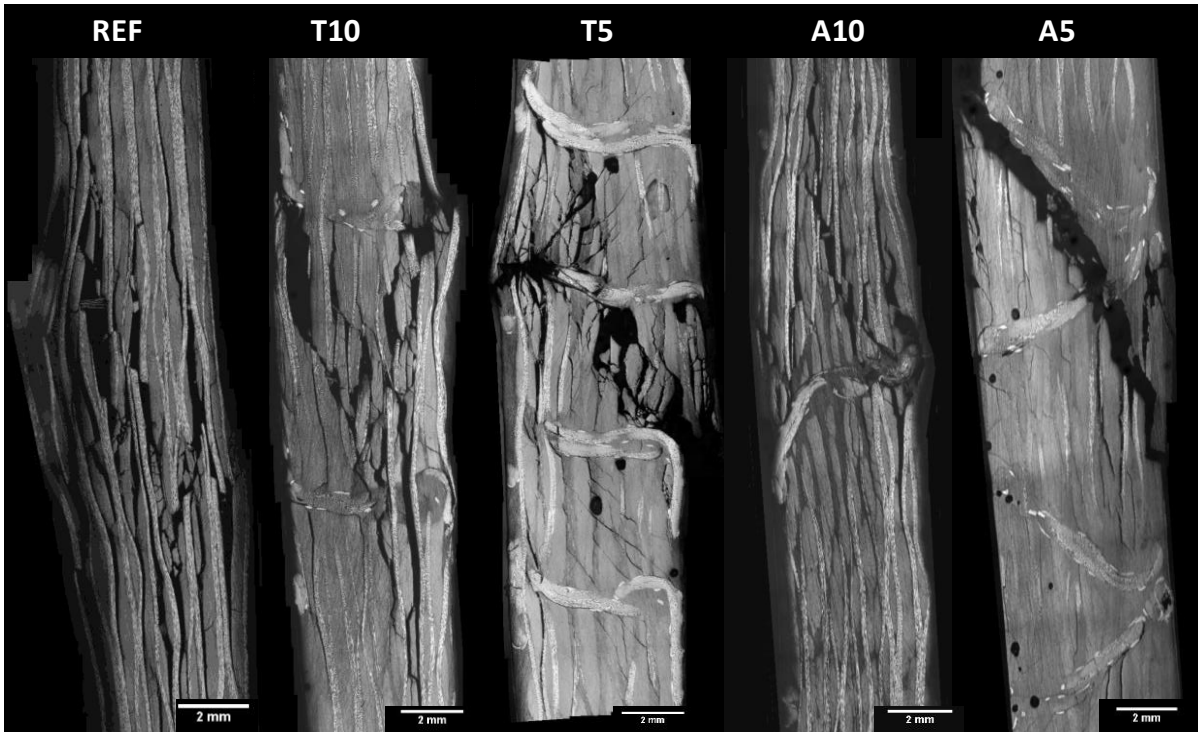


**Figure 3.27 - Micrographs of post-mortem specimens impacted at 60J and subjected to CAI tests.**

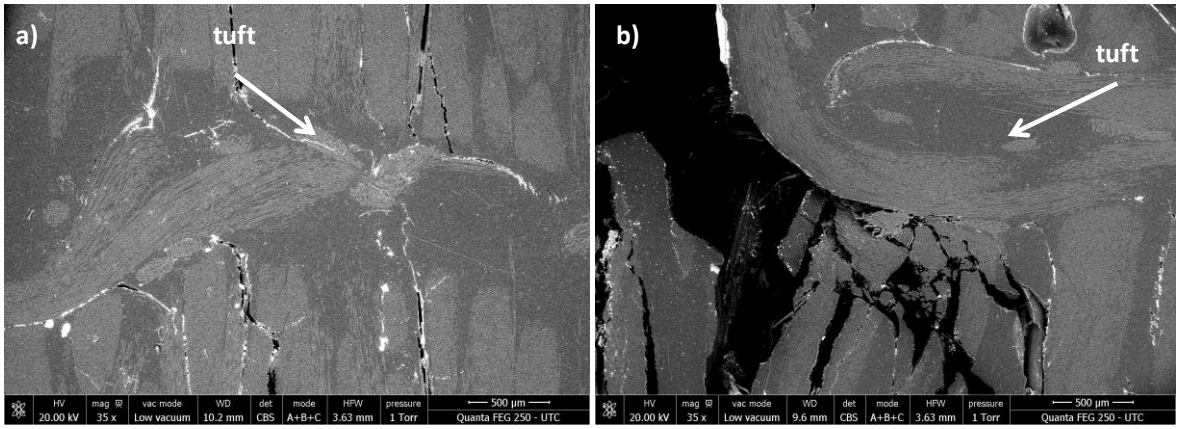


**Figure 3.28 - a) Post-mortem SEM micrographs for T5 specimens exhibiting, a) crack arrest behavior for a tuft reinforcement and, b) plies failure in the composite surface near to the tuft location.**

The specimens that achieved the best results on CAI were compared with those on CBI to evaluate the in-plane properties of the tufted composites (Table 3.5). The loss of compressive strength on the tufted composites before impact tests achieved up to 29% for the T5 configuration and 40% for the A5. This considerable reduction when inserting through-thickness reinforcements has been reported by many authors [9,18,40,41]. The development of the numerical methods for modeling the optimal tufting parameters in the composite should diminish their adverse effect on the in-plane properties. However, the tufted specimens showed greater residual ratio (CAI/CBI) in comparison to the untufted specimens (approximately 30% superior for T5 at 25J and 28% for A5 at 60J).

**Table 3.5 - Ultimate compressive strength on CBI and CAI tests, and the residual ratio (CAI/CBI)**

| Specimen | Ultimate Strength (MPa±SD) | | | Residual ratio (%) | Residual ratio (%) |
|---|---|---|---|---|---|
| | CBI | CAI 25J | CAI 60J | 25J | 60J |
| **REF** | 453,1 ± 40,9 | 176,1 ± 1.3 | 137,4 ± 1,1 | 38,9 | 30,3 |
| **T5** | 323,9 ± 28,9 | 223,5 ± 2.5 | 171,5 ± 2,9 | 69,0 | 52,9 |
| **A5** | 271,9 ± 19.7 | 178,9 ± 4.9 | 157,8 ± 4,9 | 65,8 | 58,0 |

The out-of-plane displacement characterized by DIC under CAI tests evidenced the sudden displacement that is mainly due to the local buckling. The acoustic emission activities also distinguished the behavior observed by DIC analysis owed to a considerable increase in the cumulative energy. The non-supervised clustering of the AE signals obtained during CAI loading helped to differentiate this crucial point.

It consisted of obtaining a particular cluster of acoustic signals that are related to the significant damages, which consequently lead the material to failure. The others classes of acoustic signals concern for minor damages such as matrix cracking, interlaminar crack propagation and the friction of the materials (matrix and reinforce) already damaged in the impact tests. The classification employed the signal amplitude, counts to peak, counts, and energy, as AE descriptors. The k-means method was carried out for clustering the AE signals into four classes. This method applied the parameters of Euclidian distance and random initial partitioning. The clustering process and analysis of the AE signals were performed by Noesis software.

A specific cluster of AE signals appears at the moment that the out-of-plane displacement is significant and therefore sudden failure happens. This class, designated as Class 1, is characterized by signals from lower to medium energy as well as their counts (Figure 3.29).

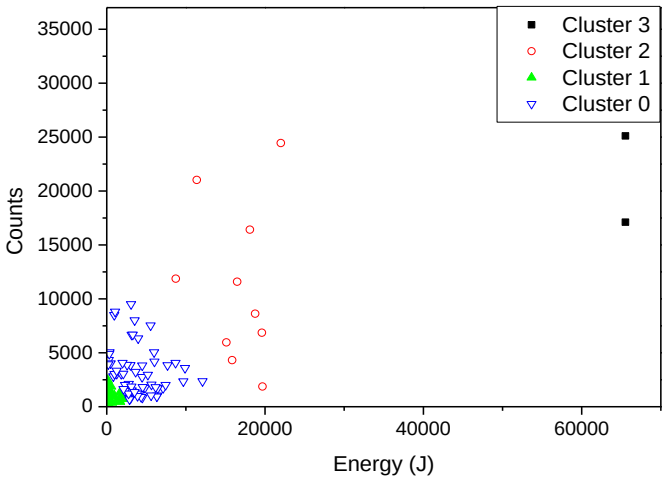


**Figure 3.29 - Clustered signals for the sample configuration A5 impacted at 25J under CAI.**

Figure 3.30 exhibits the out-of-plane displacement measured by stereo-DIC to the specimens subjected to CAI tests as well as the AE clustered signals in function of the time. The Class 1 initiates near to the crossing of the tangential lines from the out-of-plane displacement (w) curve, named $P_0$. This point concerns the beginning of the nonlinearity in the time-stress graph. However, it is difficult to define precisely this event from the curve stress-time which can lead to imprecise results. The AE clustered signals helped to localize with reasonable precision the $P_0$ from the beginning of a specific cluster of signals (Cluster 1) where the cumulative acoustic energy increases owed to the significant damages caused by buckling on CAI.

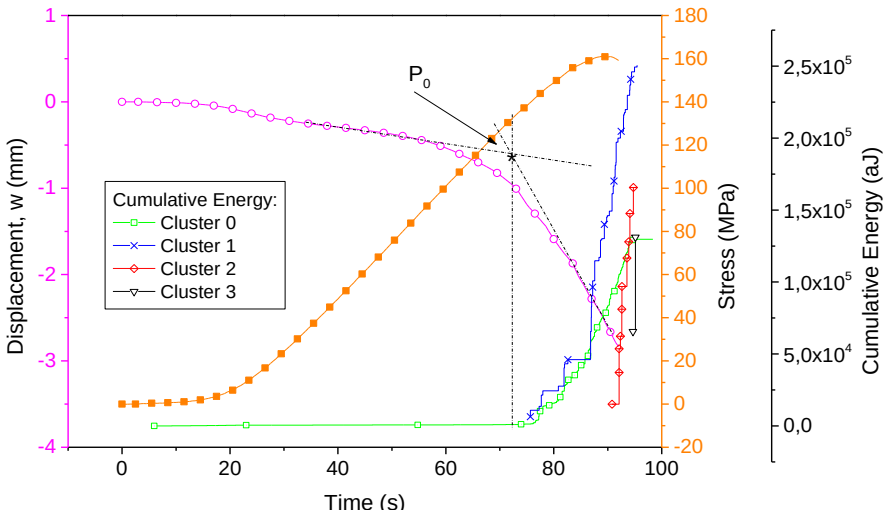


**Figure 3.30 - Clustered signals, compressive stress, and w as a time function of the sample configuration A5 on CAI previously impacted at 25J.**

Figure 3.31 and Figure 3.32 show the typical behavior of the reported Class 1 under CAI for every specimen set submitted before to 25 J and 60 J impact energy respectively. The primary goal is to compare the initial point ($P_0$) between them. Table 3.6 summarizes the normalized stress obtained at $P_0$ for the different samples. In general, the tufting changes the $P_0$, postponing the critical stress capable of generating considerable damages. Also, the tufting density plays a crucial function in increasing this critical stress. Transversal tufting presents more efficient than the angular reinforcements. The T5 samples impacted at 25 and 60 J increased $P_0$ 79% and 38% respectively in comparison to the control specimens. The A5 samples impacted at 25 and 60 J enhanced 27% and 11% respectively. The result obtained for A5 at 60 J is comparable with the T10 configuration impacted at the same energy (an increase of 13% in the $P_0$). Moreover, the considerable reduction of the $P_0$ (-28%) found for the A10 configuration at 25 J validated the investigations performed in the previous tests for the A10 configuration.

The results presented in this study confirm the efficiency of tufting reinforcements to improve the damage tolerance of the laminated composites, especially for the transversal tufting configuration. The critical stress ($P_0$) exhibited a good correlation with the results of ultimate strength on CAI tests. It means that the increase of $P_0$ delays the specimen failure under CAI loading.

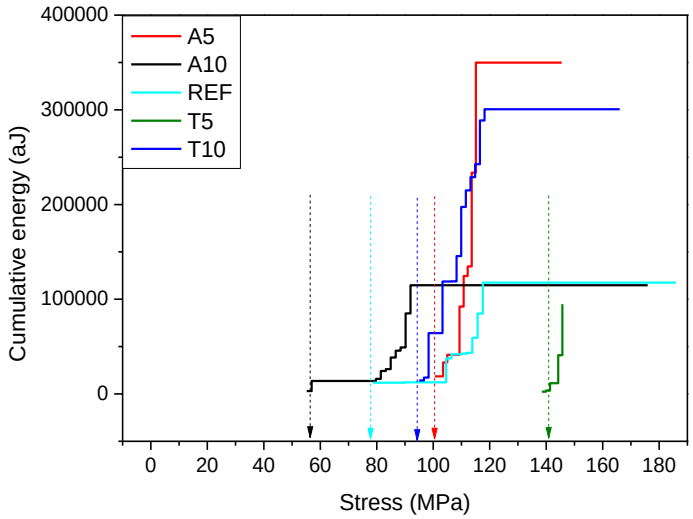


**Figure 3.31- Comparison of Class 1 from clustered AE signals of the different sample configurations under CAI tests previously impacted at 25 J.**

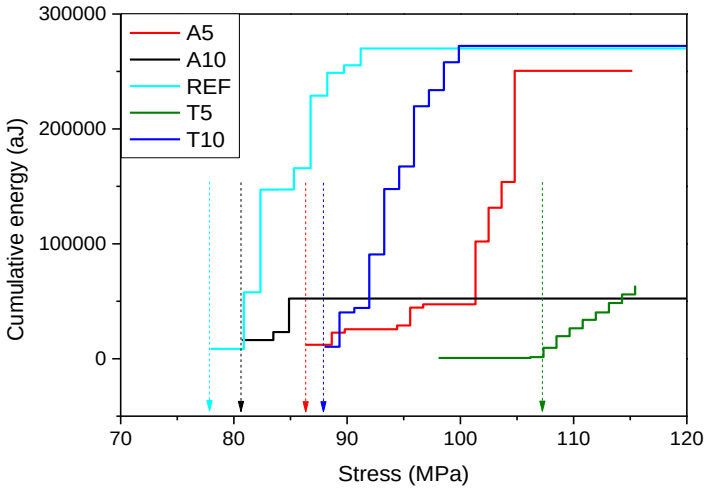


**Figure 3.32 - Comparison of Class 1 from clustered AE signals of the different sample configurations under CAI tests previously impacted at 60 J.**

**Table 3.6 - Normalized stress obtained from the cumulative energy curves (Class 1) at the $P_0$ point.**

| Specimen | Stress at $P_0$ | |
|---|---|---|
| | 25J | 60J |
| **REF** | 1,000 | 1,000 |
| **T10** | 1,197 | 1,130 |
| **T5** | 1,791 | 1,379 |
| **A10** | 0,722 | 1,037 |
| **A5** | 1,272 | 1,109 |

The results obtained in this section show that the reinforcement of composites by tufting is of some interest. The improvement, and in some cases the deterioration, of the mechanical properties, is dependent on the type and angle of reinforcement and the loading condition. Thus, for the specimens subjected to impact and CAI, the enhancement is noticeable whereas for those submitted to compression before impact there is a visible deterioration of the properties. The investigation of damage mechanisms enabled developing the understanding of the phenomena involved. The following section continues the investigation by studying the mechanical response of specimens with a local discontinuity (open hole specimens) under fatigue loading.

### 3.2.2 Laminated composite plates (Plate III)

The present section exhibits the results obtained for the open hole specimens subjected to fatigue tests. The investigation performed did not count with enough specimens of each configuration, and therefore, the results presented here provide only slight information about the behavior. Further analysis with a considerable number of specimens must be made.

However, this preliminary study makes it possible to explore the behavior of these materials under severe loading to further develop a research strategy on fatigue tests adapted to them. Section 2.2.3 and 2.3.8 detail respectively the manufacturing process and testing methods employed in the present investigation. Table 3.7 summarizes the samples designations according to the drill tool and tufting configuration.

**Table 3.7 - Specimens designations.**

| Specimen | Drill | Tufting configuration |
|---|---|---|
| **OHR_L** | Twist drill | Control specimens |
| **OHR_C** | core drill | Control specimens |
| **OH1_L** | Twist drill | 7 mm from the central axis |
| **OH1_C** | core drill | 7 mm from the central axis |
| **OH2_L** | Twist drill | 10 mm from the central axis |
| **OH2_C** | core drill | 10 mm from the central axis |

**a)** ***Quasi-static tensile tests***

The present part concerning the quasi-static tests and the evaluation of the drilling process was carried out by B. Liu in his final report of Master at *Université de Toulouse*, Institute Clément Ader. Figure 3.33 presents the ultimate strength obtained under quasi-static tensile tests. The tufted specimens decrease the ultimate strength by up to 12% comparing to the control samples. The reduction on this parameter is owed to the tufting reinforcements but also to the drilling tool. Measurements of the surface roughness were accomplished to evaluate the roughness near to the edge of the hole for the different specimen configurations. The directions of measurements are presented in Figure 3.34 as well as the values obtained in four different positions for each direction investigated. It is noticeable that the specimens drilled by core drill exhibit the highest values of roughness in the four directions measured. This can be responsible for generating superior damage extent in the edge of the holes in comparison to those performed with twist drill and consequently amplify the stress concentration in the zone. Therefore, these results validate the lower values of ultimate strength obtained for the same sets of specimens, OH1_C and OH2_C, as exhibited in Figure 3.33.

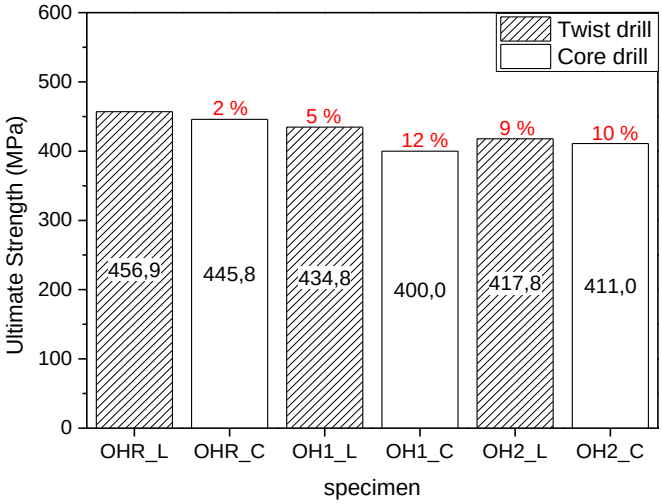


**Figure 3.33 - The ultimate strength of the specimens subjected to tensile loading.**

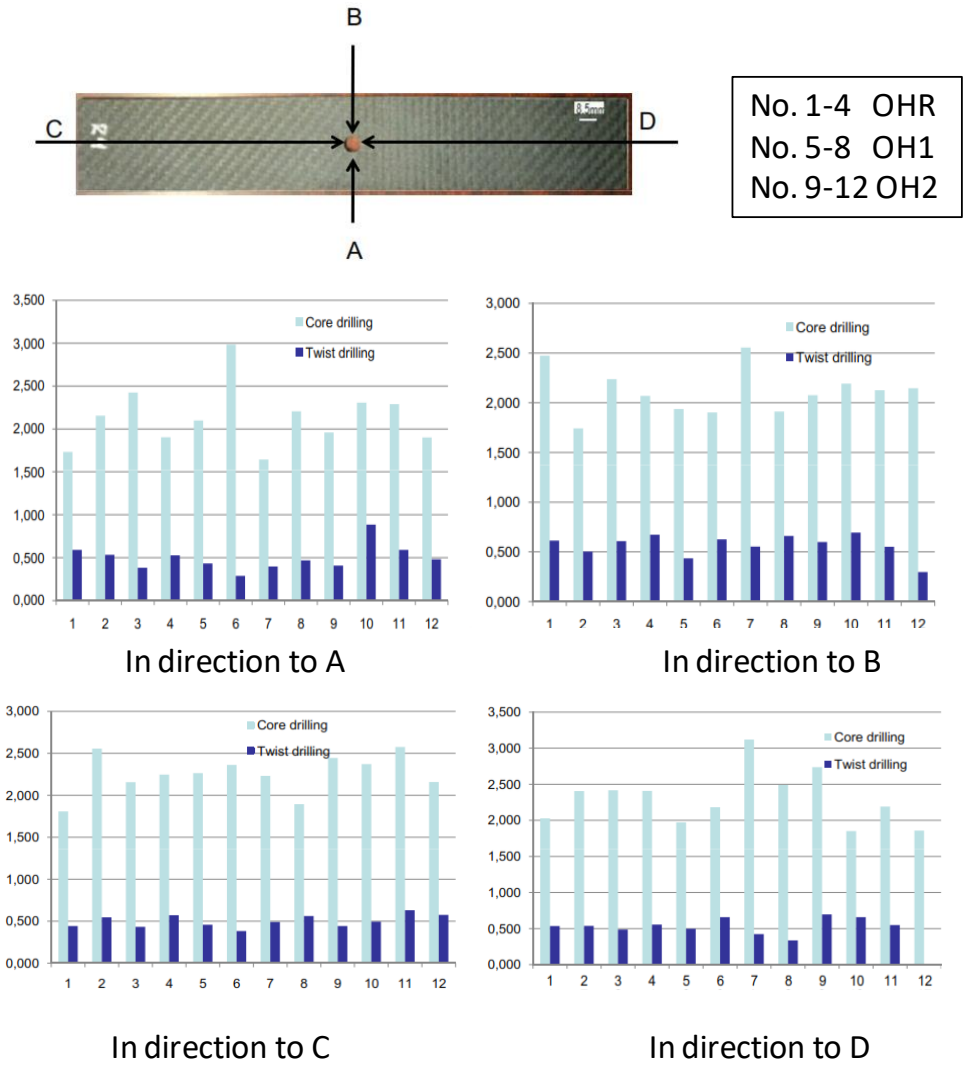


**Figure 3.34 - Roughness measurements in the principal directions (described on the top) for the specimens drilled by the twist and core tools.**

**b) *Fatigue tensile tests***

The fatigue tests comprise the investigation of the open-hole specimens submitted to load-unload cycles, fatigue loading, and tensile test until failure. During the load-unload phase, increments of 10 kN occurred until achieving 30 kN and thus, from 35 kN to 55 kN increments of 5 kN were carried out. Subsequently, fatigue tests subjected the specimens to $1x10^6$ cycles, with 2 Hz, R=0.1 and maximum force of 55 kN that corresponds approximately to 80% of the ultimate force obtained in the quasi-static tests. The tensile tests performed the complete rupture of the fatigued specimens.

The investigation of the damage evolution consisted mainly on the analysis of Young's Modulus evolution obtained from different levels of the tests. They were evaluated during the load-unload tensile tests at the beginning of the tests (E) and in the last step that concerns the loading until 55 kN (E'). Moreover, the Young's Modulus, E'', regarding the quasi-static tests that were carried out after fatigue ($1x10^6$ cycles), was also compared with the previous. The results report a negligible variation of Young's Modulus (E) by inserting tufts in the composites. Additionally, the residual stiffness related to E'/E and E''/E ratio presented insignificant reduction, especially to E'/E ratio, and achieved maximum loss of 7% for OH2_C. The present results lead to conclude that the insertion of tuft threads into the composites do not degrade the composite stiffness significantly. Moreover, this approach does not help to investigate the effect of the drill tool or tufts in the mechanical properties of the composites.

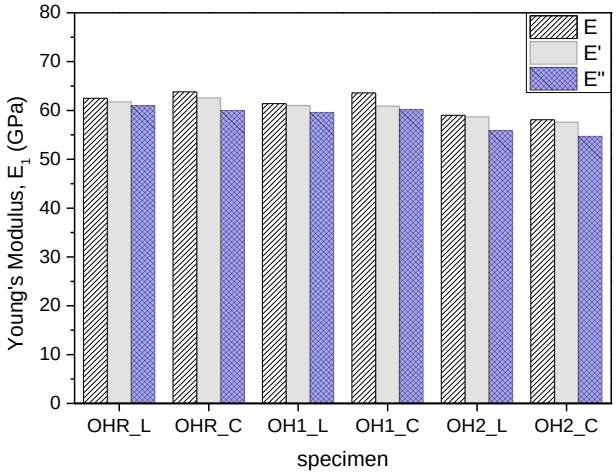


**Figure 3.35 - Comparison of Young's Modulus at the beginning (E) and the last load-unload cycle (E'), and after the fatigue test, during the tensile test (E'').**

Figure 3.36 presents the ultimate strength results for the composites subjected previously to fatigue tests. There is a general increase in the values in comparison to those found on quasi-static tensile tests that were not submitted to fatigue tests (see Figure 3.33). This behavior is different from the expected and may be owed to the use of tabs for the specimens employed to fatigue tests. Despite this, the results obtained in fatigue tests allow comparing the specimen configurations. As seen in the quasi-static tests, the specimens drilled with core drill presented the more significant reduction on the ultimate strength. This behavior concerns the increase of the damage severity caused by this drill, as already mentioned.

Moreover, the tufted composites exhibit a decrease in the ultimate strength when compared to control specimens. This agrees with the results found in the literature that report reduction on the in-plane strength of tufted composites. The degree of strength reduction is related to several parameters such as tufting density and depth, the angle of insertion, and tuft thread type/diameter. These parameters may alter considerably the number of fiber misalignments and damage in the fabric fibers that are the principal factors to the decrease of strength. However, it is negligible the difference of response between the two tufting configurations with the holes performed by the same drill tool. It seems that the drilling tool is more important than the tufting density for modifying the composite strength. Therefore, this study did not achieve its primary goal that concerns reinforcing the composites to contain the damages generated by the stress concentration in the hole. Different factors could be considered to improve the function of tuft threads in the open hole composites such as composite layup and tufting position and consequently, postpone the composites failure.

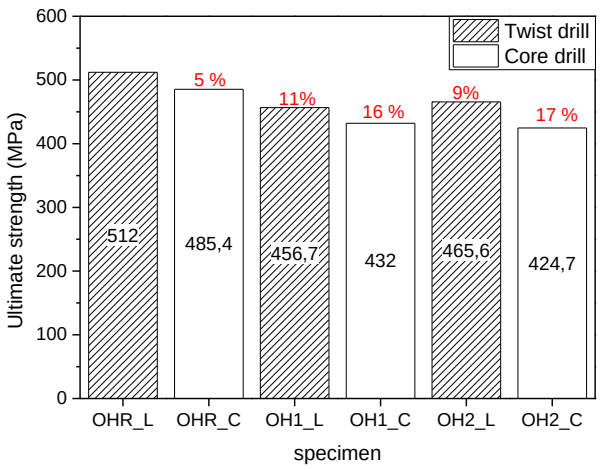


**Figure 3.36 - The ultimate strength of the specimens subjected to tensile loading, previously submitted to fatigue tests.**

Figure 3.37 shows a typical strain field response acquired by DIC for the control and tufted specimens (OH1 and OH2) when submitted to load-unload cycles. The images presented were taken at the same load of 55 kN. The difference between the significant strains ($\varepsilon_1$) of the two specimens is irrelevant. However, it is noticeable major strain spots for the tufted composites, which are related to the tufts. The small white arrows in the images illustrate the principal strain vectors and help on the understanding of the hole and tufts function in the composite strain field under loading. Additionally, a schematic illustration of the affected zones and their major and minor strain directions are summarized in Figure 3.38. They evidence the typical behavior of open hole specimens subjected to tensile tests that concerns the major strain direction acting as streamlines in a fluid flow field. The strain field is changed near to the hole due to strain concentration in the region and stabilizes parallel to the loading direction when it is distant from the hole. The tufted region also exhibits a perturbation of the strain field that is due to the strain concentration caused by the tufts. The strain magnitude near to the tuft threads can achieve the same order than in the hole region. This behavior is better exemplified in Figure 3.39 by the evolution of longitudinal strain ($\varepsilon_{yy}$) in function of distance from the edge of the hole ($(r+x_i)/r$) along the virtual gage. The data were acquired from the load-unload test at the maximum force of each cycle.

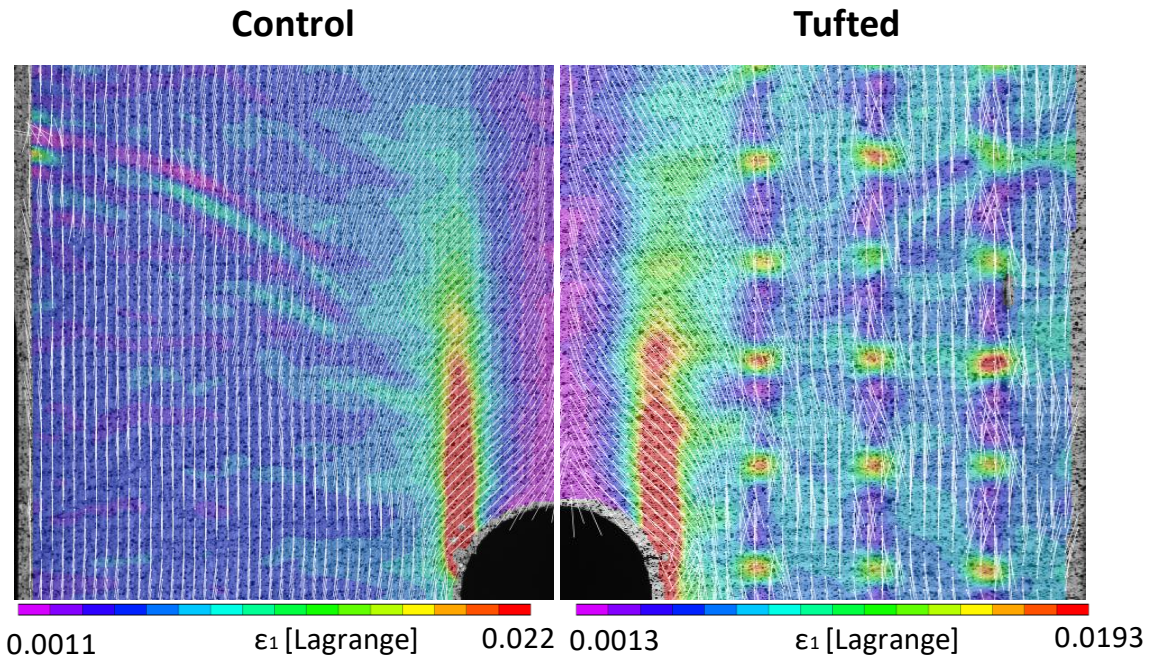


**Figure 3.37 - DIC strain field and the principal strain directions (white arrows) for the control and tufted specimens at 55 kN under load-unload cycles.**

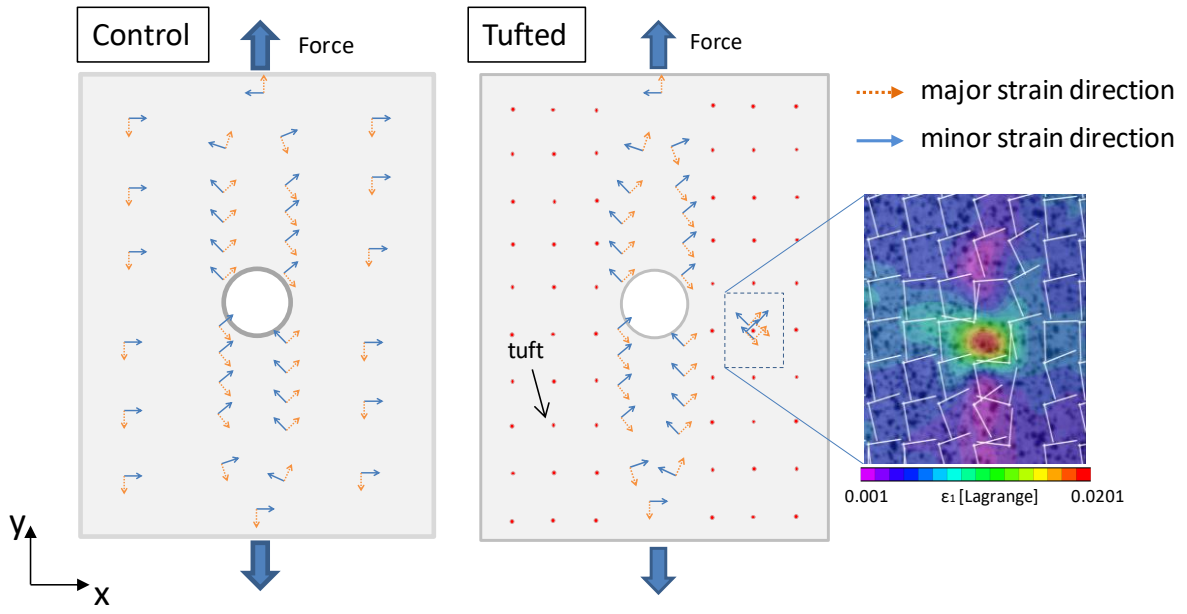


**Figure 3.38 - Schematic illustration of the principal strain vectors (major and minor) for the control and tufted specimens.**

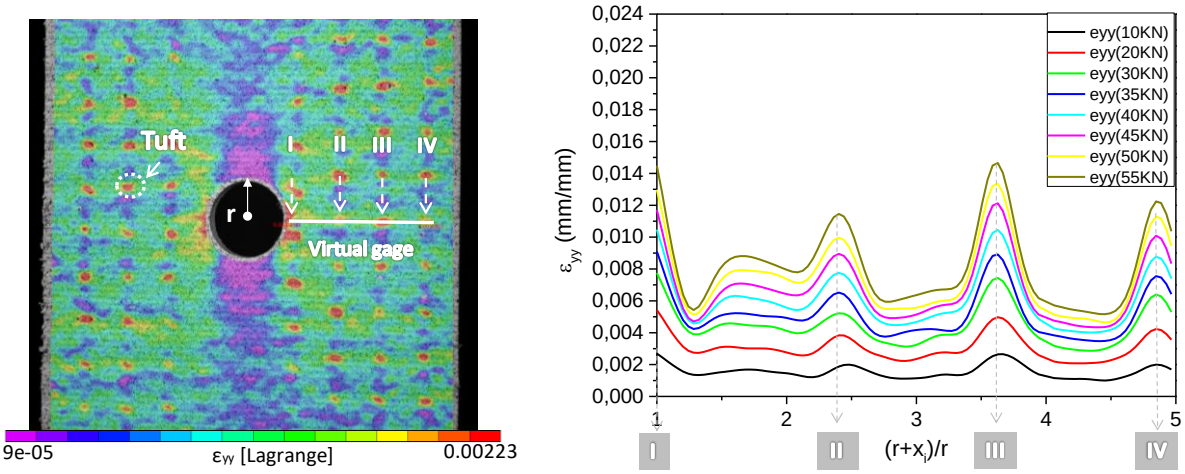


**Figure 3.39 – The typical strain distribution ($\varepsilon_{yy}$) obtained by a virtual strain gage for a tufted specimen under a load-unload cycle.**

The strain concentration factor ($K_\varepsilon$) was evaluated to better understand the contribution of tufting reinforcement and drill tool effect in the mechanical performance of the composites, especially under the elastic behavior. Beyond the elastic limit, damage phenomena initiate and thus, the monitoring of the strain evolution in the edge of the hole is performed using a parameter ($K_{D\varepsilon}$), that is measured in a similar way to the $K_\varepsilon$. Figure 3.40 schematizes an open hole specimen subjected to uniaxial loading, exemplifying the geometric strain concentration through the width. The variable is calculated according to the equation (4).

$$K_\varepsilon = \frac{\varepsilon_{max}}{\varepsilon_{nom}} \quad \textbf{(4)}$$

where,

$$\varepsilon_{nom} = \frac{W}{(W - D)}\varepsilon_\infty \quad \textbf{(5)}$$

Here, $\varepsilon_{max}$ is the maximum strain, tangent to the hole and in the direction of the applied load, and $\varepsilon_{nom}$ is the mean strain of the net section obtained from a remote strain, $\varepsilon_\infty$.

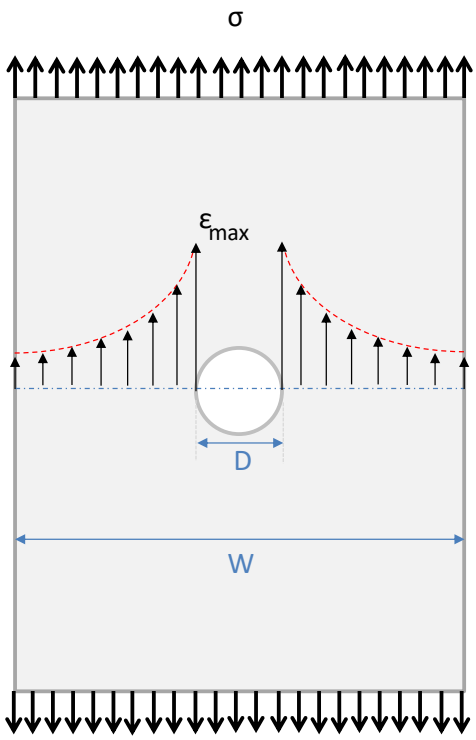


**Figure 3.40 - Schematic of the strain concentration in an open-hole specimen subject to tensile loading.**

The approach utilized in the present study used a virtual gage located at the edge of the hole, perpendicular to the longitudinal direction, to acquire $\varepsilon_{max}$. Moreover, a strain gage located distant from the stress concentration obtained the $\varepsilon_{nom}$. The distance and size of the gages were kept the same for all configurations of specimens. Figure 3.41 exemplifies the mentioned method to obtain the strain values by DIC strain field and the strain curves in function of the length ratio $((r+x_i)/r)$ for a control specimen. The data consisted of the DIC images acquired at the maximum load of each increment during the load-unload test.

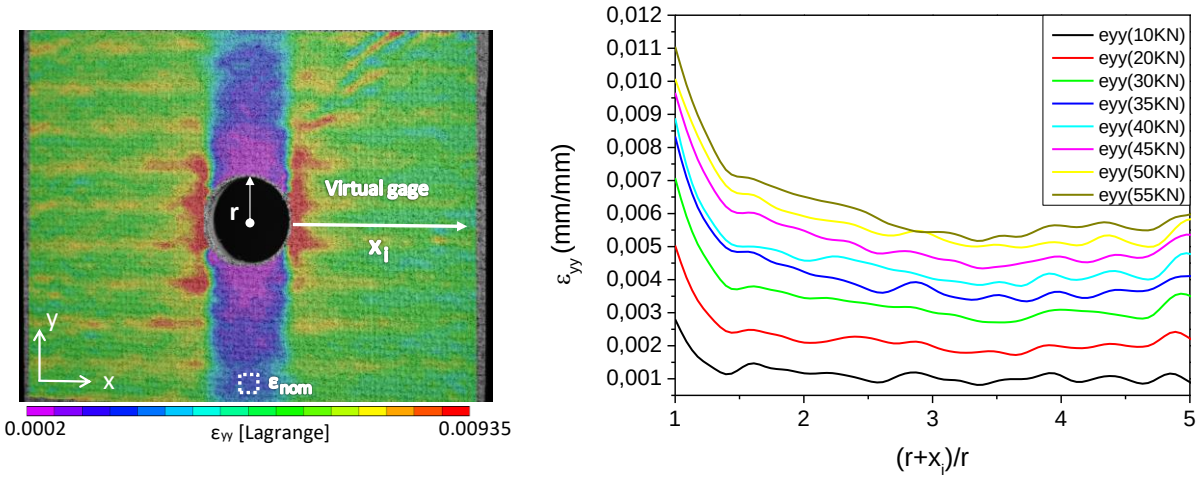


**Figure 3.41 - Representation of the method employed from the DIC images to obtain $K_\varepsilon$ and an example of the strain evolution ($\varepsilon_{yy}$) under load-unload cycles for an OHR_L specimen.**

Figure 3.42 shows the evolution of $K_\varepsilon$ during load-unload tensile cycles and fatigue loading tests. The strain data correlated by VIC-2D® refer to the images acquired at the maximum load of each increment of load-unload tests, and at increments of $4x10^4$ cycles during fatigue tests. It is noticeable a trend of the specimens drilled by the core drill tool to present superior $K_\varepsilon$. However, this response is not significant under load-unload cycles and is even contrary to the OH1 specimens (Figure 3.42b). The increase of the strain factor is negligible for all specimens in this first phase. However, when the composites are submitted to fatigue loading tests significant increase is noticeable for the specimens bored with a core drill. This sudden rise of $K_\varepsilon$ is mainly due to the considerable cracks that propagate from the hole edge to the longitudinal direction in the mentioned set of specimens.

In addition to the effect of the drill tool in the strain concentration response, it is remarked that the tufted composites amplify the Kε significantly when combined with a hole performed by core drill. This is probably due to the significant damage extent generated by this tool combined with the tuft threads that alters the local strain field and forces increase on the strain concentration near to the hole edge. On the other hand, the specimens bored by twist drill present similar values between the control and tufted specimens. We can conclude from the above discussion that drill type is primary for amplifying the stress concentration and the tuft threads act contrarily to the primary goal of improving the damage resistance, especially during fatigue tests.

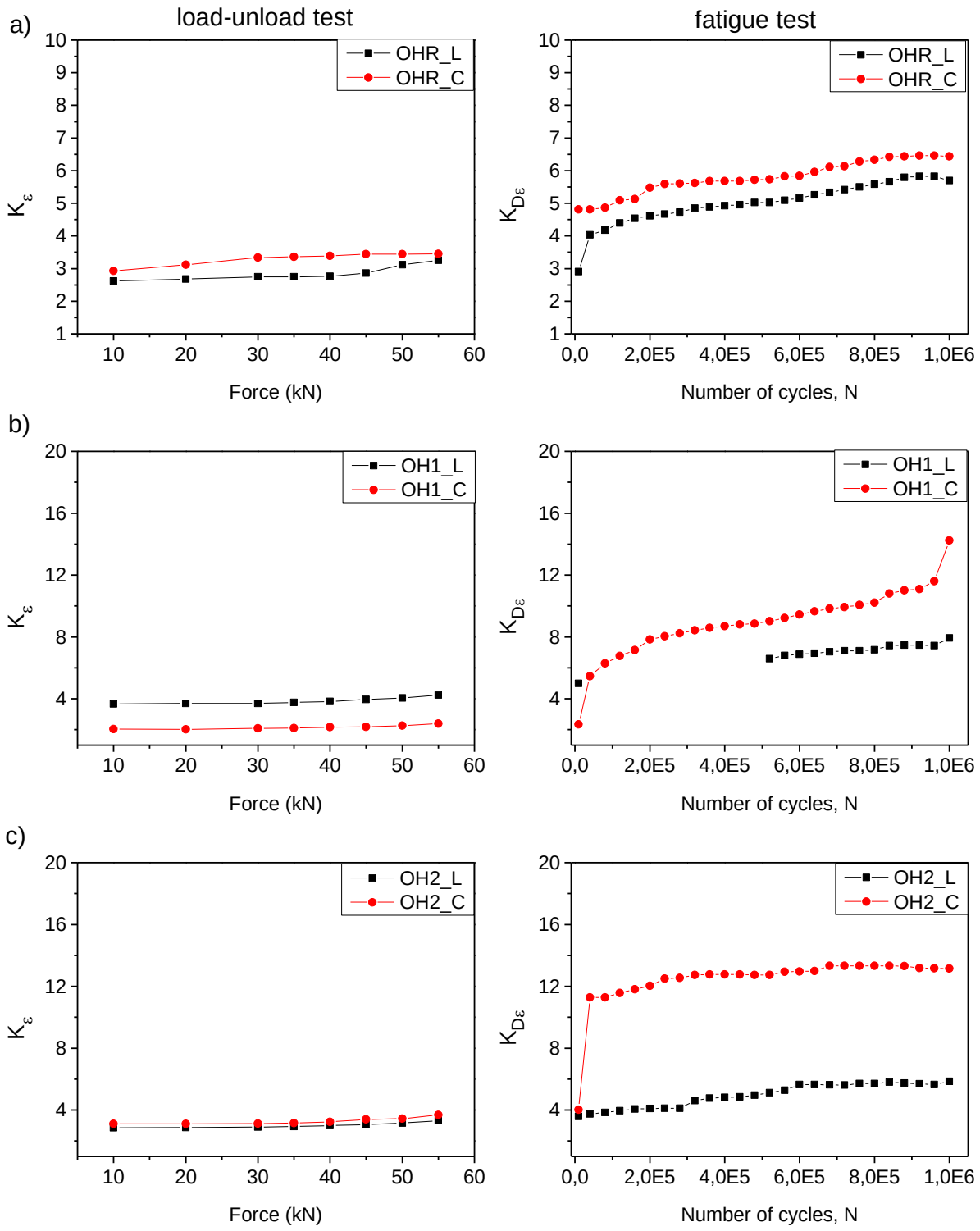


**Figure 3.42 - Strain concentration factor in function of the maximum force in the load-unload cycles and, in function of the number of cycles during fatigue tests for a) OHR_L and OHR_C, b) OH1_L and OH1_C and, c) OH2_L and OH2_C specimens respectively.**

Quasi-static tensile tests were performed subsequently to the fatigue tests. Figure 3.43 exemplifies the typical behavior of the tufted composites by DIC strain map obtained just before composite failure. The image exhibited is from the OH2_C configuration. The curve plotted on

the image exemplifies the longitudinal strain ($\varepsilon_{yy}$) distribution through the specimen cross section on the tufts position (dashed line). It seems that beyond the crack edge that amplifies the strain concentration considerably; tufts also present significant values around them. From the strain map, it is noticeable that the significant strain fields interlink the tuft zones and crack border consequently creating networks capable of propagating easier the cracks that will lead the specimen to the failure. Moreover, Figure 3.43 also presents a typical crack on the tufted region that is mainly caused by the significant strain concentration. This effect was already presented in Figure 3.39 to a tufted specimen under load-unload tests. The strain values in this zone are in the same order of magnitude than in the edge of the hole, that generates opening mode in the region and consequently, engenders cracks. This damage is visible on the whole sample and noticed for every tufted specimen analyzed in the present section.

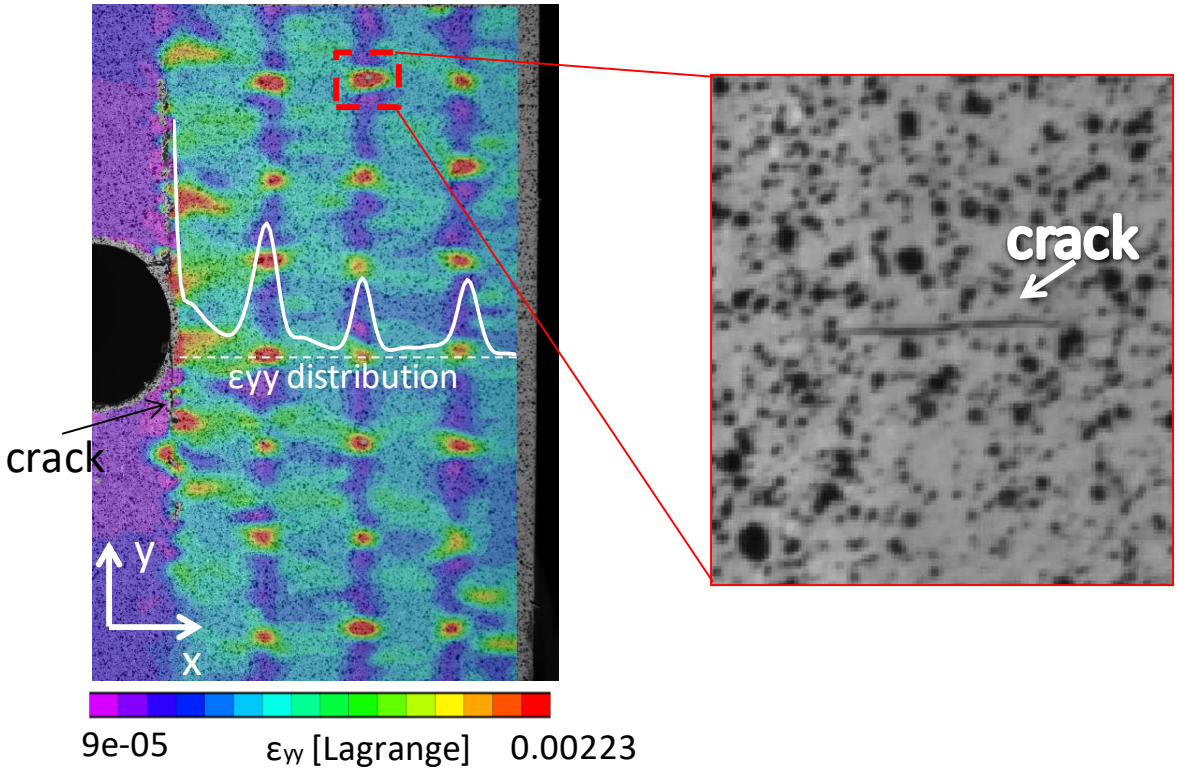


**Figure 3.43 - Example of the strain field by DIC just before failure of an OH2_C specimen.**

Figure 3.44 presents the typical post-mortem failure seen for the tufted specimens from the cross-section view of the specimen as well as the schematic illustration of the rupture seen from the specimen surface. It is noticeable the crack propagation transversally along the tuft threads, leading to the premature rupture of the specimen. This damage scenario validates the discussion about the preferential path caused by the significant strains that link the tuft zones to the crack edges. This behavior corroborates to the lower ultimate strength of the tufted specimens.

Otherwise, the control specimens present disorientated failure with a significant degree of failed tows, as shown in Figure 3.45, due to the lack of a preferred path.

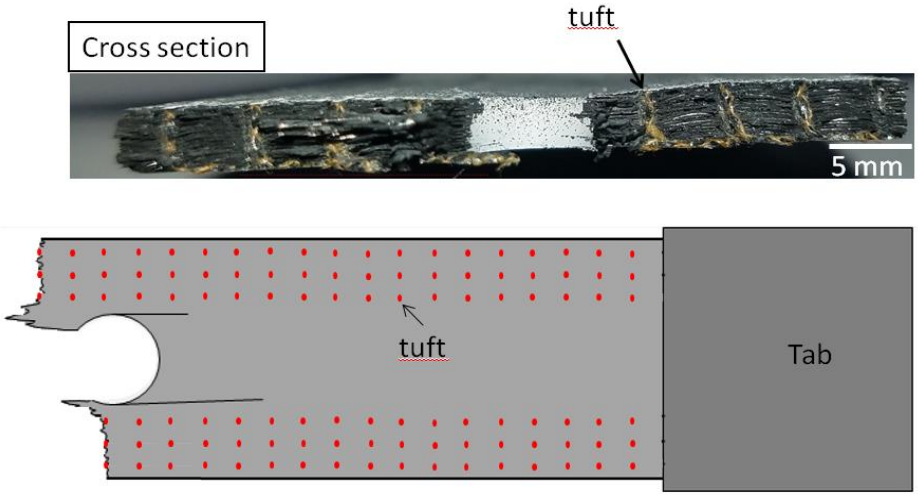


**Figure 3.44 - The typical failure of a tufted specimen.**

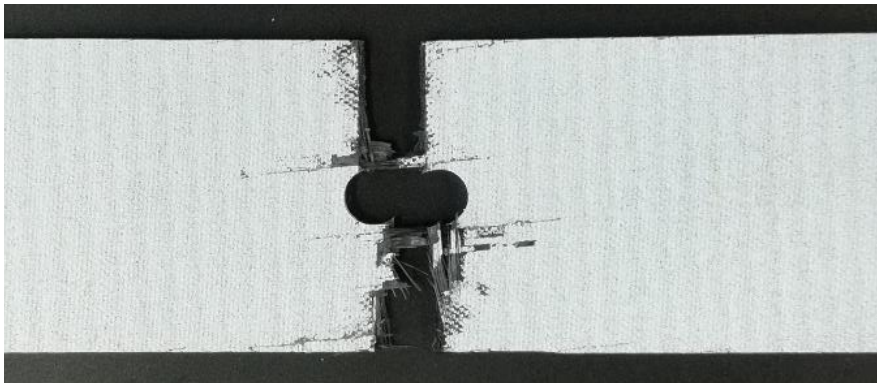

**Figure 3.45 - The typical failure of a control specimen.**

## 3.3 Conclusions

The interlaminar shear strength of the tufted materials exhibits a similar response in the longitudinal direction of the tuft rows while the transversal achieved a slight decrease up to 9% in comparison to control specimens. The characterization by DIC and in-situ microscopy under short beam shear tests reported that cracks are generated from the tuft threads. The stress concentration by the tufts leads thus, to premature damages that reduce the ultimate strength. Otherwise, the interlaminar crack propagation is arrested by tufts, which is valuable to improve the fracture toughness of the materials. Furthermore, the interlaminar shear moduli were

improved up to 330% and 134% in the longitudinal and transversal directions of tufting respectively. The bridging effect of the tuft threads causes the enhancing of the local stiffness by precluding the inter-plies sliding.

Tufted laminate composites also enhanced the impact resistance when compared to the untufted specimens. The impacted area was reduced up to 4 times for the tufted specimens reinforced with tufts in the transversal direction. The impact resistance to delamination is directly related to the tufting density and angle of insertion. The damaged area is proportional to the tufting density and presents lower values to the transversal tufting, despite that the densest configuration responded similarly at 60J for both angles of insertion. Additionally, the analysis of the dent depth created by the impact loading confirmed the tufting function to restrain the damage development. The relation between damage area and dent depth presented inversely proportional.

The compression strength before impact decreased significantly to the tufted composites and achieved a reduction of up to 40 %. It is mainly due to the defects generated by the tufting insertion such as in-plane fibers misalignment and rupture that has been reported to many authors in the literature. However, the residual ratio (CAI/CBI) increased up to 30 % and 28 % for the transversal and angular reinforcements respectively in comparison to the control materials. The analysis by AE and DIC reported that tufting reinforcements postpone the significant damages on the laminates that are responsible for the failure of the specimens. It is remarkable that tufts avoid plies opening, which is caused by the delamination process under compression load.

The ultimate strength obtained for the open-hole specimens subjected to quasi-static tensile loading showed a minor decrease when inserting tufts, achieving until 10% of loss when compared to the control specimens. Tufting reinforcements are not seen to alter the stiffness properties of the laminated composites considerably, even after the fatigue tests. The drill tools employed to perform the hole in the specimens exhibited a significant contribution to reducing the strength of the composite. Core drill tool was reported to be more destructive to generate damage in the composite and therefore, amplifying the strain concentration factor. Additionally, the tuft threads induce strain concentration in the inserted zones, which generate similar effect as small holes. They create a network that leads to a preferred path of the failure induced by the

drilled hole. Therefore, the tufted specimens reduce the residual strength after fatigue tests in comparison to untufted samples by combining the drilling and tufting effect.

The effects caused by the insertion of tufting reinforcements did not meet our expectations for the specimens subjected to fatigue tests. Indeed, the fatigue of the 2D woven composites does not generate delamination. The presence of holes, machined by different tools, also did not cause the expected damage. It would be interesting to use other stacking sequences prone to delaminate under fatigue tests.

The present chapter reported the issues generated by tufting reinforcements on the in-plane properties. The results indicate that the introduction of through-thickness reinforcements in the specimens or composite plates can cause positive or negative consequences depending on the type of stress, the location of the tufts concerning the critical zones and tufting parameters (density, angle). The unsystematic insertion of tufts in the whole structure is one of the main responsible for the reduction of the in-plane properties. It is therefore unreasonable to reinforce a composite structure entirely by tufting. The presence of the tufting reinforcements must be well localized only in the weak zones that are susceptible to significant interlaminar stresses.

Therefore, an optimized introduction of the tufts must be performed in order to diminish this matter. It includes studying the untufted specimens for the evaluation of the strain fields and damage scenario to insert the reinforcements in the weak zones that lead to significant damages and subsequent failure of the specimens.

The following chapter will discuss the tufting behavior in the stiffened composite structures.

# CHAPTER 4 INVESTIGATION OF THE MECHANICAL BEHAVIOR OF OMEGA STIFFENED COMPOSITES REINFORCED BY TUFTING

## 4.1 Introduction

The present chapter reports the study of tufting reinforcements on the composite omega stiffeners. The primary goal concerns to achieve the best parameters of the structure geometry and especially of tufting to reach optimized properties of the tufted composites in comparison to the control specimens. Therefore, mechanical investigation of the structures mainly by using multi-instrumented characterization such as acoustic emission, digital image correlation, and in-situ microscopy, allowed understanding the damage evolution and the critical points that lead to major damages in the structures. This investigation was mainly conducted by subjecting the specimens to pull-off tests, and complemented with 3-point bending tests. Pull-off tests aided in studying the behavior of the structure especially under open mode (mode I) loading condition. The 3-Point bending tests gave general information of the composites once were tested entire structures instead of small samples. Additionally, the loading conditions were more complex than the pull-off tests and can describe more realistically the structures under service.

It should be noted that, in the absence of a numerical model, the tufted structures utilized the observations of the damage scenario in the untufted structures for the positioning of the tufts. This helped in the investigation of the potential areas of weakness. However, as will be shown, the manufacturing process has a great influence on the mechanical response of the composites, and therefore it was necessary to study a considerable set of structures. This short discussion evidences the great need for the development of numerical models for predicting the tufting insertion in the structures. Nevertheless, the understandings acquired in this chapter will necessarily feed this future tool.

## 4.2 Results

### 4.2.1 Omega stiffener panel - CFRP composites (Batch I)

This section presents the results and discussion concerning the specimens from the Batch I. The two configuration of specimens, control, and tufted stiffeners, present different stiffener radius

caused especially to the tufting process that compacts the plies on the region of reinforcement, as already reported in chapter 2, which can differ the results between the two classes of structures. However, the primary goal of this section is to understand the tufts behavior in the structure as well as analyze the damage scenario of both sets of specimens to optimize the next batch of reinforced structures by tufting. The section 2.2.5 of this thesis manuscript describes the materials and manufacturing process employed. Moreover, section 2.3.10 reports information about testing methods for the pull-off, 4-point bending and 3-point bending tests. Every type of test utilized three samples of each configuration.

**a) *Pull-off tests***

Figure 4.1 shows the typical behavior for the control and tufted composite structures subjected to pull-off tests. The tufted composites present a drop of 37% of the maximum force ($F_{max}$) concerning the first significant damage. However, the work done (WD) until failure, calculated by approximating the area under the curve, presents a considerable increase of 4.5 times for the tufted structures in comparison to the control. Table 4.1 summarizes the mean values of maximum force ($F_{max}$), bending stiffness and work done (WD) found for the three samples of each specimen configuration.

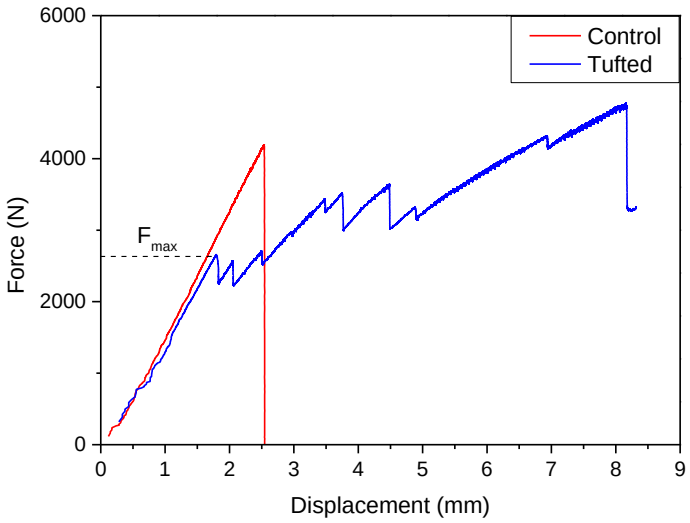


**Figure 4.1 - Typical behavior on pull-off tests to the control and tufted omega stiffeners.**

**Table 4.1 - Mean values of $F_{max}$, stiffness, and work done.**

| specimen | Fmax (N) | Stiffness (N/mm) | WD (N.mm) |
|---|---|---|---|
| **control** | 4344 ± 368 | 1689 ± 27 | 6152 ± 781 |
| **tufted** | 2584 ± 79 | 1515 ± 88 | 28725 ± 3527 |

The presented results, for the tufted specimens, are underestimated due to significant damages that initiate in the skin of the structure and therefore induce the end of the tests, which difficult further investigations. DIC analyses were carried out to study the behavior that leads the tufted structures to significant premature damage and consequently to lower $F_{max}$. DIC full-field strain was measured through the tests and investigated from a virtual gauge located in the stiffener radius (Figure 4.2).

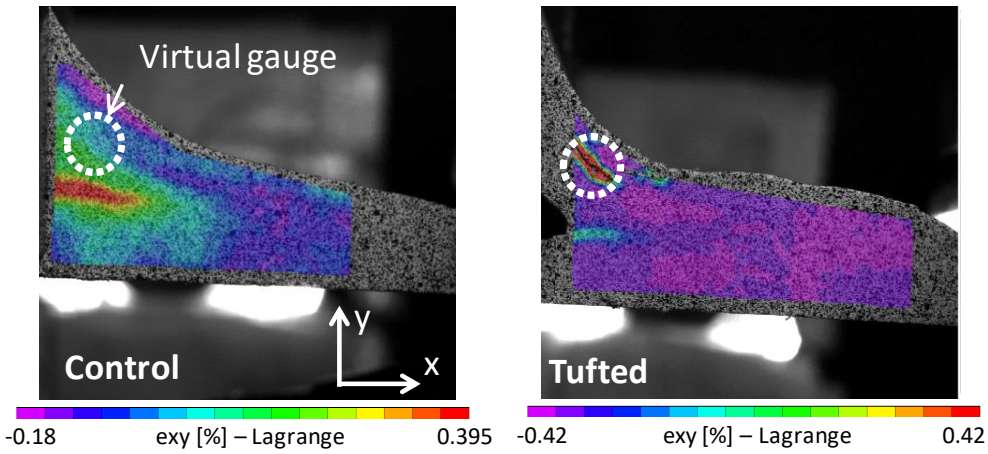


**Figure 4.2 - Out-of-plane strain field by DIC at the first significant damage for tufted specimens.**

Figure 4.3 presents the typical behavior of the average out-of-plane shear strain ($\varepsilon_{xy}$) to the specimens until their maximum force. The shear strain increases by a 3.5-fold for the tufted composites. This response is mainly due to the difference on the stiffener radius between the two structures with a diameter of 20 mm for the control against 10 mm for the tufted samples as shown in Figure 4.4. It leads to a significant strain concentration in this zone and consequently to premature damage as seen in Figure 4.2. This variation is caused by the tufting process which compacts the dry preforms, especially in the area of tuft insertion.

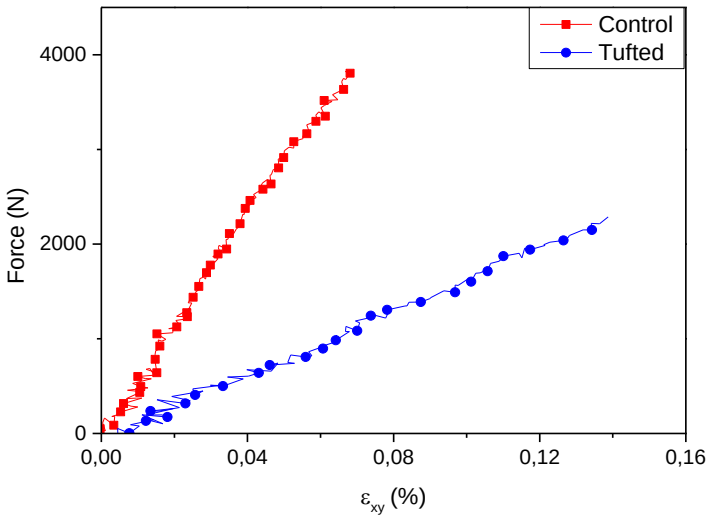


**Figure 4.3 - Out-of-plane shear strain ($\varepsilon_{xy}$) obtained from the virtual gauges in the stiffener radius.**

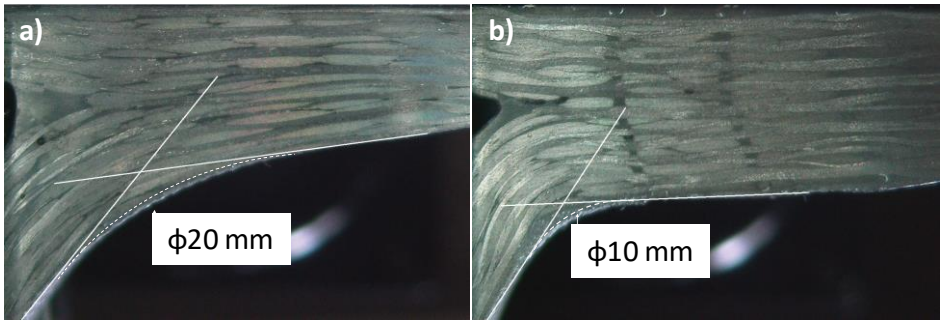


**Figure 4.4 - a) Stiffener radius on the reference and b) stiffener radius on the tufted specimens.**

Figure 4.5 and Figure 4.6 show the post-mortem images for the untufted and tufted omega stringers respectively. The fracture for the control specimens is catastrophic and separates the structure into the two parts (stiffener and skin) as already reported by several authors. It is mainly owed to the concentration of strain between the contact of the stiffener and skin, as shown in Figure 4.2. On the other hand, the tufted specimens maintain the structure joined by the crack bridging effect of the tufts. The fractography presents the significant extent of interlaminar cracks in the specimen radius, delamination in the interface between stiffener and skin as well as crack deflection throughout tuft length.

**Figure 4.5 - Post-mortem image of the non-tufted omega stringer.**

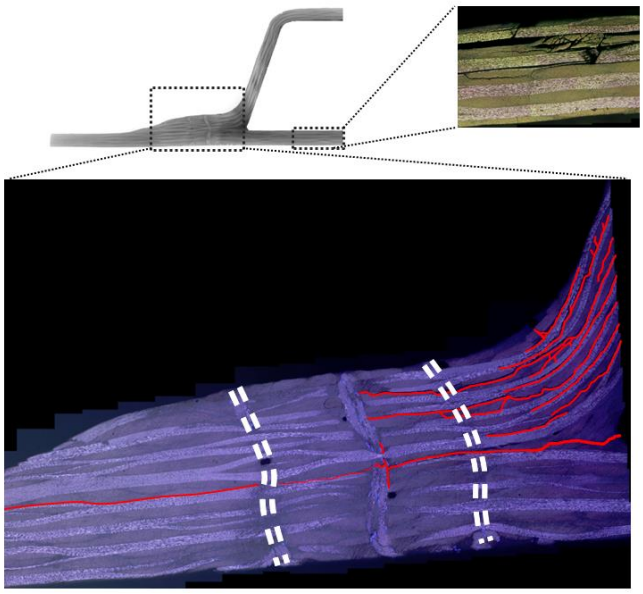

**Figure 4.6 - Optical micrograph image of the post-mortem tufted omega stringer under pull-off test**

The investigation of failure behavior of the tufted stiffeners was carried out by DIC technique and video microscopy during pull-off loading tests. Unfortunately, a further investigation concerning the failure behavior of the control specimens is not performed due to a lack of information saw on DIC and video micrographs until the sudden rupture. Figure 4.8 exhibits the main events found from the mentioned techniques that concern the points emphasized in the typical load-displacement curve that range from I-IX (Figure 4.7). They concern every significant load drop visible in the graph, which presents typical stick-slip behavior. The events from I to IV are dominated by interlaminar damages in the radius zone, as exemplified by the first load drop (an event I) in Figure 4.8. Every load drop in the range I-IV corresponds mainly to new delamination generated in the neighbor ply on the radius. The mentioned effect is due to an unstable crack growth followed by crack arrest at the nearest tuft row. Then, the load progressively increases until a crack be generated and propagated stably from a ply next to the former delaminated. The damage scenario regarding the described events I-IV is better seen in the images acquired on event V. Figure 4.9 presents a schematic of the principal strain distribution, especially concerning the critical points associated to the significant damages, obtained by DIC analysis just before the event I load drop. The stiffener radius is subjected to major strains that lead to opening loading condition and generates interlaminar damages. They are also responsible for the crack produced in the external side of the radius that propagates to the interior of the stiffener, perpendicular to the fabrics ply.

Furthermore, a dominant shear mode in the interface between the flange and skin is responsible for the delamination propagation in the mentioned zone seen in Figure 4.8 - event V. This strain behavior starts from the first tuft row until the stiffener tip. As evidenced by the events VI and VII (Figure 4.8), the cracks arrested for the tuft rows in the two important zones are subsequently branched by tuft threads and continue growing in the same direction. The slight load drop regarding the mentioned events is mainly due to the achievement of the strain energy release rate in the tufted region that consequently leads to delamination growth.

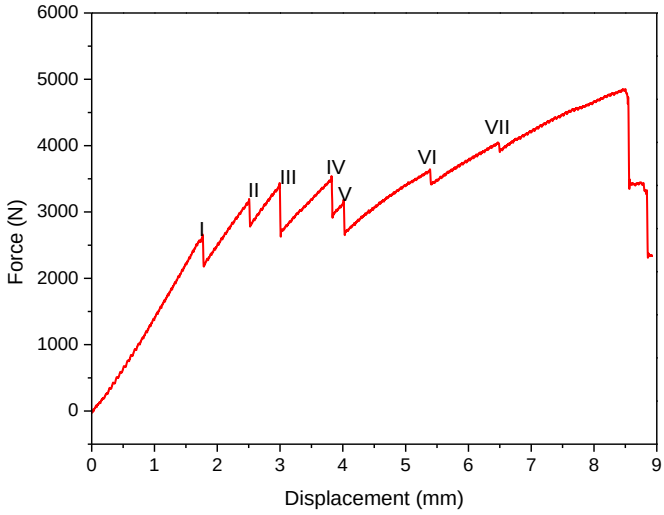


**Figure 4.7 - Typical curve force-displacement for tufted omega stiffeners.**

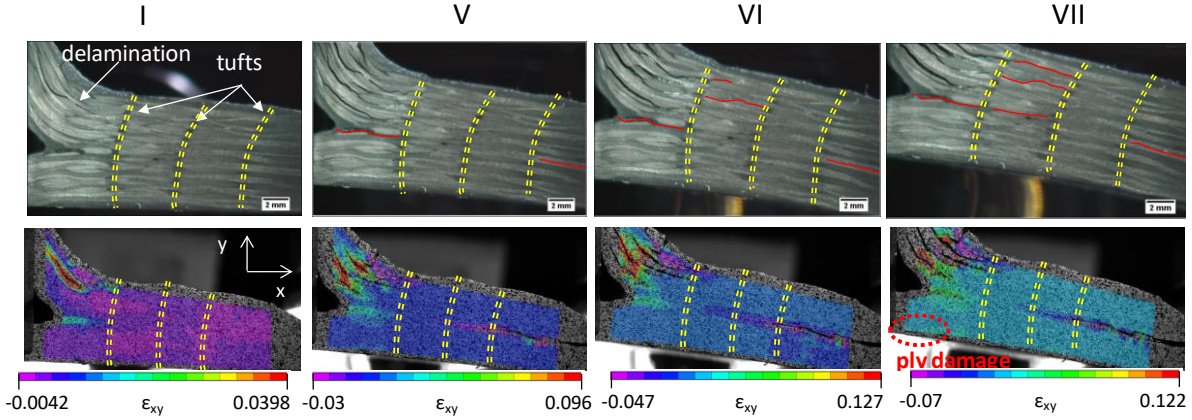


**Figure 4.8 - Failure analysis by DIC and video microscopy in the tufted specimen submitted to the pull-off test.**

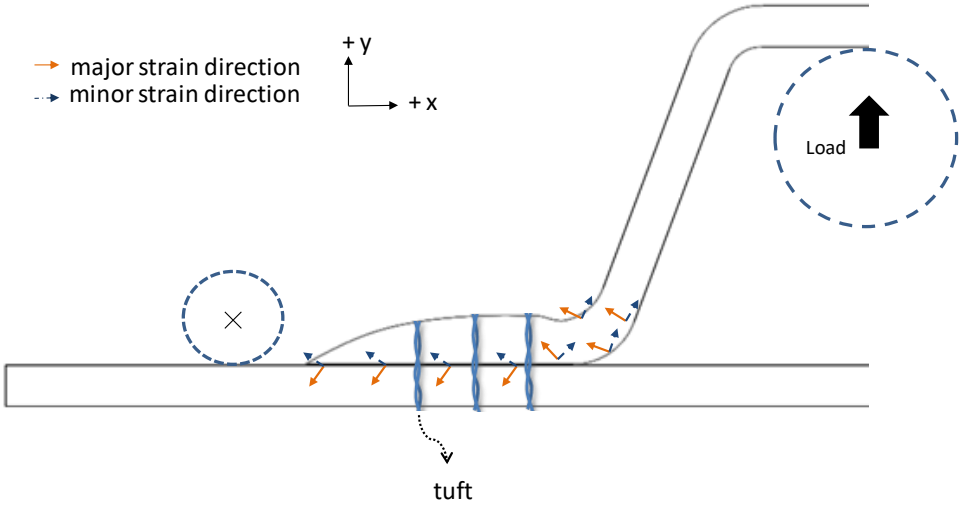


**Figure 4.9 - A schematic illustration of the strain distribution obtained just before the event I for the tufted specimens.**

## Clustering analysis of AE signals

This approach utilized the AE signals acquired during mechanical tests. The number of descriptors was evaluated by principal component analysis (PCA), which exhibited a sum of the first four eigenvalues greater than 70%. It means that the first four principal components present 70% of the information from the whole data. A single-linkage clustering was utilized to obtain the descriptors with correlation distance more significant than 70%. The typical curve of eigenvalues in function of the principal component number and, single-linkage clustering with the defined descriptors (amplitude, average frequency, RMS16, and absolute energy) are presented in Figure 4.10a and b respectively.

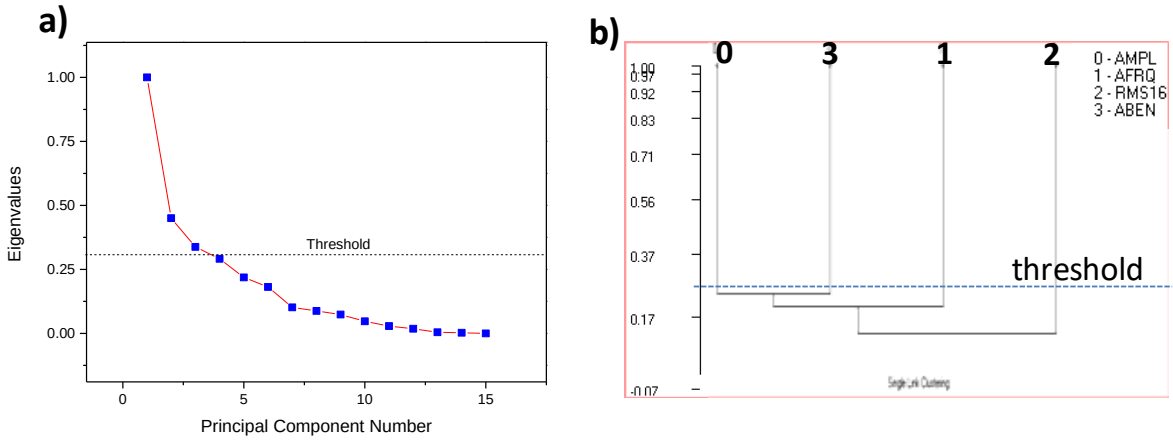


**Figure 4.10 - a) Principal component analysis for evaluating the optimal number of descriptors and, b) Single link clustering with the selected descriptors.**

Thus, clustering was carried out using the non-supervised k-means method, applying Euclidian distance and random initial partitioning. The procedure utilized the Davies-Bouldin index (DB index) to find the optimal number of clusters. The minimum value of the DB index, between a chosen range of clusters, is the optimal number of clusters to be employed in the clustering process. Figure 4.11 exemplifies a DB index analysis for a control specimen that shows two or four clusters as optimal for the clustering. The tufted specimens presented the same number of clusters obtained for the control specimens by DB index. The selection of two clusters to perform the clustering was deliberately made instead of applying 4 clusters. It is mainly due to the complexity to attribute physical phenomena to 4 clusters, that are concerned to the complex and interdependent damage phenomena involved.

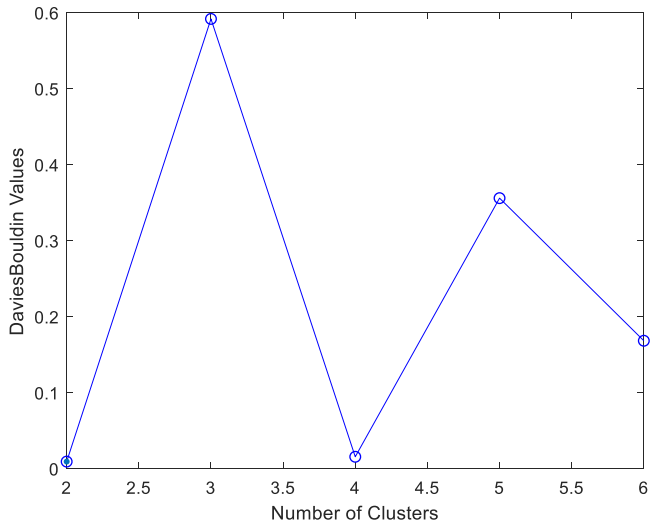


**Figure 4.11 - Example of DB index in function of the number of clusters for the AE signals obtained under pull-off test for the control specimen.**

The two clusters concerns to the minor damages generated since the beginning of the test (Cluster 1), such as matrix cracking, and significant damages (Cluster 2) capable of diminishing the structure load-bearing considerably. Some analysis of the AE signals did not evidence some significant fiber ruptures related to the threads failure which corroborates with the video micrographs. Figure 4.12 presents the center values of the AE signals features (descriptors versus class) obtained for the two classes of signals obtained in this investigation. It is noticeable the difference of characteristics between the two clusters. Cluster 1 exhibits different AE signals characteristics when compared with Cluster 2. It consists mainly of weak values of descriptors, such as AMPL, DUR, ENER, RISE, PCNT, ABEN, and IFRQ, that clearly describes minor damages during the pull-off tests. Otherwise, the mentioned descriptors present significant values for Cluster 2, which leads to attribute this cluster to the main damages in the

structure. It is also evidenced that the geometry of the radar graphs for the control structure is similar to that found for the tufted structures. This reinforces the idea that this two-classes clustering is representative of the phenomena involved.

Figure 4.13 presents the typical energy-counts curves by clusters for the control and tufted specimens respectively. The cluster 1 is characterized for its lower counts and energy values as already seen in Figure 4.12, while cluster 2 presents high energy and counts in comparison with the first class. The separation between the two classes of AE signals is remarkable, and may also indicate an efficient clustering of the acoustic signals.

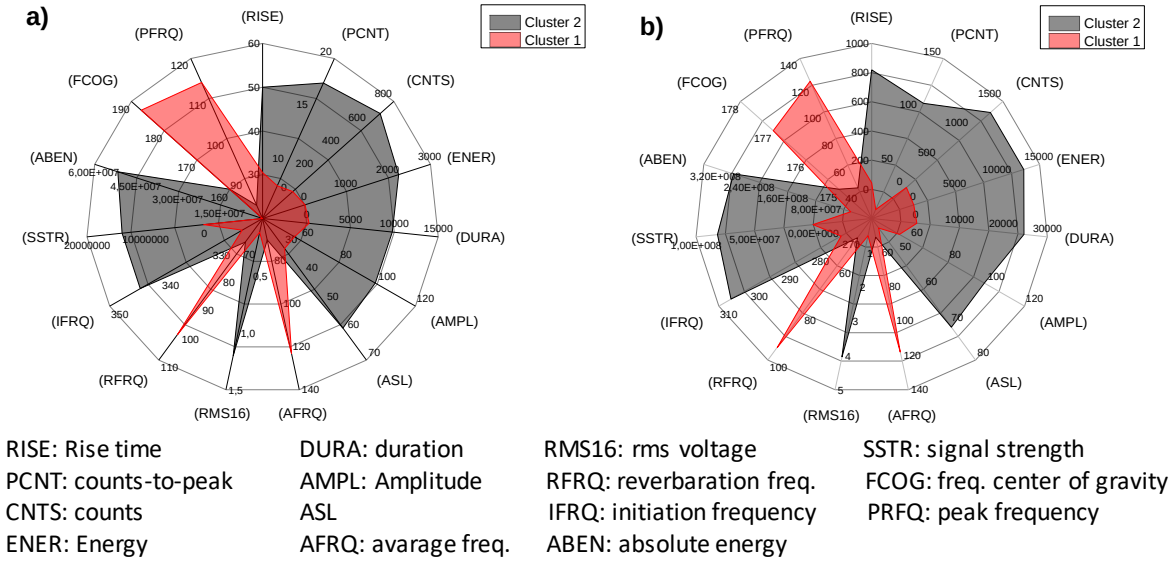


**Figure 4.12 - Radar chart of clustered AE signals for a) control and, b) tufted specimen.**

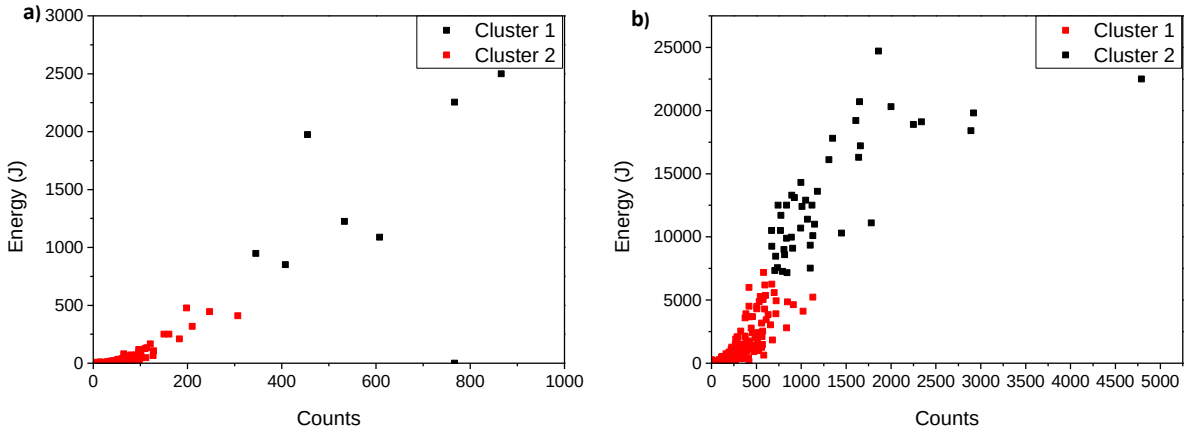


**Figure 4.13 - Example energy-counts distribution of the clustered AE signals for a) control and, b) tufted specimens.**

Figure 4.14a and b exhibit the typical behavior of AE cumulative energy for the control and tufted specimens respectively. The cumulative energy of untufted structures is significantly lower than found for tufted structures. The damages generated in the control specimens presents inferior values of acoustic signals energy, mainly due to the lower severity of them. Moreover, the number of hits for the control specimens is too inferior (e.g., 3 hits against 44 for tufted specimens in Cluster 2), which is consequently related to damage events. The results confirm the lack of information by DIC and micrographs as well as the sudden failure. The cluster 2 starts from the event I and consists of the first interlaminar cracks in the stiffener radius. The cumulative energy increases gradually at every event displayed in the graph force-displacement for this cluster.

It can be seen that the advent of the Cluster 2, for the control specimens, occurs at a load of about 2000 N, whereas for the tufted specimens this point is located at approximately 3000N. If, as supposed, this cluster of AE signal concerns to major damage, then the tufted samples have a greater damage threshold. It is worthy to verify this point by other tests, such as fatigue, in order to follow the evolution of the damage. Although the radius of curvature of the tufted structure is penalizing, it is noticeable that the presence of the tufts increases the damage tolerance of the structure considerably.

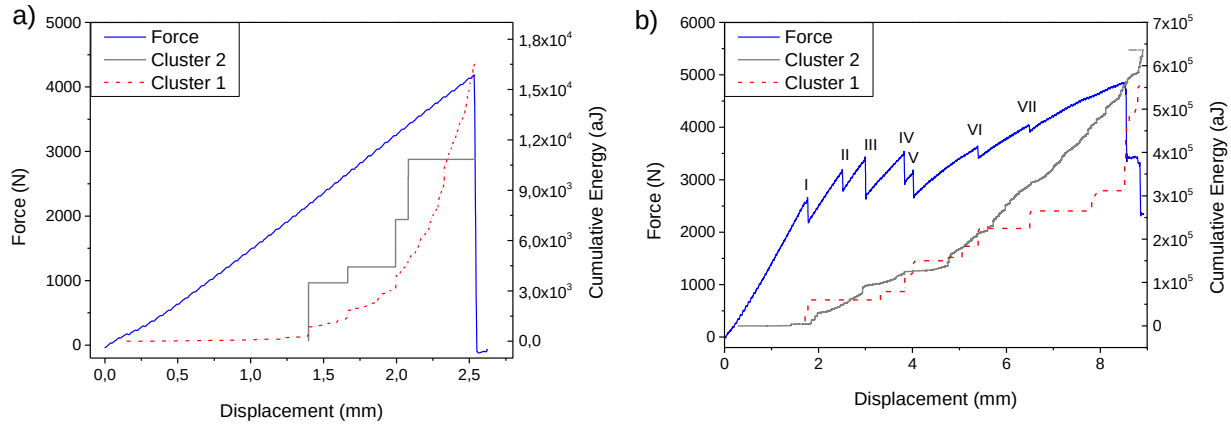


**Figure 4.14 - Typical AE cumulative energy clusters and force-displacement curves for a) control and, b) tufted structures under pull-off tests.**

### b) *4-point bending tests*

Figure 4.15 presents the typical force-displacement curves obtained during 4-point bending tests. The tests, which enable to evaluate the structures mainly on mode II loading condition,

were not performed until the complete failure for the tufted structures due to the significant displacement submitted to the structures. Tufted specimens exhibited a decrease of maximum force of about 43% in comparison with the control. The bending stiffness was also inferior for tufted composites owed to the inferior second moment of area of these specimens than the control specimens. However, the work done for tufted structures increased 5.25 times.

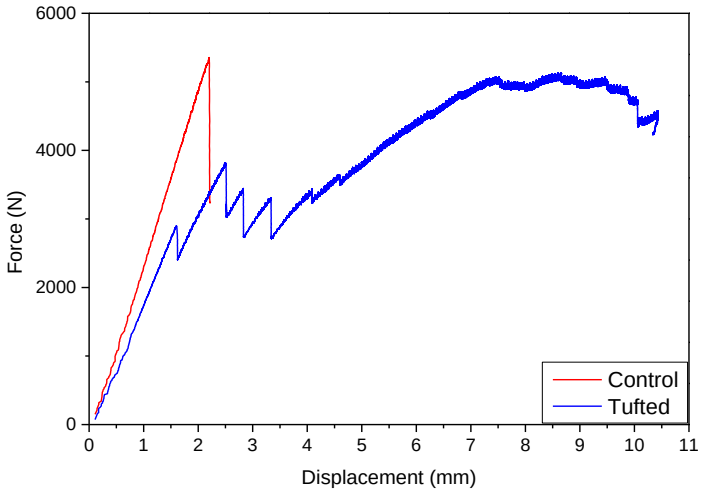


**Figure 4.15 - Typical force-displacement curves obtained during 4-point bending tests for both set of specimens.**

Table 4.2 summarizes the values of maximum force ($F_{max}$), bending stiffness and work done (WD) for both sets of specimens.

**Table 4.2 - Mean values of $F_{max}$, stiffness, and work done.**

| specimen | Fmax (N) | Stiffness (N/mm) | WD (N.mm) |
|---|---|---|---|
| **Control** | 5376 ± 1 | 2414 ± 82 | 7487±481 |
| **Tufted** | 3051 ± 1 | 1940 ± 61 | 39305±1491 |

As reported to the specimens subjected to pull-off tests, the failure mechanisms also presented unlike both specimen configurations as seen in Figure 4.16and Figure 4.17 for the untufted and tufted structures respectively. The catastrophic failure presented in Figure 4.16 that separates the stiffener and skin parts integrally, validates the sudden load drop presented in the curve for the control specimens. On the other hand, tufts restrain the interlaminar cracks and therefore, avoid the sudden failure and separation of the main parts.

**Figure 4.16 - The typical failure of control specimens.**

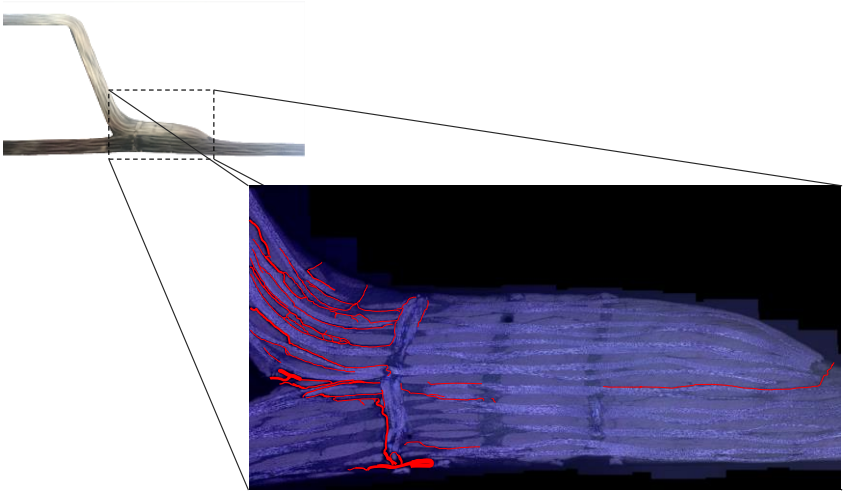

**Figure 4.17 - The typical failure of tufted specimens.**

An investigation of the strain fields in the radius region of the specimens was carried out to study the reduction of maximum force for the tufted composites. The approach was the same employed for the specimens subjected to pull-off tests, which consists of comparing the mean strain in the radius obtained by a virtual gage via VIC-2D (Figure 4.18). Once again, the tufted structures present high shear strain in comparison with the control specimens which lead to significant premature damages and consequently, lower maximum force.

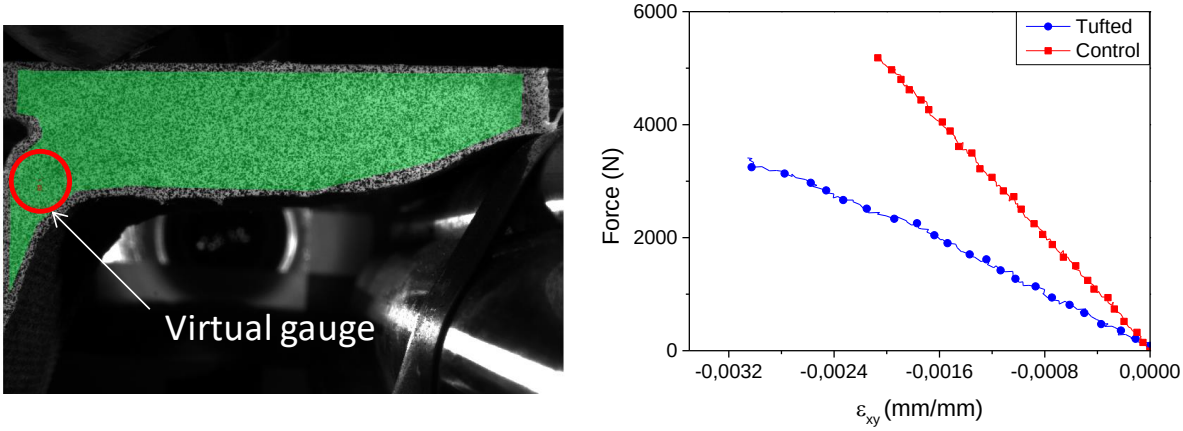


**Figure 4.18- The position of the virtual gauge employed in DIC analysis and the typical response obtained for control and tufted specimens.**

The DIC strain data acquired during tests were utilized to analyze the damage events for the tufted specimens. The typical force-displacement curve shown in Figure 4.19 demonstrates the main damages (I-VI) occurred in the structures and associate to the DIC analysis in Figure 4.20. The event I manifest as the delamination in the stiffener radius. The second event, not shown in Figure 2.20, increases the shear stress from the intern contact between the stiffener and skin. Interlaminar cracks are generated in the radius until event IV, and thus, a significant increase on the structure reloading occurs until a slight changing on the curve, designated as event V. The physical phenomenon related to this event is supposed to be caused by the achievement of the critical energy to propagate the cracks arrested in the first tuft row. Therefore, the delamination propagates from the crack initiated between flange/skin contact, and presented as the amplification of the strain along the longitudinal direction(x) between the two tuft rows. The crack propagates during the structure loading, from the event V until being arrested by the next tuft row (event VI). At the same time, delamination initiates in the opposite direction, from the outside to the interior of the stiffener; in the flange-skin interface. Moreover, significant strain is noticeable through the tuft length for the first row mainly due to the proximity of the loading roller to the tufted region which consequently leads to significant cracks along the threads as seen in Figure 4.17.

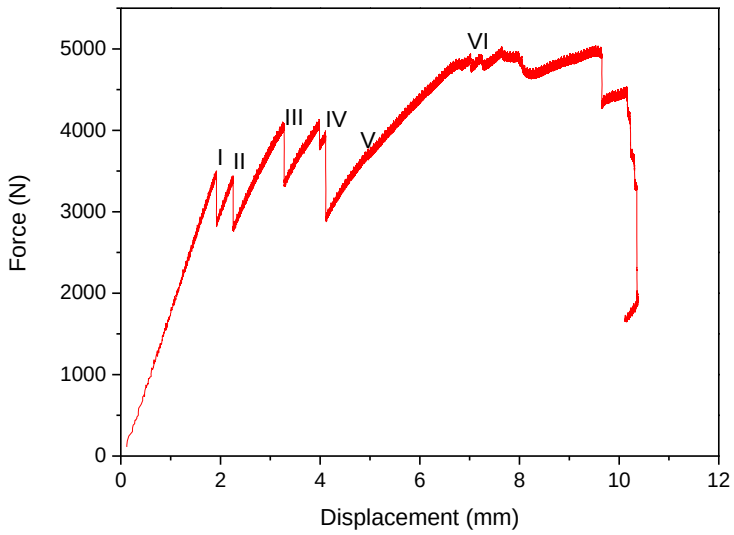


**Figure 4.19 - Typical force-displacement curve for a tufted composite and the main events from I to VI.**

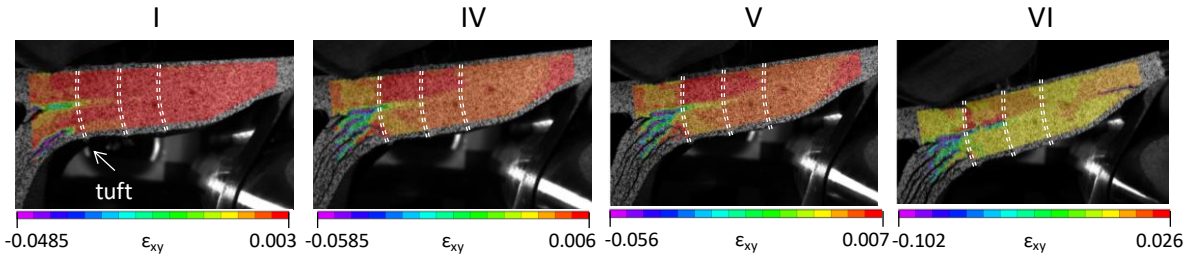


**Figure 4.20 - DIC strain fields related to the events described in Figure 4.19 for a tufted composite.**

Figure 4.21 exhibits a schematic of the typical minor and major strains of the tufted composites subjected to 4-point bending tests. The representation based on the DIC image just before event VI. Despite this, the schematic represents well the strain direction in the critical zones from the event I to VI. The opening mode occurs in the external part of the stiffener radius which led to the first considerable crack in this region. Otherwise, the interlaminar shear strain is significant in the internal part of the radius as well as in the stiffener flange until the third tuft row. This behavior is responsible for generating delamination in these regions. Moreover, through-thickness shearing located on the flange tip propagates the crack in this region that develops between flange/skin contact in the direction of the stiffener.

The presented results evidenced that the smaller stiffener radius of tufted specimens lead to significant strain concentration on the zone and consequently to premature damages. This mechanical response acts differently to the expected for 4-point bending tests, which is presumed to cause interlaminar shear strain in the interface of the stiffener flange. Therefore, a new omega stiffener design must be developed to decrease significant strain concentration in the radius zone and as therefore, increase the maximum force.

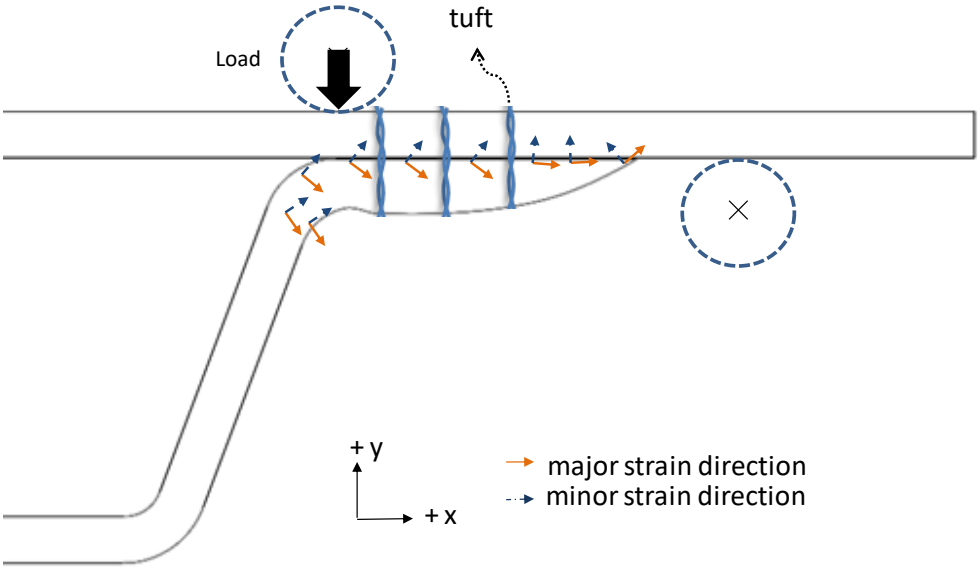


**Figure 4.21 - Typical minor and major strain directions obtained for the critical zones of tufted composites (just before event VI).**

### c) *3-point bending tests (Structure)*

The typical force-displacement curves acquired during tests is exhibited in Figure 4.22. The work done for the tufted structures was more than 5 times greater compared to control composites. However, as already reported for the previous tests of pull-off and 4-point bending, maximum force is reduced by 22 % for tufted composites. Figure 4.23 and Figure 4.24 show post-mortem micrographs obtained for the longitudinal and transversal direction of the samples respectively, as schematized. It evidences significant damage between flange/skin for control specimen from the interior of the stiffener to the flange tip. Otherwise, for tufted structures, crack propagation in the zone flange/skin is arrested by tuft threads. Significant damage extent in the stiffener radius of tufted structures led to the reduction of maximum force, as well reported in the tests above of this section. The first row was repolished to observe the damages directly in the thread, and therefore, it is verified that tuft did not fail, as highlighted in the image, and consequently, the fissures seen in the complete image of the cross-section corresponds to the branched cracks around tuft. Crack surrounds the second tuft row throughout its length due to the stress concentration generated on the top surface caused by the roller tip. Moreover, by analyzing the micrographs from the longitudinal direction of the specimens, damage events related with flexural loading are not evidenced and, it is therefore concluded that shearing is the most important loading that the structures were submitted.

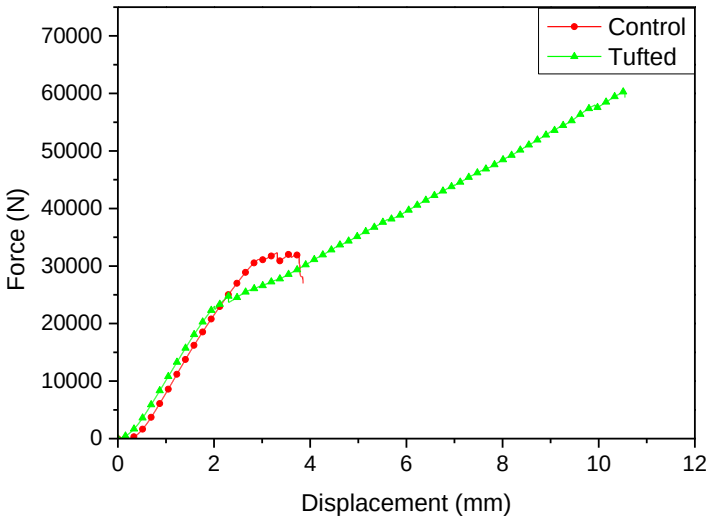


**Figure 4.22 - The typical force-displacement curves obtained under 3-point bending tests of the structures.**

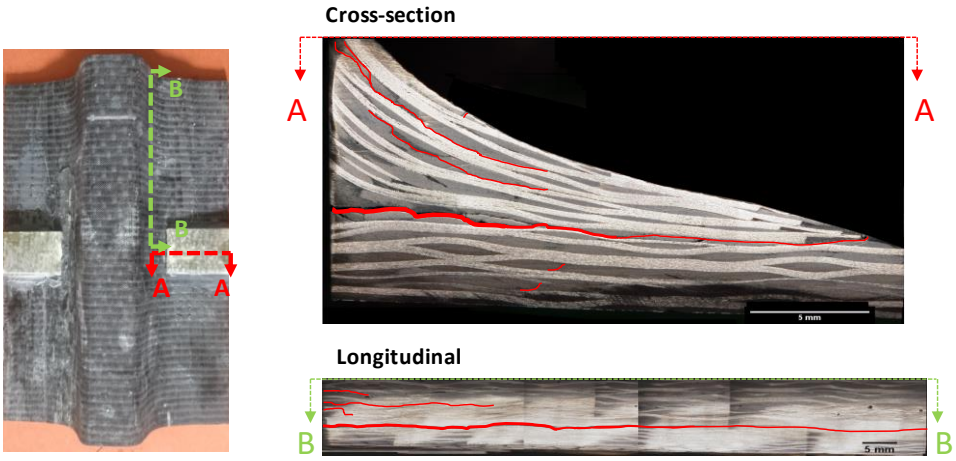


**Figure 4.23 - Post-mortem micrographs from longitudinal and cross-section of an untufted specimen.**

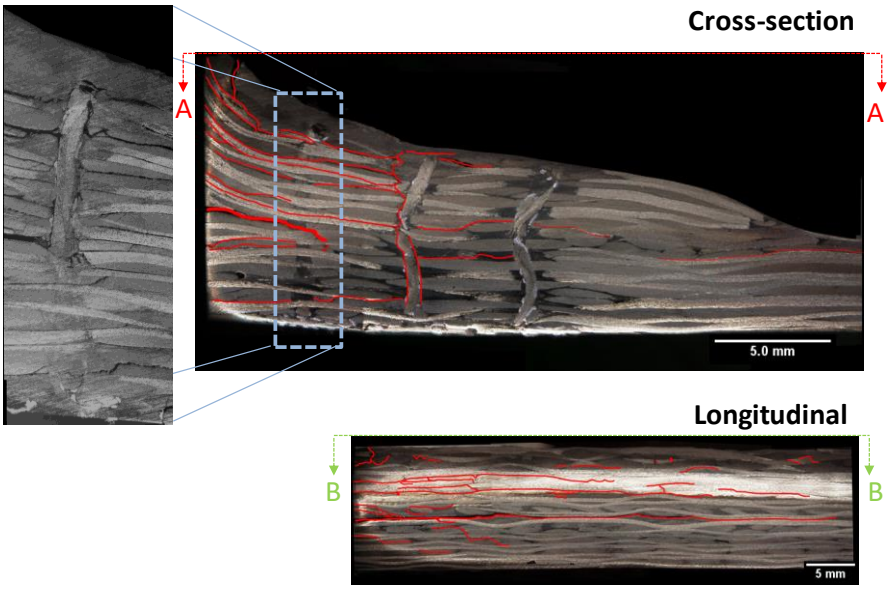


**Figure 4.24 - Post-mortem micrographs from longitudinal and cross-section of a tufted specimen.**

An investigation was carried out to analyze the displacements obtained by the load noses (crosshead displacement) and LVDT sensor centrally located in the bottom of the specimens. Figure 4.25a and b present the typical behavior for control and tufted specimens respectively. Both measures are quasi-linearly until major failure in the untufted structures, whereas, they distinct from about 25000 N for tufted composites. This effect is probably caused by the significant damages generated in the radius that leads to decrease of stiffness in the region and consequently, amplify the displacement ratio in the flange/skin zone in comparison to the center. Subsequently to this event, the structure is reloaded with some loss of its stiffness and contrary behavior is seen approximately at 40000 N. The displacement measured by LVDT presents important value from that point, most likely due to the unstable expansion of the central zone between stiffener and skin, which leads to an opening mode of the structure.

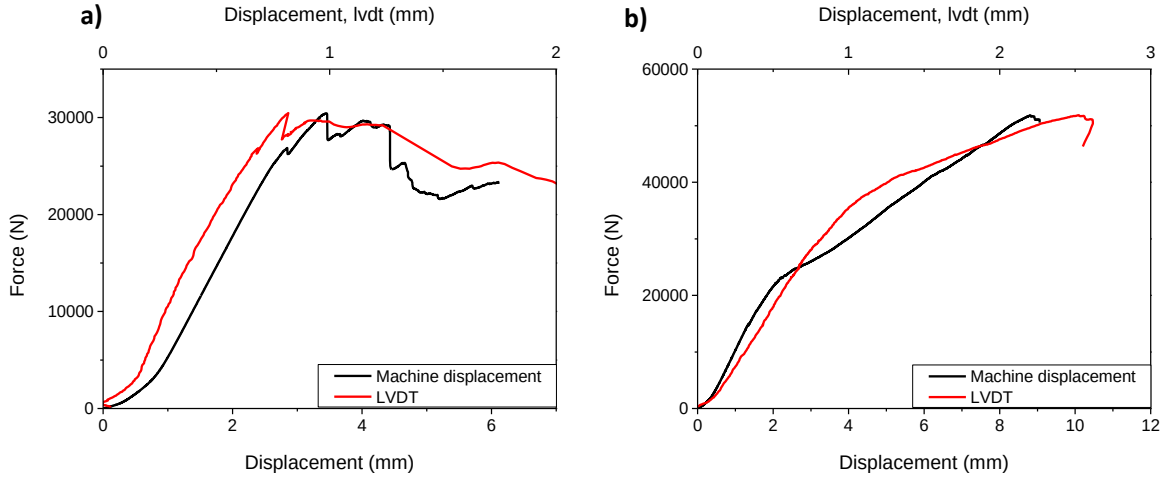


**Figure 4.25 - Typical curves of force in function of displacement measured from the load noses (machine) and LVDT sensor for a) control and, b) tufted specimens respectively.**

## Clustering analysis of AE signals

The clustering of the AE signals acquired on 3-point bending tests employed the same approach than to analyze the AE activities during the pull-off tests. An investigation by DB index found 2 clusters as optimal values for the clustering of both sets of specimens analyzed. The main parameters for clustering are:

- PCA: 4 descriptors
- Single-linkage: amplitude, average frequency, RMS16, and absolute energy
- DB index: 2 clusters

Figure 4.26a and b present the typical radar charts of center values of the AE features for the two clusters obtained from the control and tufted samples respectively. It is noticeable the difference between the two clusters. However, here also, the shape of the radars graph for the two structures remains very similar. Cluster 1 regards to minor damages, such as matrix cracks, generated from the beginning of testes. Otherwise, cluster 2 concerns significant damages that are capable of diminishing the load-bearing capacity of the structures considerably. This class of AE signals is mainly described to delamination and debonding along tuft length as shown in post-mortem micrographs in Figure 4.23 and Figure 4.24. The curves force and cumulative energy by clusters as a function of crosshead displacement are exhibited in Figure 4.27 for untufted and tufted structures respectively. Minor damage events are generated since the beginning of structure loading as presented by the cumulative energy curve for the cluster 1 with lower values until the initiation of the cluster 2. The second AE class of signals is related to interlaminar cracks of the composite that lead subsequently to the failure of the control structure. For the tufted composites, cluster 1 behaves in the same manner as for untufted specimen. Cluster 2 appears from the loss of linearity exhibited on the force-displacement curve, which is concerned with delamination propagation in the stiffener radius as already reported. The force corresponding to the beginning of the AE signals from the Cluster 2 is slightly greater for the control specimens than to the tufted. This event initiates under a lower load than seen in the control structures mainly due to the inferior stiffener radius of the tufted composites as reported in the investigation of the mechanical behavior of the specimens under pull-off tests. The evolution of cumulative energy of this specimen configuration is related to delamination and the crack bridging mechanisms of the tufted threads.

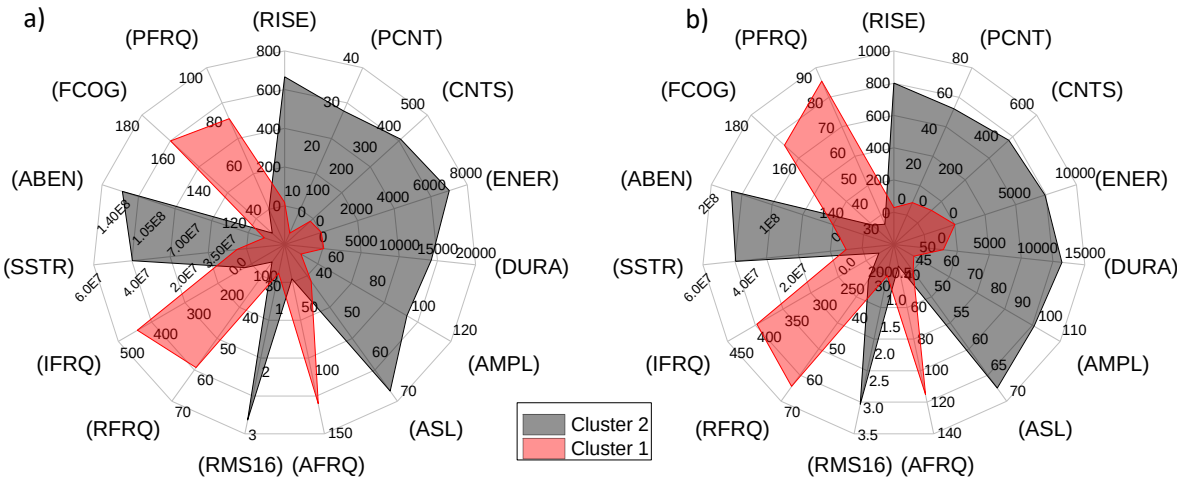


**Figure 4.26 - Typical radar graphs of the center values of AE signals features by clusters for a) control and, b) tufted specimens respectively.**

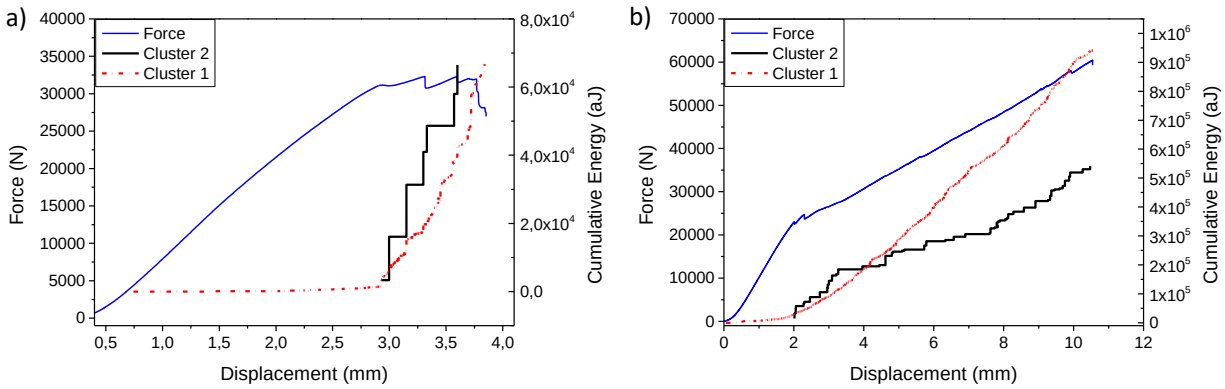


**Figure 4.27 - Typical force-displacement curves and cumulative energy-displacement by clustered signals for a) control and, b) tufted specimens respectively.**

### 4.2.2 Omega stiffeners - GFRP composites (Batch II)

This section exhibits the results and discussion of GFRP omega stiffened panel submitted to pull-off and 3-point bending tests. Three specimens of each specimen set were submitted to pull-off tests, while only one specimen for each set was subjected to 3-point bending tests. Section 2.3.10 describes more information about the testing methods utilized. Furthermore, section 2.2.5 details the manufacturing process used to obtain the structures. Differently, from the last batch (Batch I), this batch of samples presented the stiffener radius similar for every specimen manufactured. Table 4.3 shows the designations of the samples.

**Table 4.3 – Specimens description.**

| specimen | Description |
|---|---|
| **VR** | Control specimen |
| **V2T** | 2 rows in both structure sides with partial tuft insertion |
| **V3TC** | 3 rows in both structure sides with partial tuft insertion |
| **V3TL** | 3 rows in both structure sides with complete tuft insertion |

#### a) *Pull-off tests*

Figure 4.28 shows the typical force-displacement curves for each set of specimens subjected to pull-off tests. The work done (WD) for the tufted composites was significantly increased by 2.6 times for V2T specimens while V3TL and V3TC presented similar raise of 3.8 times. It is remarkable from the lower value of work done for V2T specimens, that tuft density is very significant in the interlaminar fracture toughness of the structure. However, maximum force

($F_{max}$) and stiffness were degraded by about 20% and 36% respectively when inserting tuft threads.

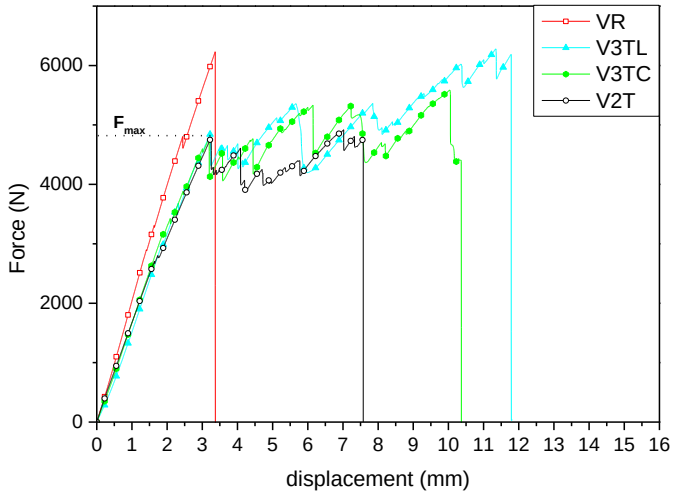


**Figure 4.28 - Typical force-displacement curves for each set of specimens under pull-off tests.**

Table 4.4 summarizes the values of $F_{max}$, stiffness, and WD obtained for each set of specimens.

**Table 4.4 - Mean values of $F_{max}$, stiffness, and work done.**

| specimen | Fmax (N) | Stiffness (N/mm) | WD (N.mm) |
|---|---|---|---|
| **V3TL** | 4526 ± 209 | 1597 ± 49 | 41139 ± 9364 |
| **V3TC** | 4508 ± 167 | 1665 ± 62 | 41898 ± 2857 |
| **V2T** | 4395 ± 325 | 1561 ± 62 | 24247 ± 2674 |
| **VR** | 6084 ± 88 | 2102 ± 127 | 10707 ± 745 |

DIC analyses were carried out to investigate the decrease of $F_{max}$ for tufted composites. Figure 4.29 exhibits shear strain field ($\varepsilon_{xy}$) provided by DIC technique for the control specimens obtained when loading force is about 4500 N. This value corresponds to the mean $F_{max}$ of tufted specimens and will support comparing the strain fields between the set of specimens. Moreover, the figure exhibits the step I and II as the shear strain fields acquired just before and after their first significant crack respectively for V3TL, V3TC, and V2T composites. It is noticeable that the shear strain concentrates in two main zones, which consists of the external side of the radius as well as the interior side, extending until the tip between the contact flange/skin. The maximum shear found on the outside region is in the same order of magnitude for every set of specimens. This indicates that tufted specimens present a stiffener radius similar to control specimens due to the employing of the new inner mold to manufacture the specimens. Despite this, premature failure is still present for the tufted structures in the radius region. Therefore, it

is concluded that the first tuft row is responsible for initiating the interlaminar crack that consequently leads to the reduction of maximum force. Furthermore, the fact that crack propagation occurs in both interlaminar directions from the tuft row excludes the possibility of its initiation far from the threads. It is because tufts must arrest the delamination and consequently, avoid the development from the other side of the reinforcement in the same step.

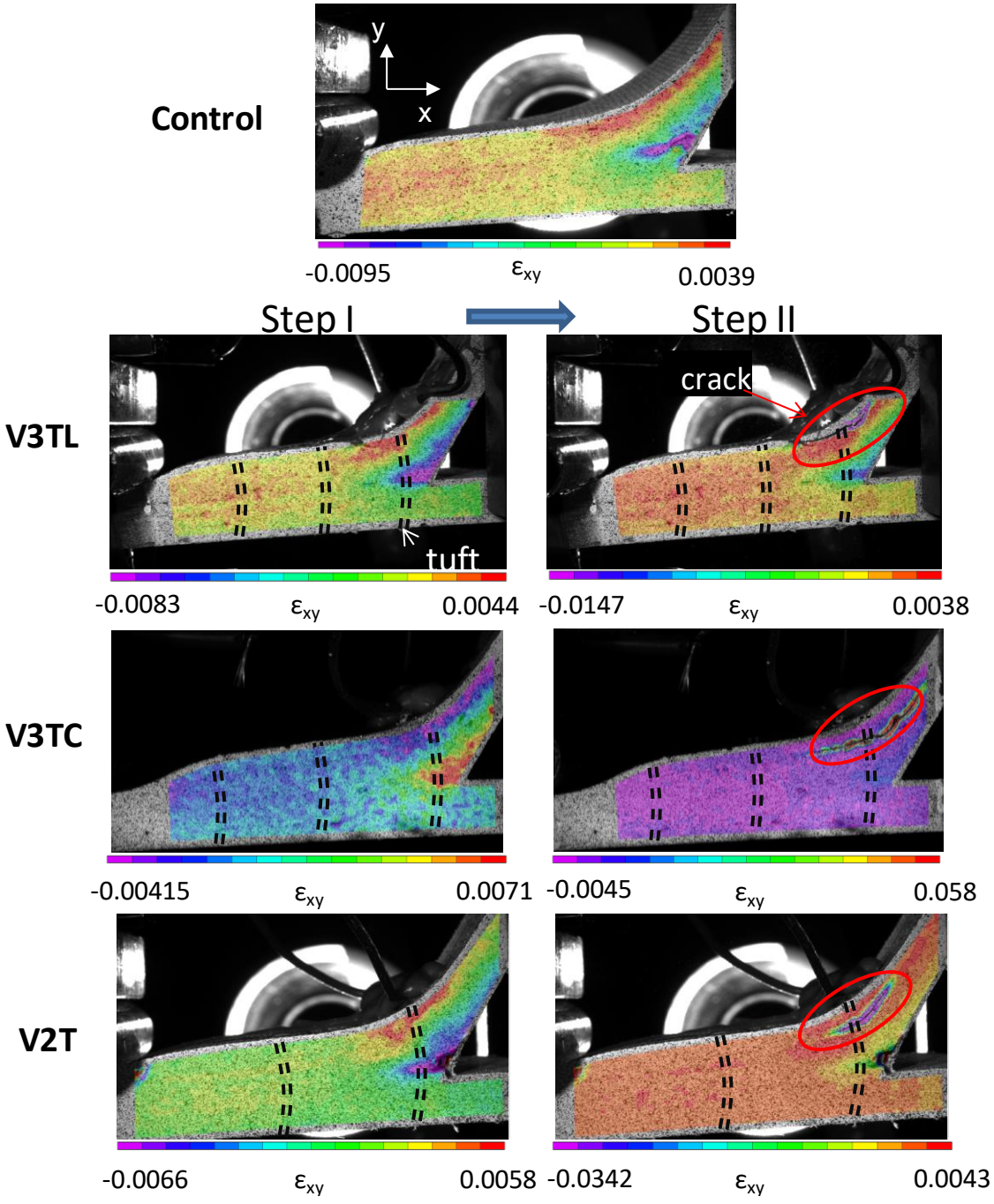


**Figure 4.29 - Typical strain fields obtained by DIC for control specimens at 4500 N and V3TL, V3TC and V2T just prior (step I) and subsequent (step II) to the first significant interlaminar crack.**

A schematic of the major and minor shear strain direction is presented in Figure 4.30 for the critical zones especially concentrated in the radius (exterior and interior). The illustration was performed from DIC maps acquired just before the first significant crack and represents a general behavior seen for all specimens set. Additionally, delamination is highlighted in the figure to clarify its location. Major strain following the external side of the radius is responsible for propagating the delamination that is created by the strain concentration around tuft threads.

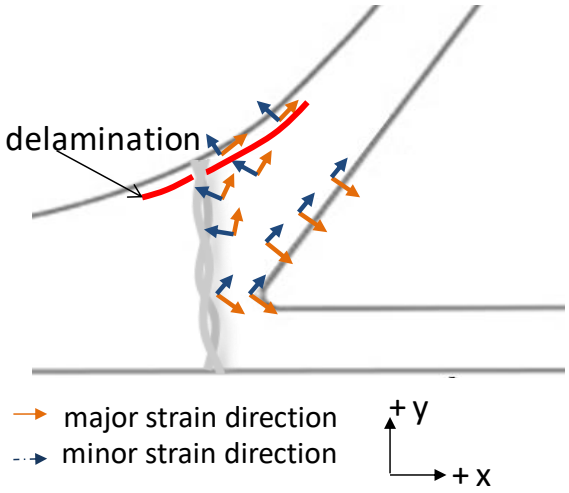


**Figure 4.30 - Schematic of major and minor strains, just before first principal damage, located on the stiffener radius.**

As already observed in the specimens of the batch I, when submitted to pull-off tests, interlaminar cracks are generated gradually on the stiffener radius and are arrested by tuft rows, which generates the stick-slip behavior in the curves. In the present batch of specimens, this behavior is performed for the second tuft row once that the first was responsible to the crack initiation in both longitudinal sides of the plies. Figure 4.31a shows the typical damage scenario before the complete rupture of the structure (Figure 4.31b). The mentioned damage events are reported similar for both sets of tufted specimens. As schematized in Figure 4.30, major strain following the profile of the external radius submit the plies to tensile loading and consequently, generates opening of the plies as indicated by the arrow in Figure 4.31a. The post-mortem photograph in Figure 4.31b demonstrates the complete failure of the tuft threads. The investigation of DIC maps evidence opening mode failure that initiates from the inner side of flange/skin contact and failure abruptly the structure.

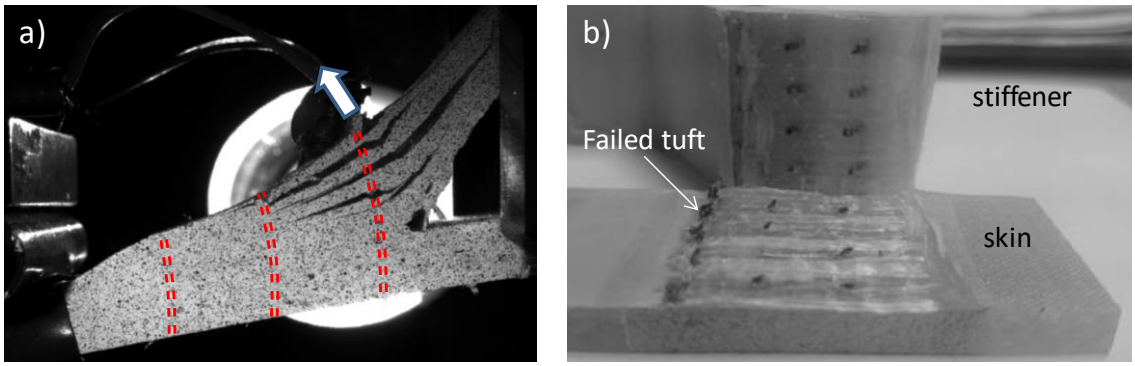


**Figure 4.31 - a) Typical damage behavior just before total failure of the structure, b) post-mortem photograph of a tufted specimen.**

### Clustering analysis of AE signals

The present study utilized the same procedure described above for classifying the acoustic emission signals of the previous tests. DB analysis evidenced two clusters for control specimens and three for the tufted specimens. PCA indicated 4 clusters as necessary to achieve more than 70% of the information contained. A single-linkage clustering was performed, obtaining the descriptors amplitude, average frequency, RMS16 and absolute energy with correlation distance greater than 70 %. The typical graph radars of the center values of AE features for the clusters obtained by k-means clustering are presented in Figure 4.32a-d for VR, V2T, V3TL, and V3TC specimens, respectively. Moreover, the typical curves force and cumulative energy by clusters, both in function of displacement, are exhibited in Figure 4.33 for all configuration in the same mentioned sequence. Cluster 1 presents typical lower values of AE signal features (Figure 4.32) that initiates from the beginning of the pull tests and attributed to minor damages as matrix cracking. The second cluster regards to significant damages, exemplified in Figure 4.33-a as slight unloading steps in the force-displacement curve. This event is not visible by DIC maps for the untufted specimens but is noticeable in the tufted composites when delamination propagates. These AE signals probably concern to interlaminar damages, such as microcracks and their coalescence that lead to delamination. Additionally, the cluster 2 is also composed by AE signals associated with debonding along tuft threads. This class can be employed to define a force threshold, especially for control specimens that do not present visible damage signal that may help to identify possible damage and consequently avoid catastrophic failure. The third cluster (Cluster 3) appears only for the tufted samples and distinguishes from the others classes of signals by the significant values of the majority of

descriptors. This characteristic, seen in the three configurations of tufted specimens, represent main damage events that are created after successive delamination of the structure, mainly concerning the rupture of the tufting thread. This cluster can aid to identify severe damage of the tufted composite that may lead in sequence to the failure of the structure. Comparing this class of AE signals, it is noticeable that its initiation is postponed for the V3T sets, especially for the V3TL specimens, which may justify their greater work done under pull-off tests due to the later major damage occurred on the tufts.

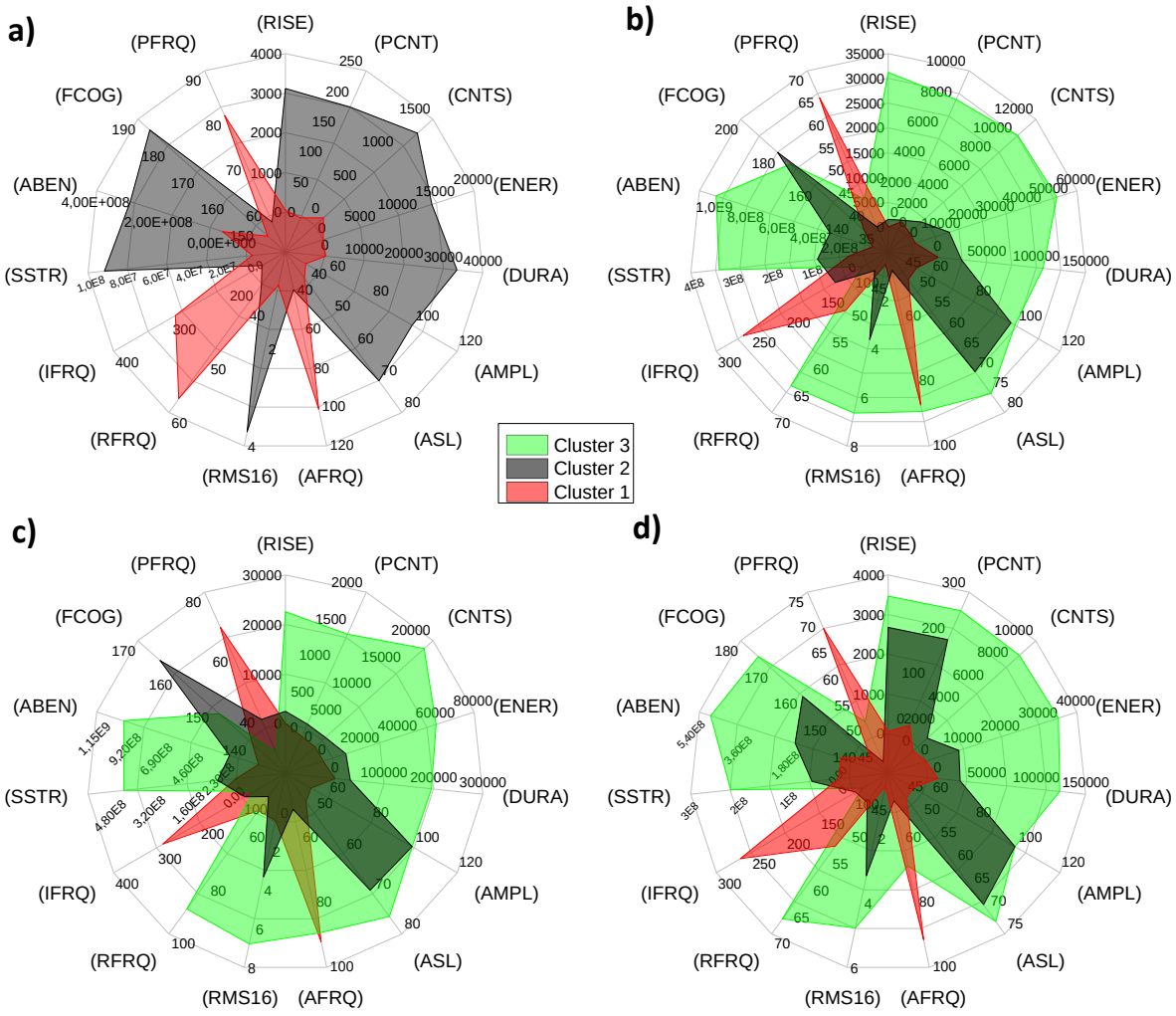


**Figure 4.32 - Typical radar graphs of the center values of AE signals features by clusters for a) control and, b) V2T, c) V3TL and d) V3TC specimens.**

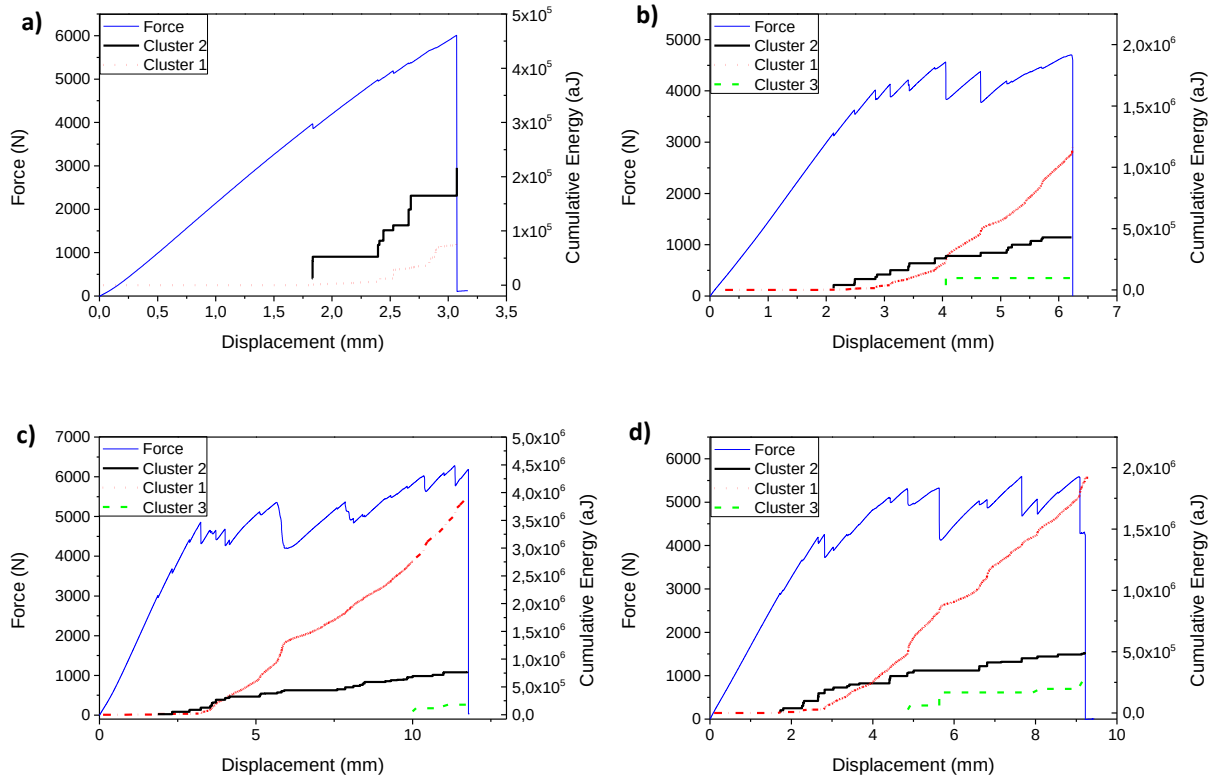


**Figure 4.33 - Typical force-displacement curves and cumulative energy-displacement by clustered signals for a) control and, b) V2T, c) V3TL and d) V3TC specimens.**

### b) *3-Point bending test (Structure- batch II)*

Figure 4.34 shows the force-displacement results for the specimens submitted to 3-point bending tests. The similarity of the curves precludes the evaluation of the tufts behavior in comparison to control structures. However, a slight decrease of the stiffness for the tufted composites is noticeable, but this worth further analysis with more specimens to better concludes. The failure of the specimens is mainly caused by the fibers rupture of the skin owed to significant deformation on this zone. The reduction of the support span may avoid this effect, which consequently would generate additional shear loading than flexural.

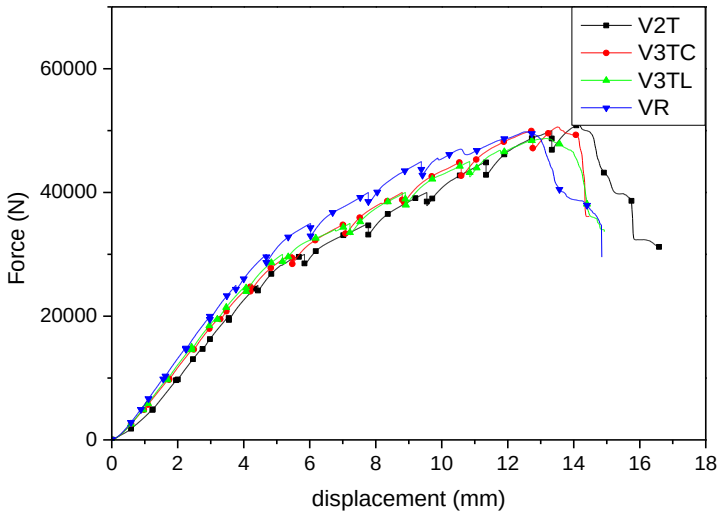


**Figure 4.34 - Force-displacement curves for all configurations of omega structures submitted to 3-point bending tests.**

Figure 4.35 exhibits the damage extent by digital photographs from the bottom of the specimens. The control specimen (Figure 4.35a) presents the larger delamination zone when compared with the tufting configurations V2T, V3TL, and V3TC, shown in Figure 4.35b-d respectively. The interlaminar cracks that achieve the internal part of the stiffener lead to the loss of loading bearing capacity because of the complete separation of the flange and skin in that region. Otherwise, tuft threads arrest the propagation of delamination and therefore, reducing the damage extent. It is noticeable that the specimens with three rows of tuft on each side (V3TC and V3TL) presented inferior damage extent.

Due to this restriction of the tufts to interlaminar crack propagation, out-of-plane deformation concentrates in the region of the load noses, which consequently leads to severe damage of the fabrics for the tufted composites. This behavior is comparable to the increase of the dent depth in the tufted specimens when subjected to impact loading seen in Chapter 3. Furthermore, V2T specimen (Figure 4.35) displayed significant delamination in a single side in comparison to the other tufted structures. This investigation corroborates with the lower results of the V2T configuration under pull-off tests among the tufted specimens.

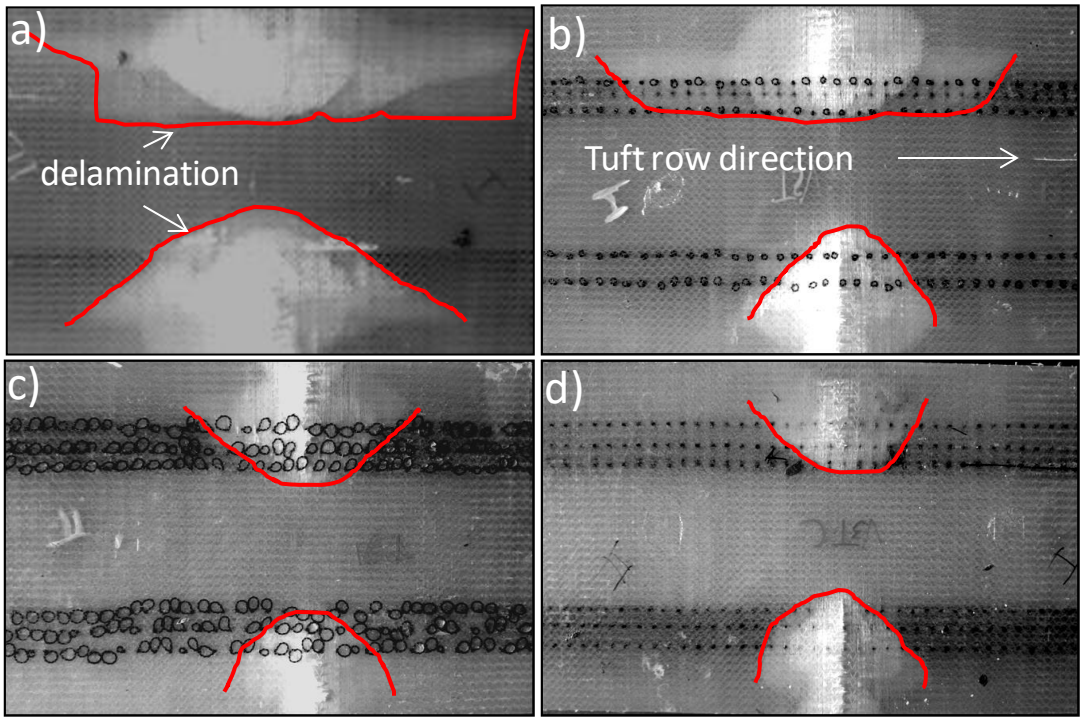


**Figure 4.35 - Post-mortem images from the bottom of the structures for a) control and, b) V2T, c) V3TL and d) V3TC omega structures.**

### Clustering analysis of AE signals

The clustering analyzes were carried out in the same manner that those previously described in this chapter. The parameters are listed below:

- PCA: 4 descriptors
- Single-linkage: amplitude, average frequency, RMS16, and absolute energy
- DB index: 2 clusters

The radar graphs regarding the two clusters of AE signals based on k-means clustering are presented in Figure 4.36a-d for VR, V2T, V3TL, and V3TC respectively. It is noticed that the shape of the radar graphs differs according to each set of structures. However, the families containing three tuft rows on each side along the stiffener (V3TL and V3TC) are very similar and distinct from the other two specimen configurations. This difference is more remarkable for the cluster 2, especially comparing to the specimens with two rows (V2T).

Figure 4.37 a-d shows the curves force and cumulative energy by clusters as a function of displacement in the same order aforementioned. The cumulative energy increases considerably in the same period that the loss of linearity in the force-displacement curves. This may be related to the decrease in structure stiffness generated by delamination.

The two classes of signals distinguish significantly between them. Cluster 1 is related to minor damages generated since the beginning, such as matrix cracks, as well as significant damages, especially regarding delamination and tuft debonding. These last damages appear just before the loss of linearity in the force-displacement curve shown in Figure 4.37. Cluster 2 concerns significant damages that are mainly attributed to the failure of fibers in the skin. This class of damage event emerges lately to the control specimen due to a better distribution of the applied load that implies in lower local deformation and consequently postpones the fibers breakage.

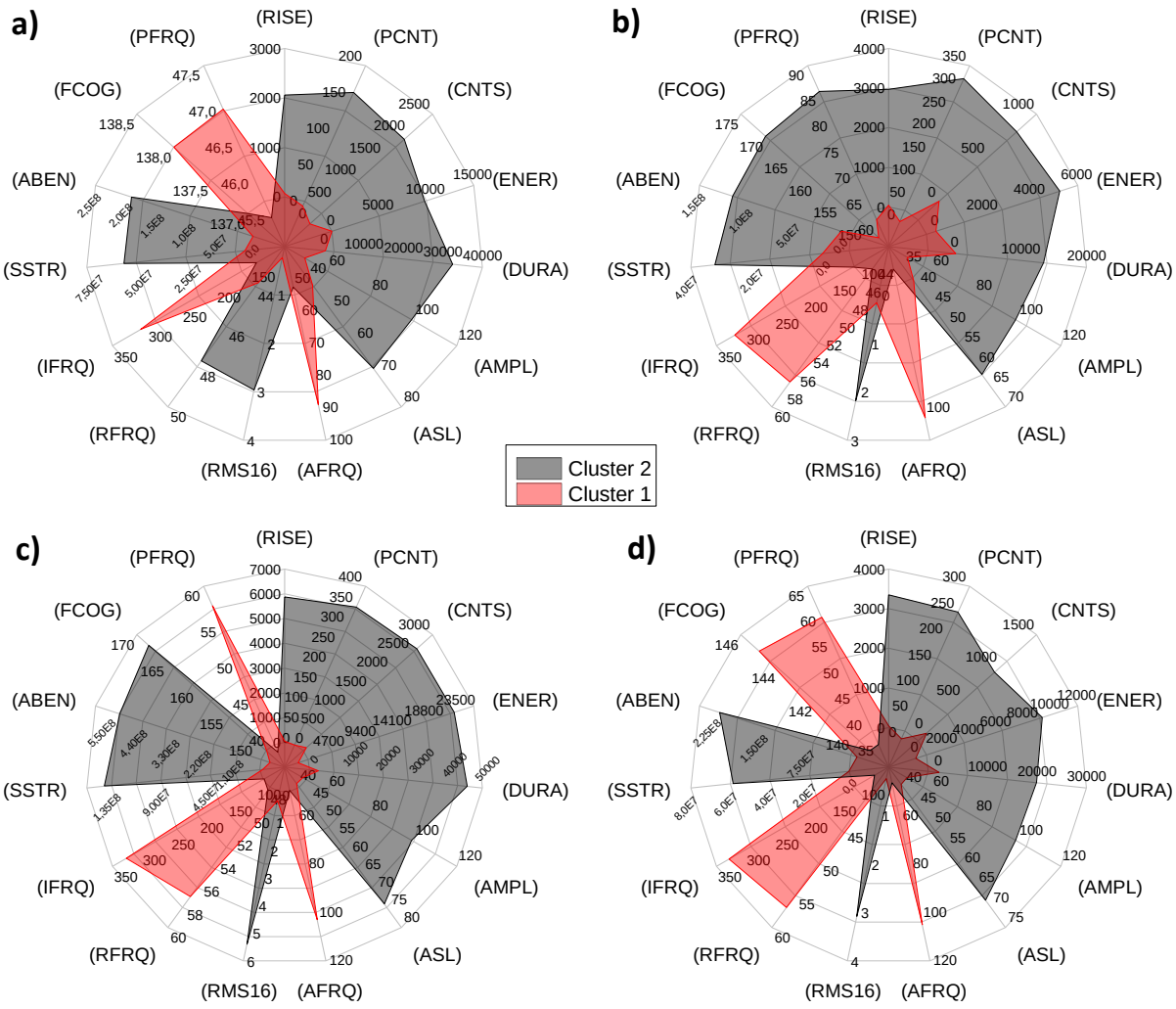


**Figure 4.36 - Typical radar graphs of the center values of AE signals features by clusters for a) control and, b) V2T, c) V3TL and d) V3TC structures.**

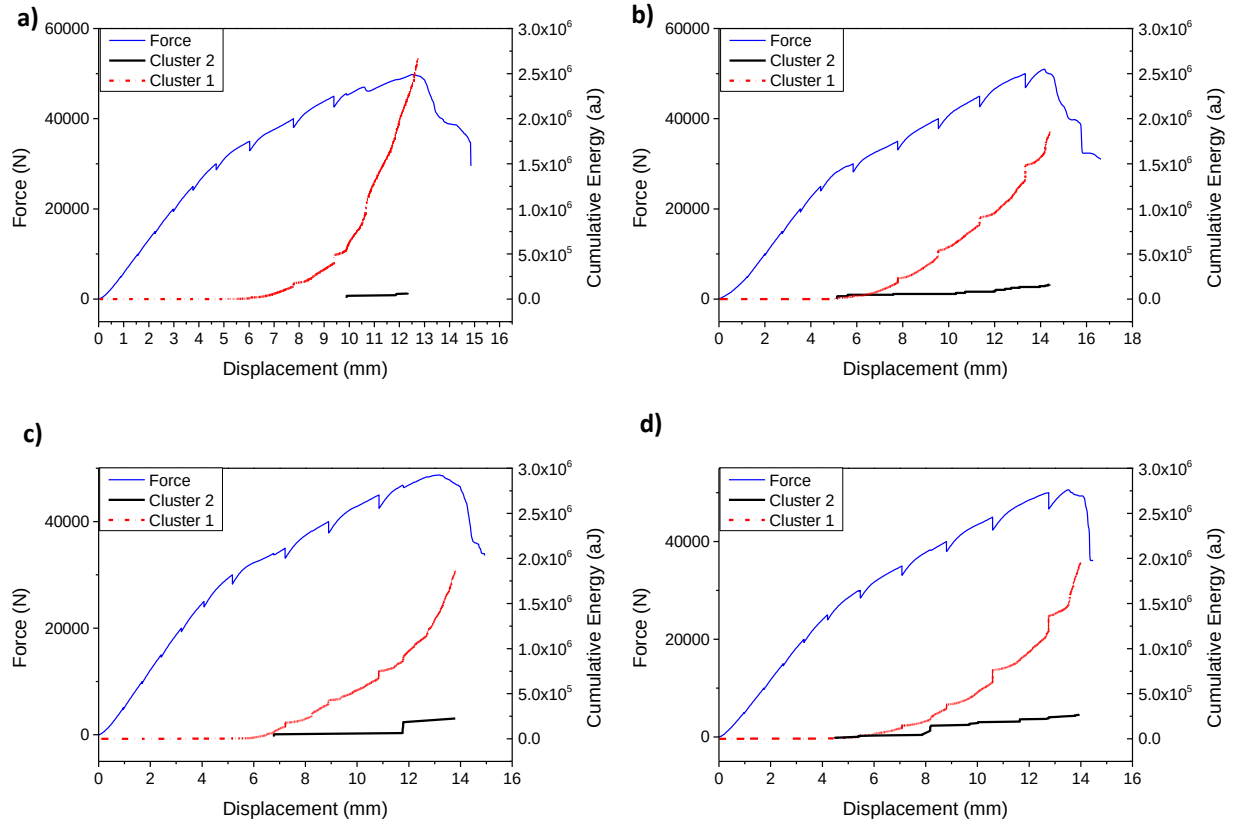


**Figure 4.37 - Typical force-displacement curves and cumulative energy-displacement by clustered signals for a) control and, b) V2T, c) V3TL and d) V3TC structures.**

### 4.2.3 Omega stiffeners - CFRP composites (Batch III)

The present batch of specimens considered the issues reported for the two previous batches, in the previous sections of this chapter, to manufacture this new set of omega stiffeners reinforced by tufting. Firstly, the new inner mold was employed to diminish the problems related to radius reduction: the increase of the stress concentration on the region leads to premature delimitations and reduction of the maximum force, especially seen for the pull-off tests response. However, the use of the new mold for manufacturing Batch II did not guide to better results of maximum force. This was mainly due to the insertion of tuft threads into the radius region that amplified the stress on the zone and led to crack propagation from the threads and as a consequence, the decrease of maximum force. Therefore, Batch III preconized a large stiffener radius and tuft reinforcements distant from the radius zone for the manufacturing.

The following section presents the results and discussion regarding the new set of specimens under pull-off and 3-point bending tests subsequently. Section 2.2.5 details the manufacturing

process used to obtain the structures. Three specimens of each configuration were submitted to pull-off tests and one specimen for each set was subjected to 3-point bending tests. Section 2.3.10 in this thesis presents more information about the testing methods utilized. Table 4.3 shows the designations of the samples.

**Table 4.5 – Specimens description.**

| specimen | Description |
|---|---|
| **REF** | Control specimen |
| **TUF1** | 1 row in each structure sides with partial tuft insertion |
| **TUF2** | 2 rows in each structure sides with partial tuft insertion |

### a) *Pull-off tests*

Figure 4.38 shows the typical behavior of the specimens under pull-off tests and their average mechanical properties summarized in Table 4.6. TUF2 samples are seen to improve the maximum force considerably, the work done until failure (WD) as well as the stiffness when compared with the REF samples. Otherwise, TUF1 presented mechanical properties inferior to the reference. Figure 4.39a exhibits the catastrophic failure for a REF sample that separates the stiffener integrally from the skin. The insertion of tuft yarns avoids the mentioned phenomenon. The through-the-thickness reinforcements work bridging the crack opening between the layers until tuft rupture and can be analyzed in Figure 4.38 especially from the TUF2 curve as a stick-slip behavior.

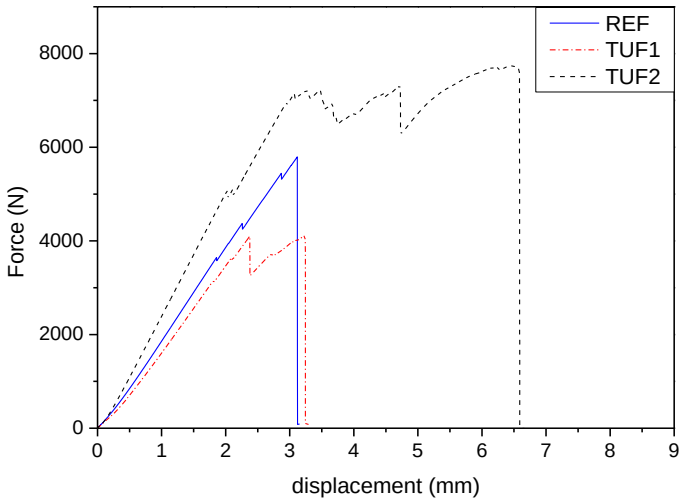


**Figure 4.38 - Typical behavior on pull-off tests for control and TUF1 and TUF2 configurations of tufted specimens.**

**Table 4.6- Mean values of Fmax, stiffness, and work done.**

| specimen | Fmax (N) | Stiffness (N/mm) | WD (N.mm) |
|---|---|---|---|
| **REF** | 5963 ± 332 | 2009 ± 34 | 10268 ± 1842 |
| **TUF1** | 3751 ± 479 | 1849 ± 91 | 8185 ± 177 |
| **TUF2** | 6614 ± 463 | 2329 ± 190 | 34643 ± 3253 |


**Figure 4.39 - Post-mortem images of a) REF, b) TUF1 and c) TUF2 specimens submitted to pull-off tests.**

The surface area of the specimens was calculated by the software Solidworks after drawing the parts from the specimens images, as exemplified in Figure 4.40. The applied approach aided to understand the stiffness difference of the omega stiffeners, mainly between control and TUF2 specimens. The areas are 1420 $mm^2$, 1440 $mm^2$ and 1523 $mm^2$ for REF, TUF1 and TUF2 respectively. These variations are related to the differences in the dimensions caused by the manufacturing process. The considerable difference in the surface area of the TUF2 specimens comparing to TUF1 and REF leads to significant increase of the second moment of area. However, the same response is not seen for TUF1 and REF, that present similar areas but a different second moment of area. This behavior is mainly caused by some difference in the flange length that may reduce the local stiffener.

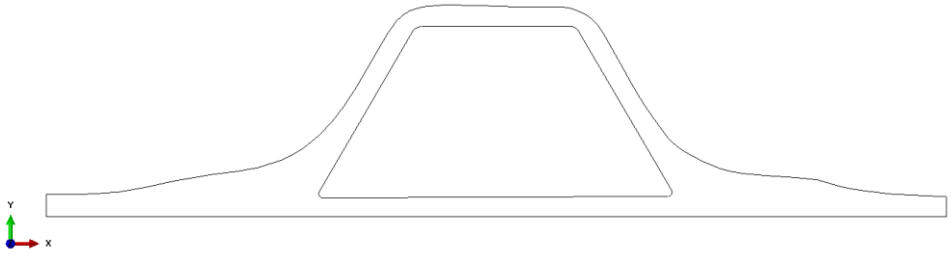

**Figure 4.40 – Schematic illustration of the TUF2 specimen format.**

The increase of resin amount in the radius region for the TUF2, which results in a significant resin pocket, was expected to reduce the structure properties as a consequence of lower mechanical properties of the resin. However, growth in the dimensions which consequently increased the second moment of area counteracted this adverse effect. Figure 4.41 shows a comparison between the deflection measured by DIC method for the images at the same load (4000 N). The measures were acquired through a virtual curve positioned as indicated in the DIC strain field in Figure 4.41. Larger deflection is seen to the structure TUF1 validating the lower stiffener of this configuration, which leads the structure to higher stress, as described by the flexural equation (6), and consequently an early crack initiation. Moreover, TUF2 specimens present a minor deflection which agrees with the significant second moment of area of this configuration.

$$\sigma_{flex} = \frac{M.y}{I_{xx}} \quad \textbf{(6)}$$

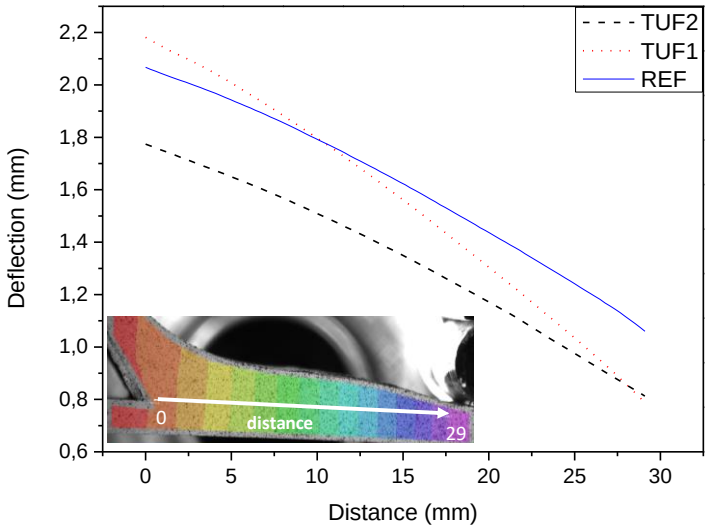


**Figure 4.41 -Typical deflection of the flange section located on the interface flange/skin for all set of specimen configuration subjected to pull-off tests.**

Figure 4.42 shows the typical damage development for the TUF2 specimens by DIC strain field and in-situ micrographs. The critical failure initiates on the external side of the flange due to a resin pocket which generates a significant strain field in the region as exhibited in Figure 4.43. This behavior occurs for all configuration of specimens. Figure 4.42a exhibits the interlaminar crack responsible for the first significant load drop (event I). It is seen that the first tuft range (from the external side) arrests the crack tip and also an important shear strain ($\varepsilon_{xy}$) is concentrated between the two rows of out-of-plane reinforcements. Furthermore, from the micrograph, it is remarked that besides crack arresting, failure propagates around the interface of the tufted yarn. The in-situ microscopy allowed distinguishing a second important event (event II), where the opening mode seems severe, and generates a possible yarn rupture, as highlighted in Figure 4.42b. Also, the crack develops between the two tufted ranges, but the transversal reinforcements restrain the opening mode (fiber bridging).

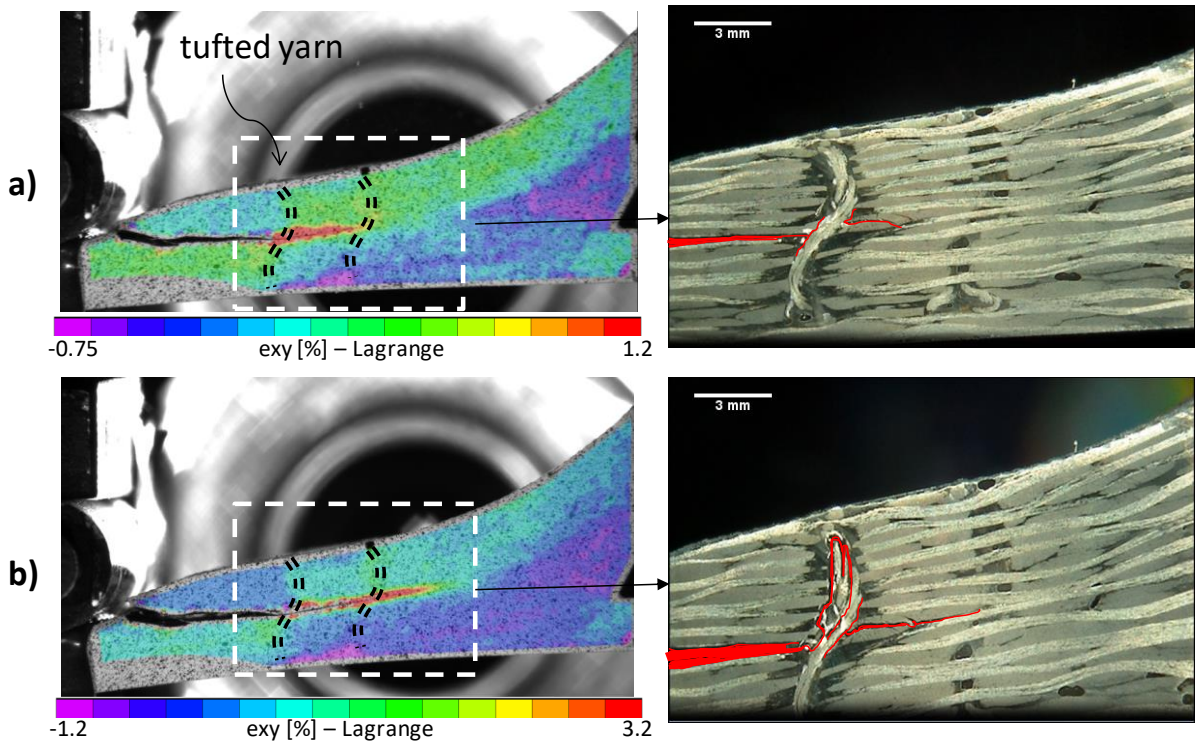


**Figure 4.42 - Typical damage development of TUF2 specimen during the pull-off test for a) first load drop and, b) the second significant load drop.**

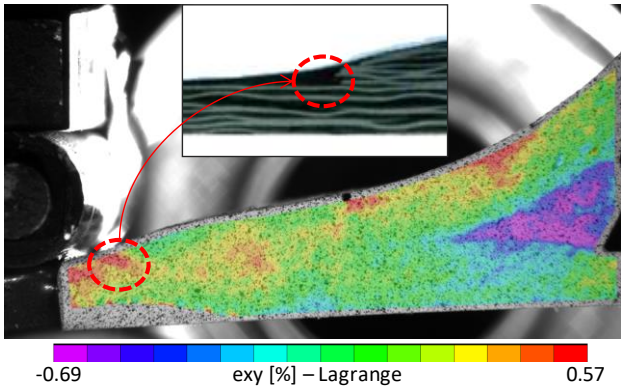


**Figure 4.43 - DIC image evidencing strain concentration on the resin pocket zone.**

Virtual extensometers by DIC method were placed on the tufted yarns region as exemplified in Figure 4.44 to evaluate the tuft behavior during the loading test of the TUF2 specimen. Figure 4.45 exhibits the typical plot of strain response from the two virtual extensometers (E1 and E2) as well as the acoustic emission cumulative energy. Both extensometers display negligible strains at the monitored regions until the delamination initiation (event I). From this point, it is seen a sudden increase on the strain, especially on E1, followed by a slight rise of cumulative energy due to a dominance of the crack opening mode (mode I) which enforces the tufted yarns to bridge the layers and contain the crack development. Subsequently to the event I, omega structure is reloaded, and extern tuft range continues to loading, which avoids a critical opening crack that may lead to specimen failure. Then, a sharp fall occurs again with a remarkable increase in cumulative energy, that is mainly related to yarn damages as already mentioned in the micrograph in Figure 4.42b. However, it seems that damages on the external tufted yarn are not sufficient to diminish its mechanical capability to contain delamination growth because E2 showed stable strain after event II when it was supposed to increase significantly during opening mode if occurs the rupture of the external tuft.

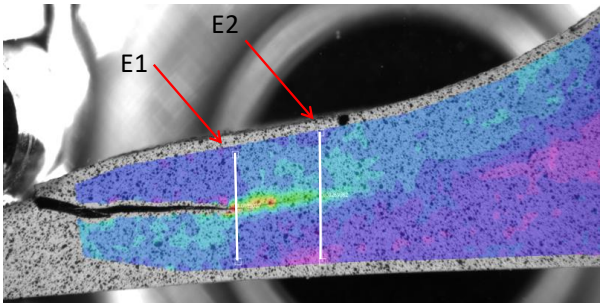


**Figure 4.44 - Schematic of the virtual extensometers employed on DIC analysis of the TUF2 specimens.**

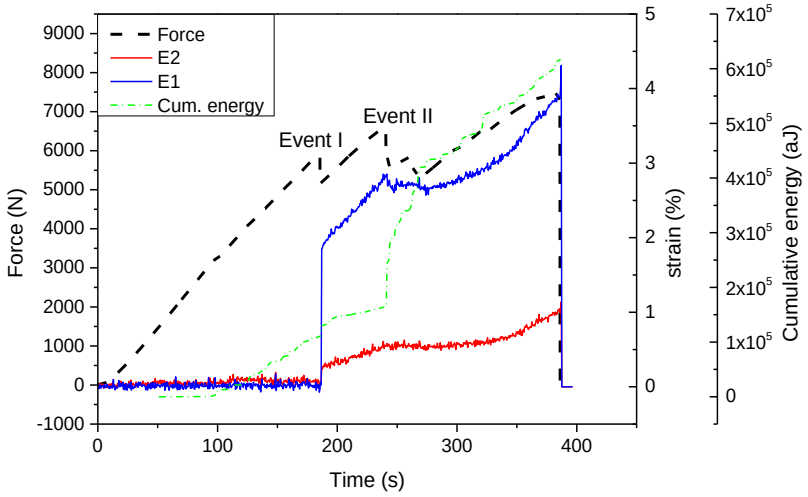


**Figure 4.45 - The typical behavior of strain by the virtual extensometers on DIC, AE cumulative energy, and force in function of time for a TUF2 specimen.**

Figure 4.46a shows a summary of the strains (major and minor direction) obtained by DIC strain field just before the crack initiation, particularly for the critical regions (resin pocket zones) in the TUF2 specimens. Contrary to previous works in open literature that have reported failure beginning on the resin fillet from the radius region, the present work demonstrates that compressive strain on this zone avoids the crack initiation there. Figure 4.46b schematizes the crack propagation and the already discussed bridging function of the tufted reinforcements.

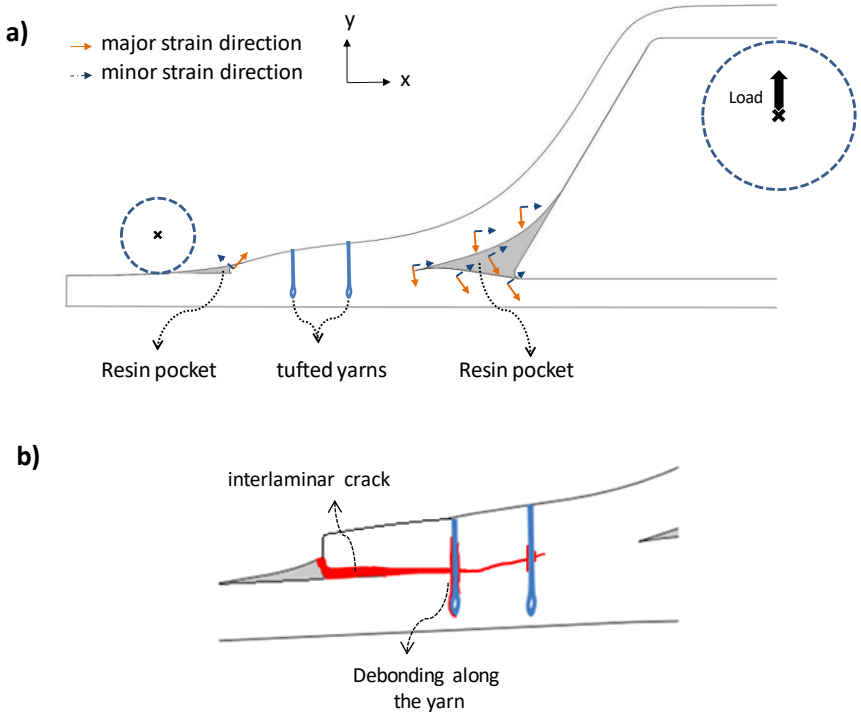


**Figure 4.46 - Schematic illustration of a) the minor and major strain directions obtained by DIC analyze just before the first event, b) the damage propagation.**

TUF1 specimens utilized the same approach to evaluate the damage mechanisms and tuft behavior. Delamination also initiates in the resin pocket on the outside region, and its development is arrested by the tufted thread as exhibited in Figure 4.47a. This significant damage, designated as the event I, is distinguished by a sharp load drop (Figure 4.48) as already reported to TUF2 specimens and a significant rise in cumulative energy. A virtual extensometer (E1), positioned in the same place that the tufted row, assisted the evaluation of the local strain. Figure 4.48 shows a slight increase in the strain from the event I obtained by this extensometer. Then, the structure reloads and the opening mode becomes significantly until the specimen failure. A sharp increase in the strain is exhibited through virtual extensometer when test reaches the event II, and an important rise in cumulative energy accompanies it. Figure 4.47b shows DIC strain field on event II, where is indicated the significant progress of the crack tip due to the lack of the second reinforcement range as seen for TUF2 configuration. Additionally, tuft debonding is identified from the micrograph. Subsequently to event II, a major increase on the strain in the tufted zone is described and leads to the failure of the structure. Figure 4.49a schematizes typical major and minor strains in the critical regions for the TUF1 specimens just before crack initiation (event I). This specimen configuration presents the same behavior as TUF2, with a compressive strain in the radius fillet and considerable shear strain in the external resin pocket. Main damages occurred in the flange zone are illustrated in Figure 4.49b which emphasize the fiber bridging function of the tufted yarn for TUF1 configuration.

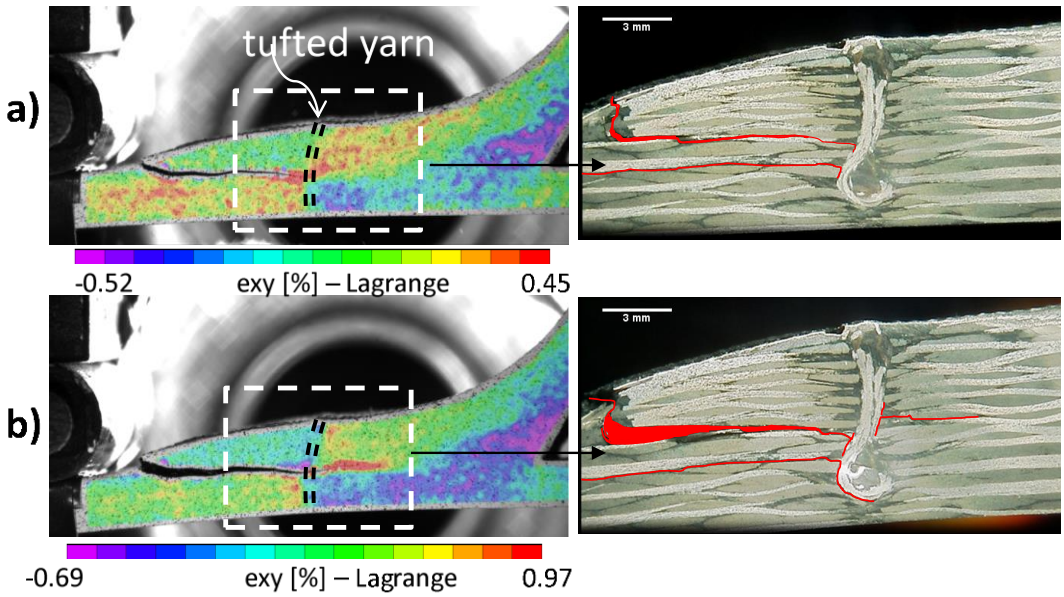


**Figure 4.47 - Typical damage development of TUF1 specimen during the pull-off test for a) first load drop and, b) the second significant load drop.**

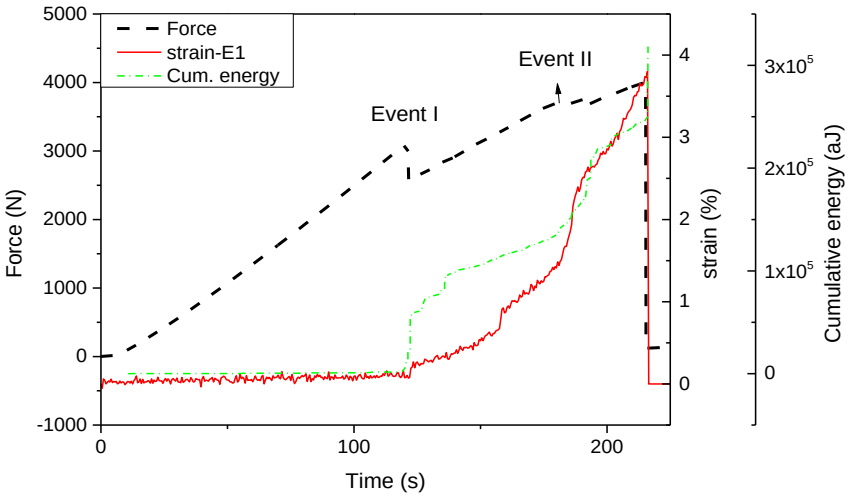


**Figure 4.48 - The typical behavior of strain by virtual extensometers on DIC, AE cumulative energy, and force in function of time for a TUF1 specimen.**

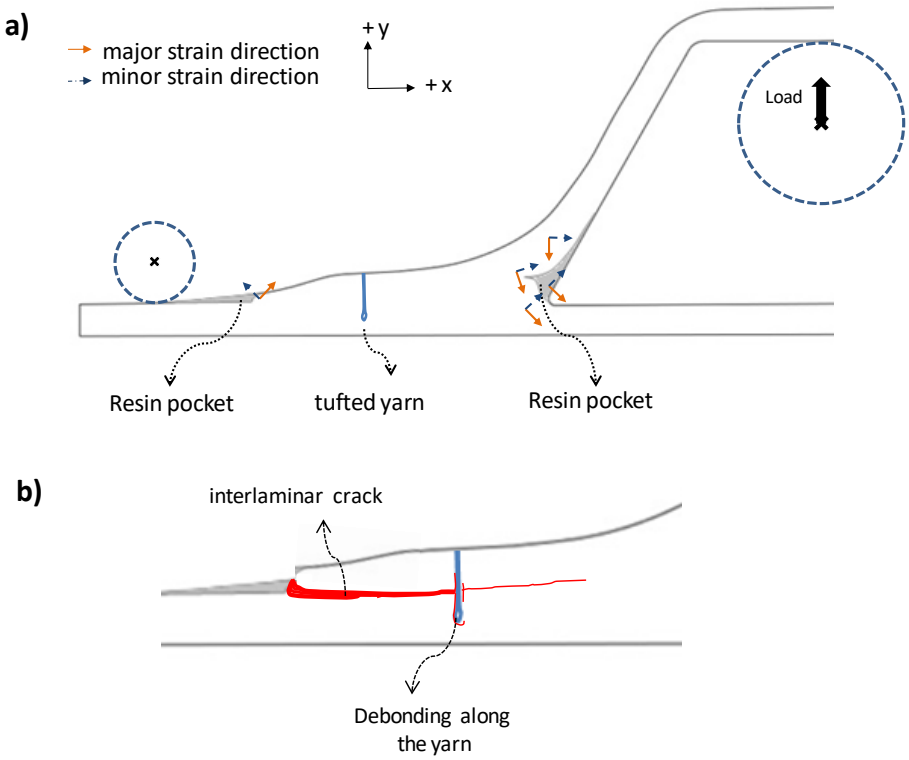


**Figure 4.49 - Schematic illustration of a) the minor and major strain directions obtained by DIC analyze just before the first event, b) the damage propagation.**

Evaluation of damage development for the reference specimens is difficult to perform due to their sudden failure. Damages are not visible by DIC strain field neither in-situ microscopy techniques. Therefore, the study based on the typical strain field by DIC shown in Figure 4.50 acquired before structure failure and usual acoustic emission signal activities in Figure 4.51 to understand the structural failure. A significant strain is concentrated in the external resin pocket

as already reported to the tufted structures. Additionally, a significant acoustic signal distinguished by high amplitude is localized near from this region just before specimen failure which leads to suppose that failure starts from external side to the radius fillet, as reported to TUF1 and TUF2 specimen configurations.

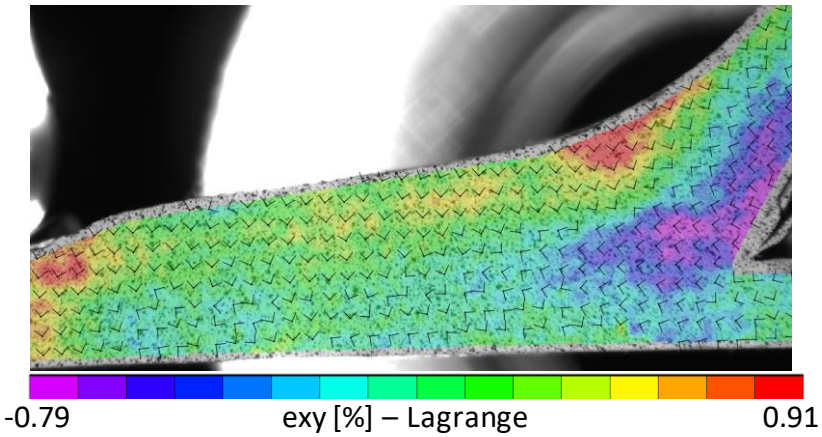


**Figure 4.50 - REF just before sudden failure with the distribution of the vectors of principal strains.**

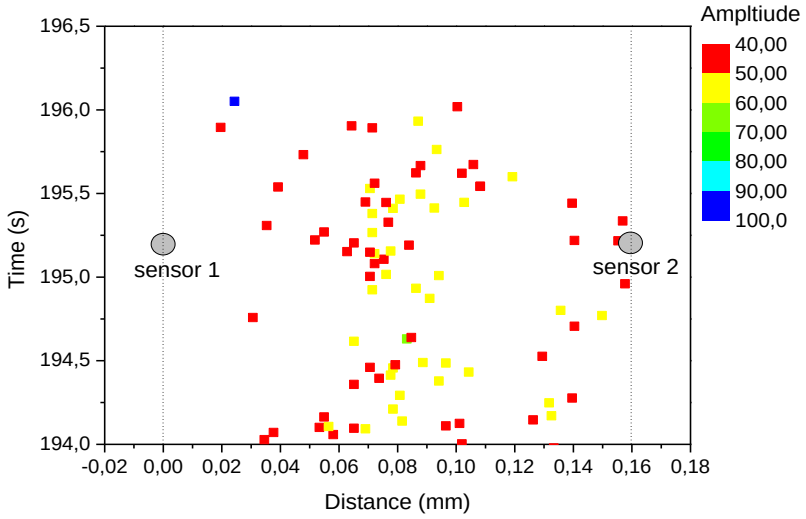


**Figure 4.51 - Location of AE signals in function of their amplitude just before the sudden collapse of the control specimen (the AE are placed on the bottom of the skin along the width of the specimens).**

## Clustering analysis of AE signals

This analysis was performed to investigate the damage events from the AE signals acquired during pull-off tests. Clustering of AE signals was carried out using the same approach reported in this chapter for the previous batch of specimens. The parameters utilized are described below:

- PCA: 4 descriptors

- Single-linkage: amplitude, average frequency, RMS16, and absolute energy
- DB index: 2 clusters

Differently from the Batch II under pull-off tests, the present set of specimens does not present the third class of acoustic signals that are related to rupture of tuft thread. This response is also in agreement with the results found to batch I subjected to the same test, and may be owed to the high stiffness of the carbon fibers in comparison to glass fiber fabrics. This contains the large deformations and avoids the threads rupture.

Figure 4.52a-c presents the typical radar graphs of AE features in function of the obtained clusters for REF, TUF1, and TUF2 specimens, respectively. The two classes have been exhibited typical behavior as already reported for the previous clustering analysis. The three radar graphs present the same general shape, with only the evolution of the values of the AE signal features. It seems that the description of the phenomena with these two clusters of acoustic signals are relevant for a first approach. Cluster 1 presents lower feature values and is related to minor damage events that initiate since the beginning of loading tests, such as matrix cracking. Otherwise, the cluster 2 corresponds to significant damages, primarily due to the high feature values of the acoustic emission signals. This class concerns to interlaminar cracks and debonding along tuft threads.

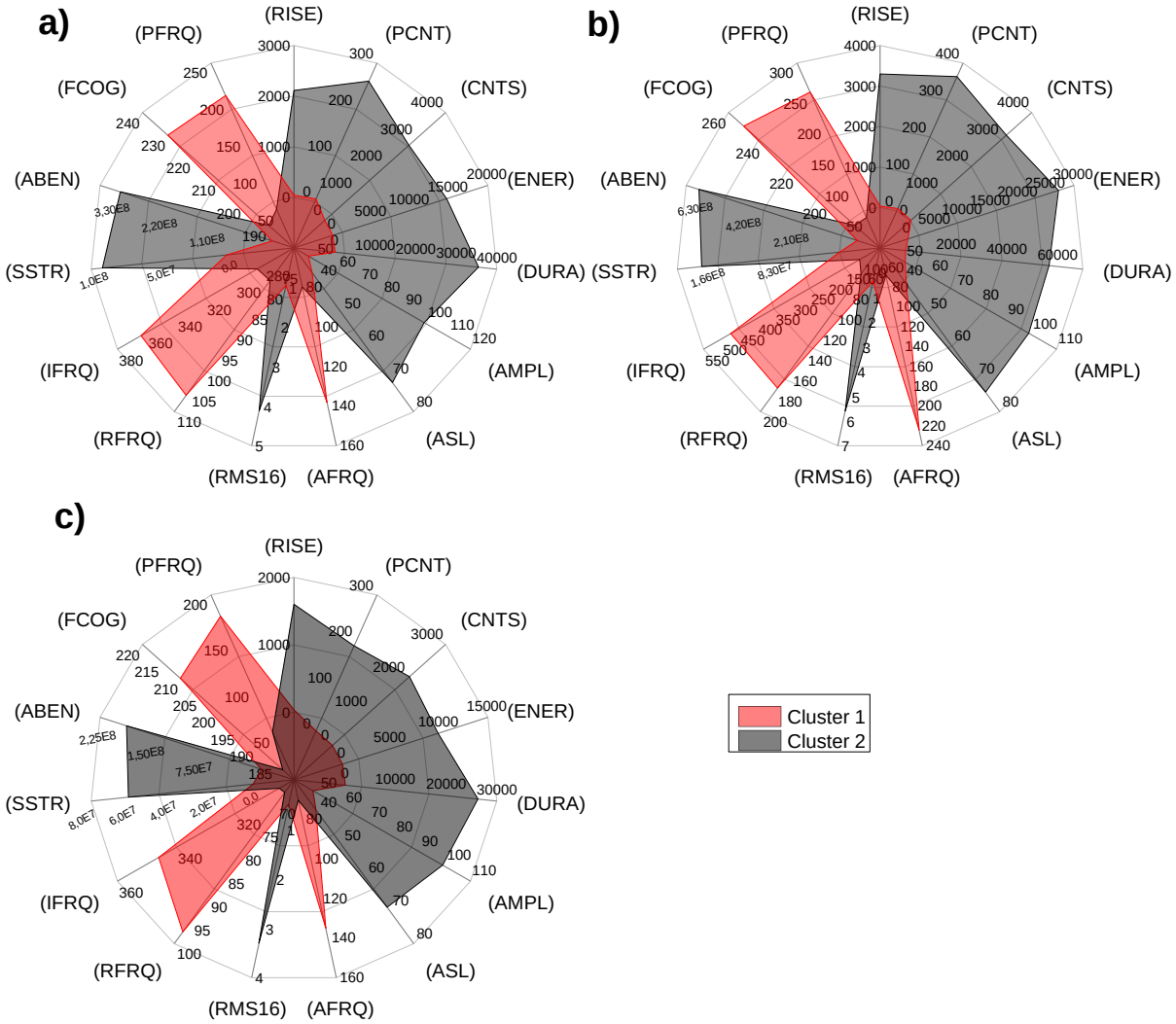


**Figure 4.52 - Typical radar graphs of the center values of AE signals features by clusters for a) REF and, b) TUF1, c) TUF2 specimens.**

The cumulative energy from each cluster, as well as the pull-off force in function of the crosshead displacement, is exhibited in Figure 4.53a-c for REF, TUF1, and TUF2 respectively. The cluster 1 presents acoustic activities since the beginning and increases significantly when the Cluster 2 appears. This last class initiates at lower loading force for the tufted specimens when compared to control samples. This behavior is mainly attributed to damage events caused in the tuft threads due to the stress concentration of these reinforcements into the composite, as already mentioned in Chapter 3. TUF1 specimens seem the most affected by the tufts due to the sudden important delamination instead of gradual damage propagation that results in the slow increase of cumulative energy until delamination, as seen for REF and TUF2 specimens.

The cluster 2 (major damage) for TUF2 amplifies rapidly compared to the TUF1. This is because of the cluster 2 for the TUF1 specimens appears when a sudden failure initiation occurs

with strong propagation until its arrest for the tuft row. The recovery is made later with a larger displacement after the observed plateau, and thus, sudden delamination leads the structure to the failure. For the TUF2 specimens, the interlaminar cracks are contained by the first tuft row (external side), which may indicate the generation of local damage until achieving the second row of tufts, explaining the evolution of cluster 2. When the first tuft row damages significantly, the second row takes place the effort, and therefore, continuous damage happens as well as the continuous evolution of cluster 2. This response is synonymous to considerable damage tolerance of the TUF2 configuration.

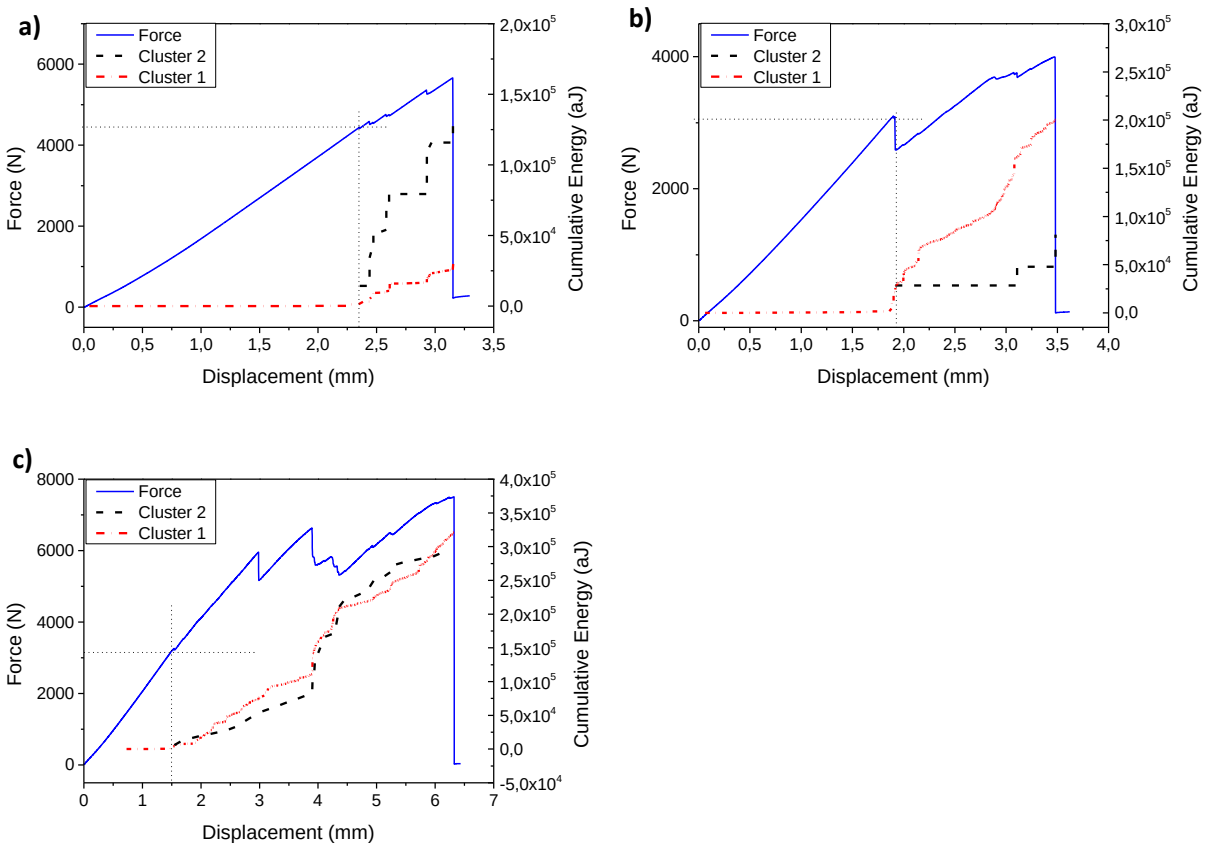


**Figure 4.53 - Typical force-displacement curves and cumulative energy-displacement by clustered signals for a) REF and, b) TUF1, c) TUF2 specimens.**

### 3-Point bending test (Structure- batch III)

Figure 4.54a-b shows the force-displacement curves acquired from the crosshead displacement and LVDT sensor respectively, for the structures subjected to 3-point bending tests. The specimens failed on the top of the stiffeners instead of the expected rupture between flange/skin interface (Figure 4.55). Nevertheless, the evaluation of the mechanical behavior of the

composite structures may be performed before this failure. The curves evidence a slight increase of the stiffness for the tufted composites that is probably owed to the rise of the second moment of area as reported to the pull-off tests, especially for TUF2 specimens. Additionally, the loss of linearity marked in Figure 4.54a is supposed to be caused by significant damage events that reduce the stiffness of the structure. Figure 4.54b exhibits better this behavior for the untufted specimen at the point concerning the loss of linearity. The abrupt increase of load with the stick-slip behavior of the LVDT displacement can be related to unloading-reloading on the measured region caused by delamination. This supports the discussion for the last batch submitted to the same test as well as the impacted specimens on chapter 3, where tuft threads restrain delamination and consequently implies on amplification of the local deformation, as acquired by LVDT. Moreover, the LVDT response validates the assumption of enhancement of structure stiffness, where the difference between the flange displacement (measured by crosshead displacement) and bottom of skin (LVDT) is lower for the tufted composites. Figure 4.56 schematizes the mentioned behavior. The difference between the point of measure by the machine crosshead and LVDT, $\Delta h$, is more significant than that exhibited for the tufted specimens, $\Delta h'$.

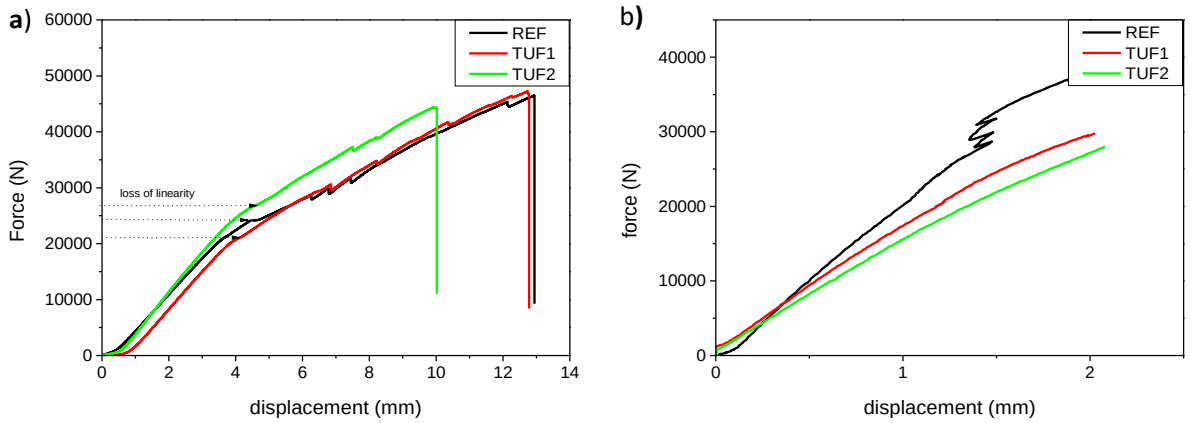


**Figure 4.54 - Force-displacement curves a) from the crosshead displacement of the machine and, b) from the LVDT sensor during 3-point bending tests.**

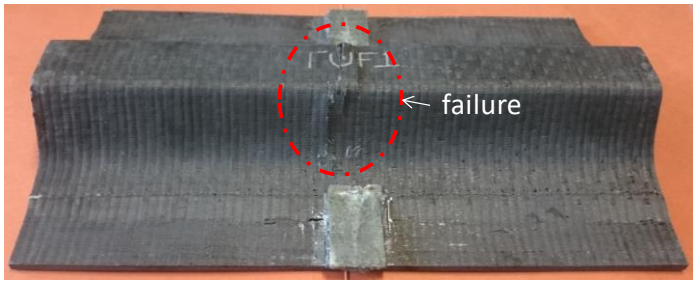


**Figure 4.55 - Typical damage found to all configuration of specimens (failure on the top of stiffener).**

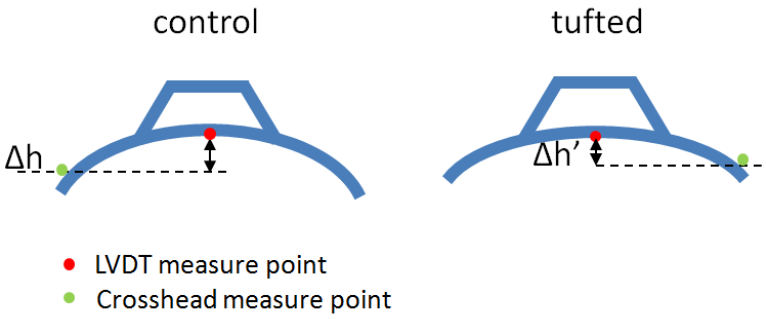


**Figure 4.56 - Schematic illustration of the difference of displacements acquired from the crosshead and LVDT sensor in different locations, presenting distinct values between control and tufted specimens.**

Post-mortem micrographs are presented in Figure 4.57a-c for REF, TUF1, and TUF2 omega stiffeners respectively. They were acquired from the cross section of the specimens in the middle of the longitudinal direction. It is noticeable that the damage extent is amplified for the untufted specimens (Figure 4.57a). Moreover, interlaminar cracks on the radius corroborate with the stiffness loss of the structures, as already reported. The tufted specimens (Figure 4.57b-c) display the cracks arrested by the tufts, which precludes the delamination propagation, as well as debonding along the tuft threads. The lower deformation during loading of the tufted structure caused especially for the enhancement of the second moment of area combined with the crack bridging effect of the tufts, diminish the crack propagation consequently.

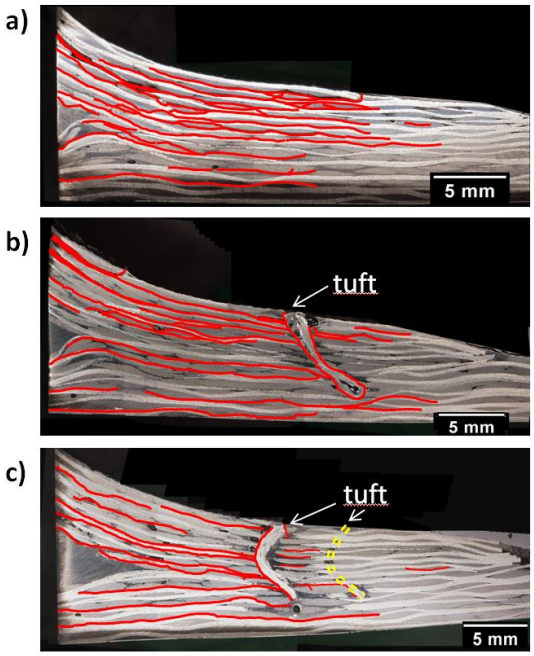


**Figure 4.57 - Post-mortem micrographs from the cross-section direction of the specimens.**

Figure 4.58 shows the number of AE hits versus time for three configurations of specimens investigated. The number of damage events that are related to the number of AE hits is mostly

increased from TUF2 to REF specimen. It corroborates with the analysis of the post-mortem micrographs in Figure 4.57, which exhibits excellent damage extent to the untufted sample and is gradually decreased until the TUF2 configuration.

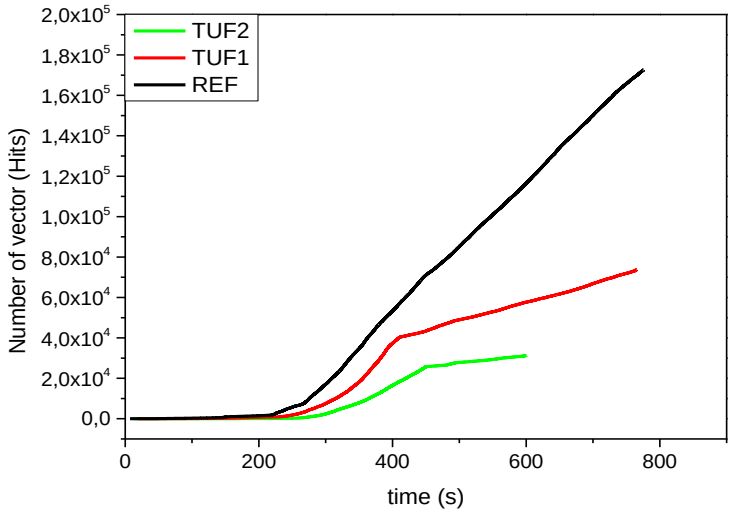


**Figure 4.58 - Number of hits versus time curves for REF, TUF1, and TUF2 composite structures.**

### Clustering analysis of AE signals

The acoustic signals were clustered to identify AE signal classes attributed to specific damage events during the mechanical tests. The same method conditions employed for clustering the AE signals in the previous mechanical analyses were utilized in this section. The parameters obtained are:

- PCA: 4 descriptors
- Single-linkage: amplitude, average frequency, RMS16, and absolute energy
- DB index: 2 clusters

The signals were clustered using the k-means method. The radar graphs concerning the center value of the signal features by clusters are presented in Figure 4.59a-c for REF, TUF1, and TUF2 respectively. Similar to the clustering of the previous mechanical tests, two classes significantly distinct from their AE signals features are displayed. Figure 4.60 presents the clusters obtained, as cumulative energy in function of the crosshead displacement as well the force-displacement curves of the specimens. The first cluster is attributed to minor damages that propagate from the beginning of the tests and increases when the structure presents a loss

of stiffness that seems to be caused by interlaminar damages on the radius of the stiffener. The AE signals concerning cluster 2, coincide with the beginning of the slight slip-stick behavior seen in the force-displacement curve (marked with dashed line). It is difficult to assume the damage type attributed to the two clusters, mainly due to the ultimate failure of the structures were out of the analyzed region, on the top of the stiffener. Despite this, it is noticeable the advantage of TUF2 specimen (Figure 4.60a) in comparison to REF (Figure 4.60b) and TUF1 (Figure 4.60c) to postpone this significant damage event that leads to structural failure. This event starts at 3700 N for TUF2 and about 2800 N for TUF1 and REF.

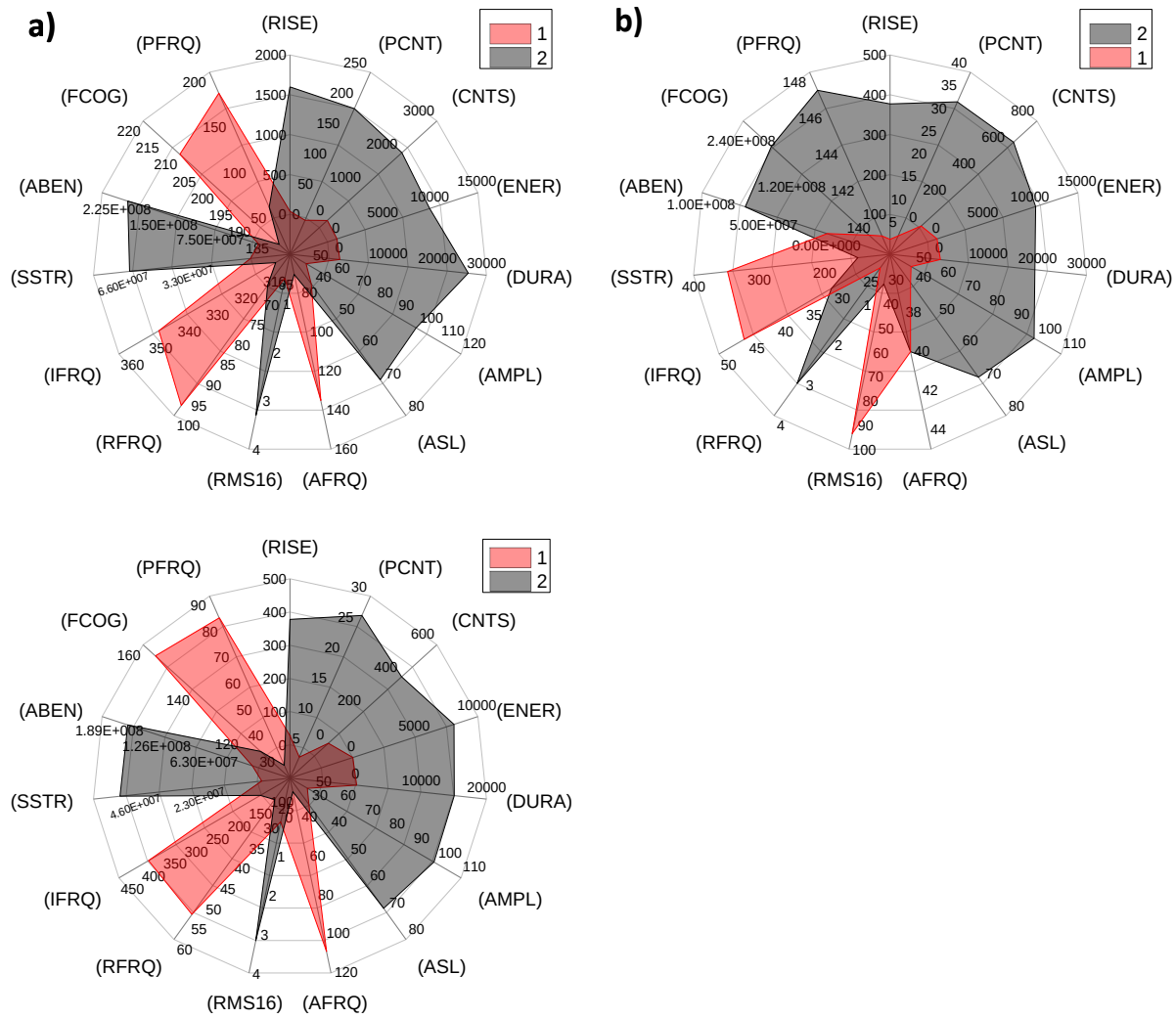


**Figure 4.59 - Typical radar graphs of the center values of AE signals features by clusters for a) REF and, b) TUF1, c) TUF2 structures.**

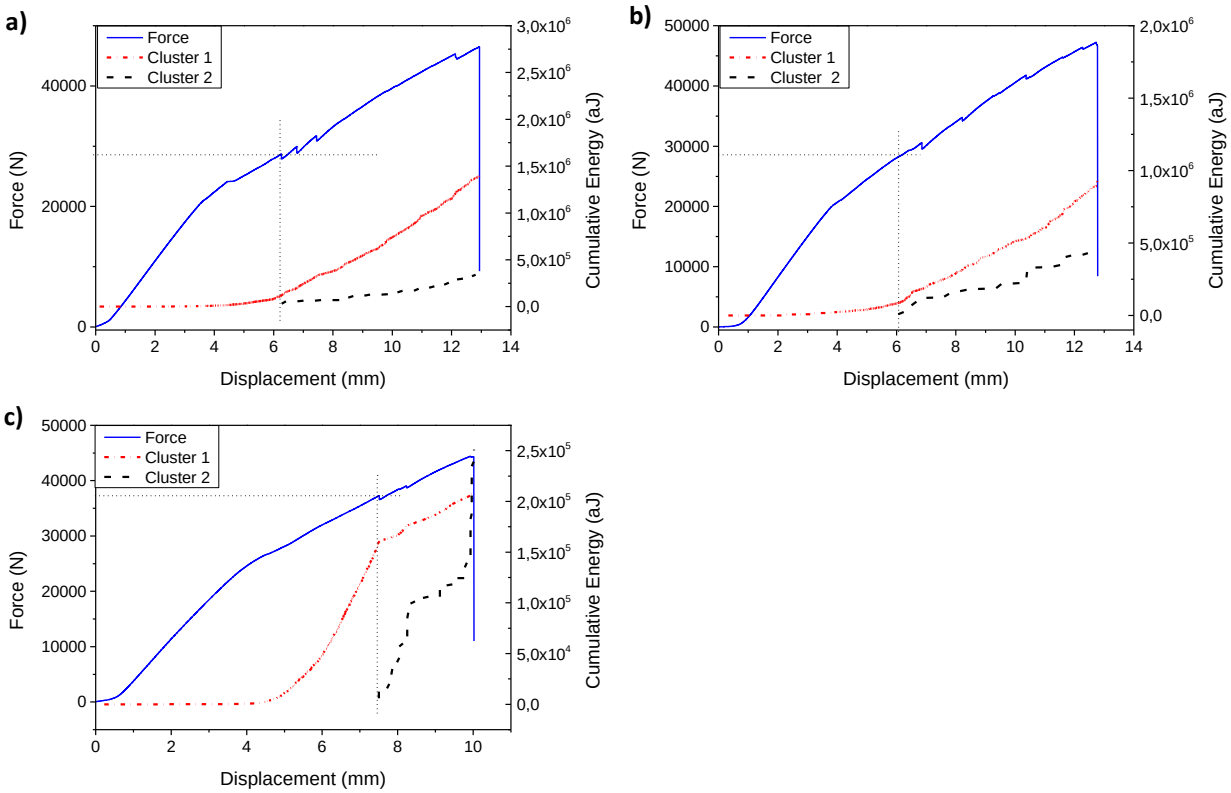


**Figure 4.60 - Typical force-displacement curves and cumulative energy-displacement by clustered signals for a) REF and, b) TUF1, c) TUF2 structures.**

## 4.3 Conclusions

The results discussed in the present chapter validated the capability of tufting reinforcements to improve the fracture toughness of composites. This technique may be advantageous to reinforce joint structures, avoiding catastrophic failure and therefore, enhancing the reliability of the structure. The development of the tufting process and the understanding of the mechanical behavior of tufted composites can improve the accuracy of the structures and consequently the safety factor or the maximum force of work (limit).

It was reported that the shape of the structure and the tufting parameters such as position, density, and depth, can alter significantly the mechanical response of the omega stiffeners, especially the maximum force under pull-off tests. This issue was resolved in two steps that consisted of the Batch II and III. Firstly, the stiffener radius was improved after an investigation from the Batch I, which presented significant stress concentration on the mentioned region for the tufted composites. This was responsible for premature failure on the radius and consequent reduction of the maximum force. However, due to insertion of tuft threads on the radius region,

Batch II continued to exhibit inferior maximum force than the control specimens. The investigations described that tufts concentrate stress along the threads and as a consequence, premature damages are generated from the reinforcements, diminishing the mechanical response of the structure. The region of first tuft row which is too close to the radius, only aggravated the crack initiation, due to the critical nature of curved areas. This behavior had been already reported in Chapter 3, for the specimens subjected to short beam shear tests. This emphasizes the concern to the optimal position of tufts insertion into the composites. Therefore, a new set of samples (Batch III) was manufactured by considering the information from the previous batches. The displacement of tuft rows from the radius, allowed to achieve maximum force superior to untufted specimens.

Additionally, tufting density was essential to improve the fracture toughness of the omega structures for the Batch III. A finite element model capable of evaluating the mechanical behavior of tufts into composite structures could avoid time and material consumption to achieve optimal results. Moreover, it could allow assessing several tufting parameters to optimize the most important properties.

The investigation regarding the tufting depth did not evidence any improvements when comparing the results for the specimens reinforced with partial and complete insertion of the tuft threads. This study was especially precluded by the premature damage generated in the stiffener radius due to the strain concentration of tufts in that zone. Future analysis should be performed between the most efficient set of specimens from the batch III, that had a partial insertion of the tufts, and a novel configuration considering the same parameters of manufacturing but with a complete insertion of the tufts.

The 3-point bending tests carried out in this work meant to submit the structures to a more realistic loading during service. Thus, the specimens from the batch I obtained the best behavior under loading in comparison to the others batches. This is due to the short distance of support rollers that diminish flexural loading and consequently gave an advantage to interlaminar shear loading. The flexural loading was responsible to the skin rupture under tests, which precluded the analysis of tufts behavior in the structure. Tufted structure from batch I, exhibited considerable work done when compared to control structure, owed to crack bridging effect inspected from post-mortem micrographs. The same result was verified by analyzing the digital photographic images of the failed specimens from batch II. The damaged area was significantly

small for tufted structures when compared to the untufted structure. Moreover, the damage extent from the cross-section of the omega structures exhibited reduction from the control to the larger tufting density in batch III.

The scope for growth of the performance of the tufted structures is far from reaching its limits. Indeed, it is believed that is still possible to optimize the contribution of the tufts. By observing the main strain directions during the various tests performed, it is noticeable that the insertion angle of the tufts perpendicular to the surface of the specimens is not the most relevant solution. Thus, as investigated and reported by Bigaud [173], the inclination of the tufts can increase the performance of the tufted composites significantly depending on the loading condition. Here again, it is seen the importance and the need to have a numerical model capable of simulating the mechanical behavior of the tufting reinforcements into the composites and therefore, optimize the insertion angle. Future work should be conducted in this direction.

The studies presented in this chapter also highlighted the great importance of the health status of the tufts on the performance of tufted structures. Therefore, the ability to monitor this status and follow it according to the loading level becomes a major issue.

The multi-instrumented analysis aided to understand the damage mechanisms during tests. However, they present limitation to characterize possible damage of the tuft threads. While in-situ microscopy depends on good resolution and precision to achieve the tuft position into the composite, acoustic emission acquires acoustic signals from the material volume, which not allow finding with accuracy the damage location and its nature. A complementary approach to the mentioned techniques is presented in the next chapter.

# CHAPTER 5 INVESTIGATION OF THE STRUCTURAL HEALTH MONITORING BY THE TUFTED THREADS

## 5.1 Introduction

The works presented in this chapter take advantage of the superior electrical conductivity of carbon fibers inserted by tufting to monitor in real time the structures. This approach consists an extra advantage to the primary purpose of reinforcing through-thickness the composites, which consists of enhancing the out-of-plane properties of the laminated composites. Therefore, it seems to be useful to obtain the variation of the electrical resistance by the tufted yarns as a strain-sensing method and damage indicator in the composite under loading. A system, which continuously monitors the composites for damages and failures, is called Structural Health Monitoring (SHM) system [236]. The SHM is liable to detect, evaluate and interpret the damages in the structure in order to improve the reliability and safety, increases the life and reduces life-cycle cost [237].

Sensors can be attached or embedded into the composite materials to monitor their hidden internal conditions and determine the real-time state of the structure. Strain gages, accelerometers, and displacement sensors have been used to monitor the composite structures. These sensors are joined to the structure's surface and consequently are affected by the adverse weather conditions [238] and also negatively by electromagnetic interference [239]. As a result of their large size, the insertion of these sensors into the composite structure becomes impracticable. Furthermore, damages as microcracks, delamination, and peel-off could not be accurately detected by the surface sensors in composite laminates [240].

Almost all achievements in the SHM field are only intended to make materials/structures sensitive by embedding sensors [241]. Different types of embedded sensors have been investigated for SHM applications, including, fiber optic sensors (FOS) [242] and piezoelectric (PZT) [243]–[245] sensors. In general, they have many advantages over the surface sensors, as higher sensitivity, the excellent capability to withstand harsh environments and more extended durability. However, these sensors are criticized because of the degradation in the mechanical properties of the host structure since they create a potential site of damage initiation.

FOS are very fragile to manipulate, which can fail during installation or even in operation, besides being easily broken [246]. Although FOS is insensitive to electromagnetic interference, PZT sensors suffer from low signal-to-noise ratios due to this interference. Also, they require high computational demand, indirect damage detection, limited interrogation distance, and rely on complex algorithms or predefined damage metrics [247]. Shape memory alloy (SMA) wire embedded into the polymer-based composites has also been applied to form a smart structure and among the many possibilities, they can be used as strain-sensing and damage detection element to monitor structural health conditions in the composites [248]. However, their weak interfacial bonding strength between the wire and its surrounding matrix limits the applications in many engineering industries [249].

The piezoresistive method has been increasingly studied as an alternative to avoid inserting sensors into the composites as well as due to its effectiveness and simplicity. Carbon fiber composites can be used as a strain sensor due to the piezoresistive nature of these fibers, which can consequently respond to strain rate [250]. Schulte and Baron [251] had firstly investigated the correlation between the internal damages and the electrical response of the carbon fiber-reinforced composites (CFRP) laminates under mechanical loading. The results prove the piezoresistive method is capable of detecting damage events. From that point, several authors have been studying this approach as a damage detection method. Ceysson et al. [252] examined the piezoresistive effect from CFRP laminates subjected to post-buckling, and three-point bending tests. The electrical measurements were capable of distinguishing significant events based on the fibers rupture that detains current flow and thus, increases the electrical resistance. This behavior was in good agreement with the increase in acoustic emission activity. Abryab et al. [253] investigated the correlation between the fiber volume fraction in CFRP laminates and their electrical resistance response. It reported the electrical resistance inversely proportional to the fiber volume fraction, with all set of specimens capable of identifying damage events.

Moreover, the electrical resistance measurements under post-buckling test (monotonic test) were able to identify the different events, as the fiber elongation and fiber breaks during the loading period, followed by the fiber contraction and the contact between broken fibers in the unloading period. Ogi and Takao [254] also studied the effect of fiber direction on the measurements of the electric resistance. The specimens investigated were 0°, 10°, 45° and 90° to the axis of the sensors. The results obtained for 0° and 90° specimens exhibited a quasi-linear behavior while 10° and 45° non-linear comportment after some point of the loading. From those

results, they create a model capable of predicting the electric resistance change as strain function to 0° and 90° specimens. The predicted gage factor for off-axis specimens was also in good agreement with the experimental results.

Ladani et al. [255] investigated the piezoresistivity in CFRP composites joints adhesively-bonded by carbon nanofibers (CNFs) to inspect damages under fatigue tests. The authors demonstrated that CNFs create a conductive network which allows detecting the debonding during tests using electric resistance measurements. A model was established to describe the relationship between the crack size and the electrical resistance of the bonded substrates.

Similarly, some authors have examined the addition of nanofillers such as carbon nanotubes (CNTs) [256]–[259], graphene [260] and carbon black (CB) [261] to increase the matrix conductivity of the FRPs and consequently their electrical resistance response under loading. Nanofillers also lead some increase in the mechanical properties of the laminate composites as interlaminar fracture toughness [255]. Although multifunctional sensing performance of the composites reinforced by nanofiller is evident, the fabrication technique provides little control over nanomaterial assembly and bulk film properties [247]. Some issues as the dispersion of nanofillers into the matrix and the significant increase of the matrix viscosity is reported in the literature [39]. Additionally, bulk film matrix reinforced by nanofillers may cause a significant weight penalty and potentially decrease of glass transition (Tg) [42]. Besides, the films have lower strength and stiffness when compared with the composite laminates and therefore have to be limited in order not to decrease the mechanical properties of the composite [49].

Studies regarding real-time monitoring of laminated composites reinforced by stitching techniques, such as tufting, are not found in the open literature. The investigations presented in this chapter consist firstly in evaluating the feasibility of the approach to detect damages created at multiple impact tests for glass and carbon fabric composites. It aided to select the materials that respond electrically better to damage evolution. Subsequently, the study of strain-sensing as well damage development by electrical resistance are performed in a foam core sandwich, and omega stiffened composite both reinforced by tufting.

## 5.2 Test methods and Results

### 5.2.1 Laminated composite plates (Plate II)

The present section concerns the results for tufted composite plates submitted to impact loading tests. This investigation aided in the study of the feasibility and sensibility to detect damages in the threads by changing on electrical resistance, which also may help in the monitoring of the composite health. More details about the materials and manufacturing process utilized for the specimens are presented in section 2.2.3.

**a)** ***Test methods***

The glass fiber and carbon fiber composites both reinforced with carbon and carbon/PBO threads, identified as GC, GZ, CC, and CZ respectively, were investigated by measurements of the electrical resistance. Table 5.1 summarizes the identification of the specimens.

**Table 5.1 - Specimens designation.**

| specimen | Fabric material | Tuft material |
|---|---|---|
| **CC** | Carbon fiber | Carbon |
| **CZ** | Carbon fiber | Carbon/PBO |
| **GC** | Glass fiber | Carbon |
| **GZ** | Glass fiber | Carbon/PBO |

The specimens were on the standard dimensions for the impact tests (100 mm x 150 mm) with the tuft rows along the longitudinal direction. The same laminated composite was submitted to various impact loading: two times with a 5 J energy and, two of 10 J. The approach meant creating progressive damage in the composite and monitor its health by measures of electrical resistance after each step. Table 5.2 summarizes the steps designations concerning the impact events utilized in this method.

**Table 5.2 – Testing approach description consisting of various impact loading.**

| Step | Description |
|---|---|
| 0 | Before impact |
| I | After 5J |
| II | After 5J |
| III | After 10J |
| IV | After 10J |

The impact tests were performed by Instron Dynatup 9250HV drop-weight impact machine, using a hemispherical indentor of 50.8 mm diameter and weight impactor adjusted to 14.2 kg. The measurements of the electrical resistance in the tuft rows (6 tufted lines in the middle of the specimens) occurred after each impact test by using 4-wire sensing to perform more accurate response. The extern points (pairs of current-carrying) injected a controlled direct current of 1 mA while the internal points (voltage-sensing electrodes) each one placed 10 mm from the external probes measured the electrical resistance.

Moreover, a specific analysis performed with a GZ specimen meant of evaluating the damaged area and heat dissipation after the impact loadings applying the same impact energies of 5 J,5 J,10 J, and 10 J successively. The measurements of electrical resistance after each impact tests were also carried out for this analysis. The infrared camera investigated the heat dissipation during the current injection of 400 mA between the 6 tuft rows in the middle of the specimen. The damaged area was characterized by C-Scan technique, scanning a zone of 50x60 mm (width x length) centralized in the impact point. Figure 5.1 shows the steps utilized for this approach.

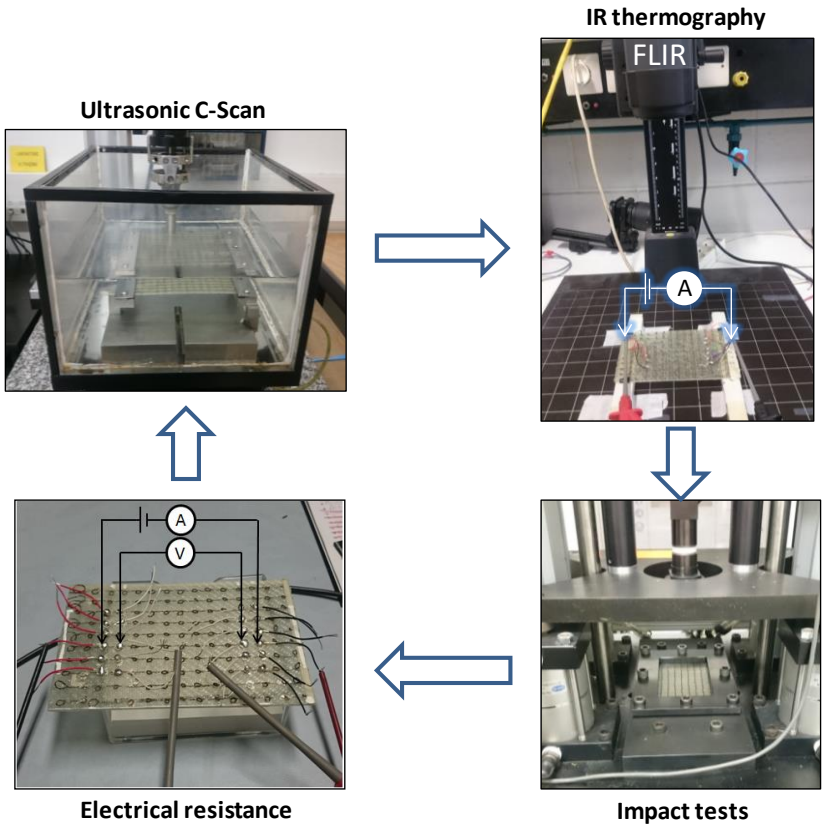


**Figure 5.1 - Experimental procedure employed in the investigation of the electrical resistance response after each impact loading.**

**b) *Results***

Figure 5.2 exhibits the typical progress of the electrical resistance for the tuft rows (1-6), measured after every impact test. It presents the rate of resistance variation (the ratio of the difference between the instantaneous resistance ($R$) value and initial resistance ($R_0$) to $R_0$) in function of the step (impact event). The resistance measurements of carbon fabric composites reinforced by carbon and carbon/PBO threads are presented in Figure 5.2a and b respectively. Both specimens exhibit instability in the values of resistance especially because carbon fibers threads reinforce the carbon fabrics. It generates leakage current from the injected points (tufts) to the fabrics due to their same electrical conductivity, which prevents the analysis of damage events by electrical measurements. Otherwise, due to the insulating properties of glass fibers, the electrical resistance response is more stable and efficient to the damages created at every test in both specimens set, GZ and GC, presented in Figure 5.2c and d respectively. Glass fabrics create a insulate media, which aids the injected current flowing primarily through the tufts. The impact loadings generate progressive damage on the composite and consequently to the tuft threads. It increases resistance to the current flow and therefore, raises the electrical resistance response. The resistance values for the glass fabrics specimens amplify significantly on the rows located from the middle of the samples, rows 3-4 and rows 2-3 for GZ and GC respectively because they are nearer from the impacted zone. It results in significant damages in that region. In general, the mentioned rows were able to respond gradually to the multiple impacts with continuing increase on electrical resistance. Furthermore, the other rows also responded to damages in the same manner, even if their response is weaker in comparison to the tufts mentioned above.

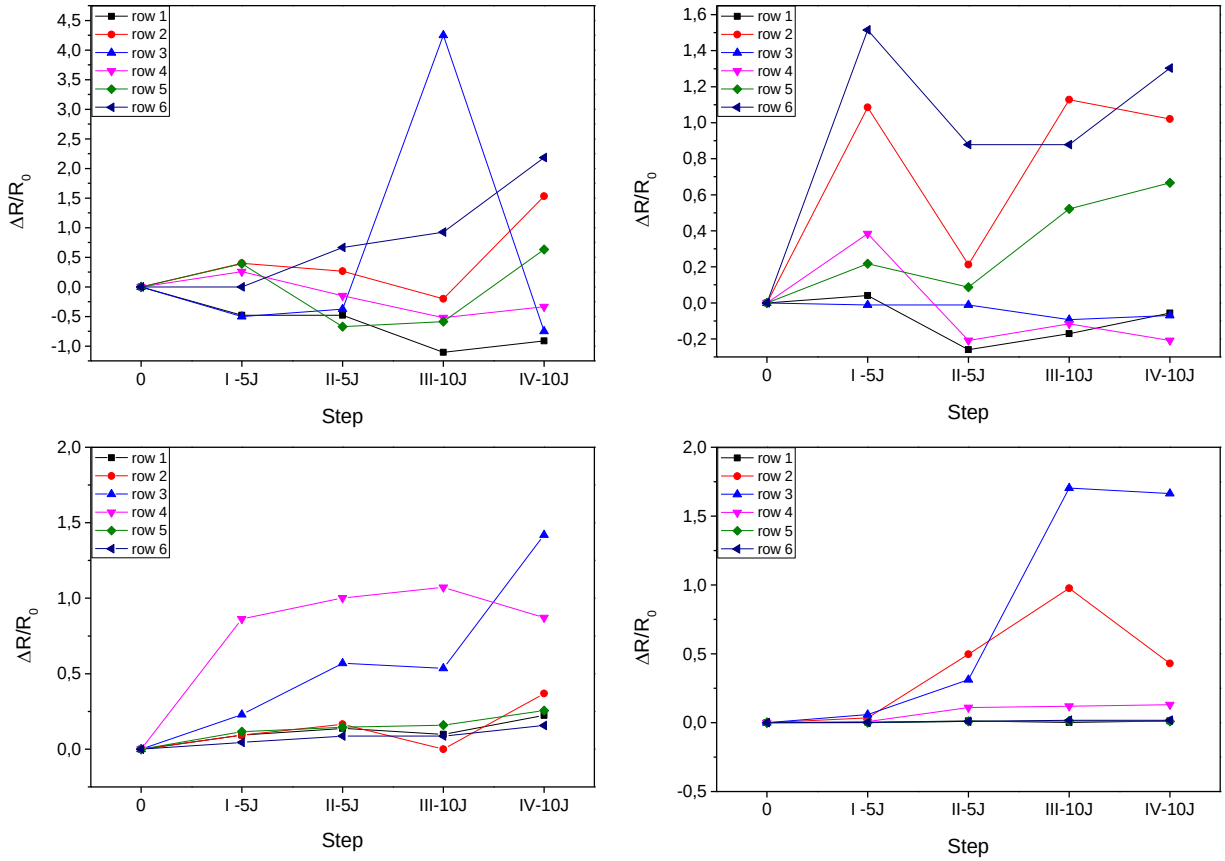


**Figure 5.2 - Electrical resistance measurements through different tuft rows after every impact testing of, a) CC, b) CZ, c) GZ and, d) GC specimens.**

Figure 5.3 presents the characterizations performed before and after impact tests by C-Scan and infrared thermography (IRT) for the GZ specimen. Photographic images were also taken after every step to evaluate by the naked eye the detrimental effects. The first step is not visually characterized by IRT and C-Scan but is observable in the photographic image from a fissure located under the row 4 that results in a significant increase on electrical resistance as seen in Figure 5.2c. IRT characterizes step II as a slight increase of temperature gradient in row 4. The heat concentration is a consequence of the damages or even a shrinkage of the threads generated during impact. They difficult the current flow and therefore, increase temperature gradient by Joule effect in the region. The photographic image presents a visible fissure in the same zone (highlighted in the image) what validates this event. The damage appears behind the tuft threads that connect one inserted point to the next, which may preclude the ultrasonic C-Scan analysis of this occurrence. The rise in the amplitude of C-Scan images is considerable from the step III to IV and consists of significant damages created in the plate by impact loadings. Additionally, the heat spots (rows 3 and 4) in IRT images also reports these mentioned events. The photographs acquired for the steps III and IV validate the characterization performed by both techniques, with a considerable increase of the cracks through the tufting direction.

This approach enables monitoring the health of tufts. Once that tufted threads are essential to the out-of-plane properties of laminated composites, monitoring their health may also be essential for analyzing the structural condition of the tufted composites. The electrical method as employed in this investigation can also validate the manufacturing process by evaluating the electrical resistance of the tufts. A tuft that presents a significant deviation from the mean value of resistance may have had issues during the tufting process such as incomplete insertion of the tuft, unloosening, or considerable damage on the thread.

According to the results obtained in this investigation, different thread materials with a superior conductivity than carbon fibers must be employed to reinforce carbon fabrics in order to carry out health monitoring from the threads. However, both threads (carbon and carbon/PBO) utilized to reinforce the glass fabric samples presented stable response, increasing electrical resistance while growing the damage extent (related to the number of impact events). The following studies in the present work utilized only carbon/PBO threads for the analyses of strain sensing and health monitoring of the tufted structures. These strands present mechanical advantages against the neat carbon threads. Bigaud [173] reported that carbon yarns wrapped with PBO yarns are better to protect the thread health during the tufting process, from the reel until the thread deposition into the preform. This behavior leads the carbon/PBO threads to have better mechanical properties when compared to the neat carbon yarns, which may impact the composite properties.

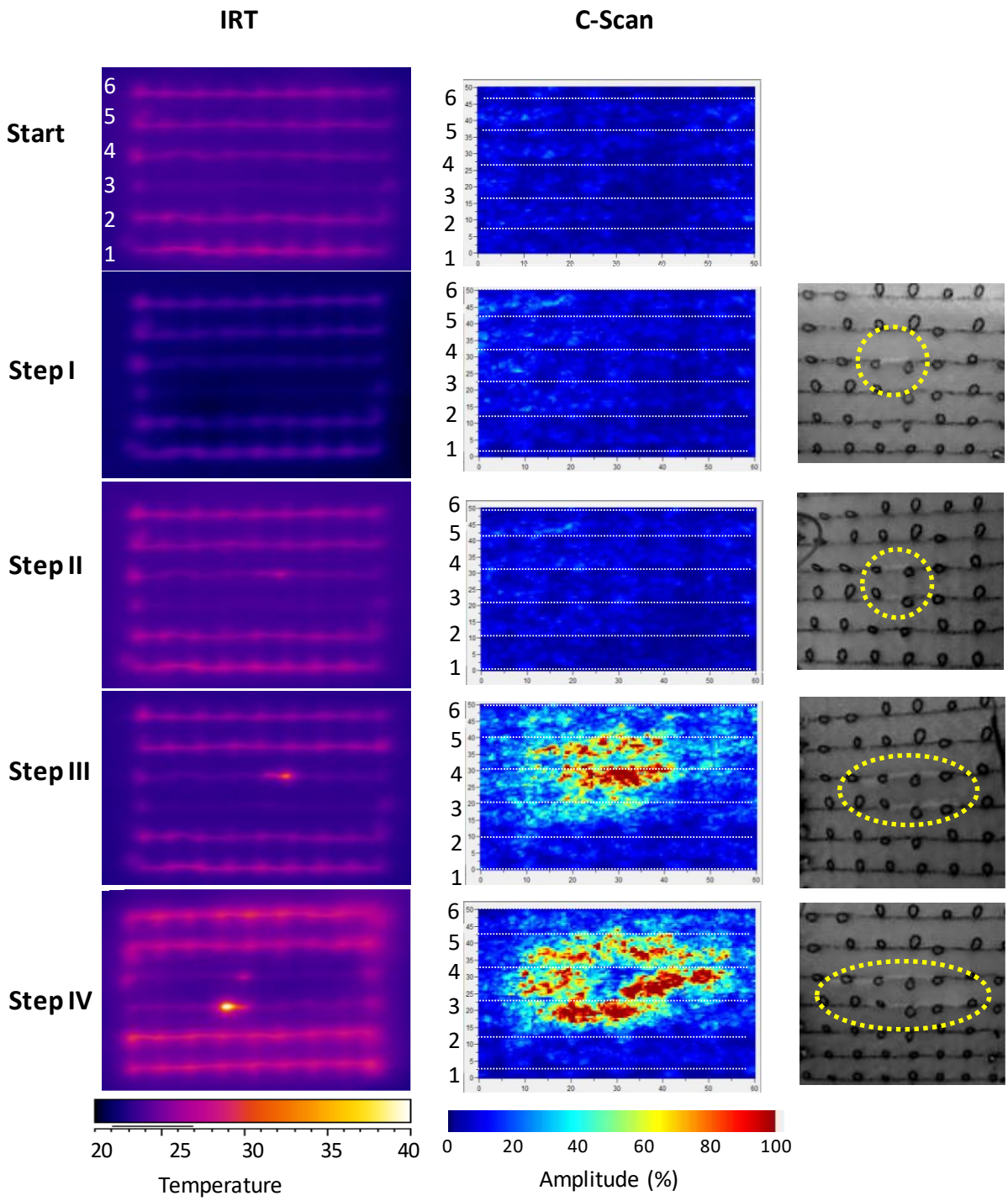


**Figure 5.3 - IRT, C-Scan and photographic images performed after every impact test for the GZ specimen.**

### 5.2.2 Tufted sandwich panels

This section investigates the piezoresistive effect of the foam core sandwich panels reinforced by tufting. Section 2.2.4 in this thesis describes the materials and manufacturing process utilized

to obtain the specimens. The mechanical tests performed in this section utilized three specimens for the evaluation under each loading condition.

**a)** ***Test methods***

**Flatwise compression test**

Compression tests were carried out for investigation of electrical resistance response of the tufted sandwich composites under progressive static loading. Firstly, three specimens were submitted to multi-step compression tests, incrementing each step by 500 N and maintaining constant 2 minutes until the next increment. This procedure allows understanding the electrical response while loading the specimens as well as the stability of the measurements while maintaining the load. Furthermore, compressive cyclic tests subjected three samples to an incremental loading of 500 N and subsequent unloading at every step. The load was maintained for 1 minute in both loading/unloading phases to comprehend the electrical behavior of the specimens better.

The specimens of 50x50 mm (width and length) were according to the specifications provided in ASTM C365-0 [262]. The tests were carried out with a crosshead speed of 1 mm/min and elongation measured by LVDT. The two-wire method was employed to measure the electrical resistance throughout tests from a single tufted range row (Figure 5.4a). The flatwise compression test apparatus utilized is exhibited in Figure 5.4b.

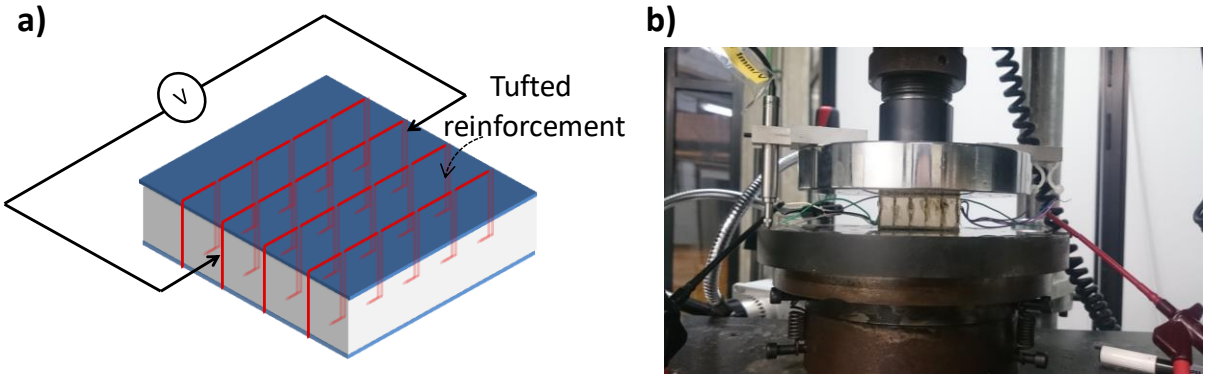


**Figure 5.4 - a) Scheme of the two-wire electrical measurement from the tufted yarn, b) Flatwise compressive test apparatus.**

**Impact test**

The specimens subjected to impact loading meant to create progressive damage. Therefore, four specimens were submitted to 5J and subsequently 10J impact energy by Instron Dynatup 9250HV drop-weight impact machine. It was applied a hemispherical indentor with a diameter of 50.8 mm and weight impactor adjusted to 14.2 kg. Additionally, the specimens of 100x150 mm were prepared according to ASTM D7136-15 standard [195].

Figure 5.5a schematizes the test set up from the longitudinal cross-sectional view. The out-of-plane displacement was acquired from the bottom side of the sample (opposite to the impacted surface) using a laser sensor placed in the middle of the sandwich plate. Moreover, two-wire approach monitored the electrical resistance from a single range localized in the center of the plate width during the impact loading and had its connection between the electrical probes and tufted yarn made by soldering electrical wires in the tuft extremities (60 mm distant from each connection point in the longitudinal axis). Figure 5.5b shows the sandwich composite restrained in the machine support ready for the impact testing.

Ultrasonic C-Scan evaluated the damage evolution at each stage of the sandwich plates (before impact tests and after every impact loading). The procedure utilized the images built with eco rebound from the back surface to characterize the damaged zone. The size of the scanned area was 50x60 mm (width x length) and had been positioned symmetrically from the impacted point.

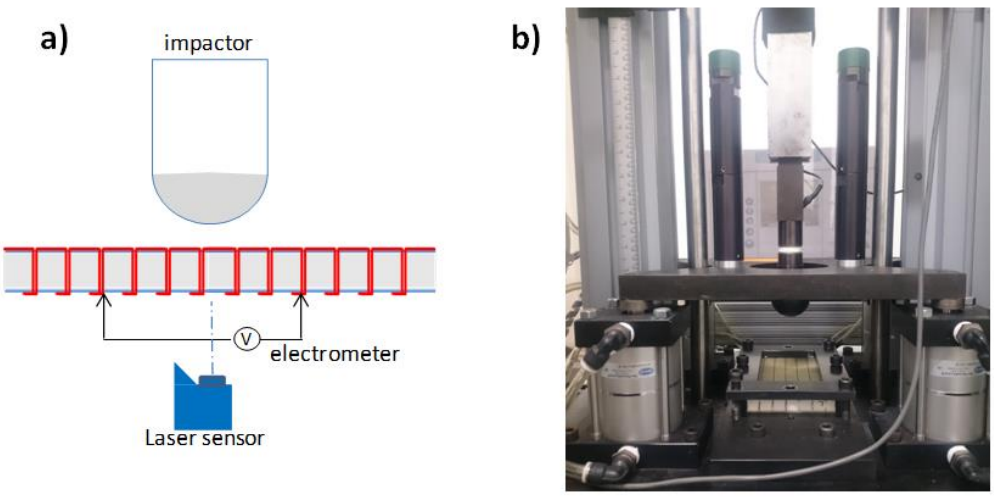


**Figure 5.5 - a) Schematic illustration of the electrical and out-of-plane displacement measurements during impact tests, b) Impact test apparatus.**

The infrared camera (IR) was applied based on the Joule heating effect when electrical current is imposed through the tufts to investigate the damage evolution in the sandwich specimens after submitted to impact tests. Electrical current (400 mA) was injected by an electrometer in the four central tuft ranges and had the heating response measured during 25 seconds by FLIR camera at 340 mm from the surface of the sandwich plate as shown in Figure 5.6. In order to compare the thermal response of the specimens at every event (before impact, after 5 and 10J impact energies), the images analyzed were taken at 25s after the injection of electrical current for stabilizing the system.

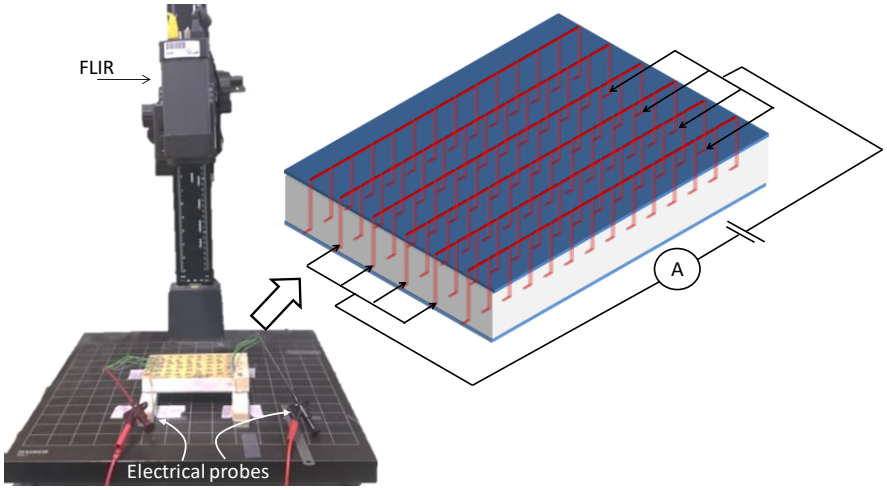


**Figure 5.6- Infrared thermography when imposing an electrical current in the tufted yarns.**

**b) *Results***

**Flatwise compression test**

Figure 5.7 presents a typical response of the electrical resistance measured from a central tuft row under the multi-step compression test. It shows the stress-time evolution and the rate of resistance variation. Electrical resistance presents a slight decrease during initial steps (I-III) due to the reduction in the tuft length from the early state ($L'$) to the subsequent step ($L''$) as shown in Figure 5.8. The equation (7) explains this behavior that considers the length directly proportional to the electrical resistance ($R$).

$$R = \rho \frac{\mathrm{L}}{A} \tag{7}$$

Where L is the length of the conductor (m), A is the cross-sectional area of the conductor ($m^2$), and ρ is the electrical resistivity of the material (Ω.m). As expected, $R$ maintains stable during

load plateau once there is no load variation. From the step IV, the decrease of electrical resistance during the loading ramp disappeared. Instead, *R* starts to raise through load ramp owing to the damages especially generated in the tuft. This behavior counteracts the phenomena already explained which reduces the electrical resistance by shrinking the tufts longitudinally. A remarkable increase of the *R* is achieved mainly by the fibers rupture in the tufting thread until its complete failure, characterized as the sharp rise in the final step. These damages obstruct the current flow and therefore raise the electrical resistance. The others tuft rows measured at every loading plateau also evidenced the rising of electrical resistance as shown in Figure 5.9. The values of resistance become more significant in step V, as already reported to the continuous measurement of the tuft row 3, and they are related to the significant damages when the load is amplified.

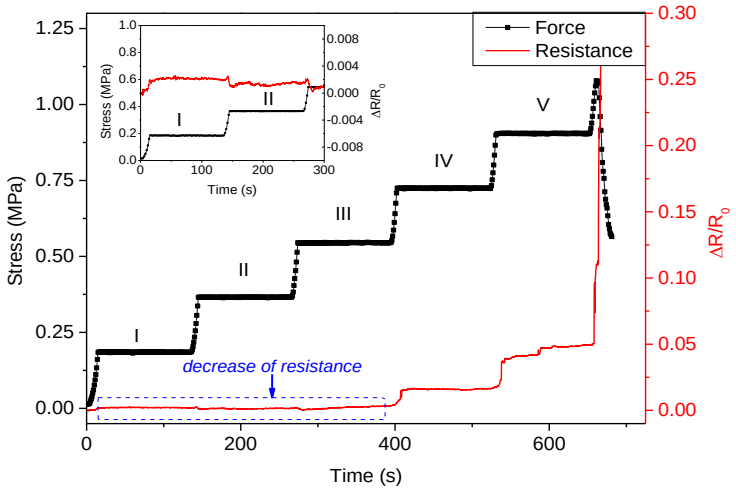


**Figure 5.7 - Typical electrical resistance response to multi-step compressive test (the top of the curve highlights the slight drop of resistance).**

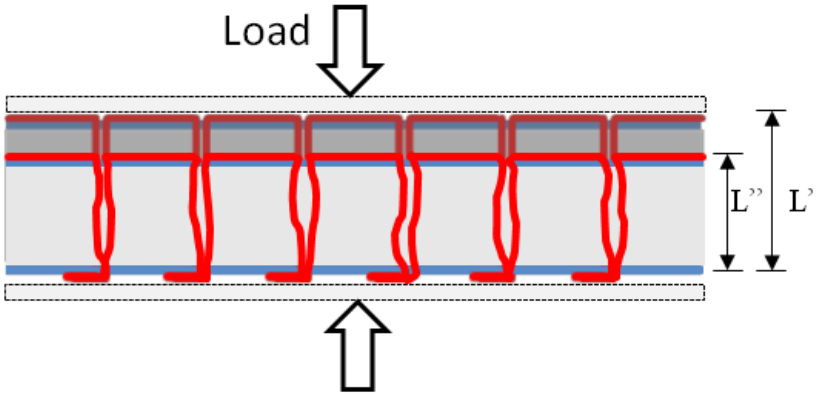


**Figure 5.8 - Schematization of the thread length response to the compressive loading.**

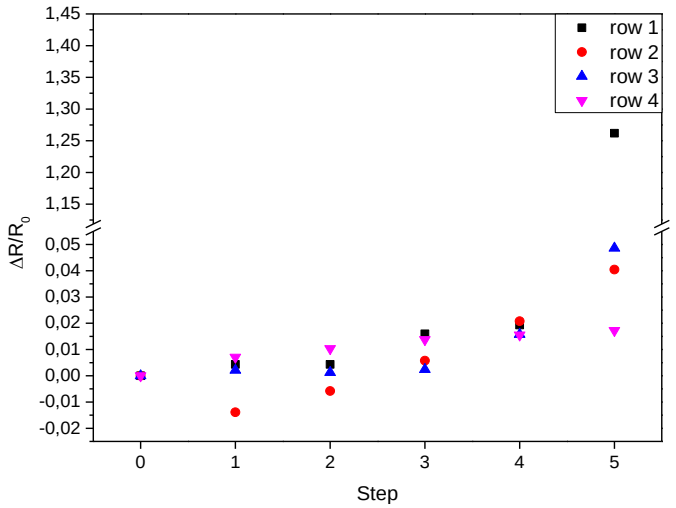


**Figure 5.9 - Electrical resistance response measured in the tuft rows during the loading plateaus (steps) on the multi-step compressive test.**

Figure 5.10 shows the typical response during cyclic compressive loading. Significant damage can be distinguished from the curve at about 0.83 MPa where occurs a slight drop in stress. Moreover, a great residual strain after the unloading in the last cycle is capable of characterizing the mentioned stress as crucial to the structural health.

Figure 5.11 exhibits the typical behavior of the electrical resistance acquired during the cyclic loading tests. From the cycle III, *R* exhibits a significant response followed by the increase and decrease during the loading and unloading ramp respectively. The electrical measurements were also capable of obtaining the response of the yield stress occurred on each begin of the plateau. Furthermore, *R* starts increasing at the unload level from cycle III and evolutes until the last cycle (V) due to the growth in the loading which consequently leads to significant damages. The considerably increasing of electrical resistance seen in cycle V, from the loading ramp to the plateau at the end of the test, is likely due to the significant damages at about 0.83MPa, as already discussed for Figure 5.10.

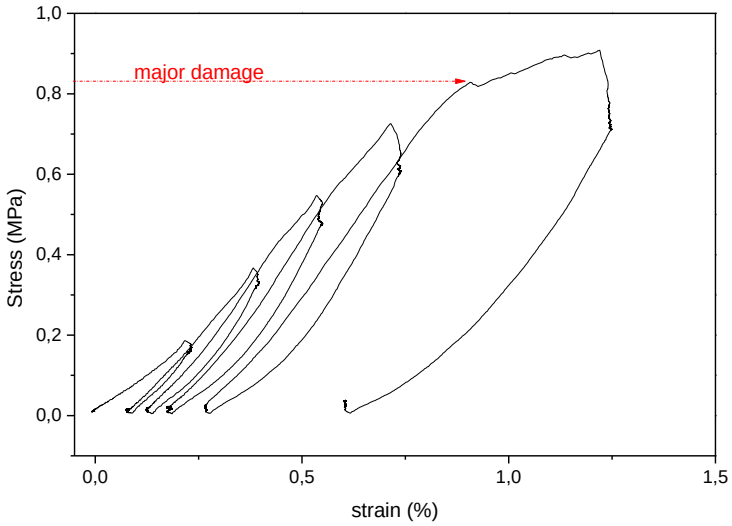


**Figure 5.10 - The typical behavior of a tufted sandwich sample under cyclic compressive loading.**

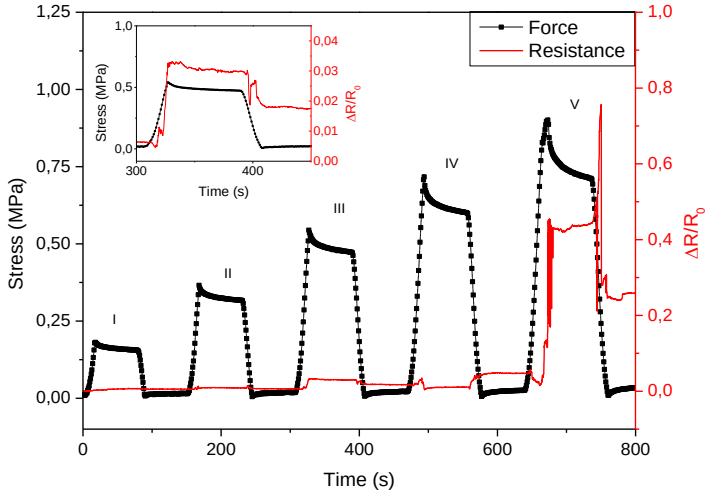


**Figure 5.11 - Typical electrical resistance behavior under cyclic compressive test.**

## Impact tests

Figure 5.12 and Figure 5.13 present typical behavior for the specimens subjected to impact energies of 5J and 10J respectively. In both experiments, the electrical measurement was able to respond to impact loadings. Figure 5.14 schematizes possible events which occurred during the impact tests that induced the variation of the electrical resistance. In the beginning, a localized compression on the surface reduces the transversal section of tuft (highlighted in Figure 5.14 as the transversal view), leading to an increase of electrical resistance by piezoresistive effect, as seen in equation (7). This behavior is amplified owed to longitudinal compressive stress imposed on the top surface, that also compress the tufts and detain the

current flow. Moreover, damages generated in the specimens under impact tests, especially when emerged in the tufted threads, may increase the *R*. A significant electrical resistance is subsequently noticed when unloading the structure due to the association of damages and residual strain created during impact testing.

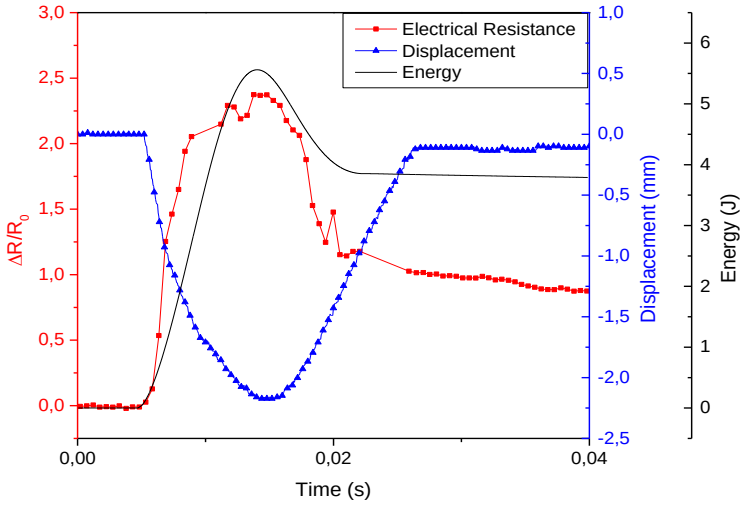


**Figure 5.12 - Typical response of the electrical resistance during the impact test of 5J energy.**

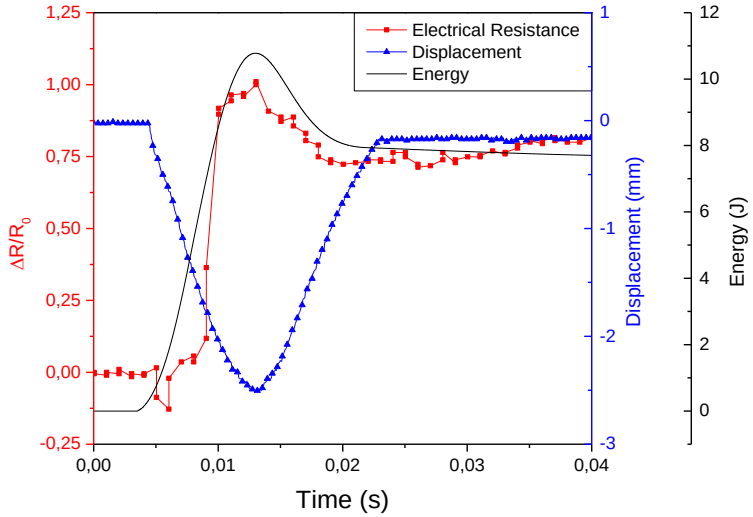


**Figure 5.13 - Typical response of the electrical resistance during the impact test of 10J energy.**

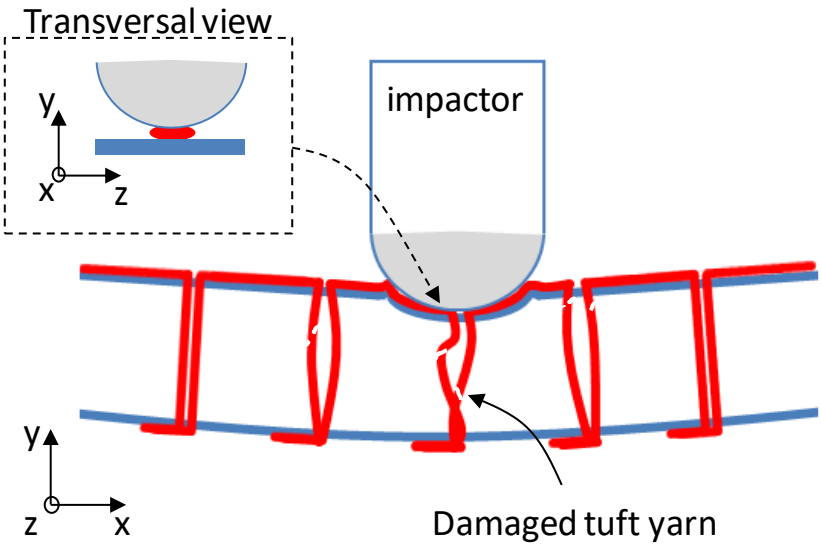


**Figure 5.14 - Schematization of the impact loading behavior in the tufted threads.**

Evaluation of the damage evolution by the infrared camera and ultrasonic C-scan technique is exhibited in Figure 5.15 as the typical response of the samples tested. Figure 5.15a presents the initial measurement performed before the impact test. It is noteworthy that by imposing the current flow, the temperature gradient is detected in the tufts due to the Joule effect. As expected, the ultrasonic image does not present visible damages or apparent defaults and shows a superior amplitude localized in the tufted region. Then, the specimen impacted at 5 J (Figure 5.15b) exhibits slight deterioration in the area displayed on the C-scan image, which is validated by the IR image due to temperature concentration (spots) as well as fading of the third tuft row located in the damaged region. A significant increase in electrical resistance, owed to the severe damage in the tuft, limits the Joule effect that is responsible for heating the conductor and consequently its measurement by IRT technique, which causes the suppression of the tufted line.

The same specimens were impacted at 10J and presented its post-impact analysis in Figure 5.15c. The temperature gradient is again amplified together with the spotting amount due to damage development and corroborates with the C-Scan image, presented as an accumulation of superior amplitude in the impacted region. Additionally, Figure 5.16 shows the measurements of electrical resistance acquired for each tuft rows (1-4) presented in Figure 5.15, before and post-impact tests. It validates the temperature rise from the IR images thanks to the increase of the Joule effect when increasing *R* after impact. Besides, high electrical resistance in row 3 compared to the other rows is responsible for the lack of temperature gradient in the same.

Figure 5.17 exhibits microscopy analysis of the specimen impacted at 10 J. A complete failure of the tuft threads is presented to the third row and confirms the sharp increase of the electrical resistance as already mentioned. Moreover, row 2 shows partial failure, which difficulties current flow but continues operational by remained undamaged fibers in the tuft and some possible contact between the broken surfaces of the fibers. The localized damage in the microscopy images corroborates with the large spots seen in the IRT maps (Figure 5.15b and Figure 5.15c).

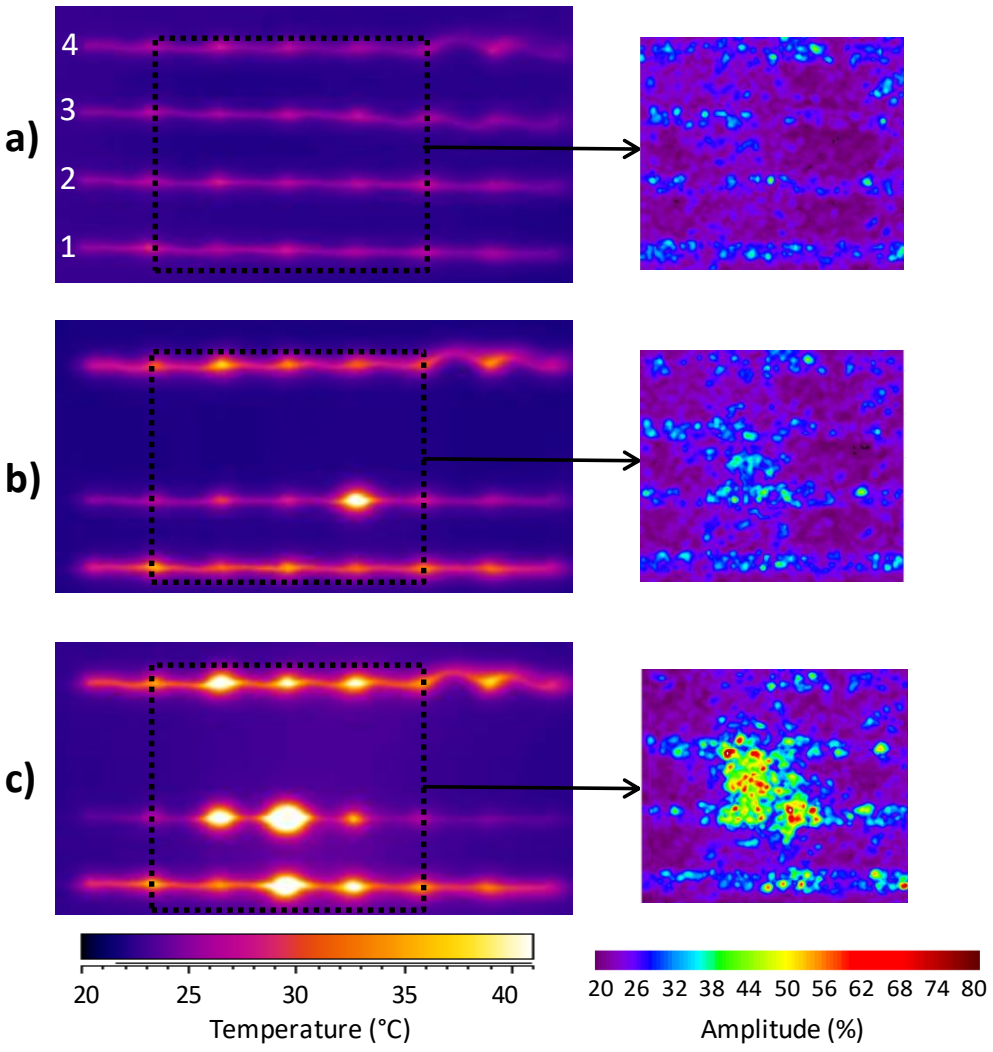


**Figure 5.15 - Infrared thermography (left) and ultrasonic C-Scan inspection (right) comparison for a) non-impacted, b) impacted at 5J and c) at 10J sample.**

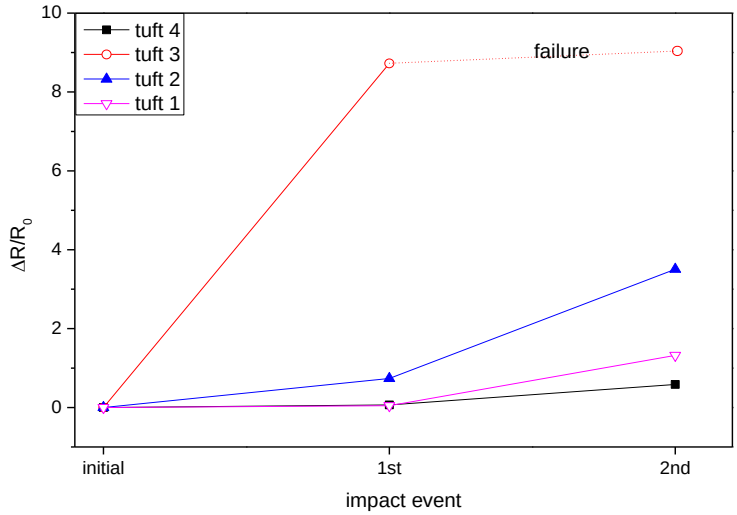


**Figure 5.16 - The typical behavior of the electrical resistance measured before and post-impact tests in the tuft rows (numbered according to Fig. 12a).**

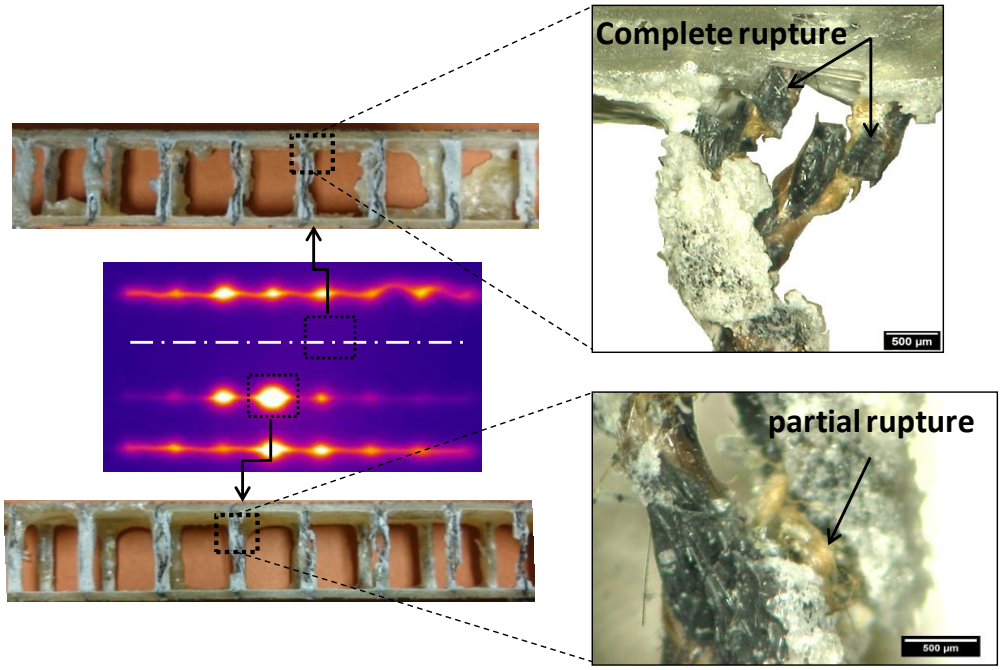


**Figure 5.17 - Microscrograph of a specimen subjected to 10J impact exhibiting damages in tuft rows in agreement with IRT.**

### 5.2.3 Omega stiffeners - GFRP composites (Batch II)

#### a) *Test methods*

The parameters employed in the pull-off and 3-point bending tests are described in section 2.3.10. Additionally, section 4.2.2 defines the detailed mechanical analysis utilized for

investigating the mechanical behavior of omega stiffeners. Table 4.3 shows the designations of the samples utilized in the present study.

**Table 5.3 – Specimens description**

| specimen | Description |
|---|---|
| **VR** | Control specimen |
| **V2T** | 2 rows in both structure sides with partial tuft insertion |
| **V3TC** | 3 rows in both structure sides with partial tuft insertion |
| **V3TL** | 3 rows in both structure sides with complete tuft insertion |

### Pull-off tests

The two-wire measurement was employed to acquire the electrical resistance from the intern tuft row on both sides of the omega structure by using digital electrometers. Figure 5.18 exhibits the test apparatus for investigating the omega stringers under pull-off tests and its schematic illustration (symmetrical to the longitudinal center of the sample).

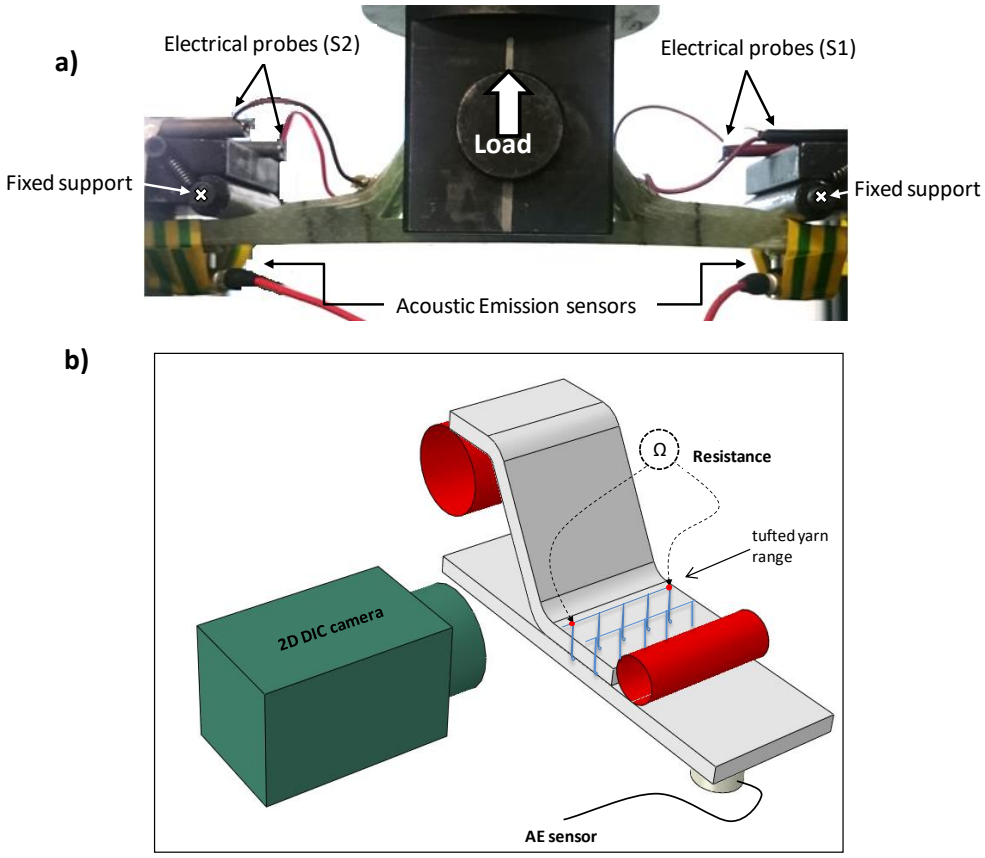


**Figure 5.18- a) Pull-off test setup showing the electrical probes and AE sensors, b) Schematic of the multi-instrumentation utilized to characterize the samples under tests.**

**3-Point bending tests**

The tests investigated the response of electrical resistance for the stiffeners from the Batch II. It was carried out by 4-wire measurements performed in a single tuft row from each side of the stringer. The tuft rows that monitored the electrical resistance in-situ consisted of the most interns, near to the stiffener radius. Figure 5.19 exhibits the schematic of the 4-wire method employed in the test as well as the selected rows.

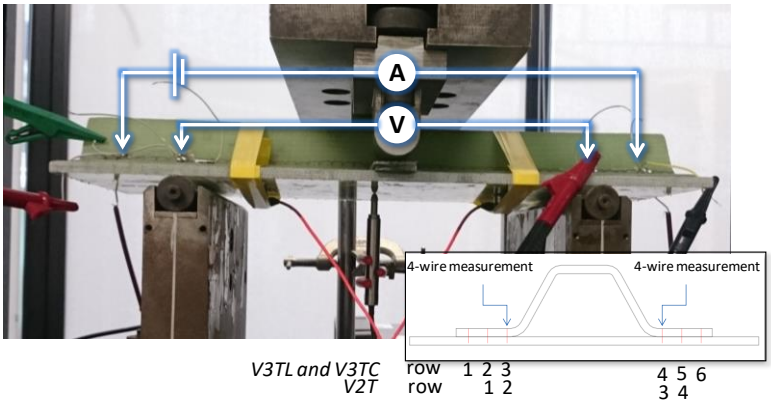


**Figure 5.19 - Test setup carried out for Batch II specimens with electrical measurements.**

**b)** ***Results***

**Pull-off tests**

Figure 5.20 presents the typical load-time response of omega stiffeners subjected to pull-off loading as well as the cumulative energy and the normalized resistance obtained by AE and electrical measurements respectively. Cumulative energy also evidences the load drop events exhibited in the load-time curve as an increase in its value. It is mainly owed to the damages generated in the composite under loading. The electrical resistance on both sides of the structure describes the mentioned behavior. The asymmetry noticed for the electrical resistance behavior is due to a considerable strain concentration in the beginning for the right side ($\varepsilon_{yy}$ = 13.9%) against 0.51% in the left, as shown in Figure 5.21.

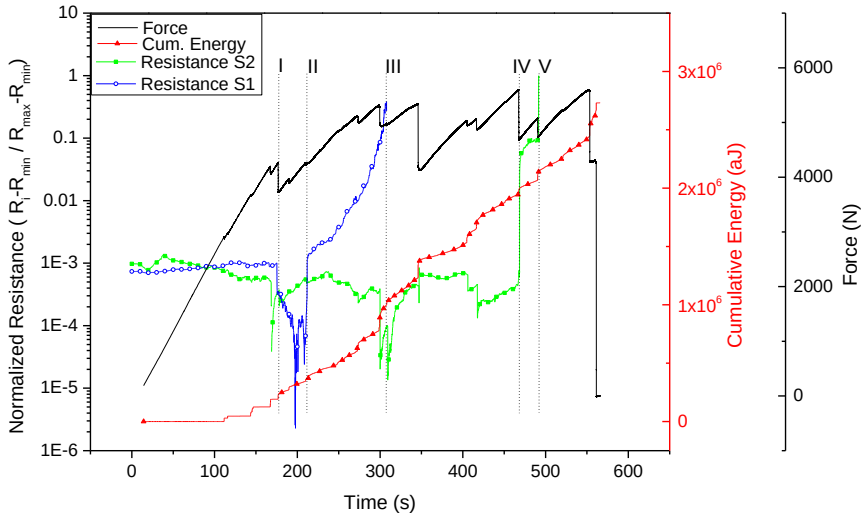


**Figure 5.20-Typical behavior of the load, electric resistance (S1, S2) and cumulative AE energy vs. time during a pull-off test.**

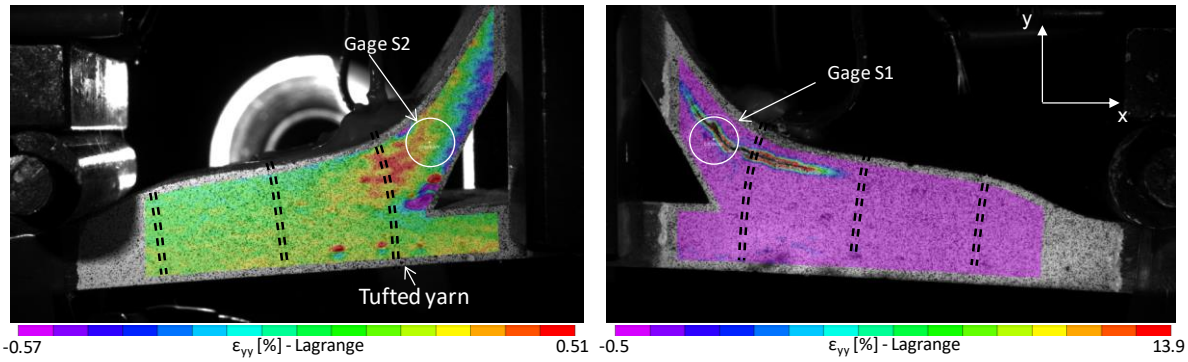


**Figure 5.21 - Longitudinal strain ($\varepsilon_{yy}$) field at the event I.**

The significant strain in the stiffener radius leads to delamination in the region (Figure 5.21). This event is highlighted in Figure 5.20 and designated as the event I. It is remarkable that the delamination evokes a sharp fall of the electrical resistance, which can be better verified to the measurements in the sensor S1, once that the failure occurs on the same side. This behavior is probably the combination of two simultaneous phenomena: the unloading post damage, seen as a sharp drop of the structure loading that also unloads the tuft threads and therefore leads their section area to enlarge, and to the delamination that debonds the resin from the yarns and consequently diminishes the electric resistance. Figure 5.22 schematizes these behaviors just before (Figure 5.22a) and after (Figure 5.22c) the event I. Figure 5.22a exemplifies the reduction in the section area ($A_1$) of the yarns, which also leads to an increase in length (L) when submitted to a longitudinal strain. It conducts to fibers straightening and consequently increases the electrical resistance (R) as described in equation (7).

Besides, the straightening can induce changes in the contact network by reducing the number of contacts between fibers as already reported by Schulte [251] and Angelidis et al. [263] and consequently, increases the electrical resistance as exemplified in Figure 5.22b. Otherwise, Figure 5.22c schematizes the tufted zone when delaminated, with a small region around tuft thread debonded from the resin (on dark) as well as an increase of tuft cross section due to the unloading of the composite structure.

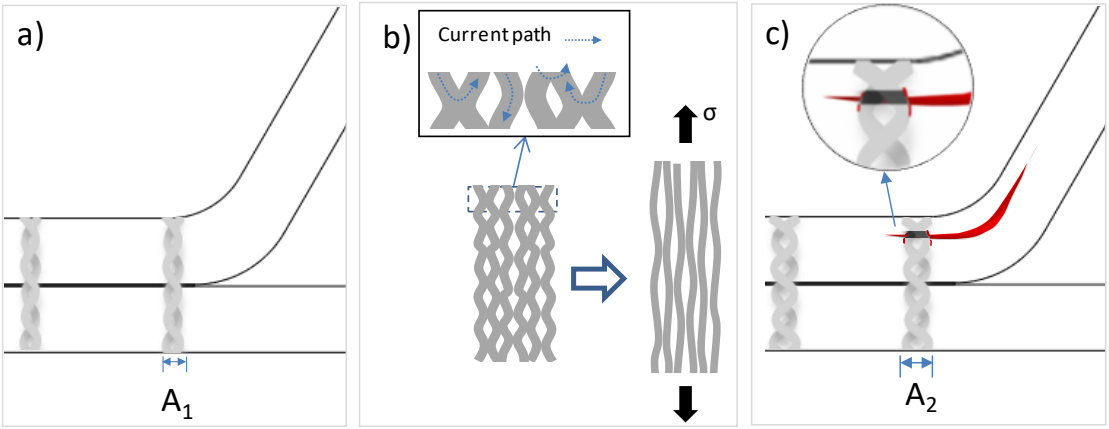


**Figure 5.22 - Schematic illustration of a tuft thread before the event I (during load phase), b) a detailed representation of a tuft yarn behavior under loading, c) delamination post event I (unloading phase).**

The delamination propagation is better shown in Figure 5.23, by a photographic image taken from the top of the structure (Figure 5.23a) and schematized in Figure 5.23b. The tuft reinforcements arrest the crack progression and lead to interlaminar crack branching as exemplified in Figure 5.22c by resin debonding. This behavior that maintains the laminate plies together, known as crack bridging, increases the fracture toughness significantly.

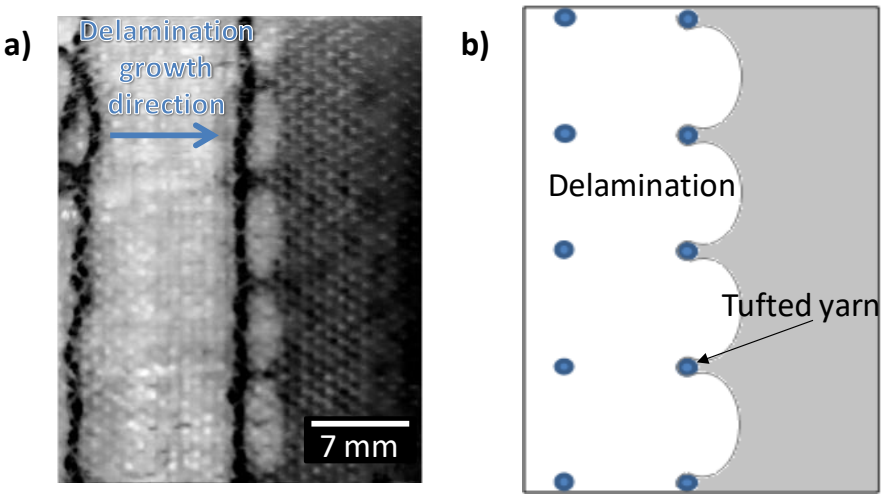


**Figure 5.23 -. a) Image from the top of the omega stringer on the flange region and b) a scheme showing the delamination (white zone) and the tufted yarns.**

Figure 5.24 describes the mentioned behavior from a virtual strain gage (see Figure 5.21) acquired by DIC strain-fields positioned on the radius fillet of the structure (gage S2 to the left and gage S1 to the right). The results obtained to the virtual gages in the y-direction, $\varepsilon_{yy}$ strain, reveal higher strain concentration on the S1 region. Furthermore, it is evident that the electrical resistance measured from the left side, where the strain acquired by the virtual strain gage is negligible until the event IV, is capable of determining the damage events that occur on the right side (gage S1). It is mainly due to the unloading of the structure during the main damages that are not evidenced by the gage S2.

However, the result obtained from the gage S1 that exhibits a growth of the localized mean strain during the delamination (event I) is not in agreement with the piezoresistive effect. The reduction in electrical resistance must be related to a decrease in the local strain $\varepsilon_{yy}$ during delamination, due to a decrease of the tuft length. Therefore, a new strain analysis was performed on a different region to avoid the crack edges that concentrates the strain significantly what could put out of sight the global response.

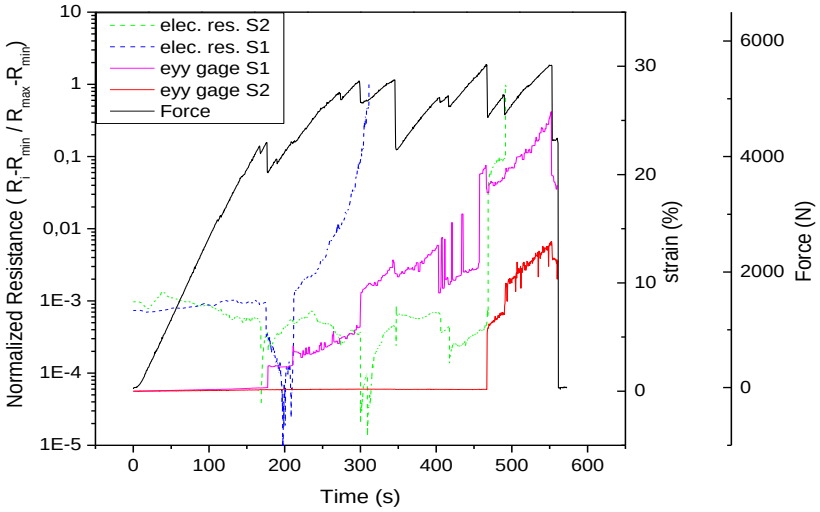


**Figure 5.24 -The typical behavior of the $\varepsilon_{yy}$ strain obtained by virtual strain gages from DIC method and their electric resistance measurements vs. time under pull-off test.**

Figure 5.25 shows the virtual extensometer utilized to acquire the longitudinal strain ($\varepsilon_{yy}$), positioned according to the first tufting range location. The result indicates a strain drop when a crack initiates due to the structure unloading. Despite the lower strain values when compared to the virtual gage on the radius S1, the result is enough to change the electrical response. It is probably due to the significant length of tuft comparing to the crack region, which has a significant influence on the electrical resistance as described in equation (7).

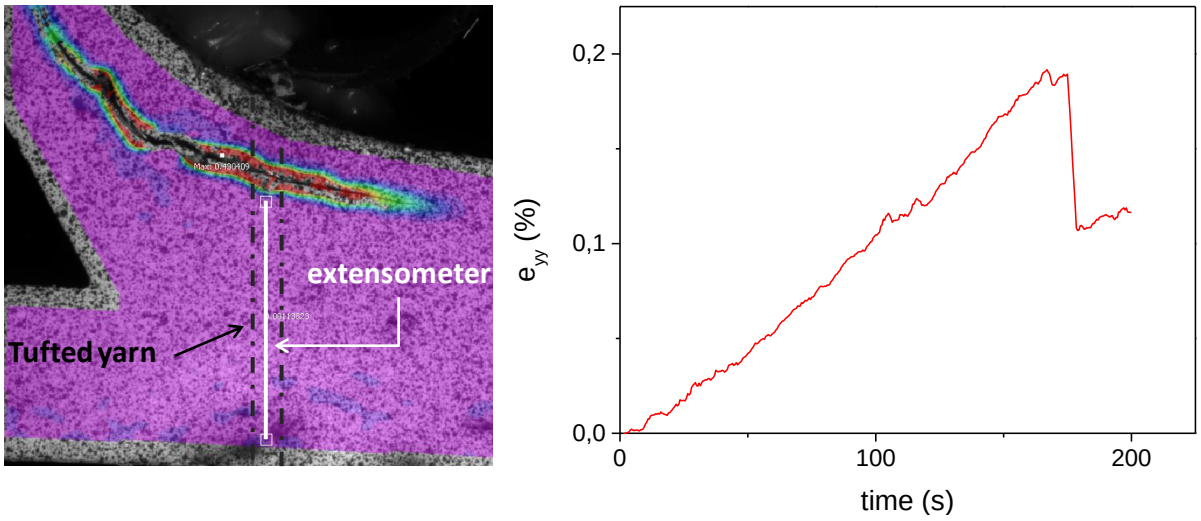


**Figure 5.25 - Virtual extensometer by DIC method employed on the tufted yarn range.**

Electrical responses between event I and II confirmed the behavior already explained in Figure 5.22 regarding the loading and electrical resistance. The delamination on the right side causes the unloading of the structure and consequently leads to a decrease of electrical resistance, while the left side (sensor 2) is slightly loaded and exhibits increase on its electrical resistance response. A progressive amplification of the strain on the side of sensor 1, subsequently to event II, leads to an increase of *R* until the tuft rupture, at this moment described as a significant augmentation of the electrical resistance (event III).

The events between III and IV characterized by the sensor S2 are mainly owing to the damages occurred on the right side (sensor 1) as previously described from the virtual gages results obtained by DIC. The delaminations shown in Figure 5.26 correspond to the images taken just before the sharp rise of electrical resistance concerning the event IV. The delamination generated on the side of the sensor 2 characterizes the event IV (Figure 5.27). It is remarkable a sharp increase in resistance and strain from the virtual gage S2. The strain raise after the delamination initiation acts differently from the expected, as already reported for the results from the gage S1. Therefore, a virtual extensometer was placed under the crack, similarly to that performed on the right side, to avoid the high strain of the crack edge. It was also distinguished a strain ($\varepsilon_{yy}$) increase which can be due to quickly sequence of the events, from delamination (event IV) to the tuft rupture (event V), and consequently did not let enough time to unload the structure.

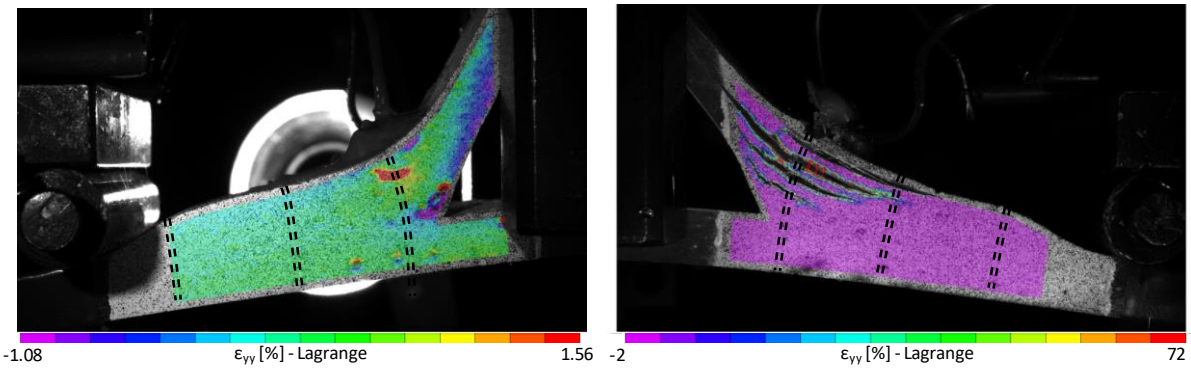


**Figure 5.26 - Longitudinal strain ($\varepsilon_{yy}$) field by DIC method obtained just before the event IV.**

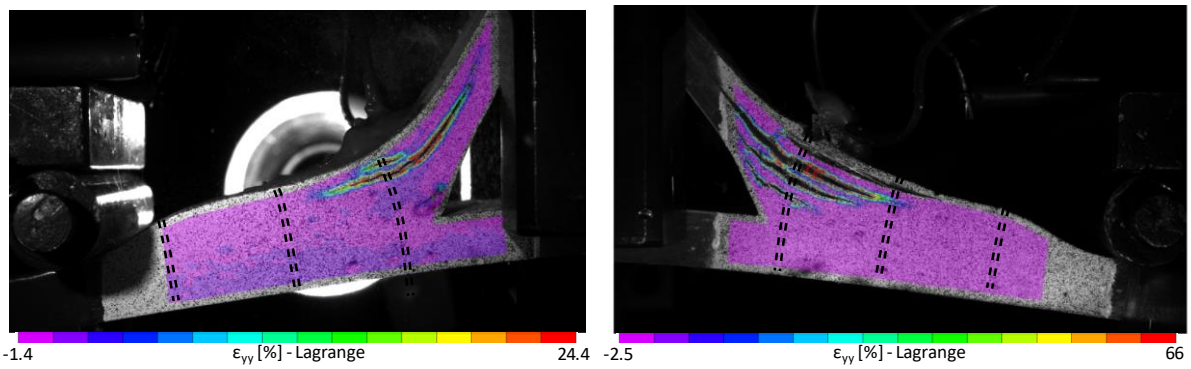


**Figure 5.27-Longitudinal strain ($\varepsilon_{yy}$) field by DIC method at the event IV.**

The clustering analysis presented corresponds to the investigation exhibited in section 4.2.2 for the batch II of specimens subjected to pull-off tests. The approach consisted of evaluating the number of clusters by the DB index method. Then, the number of AE descriptors found by PCA analysis and, the descriptors selected by single-linkage clustering. The analysis employed the amplitude, average frequency, RMS16 and absolute energy as AE descriptors. The non-supervised clustering used the k-means method, applying the Euclidian distance and random initial partitioning.

The analysis by DB index reported an increase in the number of classes of AE signals from two for the control specimens, to three for the tufted samples. This is mainly due to damages related to tuft threads. These results validate the findings obtained by the DIC and electric resistance analysis during the pull-off tests regarding the major damages in the tufts. The three clusters of acoustic signals corresponded to the matrix cracking, delamination and tuft yarns rupture (Cluster 1, 2 and 3 respectively). Figure 5.28 exhibits the typical radar graph of the AE clustered signals in function of their features for the specimen configuration V3TC. The typical curve energy-counts, shown in Figure 5.29, discriminate the clustered signals during pull-off tests and validate the significant distinction between the three classes of acoustic signals in function of the two features.

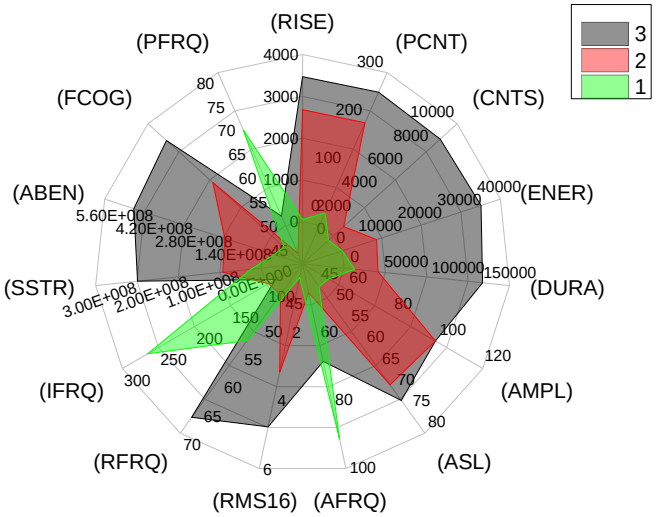


**Figure 5.28 - Radar graph of the typical behavior of the three clusters in function of their AE signal features.**

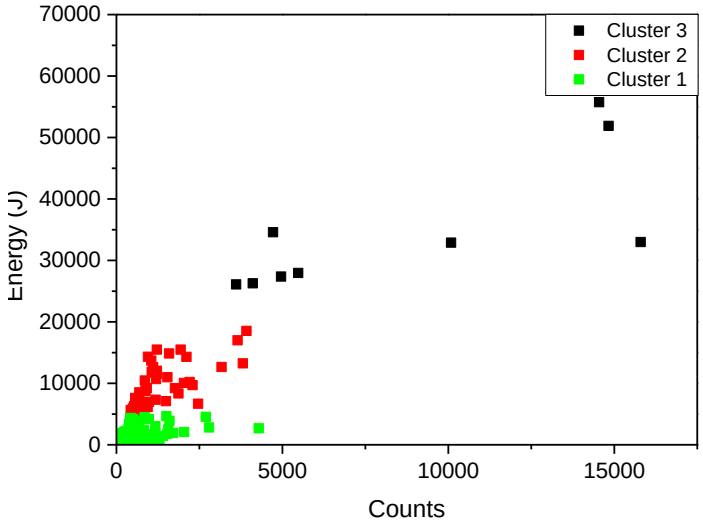


**Figure 5.29 – Typical energy-counts distribution of the clustered AE signals for V3TC specimens.**

Cluster 1 is seen to have the lowest values among the total of descriptors selected. This cluster is uniquely related to the matrix cracking, which is recognized mainly for its low energy and amplitude on the acoustic signals. Besides, the short duration and a small number of peak counts of the signals confirm Cluster 1 as damages in the matrix. Figure 5.30a shows a typical waveform obtained for this cluster. Cluster 2 differs from Cluster 1 especially to the superior response of the amplitude and peak counts that concerns to interlaminar damages, such as delamination and fiber bridging of the glass fabric reinforcements. Figure 5.30b exhibits a typical waveform for the cluster 2. Afterward, Cluster 3 exhibits high values to the four descriptors employed. From these results, this cluster is supposed to be related to tufted yarn rupture. Figure 5.30c shows a typical waveform from this class characterized by the high amplitude, energy, and duration.

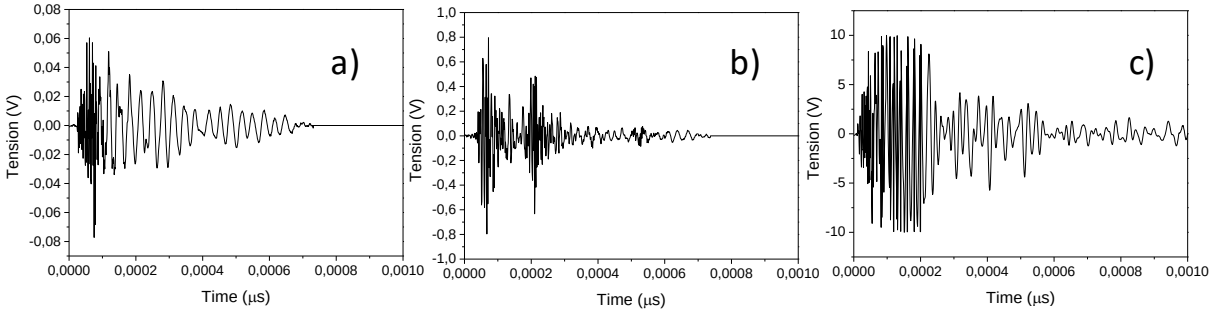


**Figure 5.30 - Typical waveform for the three different clusters obtained in the non-supervised clustering.**

Figure 5.31 presents the typical response of the cumulative energy by clusters during the pull-off test. The Cluster 3 initiates from the yarn rupture characterized by electrical resistance measurements. Additionally, the second rise in its cumulative energy may be associated with the failure in the following row of tuft reinforcement which was not electrically measured. The tuft rupture in the other side of the structure is also identified by the acoustic signals, as a cumulative increase in this event. Subsequently, this response rises again probably due to a tuft failure at the same side of the last damaged range.

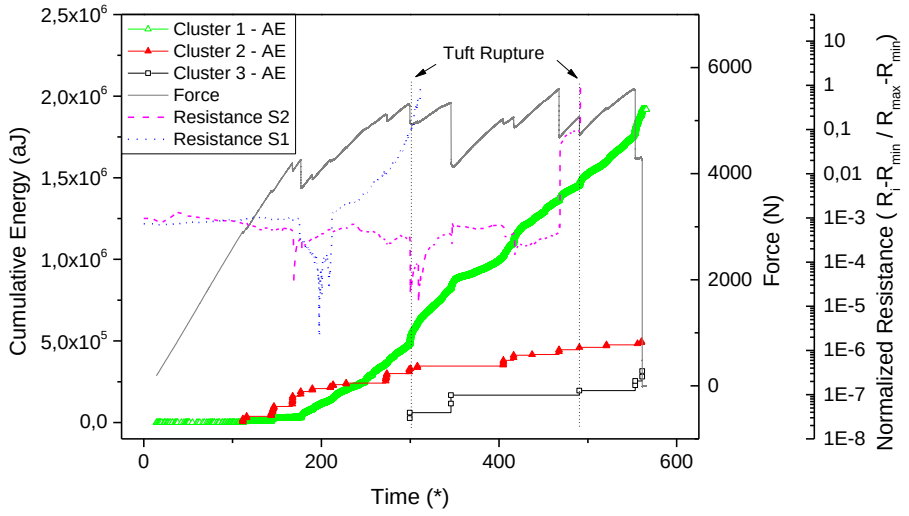


**Figure 5.31 – The typical behavior of the cumulative AE energy by clusters, electric resistance (S1 and S2) and load vs. time.**

## 3-Point bending test

Figure 5.32 exhibits the electrical resistance measurements acquired during the 3-point bending test as well as the cumulative energy curves represented by the three clusters of classified AE signals. The number of AE descriptors based on the principal component analysis (PCA) by obtaining a sum of the first four eigenvalues greater than 70%. A single-linkage clustering was

employed to achieve the descriptors with distance correlation greater than 70%. The analysis employed the amplitude, absolute energy, RMS and average frequency as AE descriptors. Thus, clustering was carried out using the non-supervised k-means method, applying Euclidian distance and random initial partitioning. The selection of the number of clusters based on DB index analysis. They consisted of two class of AE signals regarding the minor damages (Cluster 1), that concerns of acoustic events generated since the beginning of the test, and major damages (Cluster 2) capable of diminishing the structure load-bearing considerably.

The tuft rows (II and III) measured during the test are from both sides of the stiffener, near to the radius zone. Figure 5.33 presents the values of electrical resistance monitored at each load plateau after the increment of 5000 N. The main events exhibited in Figure 5.32 and Figure 5.33 are seen to be related to significant damages in the specimen. The event I described by a slight difference of electrical resistance in row III (Figure 5.32) is better seen in Figure 5.33 from a considerable increase of resistance in row IV. The loss of linearity in the force-time curve and the arising of AE cumulative energy of cluster 2, corroborate to the electrical response found to this event. Tuft row II is not in agreement with the results presented for the others tufts and may be related to an unbalanced loading of the structure. A gradual decrease of resistance is seen in the event I, caused by possible unloading of the structure in the same side or even delamination, which may reduce the electrical resistance as already reported in the studies above. Additionally, the opposite side composed of row III and IV counteracted the delamination that is described to reduce the electrical resistance during pull-off tests. Figure 5.34 illustrates the behavior regarding the growth of electrical resistance from a longitudinal view of the specimen (along with the stiffener).

The loading mechanisms involved in the tests are complex but is thought that a mixed condition between the flexure and out-of-plane shear loading are the most important to affect the electrical response. Flexural loading generates compressive stress from the neutral line to the maximum value on the top of the specimen surface, which is responsible for shrinking the tuft threads. Shear stress also reduces the threads cross-section, hindering the current flow and therefore, increasing the electrical resistance. Tensile stress generated in the opposite surface may enlarge the loop length and as a consequence, reduce thread cross-section that contributes to the rise of electrical resistance. It is also amplified with damage extent at increasing of the load. The response is mainly attributed to damages in tuft threads but can indicate significant damages in the composites. Event II, presented as a significant increase in the electrical resistance of the

tuft row III and IV, appears about 42000N and can indicate a threshold to the structure. The cumulative energy curve presents a slight increase in this event for the Class 2, despite Class 1 continues rising. The electrical resistance in row III increases until major failure of the structure, while the tuft row II in opposite side, decreases due to a possible unbalance of the loading as already mentioned.

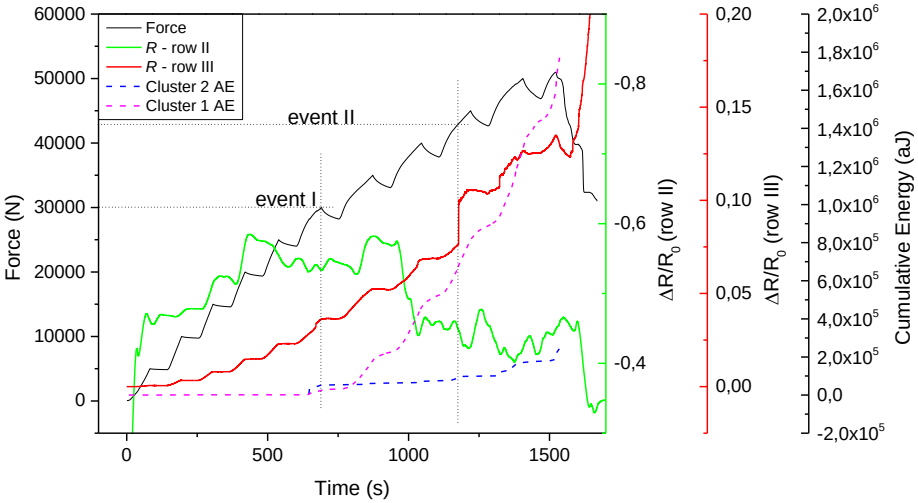


**Figure 5.32 – Load, electrical resistance in both sides of stiffeners, and cumulative AE energy by clusters vs. time during 3-point bending test of the V2T specimen.**

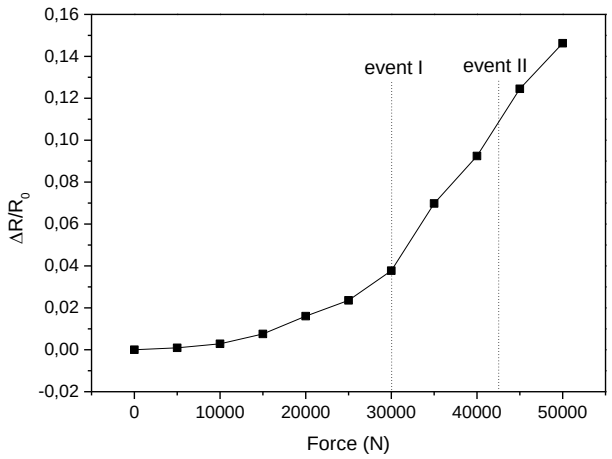


**Figure 5.33 – Electrical resistance versus force measured from the tuft row IV of the V2T specimen subjected to 3-point bending.**

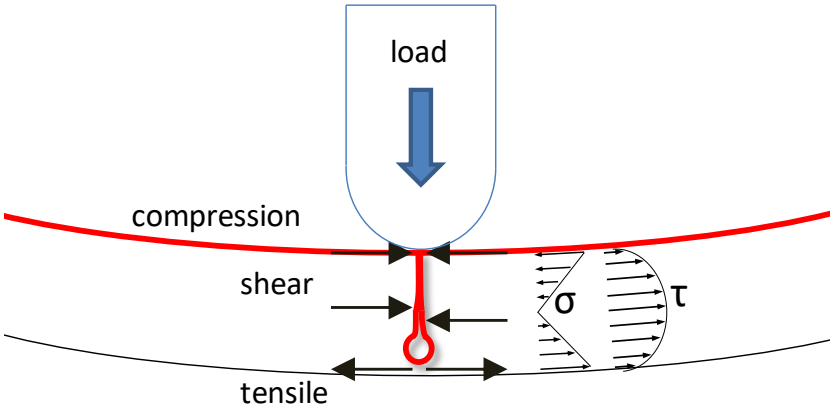


**Figure 5.34 – Schematic illustration of the stress distribution in a single tuft under a 3-point bending test (longitudinal direction).**

Figure 5.35 and Figure 5.36 exhibit the investigation of electrical resistance for the V3TC specimen. The measurements were carried out in the same manner as for the V2T sample. The rows I, II and III consist of the tufts on the same side of the stiffener, from outside to inside direction of the structure, while rows V to VI are in the opposite region and are positioned from radius zone in the direction to the outside. The clustering of AE signals maintained the same approach utilized for the V2T specimen. The event I is characterized as the first considerable increase of the *R* for the tuft row III, from one load increment to the next (Figure 5.35). This occurrence is correlated with the beginning of the cumulative energy - Cluster 2. Figure 5.36 also shows the same behavior for the rows I, II and V, represented as a significant change in the curve slope of the electrical resistance. Additionally, the onset of non-linearity exhibited in the force-time curve also indicates the event I.

The second event can be observed from the measurements in row III as a substantial increase in *R* compared to the previous response, while row V presents this event as a drop in electrical resistance. The event III is characterized as the considerable rise of cumulative energy of the Cluster 2 as well as of electrical resistance in row IV, which may indicate a significant damage event in the specimen. The measurements performed during the load plateau presented in Figure 5.36, especially for the tufts in the same side of row IV, did not evidence this behavior, which suggests a located damage in the analyzed tuft row. Row IV responds for the second time, at the subsequent load increment, with a sharp increase of electrical resistance (event IV). The same behavior was found in the others rows, mainly associated with tuft rows V and VI that are on the same side of the structure.

In summary to the mentioned occurrences, the electrical resistance loses its stable behavior from the first event until the structure failure, as a response to the damages generated in the

tufts and probably in the composite structure. The start point agrees with the beginning of AE-cluster 2, and the main events from that are also marked by the increase of cumulative energy, even if slight. It has been demonstrated, for the two sets of specimens V2T and V3TC, that the electrical measurement approach is strain-sensing and capable of monitoring significant damages.

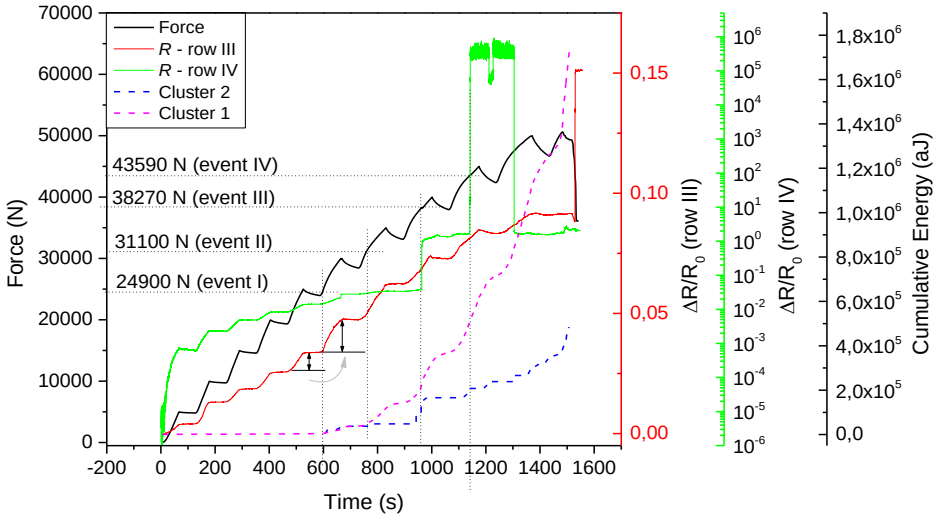


**Figure 5.35 - Load, electrical resistance in both sides of stiffeners, and clustered cumulative AE energy vs. time during 3-point bending test of V3TC specimen.**

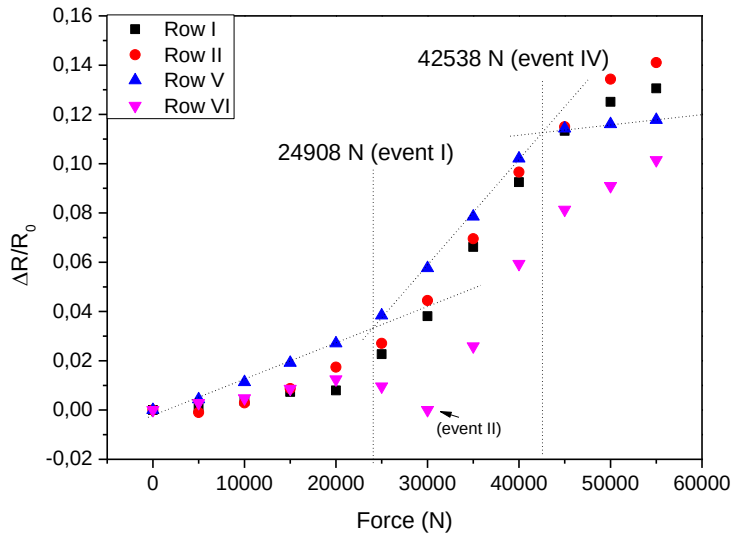


**Figure 5.36 - Electrical resistance versus force of the tuft rows from V3TC specimen, acquired at every load increment during the 3-point bending test.**

Figure 5.37 presents an opposite behavior for the V3TL in comparison to the V2T and V3TC specimens. Electrical resistance in both sides is seen to decrease while loading is amplified. It is mainly due to tuft loops that are intentionally left in the structure surface, owed to a complete tufting insertion. The contact between the loops, as exemplified in Figure 5.38, facilitate the current flow through the tufts and consequently, diminishes the electrical resistance. The

reduction in resistance occurs gradually and may be owed to the deformation in the loops region that can break the resin layer between two adjacent loops and then, improve their contact. It seems that this effect counteracts the already discussed physical phenomenon that leads to the growth of electrical resistance. Therefore, tufting reinforcement must be planned to avoid the contact of loops and the disturbance of electrical measurements respectively.

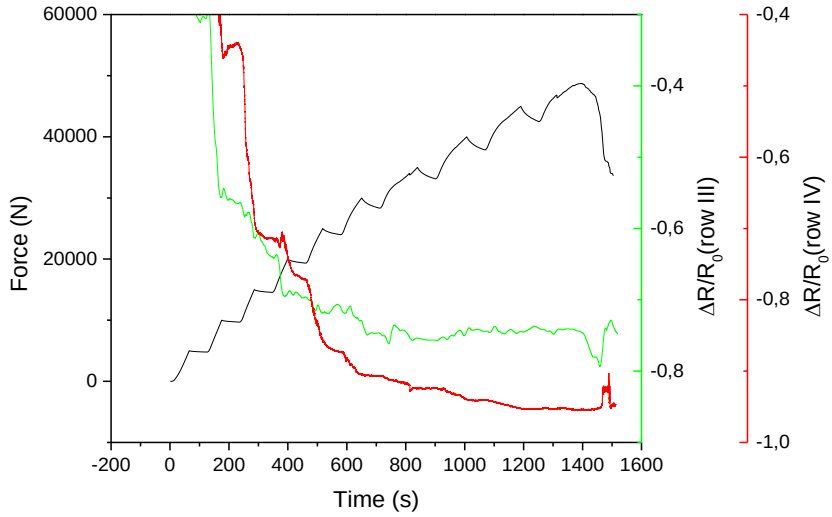


**Figure 5.37 – Load and electrical resistance on both sides of stiffeners vs. time acquired from V3TL specimen during 3-point bending test.**

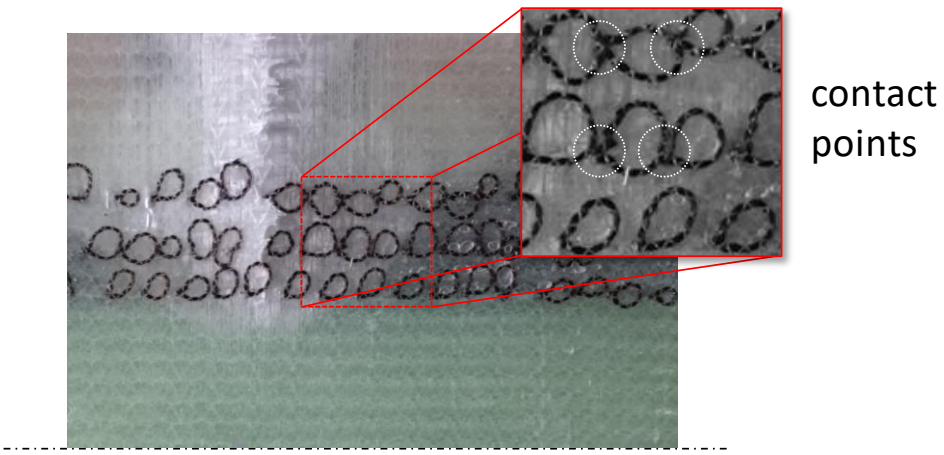


**Figure 5.38 – The photographic image of the bottom surface of V3TL specimen, emphasizing the contact point between tuft loops.**

## 5.3 Conclusions

The carbon tuft threads utilized for reinforcing the GFRP laminate plates were valuable to monitor progressive damage by multiple impact tests in laminate plates and foam core sandwich

plates. The electrical resistance of the tufts reports an increase when the laminate composite is subjected to impact loading. This behavior is progressive with the number of impact tests, which consequently increase the damage extent in composites. Although the monitoring is made through the tuft threads, their structural role in the laminated composites leads to considerable information about the state of health of the structure. Future work may explore the electrical resistance response as a method to qualify the severity of the damages by investigating the relation of residual strength with electrical resistance. It should be employed as a threshold to validate the structure in service.

The strain-sensing and damage monitoring capability of this approach were investigated during static tests using flatwise compression in sandwich plates and, pull-off and 3-point bending in omega stiffeners. Flatwise compression tests exhibited a good correlation between electrical resistance and loading. Moreover, major damages in the composites led to a significant increase in electrical resistance. It is caused by damages generated in the tuft threads, which difficult current flow and consequently amplify the resistance. This measurement method present stability when maintaining the load at the different steps. Furthermore, the measurements of electrical resistance during pull-off and 3-point bending tests of the omega stiffeners responded to increasing strain as well as to significant damages. The tufts were able to react to physical phenomena, such as delamination, with electrical resistance variation while loading the specimens.

Electrical resistance response was also in good agreement with the measurements of out-of-plane displacements and impact energy in the structures during impact tests. The increase of the electrical resistance throughout the loading period consists of a combination of events (piezoresistive effect, surface strictness and damage development in the tufted thread). Additionally, the increasing of electrical resistance after the unload period is owed to damages and residual strain created during the tests.

The evaluation of damage development after impact tests by infrared thermography while inducing current flow through tuft threads seems promising to detect a damaged region and can be used as a complementary method to ultrasonic C-Scan. The localized temperature rise detected by IRT allows the detection of damages in the tuft threads and possibly to the composite structure. The elevated temperature spots concern the resistance at the current flow generated in the damaged regions of the tufts. This effect, known as the Joule effect, increase the heat dissipated in the damaged region and allows the characterization. C-Scan imaging

validates the thermography analysis, displaying significant damages (as an increase of amplitude) in the same region of the heat concentration. However, thermography method presents a limit to acquire temperature gradient in well-damaged threads, owed to a considerable increase of electrical resistance. Despite this, adjacent tuft rows which continue under resistance threshold are capable of indicating the damaged zone.

This approach has presented its ability to monitor structural health using in-situ electrical resistance measurements for both quasi-static and dynamic tests. It avoids the insertion of sensors that can reduce the mechanical properties considerably. Additionally, improvements in out-of-plane mechanical properties by tufted reinforcements can be considered to use this technique as structural health monitoring. However, the results obtained are qualitative, and consequently, it would be interesting to correlate the variation of resistance to a quantitative magnitude such as deformation. It would help to quantify the damage extent and thus, enhance the health monitoring of structures.

# GENERAL CONCLUSIONS AND PERSPECTIVES

This study consisted of the investigation of tufted laminate composites subject to different loading conditions. Analyses of the in-plane and out-of-plane mechanical properties of the composites allowed the understanding of the tufting reinforcements to fracture toughness, damage tolerance, and strength. This investigation was supported by the manufacturing of various types of structures such as composite plates, foam cored sandwich plates and, omega stiffeners. Additionally, the multi-instrumented characterization during mechanical tests especially by DIC, AE, and in-situ microscopy assisted in the evaluation of the tufting effect in the laminates and helps to optimize the next generations of structures.

The main conclusions of this study are as follows:

- The insertion of tufts decreased the in-plane strength of the laminated composites. The reduction achieved values up to 40% and 10% for the specimens subjected to compression and open hole tensile tests respectively.
- The compressive strength is related to the tufting angle and was less significant for the inclined reinforcements than to the transversal tufting.
- Tuft threads induced strain concentration around them when subjected to open hole tensile tests. This behavior, that is similar than for a small hole, generates a preferential path to the significant cracks that will drive the structure to fail.
- Tufting reinforcements are not crucial to postpone the crack propagation created by the stress concentration in the open hole specimens during fatigue and tensile tests.
- Short beam shear tests allowed the study of tufting effect in the shear strength and modulus. These properties are dependent on the principal directions of the tuft rows (following the weft and warp direction of the fabrics). Interlaminar shear strength presented a negligible difference in the longitudinal direction but, a slight reduction of 9% in the perpendicular direction of the tufts. However, interlaminar shear moduli increased up to 330% and 134% in the longitudinal and perpendicular directions of tufting respectively when compared to the control specimens.
- The angle of tufting reinforcement was noteworthy to the interlaminar shear properties of the specimens subjected to short beam shear tests. The interlaminar shear modulus presented more significant results in the samples tufted transversally.

- Tuft threads were responsible for the stress concentration zone under short beam shear tests that led to the initiation of cracks from them and consequence interlaminar propagation until being arrested in the next tuft row. This behavior may be responsible to the lower ultimate strength.
- The tuft reinforcements reduced the delamination development significantly under drop-weight impact loading. This response was inversely proportional to the tufting density and achieved reductions of 4 times in the damaged area for the transversal tufts in comparison to untufted specimens.
- CAI strength reports considerable improvement for the tufted specimens. This response was proportional to the tufting density and achieved values up to 27 % for the transversal tufting.
- Fracture toughness of the tufted omega stiffeners submitted to pull-off tests increased up to 4.5 times in comparison to untufted specimens.
- The maximum force of the tufted stiffener panels depends on the stiffeners radius as well as the tufting location. The development of the mentioned factors allowed to achieve a set of tufted samples with maximum force and fracture toughness 11 % and 3.4-fold superior to the control structures.
- Tufted omega stiffeners presented a significant increase of the fracture toughness up to 5 times when subjected to 3-point bending tests. It is noticeable a lower damaged area in comparison to the control specimens due to the arresting of delamination by the tuft threads.
- The various types of GFRP specimens (plates, sandwich plates, and omega stiffeners) exhibited strain sensing and the capability of monitoring damages during quasi-static and dynamic loading tests. This behavior occurred owing to the piezoresistive effect of the carbon fibers employed as tuft threads.
- Infrared thermography is capable of characterizing damages due to difficulties in flowing the current through the tufts, which consequently increase the heat by Joule Effect. This novel approach seems promising to detect damages in the tufts and thus, potential damages in the composite laminate. Additionally, it may be utilized as a supplementary technique to C-Scan.
- The electrical resistance monitoring of the tuft threads allows acquiring information about their health under loading. This method fulfills a gap let for the other techniques employed for characterizing the composites such as DIC (on the surface procedure) and

AE (volumetric technique) that cannot obtain precise information about the tufts. Moreover, it could contribute to the numerical modeling of tufted composites.

All of these findings show the complexity of reinforcing composites in the through-thickness direction. Several parameters affect the mechanical properties of the structures significantly, such as the shape of the structure, the location of the reinforcements, the tufting density and angle of insertion. These parameters are very sensitive and can alter the mechanical performance of the composites significantly. For example, poor positioning of the tufts of a few millimeters can degrade the mechanical properties and the service life of the structure. However, an optimum positioning allows a noticeable improvement of these same properties with a considerable enhancement of the damage tolerance.

This thesis focused on what was above described, as well as to help identify some of the damaging behavior of these materials. There is still much to be done in order to the 3D composites reach the same level of understanding about their mechanical behavior than the 2D laminated composites.

If there was a hierarchy of perspectives to be done, modeling of composite structures reinforced by tufting should be placed at the top of the list. Indeed, the numerical modeling seems essential to positioning the through-thickness reinforcements appropriately. The parameters concerning the insertion in the material, such as position, the density of reinforcement and angle, are indispensable to the excellent performance of the composites strictly and highly depends on the loading condition and shape of the structure. However, as we are aware, the task is far to be easily accomplished, due to the complexity of the phenomena involved. This work presents a first attempt to perform a numerical model. It was decided to be conservative and avoid some imbalance by integrating this part into the main body of the thesis.

This finite element modeling has employed cohesive elements for the simulation of delamination and beam elements to simulate the tufts. The approach is distant to be accurate and the results obtained, although encouraging, do not seem sufficiently mature to be presented. Appendix A presents a summary of this study. Nevertheless, what emerges is that the physical modeling of the tufts must be made because the inaccuracy of the homogenization approach employed as in this investigation. Indeed, the tufts play a very important role in the mechanical behavior of the structure to not be well represented. The evaluation of strain and stress state on the tufts is essential. The mesostructured local (local defects, rich resin zone around the tufts,

tuft misalignment) must be considered since, as already seen, is responsible for the damage initiation. This type of work should be conducted in parallel with experimental investigations. The dialogue between mechanical tests and numerical simulation is necessary for the development of robust modeling approaches.

Another aspect that seems interesting to continue the development involves monitoring the health status of the tufts by the piezoresistive effect. It will be necessary for the future that this approach associate fully with other techniques of inspection for the analysis of the damage behavior of this type of structures.

However, it is essential to find a manner to apply this technique to structures with carbon reinforcements. Based on this concern, the primary goal of this further analysis regards the improvement of the electrical conductivity of the tufts about the carbon fabric plies. This may create a preferential path in the tuft threads and consequently, allow the strain sensing analysis and damage monitoring of the carbon fiber reinforced polymers reinforced by tufting.

The structural health monitoring by piezoresistive effect should also be modeled to predict the electrical response under loading and therefore, be able to properly assess the damage state of the structure or at least of the joints. This makes the problem multi-physics but certainly very interesting to address.

# PUBLICATIONS

The publications resulting out of this thesis work are listed below.

**Journal articles:**

A.T. Martins, Z. Aboura, W. Harizi, A. Laksimi, K. Khellil. Analysis of the impact and compression after impact behavior of tufted laminated composites. *Composite Structures*, 2018, vol. 184, p. 352-361.

J. Bigaud, Z. Aboura, A.T. Martins, S. Verger. Analysis of the mechanical behavior of composite t-joints reinforced by one side stitching. *Composite Structures*, 2018, vol. 184, p. 249-255.

A.T. Martins, Z. Aboura, W. Harizi, A. Laksimi, K. Hamdi. Structural health monitoring by the piezoresistive response of tufted reinforcements in sandwich composite panels. *Composite Structures*, submitted.

A.T. Martins, Z. Aboura, W. Harizi, A. Laksimi, K. Khellil. Structural health monitoring for GFRP composite by piezoresistive response in the tufted reinforcements. *Composite Structures*, submitted.

**Conference papers:**

A.T. Martins, Z. Aboura, A. Laksimi, K. Khellil. In-situ structural health monitoring of glass fiber reinforced composites by tufted reinforcement. In: *13th International Conference on Textile Composites (TexComp 13)*, 2018.

A.T. Martins, Z. Aboura, A. Laksimi, K. Khellil, W. Harizi. An experimental study of the mechanical behavior of omega stiffeners reinforced by tufting process. In: *International Symposium on Air/Craft Materials* (*ACMA*), 2018.

Z. Aboura , A.T. Martins. On the advantage of an out-of-plane reinforcement of laminate composites. In: *Chinese-Franco Symposium on Damage and Fracture of Composite Structures: Analyses and Monitoring, 2017*.

A.T. Martins, K. Khellil, Z. Aboura, A Laksimi. Etude du comportement à l'impact et compression post impact de composites à renfort tissu de carbone assemblée par tufting. In : *JNC20 -Journée Nationale sur les Composites*, 2017.

A.T. Martins, K. Khellil, J. Bigaud, Z. Aboura. Effects of tufting parameters on the impact properties of carbon fabric composites. In: *BCCM-3 – Brazilian Conference on Composite Materials*, 2016.

# REFERENCES

[1] B. C. Jin, X. Li, R. Mier, A. Pun, S. Joshi, and S. Nutt, “Parametric modeling , higher order FEA and experimental investigation of hat-stiffened composite panels,” *Compos. Struct.*, vol. 128, pp. 207–220, 2015.

[2] M. R. Wisnom, “The role of delamination in failure of fibre-reinforced composites,” *Phil. Trans. R. Soc. A*, vol. 370, pp. 1850–1870, 2012.

[3] S. A. Ngah and A. C. Taylor, “Fracture behaviour of rubber- and silica nanoparticle-toughened glass fibre composites under static and fatigue loading,” *Compos. Part A*, vol. 109, pp. 239–256, 2018.

[4] M. R. Ricciardi, I. Papa, A. Langella, T. Langella, V. Lopresto, and V. Antonucci, “Mechanical properties of glass fi bre composites based on nitrile rubber toughened modified epoxy resin,” *Compos. Part B*, vol. 139, pp. 259–267, 2018.

[5] L. L. Sobrinho, V. M. A. Calado, and F. L. Bastian, “Effects of Rubber Addition to an Epoxy Resin and Its Fiber Glass-Reinforced Composite,” *Polym. Compos.*, vol. 33, no. 2, pp. 295–305, 2012.

[6] C. Yan, K. Xiao, L. I. N. Ye, and Y. W. Mai, “Numerical and experimental studies on the fracture behavior of rubber-toughened epoxy in bulk specimen and laminated composites,” *J. Mater. Sci.*, vol. 7, no. 5, pp. 921–927, 2006.

[7] E. I. Sue, H. J., Jones, R. E., & Garcia-Meitin, “Fracture behaviour of model toughened composites under Mod e l and Mode II delaminations,” *J. Mater. Sci.*, vol. 28, no. 23, pp. 6381–6391, 1993.

[8] N. H. Nash, T. M. Young, P. T. Mcgrail, and W. F. Stanley, “Inclusion of a thermoplastic phase to improve impact and post-impact performances of carbon fibre reinforced thermosetting composites — A review,” *Mater. Des.*, vol. 85, pp. 582–597, 2015.

[9] I. Mujika, F., De Benito, A., Fernandez, B., Vazquez, A., Llano-Ponte, R., & Mondragon, “Woven Reinforced Epoxy Matrix Composites . A Study on the Influence of Matrix Modification With Polysulfone,” *Polym. Compos.*, vol. 2, no. 3, pp. 372–382, 2002.

[10] L. Bonnaud, J. P. Pascault, H. Sautereau, and B. J. Verne, “Effect of Reinforcing Glass Fibers on Morphology and Properties of Thermoplastic Modified Epoxy-Aromatic Diamine Matrix,” *Polym. Compos.*, vol. 25, no. 4, pp. 368–374, 2004.

[11] T. Nakamura, Y., Yamaguchi, M., Okubo, M., & Matsumoto, “Effects of Particle Size on Mechanical and Impact Properties of Epoxy Resin Filled with Spherical Silica,” *J. Appl. Polym. Sci.*, vol. 45, no. 7, pp. 1281–1289, 1992.

[12] J. Lee and A. F. Yee, “Fracture Behavior of Glass Bead Filled Epoxies : Cleaning Process of Glass Beads,” *J. Appl. Polym. Sci.*, vol. 79, pp. 1371–1383, 2001.

[13] J. Lee and A. F. Yee, “Inorganic particle toughening II : toughening mechanisms of glass bead filled epoxies,” *Polymer (Guildf).*, vol. 42, pp. 589–597, 2001.

[14] T. Kawaguchi and R. A. Pearson, “The effect of particle – matrix adhesion on the mechanical behavior of glass filled epoxies . Part 2 . A study on fracture toughness,” *Polymer (Guildf).*, vol. 44, pp. 4239–4247, 2003.

[15] C. M. Manjunatha, S. Sprenger, A. C. Taylor, and A. J. Kinloch, “The Tensile Fatigue Behaviour of a Glass-Fiber Reinforced-Plastic Composite Using a Hybrid-Toughened Epoxy Matrix,” *J. Compos. Mater.*, vol. 44, pp. 2095–2109, 2010.

[16] R. A. P. Bahereh T. Marouf, Yiu-Wing Mai, Reza Bagheri, “Toughening of Epoxy Nanocomposites : Nano and Hybrid Effects Toughening of Epoxy Nanocomposites : Nano and Hybrid Effects,” *Polym. Rev.*, vol. 56, no. 1, pp. 70–112, 2016.

[17] H. R. Azimi, R. A. Pearson, and R. W. Hertzberg, “Fatigue of Hybrid Epoxy Composites : Epoxies Containing Rubber and Hollow Glass Spheres,” *Polym. Eng. Sci.*, vol. 36, no. 16, pp. 2352–2365, 1996.

[18] M. Rutnakornpituk, “Thermoplastic Toughened Epoxy Networks and Their Toughening Mechanisms in Some Systems,” *Naresuan Univ. J.*, vol. 13, no. 1, pp. 73–83, 2005.

[19] D. J. Turmel and I. K. Partridge, “Heterogeneous phase separation around fibres in epoxy/PEI blends and its effect on composite delamination resistance,” *Compos. Sci. Technol.*, vol. 57, pp. 1001–1007, 1997.

[20] L. Tang, H. Zhang, S. Sprenger, L. Ye, and Z. Zhang, “Fracture mechanisms of epoxy-based ternary composites filled with rigid-soft particles,” *Compos. Sci. Technol.*, vol. 72, pp. 558–565, 2012.

[21] J. L. Cawse and J. L. Stanford, “Rubber-toughened polyurethane network and composite materials,” *Polymer (Guildf).*, vol. 28, no. 3, pp. 356–367, 1986.

[22] J. M. Scott and D. C. Phillips, “Carbon fibre composites with rubber toughened matrices,” *J. Mater. Sci.*, vol. 10, pp. 551–562, 1975.

[23] N. G. Ozdemir, T. Zhang, I. Aspin, F. Scarpa, H. Hadavinia, and Y. Song, “Toughening of carbon fibre reinforced polymer composites with rubber nanoparticles for advanced industrial applications,” *eXPRESS Polym. Lett.*, vol. 10, no. 5, pp. 394–407, 2016.

[24] J. Kong, R. Ning, and Y. Tang, “Study on modification of epoxy resins with acrylate liquid rubber,” *J. Mater. Sci.*, vol. 1, no. 5, pp. 1639–1641, 2006.

[25] M. Jun, M. S. Mo, X. S. Du, S. R. Dai, and I. Luck, “Study of Epoxy Toughened by In Situ Formed Rubber Nanoparticles,” *J. Appl. Polym. Sci.*, vol. 110, no. 1, pp. 304–312, 2008.

[26] Q. Le, H. Kuan, J. Dai, I. Zaman, L. Luong, and J. Ma, “Structure e property relations of 55 nm particle-toughened epoxy,” *Polymer (Guildf).*, vol. 51, no. 21, pp. 4867–4879, 2010.

[27] M. R. Groleau, Y. Shi, A. F. Yee, J. L. Bertram, H. J. Sueb, and P. C. Yang, “Mode II fracture of composites interlayered with nylon particles.,” *Compos. Sci. Technol.*, vol. 56, pp. 1223–1240, 1996.

[28] A. R. Jones, C. A. Watkins, S. R. White, and N. R. Sottos, “Self-healing thermoplastic-toughened epoxy,” *Polymer (Guildf).*, vol. 74, pp. 254–261, 2015.

[29] D. J. Hourston, J. M. Lane, and H. X. Zhang, “Toughening of Epoxy Resins with Thermoplastics : 3 . An Investigation into the Effects of Composition on the Properties of Epoxy Resin Blends,” *Polym. Int.*, vol. 42, pp. 349–355, 1997.

[30] P. T. Mcgrail and S. D. Jenkinst, “Some aspects of interlaminar toughening : reactively

terminated thermoplastic particles in thermoset composites," *Polymer (Guildf).*, vol. 34, no. 4, pp. 677–683, 1993.

[31] Z. Wu, X. Yi, and A. Wilkinson, "Interlaminar fracture toughness of carbon fi bre / RTM6-2 composites toughened with thermoplastic-coated fabric reinforcement," *Compos. Part B*, vol. 130, pp. 192–199, 2017.

[32] P. Van Velthem *et al.*, "Influence of thermoplastic diffusion on morphology gradient and on delamination toughness of RTM-manufactured composites," *Compos. Part A Appl. Sci. Manuf.*, vol. 72, pp. 175–183, 2015.

[33] D. J. Bull, A. E. Scott, S. M. Spearing, and I. Sinclair, "The influence of toughening-particles in CFRPs on low velocity impact damage resistance performance," *Compos. Part A Appl. Sci. Manuf.*, vol. 58, pp. 47–55, 2014.

[34] D. J. Bull, S. M. Spearing, I. Sinclair, and L. Helfen, "Three-dimensional assessment of low velocity impact damage in particle toughened composite laminates using micro-focus X-ray computed tomography and synchrotron radiation laminography," *Compos. Part A Appl. Sci. Manuf.*, vol. 52, pp. 62–69, 2013.

[35] Chris DeArmitt and M. Hancock, "Filled Thermoplastics," in *Particulate-Filled Polymer Composites*, 2nd ed., R. N. Rothon, Ed. Filled Polymer Composites Second Edition Editor R.N. Rothon Rapra Technology Limited, 2014, p. 544.

[36] J. Lee and A. F. Yee, "Inorganic particle toughening I : micro-mechanical deformations in the fracture of glass bead filled epoxies," *Polymer (Guildf).*, vol. 42, pp. 577–588, 2001.

[37] M. Shariati, G. A. Farzi, A. Dadrasi, M. Amiri, and R. R. Meybodi, "An Experimental Study on Toughening Mechanisms of Fillers in Epoxy / Silica Nanocomposites," *Int. J. Nanosci. Nanotechnol.*, vol. 11, no. 3, pp. 193–199, 2015.

[38] A. J. Kinloch, D. L. Maxwell, and R. J. Young, "The fracture of hybrid-particulate composites," *J. Mater. Sci.*, vol. 20, no. 11, pp. 4169–4184, 1985.

[39] A. J. Kinloch, K. Masania, A. C. Taylor, S. Sprenger, and D. Egan, "The fracture of glass-fibre-reinforced epoxy composites using nanoparticle-modified matrices," *J.*

*Mater. Sci.*, vol. 43, no. 3, pp. 1151–1154, 2008.

[40] K. N. Shivakumar and R. Panduranga, "Interleaved Polymer Matrix Composites - A Review," in *54th AIAA/ASME/ASCE/AHS/ASC Structures, Structural Dynamics, and Materials Conference*, 2013, no. May 2015.

[41] I. M. De Rosa, C. Santulli, F. Sarasini, and M. Valente, "Post-impact damage characterization of hybrid configurations of jute/glass polyester laminates using acoustic emission and IR thermography," *Compos. Sci. Technol.*, vol. 69, no. 7–8, pp. 1142–1150, 2009.

[42] C. T. Sun and S. Rechak, "Optimal use of adhesive layers in reducing impact damage in composite laminates," *J. Reinf. Plast. Compos.*, vol. 9, pp. 569–582, 1990.

[43] D. W. Y. Wong, H. Zhang, E. Bilotti, and T. Peijs, "Interlaminar toughening of woven fabric carbon / epoxy composite laminates using hybrid aramid / phenoxy interleaves," *Compos. Part A Appl. Sci. Manuf.*, vol. 101, pp. 151–159, 2017.

[44] A. A. J. M. Peijs, R. W. Venderbosch, and P. J. Lemstra, "Hybrid composites based on polyethylene and carbon fibres Part 3 : Impact resistant structural composites through damage management," *Composites*, vol. 21, no. 6, pp. 522–530, 1990.

[45] M. Hojo, S. Matsuda, and M. Tanaka, "Mode I delamination fatigue properties of interlayer-toughened CF/epoxy laminates," *Compos. Sci. Technol.*, vol. 66, pp. 665–675, 2006.

[46] K. Shivakumar, S. Lingaiah, and H. Chen, "Polymer Nanofabric Interleaved Composite Laminates," in *50th AIAA/ASME/ASCE/AHS/ASC Structures, Structural Dynamics, and Materials Conference*, 2009, no. May, pp. 1–10.

[47] H. Ning *et al.*, "Toughening effect of CB-epoxy interleaf on the interlaminar mechanical properties of CFRP laminates," *Compos. Part A Appl. Sci. Manuf.*, vol. 68, pp. 226–234, 2015.

[48] N. Zheng, Y. Huang, H. Liu, J. Gao, and Y. Mai, "Improvement of interlaminar fracture toughness in carbon fiber/epoxy composites with carbon nanotubes/polysulfone interleaves," *Compos. Sci. Technol.*, vol. 140, pp. 8–15, 2017.

[49] H. A. Maples, O. Smith, C. Burgstaller, P. Robinson, and A. Bismarck, “Improving the ply / interleaf interface in carbon fi bre reinforced composites with variable stiffness,” *Compos. Sci. Technol.*, vol. 128, pp. 185–192, 2016.

[50] M. Sohn and X. Hu, “Mode II delamination toughness of carbon-fibre/epoxy composites with chopped Kevlar fibre reinforcement,” *Compos. Sci. Technol.*, vol. 52, no. 3, pp. 439–448, 1994.

[51] M. Ansar, W. Xinwei, and Z. Chouwei, “Modeling strategies of 3D woven composites : A review,” *Compos. Struct.*, vol. 93, pp. 1947–1963, 2011.

[52] A. P. Mouritz, M. K. Bannister, P. J. Falzon, and K. H. Leong, “Review of applications for advanced three-dimensional fibre textile composites,” *Compos. Part A Appl. Sci. Manuf.*, vol. 30, pp. 1445–1461, 1999.

[53] “3D weaving,” *Axis Composites*, 2012. [Online]. Available: http://www.axis-composites.com/3d weaving.html. [Accessed: 10-Jun-2018].

[54] G. Stegschuster, K. Pingkarawat, B. Wendland, and A. P. Mouritz, “Experimental determination of the mode I delamination fracture and fatigue properties of thin 3D woven composites,” *Compos. Part A Appl. Sci. Manuf.*, vol. 84, pp. 308–315, 2016.

[55] J. Brandt, K. Drechslef, and F. Arendts, “Mechanical performance of composites based on various three-dimensional woven-fibre preforms,” *Compos. Sci. Technol.*, vol. 56, pp. 381–386, 1996.

[56] A. P. Mouritz, C. Baini, and I. Herszberg, “Mode I interlaminar fracture toughness properties of advanced textile fibreglass composites,” *Compos. Part A Appl. Sci. Manuf.*, vol. 30, pp. 859–870, 1999.

[57] K. R. Hart, P. X. L. Chia, L. E. Sheridan, E. D. Wetzel, N. R. Sottos, and S. R. White, “Composites : Part A Mechanisms and characterization of impact damage in 2D and 3D woven fiber-reinforced composites,” *Compos. Part A*, vol. 101, pp. 432–443, 2017.

[58] B. K. Behera and B. P. Dash, “Mechanical behavior of 3D woven composites,” *J. Mater.*, vol. 67, pp. 261–271, 2015.

[59] "Carbon Twisting," *Concordia Fibers*. [Online]. Available: http://www.concordiafibers.com/carbon-twisting.html. [Accessed: 07-Jun-2018].

[60] G. Gardiner, "Albany Engineered Composites: Weaving the Future in 3-D," *CompositesWorld*, 2014. .

[61] T. Sontag, H. Yang, T. Gries, and F. Ko, "Recent advances in 3D braiding technology," in *Advances in 3D Textiles*, 2015, pp. 153–181.

[62] K. Bilisik, "Cartesian 3D braiding," in *Advances in Braiding Technology*, Elsevier Ltd, 2016, pp. 107–145.

[63] F. K. Ko, "Developments of high damage tolerant, net shape composites through textile structural design," *Metall. Soc. Inc*, pp. 1201–1210, 1985.

[64] Q.D. Yang , K.L. Rugg, B.N. Cox, M.C. Shaw, "Failure in the junction region of T-stiffeners : 3D-braided vs . 2D tape laminate stiffeners," *Int. J. of Solids and Structures.*, pp. 1653-1668, 2003.

[65] Y. Wang and D. Zhao, "Effect of Fabric Structures on the Mechanical Properties of 3-D Textile Composites," *J. Ind. Text.*, vol. 35, no. 3, pp. 239–256, 2006.

[66] R. M. Crane and E. T. Camponeschi Jr, "Experimental and Analytical Characterization of Multidimensionally Braided Graphite/Epoxy Composites," *Exp. Mech.*, pp. 259–266, 1986.

[67] "Layer to Layer 3D Interlock Braiding Machine for advanced composite preform," *Komachine*. [Online]. Available: https://www.komachine.com/en/product/34863/. [Accessed: 08-Jun-2018].

[68] A. Bogdanovich and D. Mungalov, "Recent advancements in manufacturing 3D braided preforms and composites," in *Proc ACUN-4 Composite systems-macro composites, micro composites, nanocomposites*, 2002.

[69] F. Bend and M. Bannister, "Development and application of advanced textile composites," in *Proceedings I MECH E Part L Journal of Materials:Design and Applications*, 2004, vol. 218, no. 3, pp. 253–260.

[70] “Fracture behaviour and damage growth in knitted carbon fibre fabric reinforced polyethylmethylacrylate,” *Plast. Rubber Compos. Process. Apl.*, vol. 25, no. 3, pp. 109–114, 1996.

[71] H. B. Dextef and G. H. Haskob, “Mechanical properties and damage tolerance of multiaxial warp-knit composites,” *Compos. Sci. Technol.*, vol. 56, no. 3, pp. 367–380, 1996.

[72] S. Ramakrishna and H. Hamada, “Impact Damage Resistance of Knitted Glass Fiber Fabric Reinforced Polypropylene Composites,” *Sci. Eng. Compos. Mater.*, vol. 4, no. 2, pp. 61–72, 1995.

[73] S. Chou, H. Chen, and C. Lai, “The fatigue properties of weft-knit fabric reinforced epoxy resin composites,” *Compos. Sci. Technol.*, vol. 45, pp. 283–291, 1992.

[74] Z. Guo, “Developments in 3D knitted structures,” in *Specialist Yarn and Fabric Structures: Developments and Applications*, 2011, pp. 109–117.

[75] Gabriel O. Shonaike and S. G. Advani, Eds., *Advanced Polymeric Materials - Structure Property Relationships*. CRC Press, 2003.

[76] T. M. Koh, “Improving the mechanical properties of aerospace carbon fibre-epoxy joints by z-pinning,” RMIT University, 2012.

[77] I. K. Partridge, M. Yasaee, G. Allegri, and J. K. Lander, “Damage-tolerant composite structures by Z-pinning,” in *Toughening Mechanisms in Composite Materials*, Elsevier Ltd., 2015, pp. 161–189.

[78] D. J. Barrett, “The mechanics of z-fiber reinforcement,” *Compos. Struct.*, vol. 36, pp. 23–32, 1996.

[79] J. W. G. Treiber, “Performance of tufted carbon fibre / epoxy composites,” Cranfield University, 2011.

[80] J. Toral *et al.*, “Analyse multi-niveau de jonctions économiques par cloutage = Multi-level analysis of low-cost Z-pinned junctions,” in *AMAC*, 2009, p. 10.

[81] J. K. Lander, “Designing with z-pins: locally reinforced composite structures,” Cranfield University, 2008.

[82] M. Bannister, I. Herszberg, A. Nicolaidis, F. Coman, and K. H. Leong, “The manufacture of glass / epoxy composites with multilayer woven architectures,” *Compos. Part A Appl. Sci. Manuf.*, vol. 29, no. A, pp. 293–300, 1998.

[83] D. D. Cartié *et al.*, “Automated manufacture of 3D reinforced aerospace composite structures,” *Int. J. Struct. Integr.*, vol. 3, no. 1, pp. 22–40, 2014.

[84] K. Pingkarawat and A. P. Mouritz, “Comparative study of metal and composite z-pins for delamination fracture and fatigue strengthening of composites,” *Eng. Fract. Mech.*, vol. 154, pp. 180–190, 2016.

[85] J. J. Childress and G. Freitas, “Z-direction pinning of composite laminates for increased survivability,” in *Aerospace Design Conference*, 1992, p. 1099.

[86] D. D. R. Cartié and I. K. Partridge, “Delamination behaviour of z-pinned laminates,” in *European Structural Integrity Society*, vol. 27, pp. 27–36.

[87] I. K. Partridge and D. D. R. Cartie, “Delamination resistant laminates by Z-Fiber w pinning : Part I manufacture and fracture performance,” *Compos. Part A Appl. Sci. Manuf.*, vol. 36, pp. 55–64, 2005.

[88] D. D. R. Cartié, “Effect of Z-Fibres on the Delamination Behaviour of Carbon Fibre I Epoxy Laminates,” Cranfield University, 2000.

[89] A. Rezai *et al.*, “Interlaminar Damage Resistance of Z-fiber Reinforced Structural CFRP,” in *3th international conference on composite materials*, 2001, pp. 25–29.

[90] G. Freitas, C. Magee, P. Dardzinski, and T. Fusco, “Fiber insertion process for improved damage tolerance in aircraft laminates,” *J. Adv. Mater.*, vol. 25, no. 4, pp. 36–43, 1994.

[91] K. L. Rugg, B. N. Cox, and R. Massabo, “Mixed mode delamination of polymer composite laminates reinforced through the thickness by z- fibers,” *Compos. Part A Appl. Sci. Manuf.*, vol. 33, pp. 177–190, 2002.

[92] D. D. R. Cartié, G. Dell'Anno, E. Poulin, and I. K. Partridge, "3D reinforcement of stiffener-to-skin T-joints by Z-pinning and tufting," *Eng. Fract. Mech.*, vol. 73, no. 16, pp. 2532–2540, 2006.

[93] Y. Park, B. Lee, J. Kweon, J. Choi, and I. Choi, "The strength of composite bonded T-joints transversely reinforced by carbon pins," *Compos. Struct.*, vol. 94, pp. 625–634, 2012.

[94] G. Allegri and X. Zhang, "On the delamination and debond suppression in structural joints by Z-fibre pinning," *Compos. Part A Appl. Sci. Manuf.*, vol. 38, pp. 1107–1115, 2007.

[95] M. Grassi, A. Clarke, N. Khemiri, and M. Gaitonde, "Analysis of through-thickness reinforcements effects on the failure modes of a composite rib foot," in *European Conference on Composite Materials, ECCM 11*, 2004, pp. 1–10.

[96] J. Toral Vazquez *et al.*, "Multi-level analysis of low-cost Z-pinned composite joints Part 2 : Joint behaviour," *Compos. Part A Appl. Sci. Manuf.*, vol. 42, no. 12, pp. 2082–2092, 2011.

[97] P. Chang, A. P. Mouritz, and B. N. Cox, "Properties and failure mechanisms of z-pinned laminates in monotonic and cyclic tension," *Compos. Part A Appl. Sci. Manuf.*, vol. 37, pp. 1501–1513, 2006.

[98] X. Zhang, L. Hounslow, and M. Grassi, "Improvement of low-velocity impact and compression-after-impact performance by z-fibre pinning," *Compos. Sci. Technol.*, vol. 66, pp. 2785–2794, 2006.

[99] A. P. Mouritz, "Compression properties of z-pinned composite laminates," *Compos. Sci. Technol.*, vol. 67, pp. 3110–3120, 2007.

[100] M. Grassi, X. Zhang, and M. Meo, "Prediction of stiffness and stresses in z-fibre reinforced composite laminates," *Compos. Part A Appl. Sci. Manuf.*, vol. 33, pp. 1653–1664, 2002.

[101] P. Chang, A. P. Mouritz, and B. N. Cox, "Flexural properties of z-pinned laminates," *Compos. Part A Appl. Sci. Manuf.*, vol. 38, pp. 244–251, 2007.

[102] A. P. Mouritz, "Review of z-pinned composite laminates," *Compos. Part A Appl. Sci. Manuf.*, vol. 38, no. 12, pp. 2383–2397, 2007.

[103] T. Abe, K. Hayashi, T. Sato, S. Yamane, and T. Hirokawa, "A-VARTM process and z-anchor technology for primary aircraft structures," in *Proceedings of the 24th international SAMPE Europe conference*, 2003, pp. 87–94.

[104] T. Kusaka, "Toughening mechanisms in Zanchor-reinforced composites," in *Toughening Mechanisms in Composite Materials*, Elsevier Ltd., 2015, pp. 235–261.

[105] T. Kusaka, K. Watanabe, M. Hojo, T. Fukuoka, and M. Ishibashi, "Fracture behaviour and toughening mechanism in Z-anchor reinforced composites under mode I loading," *Eng. Fract. Mech.*, vol. 96, no. 14, pp. 433–446, 2012.

[106] T. Kusaka, K. Watanabe, M. Hojo, T. Fukuoka, and M. Ishibashi, "Fracture behavior and toughening mechanism in Zanchor reinforced composites under mode II loading," *Compos. Sci. Technol.*, vol. 69, no. 14, pp. 2323–2330, 2009.

[107] M. Hojo, K. Nakashima, T. Kusaka, M. Tanaka, and T. Adachi, "Mode I fatigue delamination of Zanchor-reinforced CF / epoxy laminates," *Int. J. Fatigue*, vol. 32, no. 1, pp. 37–45, 2010.

[108] M. B. Dow and D. L. Smith, "Damage-tolerant composite materials produced by stitching carbon fibers," in *21st International SAMPE Technical Conference*, 1989, p. 11.

[109] H. B. Dexter and J. G. Funk, "Impact resistance and interlaminar fracture toughness of through-the-thickness reinforced graphite/epoxy," in *27th Structures, Structural Dynamics and Materials Conference*, 1989, p. 1020.

[110] K. Dransfield, C. Baillie, Y. Mai, K. Dransfield, C. Baillie, and Y. Mai, "Improving the delamination resistance of CFRP by stitching—a review," *Compos. Sci. Technol.*, vol. 50, pp. 305–317, 1994.

[111] M. B. Dow and H. B. Dexter, "Development of Stitched , Braided and Woven Composite Structures in the ACT Program and at Langley Research Center (1985-1997)- Summary and bibliography," Hampton, Virginia, 1997.

[112] A. Morales, “Structural stitching of textile preforms,” *Adv. Mater. Look. Ahead to 21 st Century*, pp. 1217–1230, 1990.

[113] A. Ogale and P. Mitschang, “Tailoring of Textile Preforms for Fibre-reinforced Polymer Composites,” *J. Ind. Text.*, vol. 34, no. 2, pp. 77–96, 2004.

[114] A. P. Mouritz and B. N. Cox, “A mechanistic approach to the properties of stitched laminates,” *Compos. Part A Appl. Sci. Manuf.*, vol. 31, pp. 1–27, 2000.

[115] F. Aymerich, C. Pani, and P. Priolo, “Effect of stitching on the low-velocity impact response of [03/903]s graphite/epoxy laminates,” *Compos. Part A Appl. Sci. Manuf.*, vol. 38, pp. 1174–1182, 2007.

[116] D. M. Lombetti, A. A. Skordos, and I. K. Partridge, “Delamination performance of tufted carbon/epoxy composites made by automated dry fibre placement,” in *Proceedings of the 19th International Conference on Composite Materials (ICCM-19).*, pp. 1–7.

[117] L. Chen, P. G. Ifju, and B. V. Sankar, “A Novel Double Cantilever Beam Test for Stitched Composite Laminates,” *J. Compos. Mater.*, vol. 35, no. 13, pp. 1137–1149, 2000.

[118] L. K. Jain and Y.-W. Mai, “Recent work on stitching of laminated composites–theoretical analysis and experiments,” in *Proceedings of the ICCM-11*, 1997.

[119] K. A. Dransfield, L. K. Jainb, and Y. Mai, “On the effects of stitching in CFRPs—I. Mode I delamination toughness,” *Compos. Sci. Technol.*, vol. 58, no. 6, pp. 815–827, 1998.

[120] V. A. Guénon, T. W. Chou, and J. W. Gillespie, “Toughness properties of a three-dimensional carbon-epoxy composite,” *J. Mater. Sci.*, vol. 24, no. 11, pp. 4168–4175, 1989.

[121] S. Hashemi, A. J. Kinloch, and J. G. Williams, “The effects of geometry, rate and temperature on the mode I, mode II and mixed-mode I/II interlaminar fracture of carbon-fibre/poly (ether-ether ketone) composites,” *J. Compos. Mater.*, vol. 24, no. 9, pp. 918–956, 1990.

[122] Z. Aboura, M. L. Benzeggagh, F. Billaut, and B. Dambrine, “Mode I interlaminar failure of stitched textile composites materials: Proposition of predictive reinforcement model,” in *Proceedings of the ICCM-10*, 1995.

[123] L. K. Jain, K. A. Dransfield, and Y. W. Mai, “Effect of reinforcing tabs on the mode I delamination toughness of stitched CFRPs,” *J. Compos. Mater.*, vol. 32, no. 22, pp. 2016–2041, 1998.

[124] B. V Sankar and S. K. Sharmab, “Mode II delamination toughness of stitched graphite/epoxy textile composites,” *Compos. Sci. Technol.*, vol. 57, no. 7, pp. 729–737, 1997.

[125] L. K. Jain, K. A. Dransfieldb, and Y. Ma, “On the effects of stitching in CFRPs—II. Mode II delamination toughness,” *Compos. Sci. Technol.*, vol. 58, no. 6, pp. 829–837, 1998.

[126] L. K. Jain and Y. Ma, “Determination of mode II delamination toughness of stitched laminated composites,” *Compos. Sci. Technol.*, vol. 55, no. 3, pp. 241–253, 1995.

[127] Y. Ogo, “The effect of stitching on in-plane and interlaminar properties of carbon-epoxy fabric laminates,” University of Delaware, 1987.

[128] L. K. Jain, K. Dransfleld, Y. W. Mai, and C. Baillie, “Improvement of interlaminar properties in advanced fibre composites with through-thickness reinforcement,” *Coop. Res. Cent. Aerosp. Struct. Ltd., CRC-AS TM94012*, 1994.

[129] M. Ravandi, W. S. Teo, L. Q. N. Tran, M. S. Yong, and T. E. Tay, “The effects of through-the-thickness stitching on the Mode I interlaminar fracture toughness of flax/epoxy composite laminates,” *J. Mater. Des.*, vol. 109, pp. 659–669, 2016.

[130] J. G. Funk, H. B. Dexter, and S. J. Lubowinski, “Experimental evaluation of stitched graphite/epoxy composites,” in *NASA Conference Publication*, 1985, vol. 2420, pp. 185–205.

[131] K. R. Vijayakumar and U. T. Rasheed, “Impact damage resistance of thin stitched carbon / epoxy laminates Impact damage resistance of thin stitched carbon / epoxy laminates,” in *Journal of Physics: Conference Series*, 2015, vol. 628, no. 1, p. 012099.

[132] E. Wu and J. Wang, “Behavior of Stitched Laminates under In-Plane Tensile and Transverse Impact Loading,” *J. Compos. Mater.*, vol. 29, no. 17, pp. 2254–2279, 1995.

[133] W. C. Chung, B. Z. Jang, L. R. Hwang, and R. C. Wilcox, “Fracture Behavior in Stitched Multidirectional Composites,” *Mater. Sci. Eng. A*, vol. 112, pp. 157–173, 1989.

[134] M. V. Hosur, U. K. Vaidya, C. Ulven, and S. Jeelani, “Performance of stitched / unstitched woven carbon / epoxy composites under high velocity impact loading,” *Compos. Struct.*, vol. 64, no. 3–4, pp. 455–466, 2004.

[135] F. Larsson, “Damage tolerance of a stitched carbon/epoxy laminate,” *Compos. Part A Appl. Sci. Manuf.*, vol. 28, no. 11, pp. 923–934, 1997.

[136] A. P. Mouritz, “Ballistic impact and explosive blast resistance of stitched composites,” *Compos. Part B Eng.*, vol. 32, no. 5, pp. 431–439, 2001.

[137] G. L. Farley, B. T. Smith, and J. Maiden, “Compression Response of Thick Layer Composite Laminates with Through- the-Thickness Reinforcement,” *J. Reinf. Plast. Compos.*, vol. 11, no. 7, pp. 787–810, 1992.

[138] T. J. Kang and S. H. Lee, “Effect of stitching on the mechanical and impact properties of woven laminate composite,” *J. Compos. Mater.*, vol. 28, no. 16, pp. 1574–1587, 1994.

[139] G. L. Farley and L. C. Dickinson, “Removal of Surface Loop from Stitched Composites Can Improve Compression and Compression-after-Impact Strengths,” *J. Reinf. Plast. Compos.*, vol. 11, pp. 633–642, 1992.

[140] C. Scarponi, A. M. Perillo, L. Cutillo, and C. Foglio, “Advanced TTT composite materials for aeronautical purposes : Compression after impact ( CAI ) behaviour,” *Compos. Part B Eng.*, vol. 38, no. 2, pp. 258–264, 2007.

[141] V. Sankar and K. Sharma, “Effects of stitching on fracture toughness of uniweave textile graphite/epoxy laminates,” in *Nasa Research Center Mechanics of Textile Composites Conference*, 1995, pp. 481–507.

[142] A. Yudhanto, N. Watanabe, Y. Iwahori, and H. Hoshi, “The effects of stitch orientation on the tensile and open hole tension properties of carbon/epoxy plain weave laminates,”

*Mater. Des.*, vol. 35, pp. 563–571, 2012.

[143] F. Billaut, "Mechanical behavior of 3-D graphite/epoxy composites," Technomic Publishing Co., Inc., Lancaster, PA (United States), 1994.

[144] A. P. Mouritz, K. H. Leong, and I. Herszberg, "A review of the effect of stitching on the in-plane mechanical properties of fibre-reinforced polymer composites," *Compos. Part A Appl. Sci. Manuf.*, vol. 28, no. A, pp. 979–991, 1997.

[145] X. Du, F. Xue, and Z. Gu, "Experimental study of the effect of stitching on strength of a composite laminate," in *Proceedings of the international symposium on composite materials & structures*, 1986, pp. 10–13.

[146] R. Kamiya and T. Chou, "Strength and Failure Behavior of Stitched Carbon / Epoxy Composites," *Metall. Mater. Trans. A*, vol. 31, no. 13, pp. 899–909, 2000.

[147] D. M. Lombetti, "Tufting of complex composite structures," Cranfield University, 2015.

[148] C. Sickinger and A. Herrmann, "Structural Stitching as a Method to design High-Performance Composites in Future," *Proc. TechTextil Symp.*, 2001.

[149] K. S. L. Keilmann, "Innovative techniques to connect technical textiles," in *Society for the Advancement of Material and Process Engineering. International SAMPE Europe conference*, 2002, pp. 565–567.

[150] P. Mitschang, "Structural stitching of non-crimp fabric preforms for composites," in *Non-crimp fabric composites*, Woodhead Publishing Limited, 2011, pp. 67–83.

[151] J. Wittig, "Recent development in the robotic stitching technology for textile structural composites," *J. Text. apparel, Technol. Manag.*, vol. 2, no. 1, pp. 1–8, 2001.

[152] W. Trabelsi, L. Michel, and R. Othomene, "Effects of Stitching on Delamination of Satin Weave Carbon-Epoxy Laminates Under Mode I , Mode II and Mixed-Mode I / II Loadings," *Appl. Compos. Mater.*, vol. 17, no. 6, pp. 575–595, 2010.

[153] C. Leduc, S. Joncas, and J. Leclerc, "Effect of process parameters on damage tolerance of carbon epoxy laminate preformed using one-sided stitching," in *In ECCM16-16th*

*European Conference on Composite Materials*, 2014, no. June, pp. 22–26.

[154] T. Buns, “Préformage de pièces composites 3D par couture" one-sided" et renforcement par touffetage,” École de Technologie Supérieure du Québec, 2015.

[155] J. Bigaud, Z. Aboura, A. T. Martins, and S. Verger, “Analysis of the mechanical behavior of composite T-joints reinforced by one side stitching,” *Compos. Struct.*, vol. 184, pp. 249–255, 2018.

[156] J. Sloan, “Integrated, optimized aircraft door,” *CompositesWorld*, 2012. .

[157] A. Riccio, P. Linde, A. Raimondo, A. Buompane, and A. Sellitto, “On the use of selective stitching in stiffened composite panels to prevent skin-stringer debonding,” *Compos. Part B Eng.*, vol. 124, pp. 64–75, 2017.

[158] S. Black, “An Elegant Solution For A Big Composite Part - The rear pressure bulkhead for the Airbus A380 employs resin film infusion,” *CompositesWorld*, 2003. .

[159] M. Herkt, “Process chain for a robot assisted manufacturing of sewed fiber reinforced preforms,” University of Stuttgart, 2014.

[160] A. Mouritz, “Fatigue of 3D textile-reinforced composites,” in *Fatigue of Textile Composites*, Elsevier, 2015, p. 255.

[161] D. Karuppannan *et al.*, “Effect of Tufting on Mechanical Properties of Laminated Composites,” in *ISAMPE National Conference on composite Materials*, 2012, pp. 2–3.

[162] A. P. Mouritz and B. N. Cox, “A mechanistic interpretation of the comparative in-plane mechanical properties of 3D woven, stitched and pinned composites,” *Compos. Part A Appl. Sci. Manuf.*, vol. 41, no. 6, pp. 709–728, 2010.

[163] G. Dell’Anno *et al.*, “Exploring mechanical property balance in tufted carbon fabric/epoxy composites,” *Compos. Part A Appl. Sci. Manuf.*, vol. 38, no. 11, pp. 2366–2373, 2007.

[164] M. Colin de Verdiere *et al.*, “Evaluation of the mechanical and damage behaviour of tufted non crimped fabric composites using full field measurements,” *Compos. Sci.*

*Technol.*, vol. 69, no. 2, pp. 131–138, 2009.

[165] A. Yudhanto, N. Watanabe, Y. Iwahori, and H. Hoshi, "Compression properties and damage mechanisms of stitched carbon / epoxy composites," *Compos. Sci. Technol.*, vol. 86, pp. 52–60, 2013.

[166] V. Carvelli, V. Koissin, J. Kustermans, S. V Lomov, V. N. Tomaselli, and B. Van Den Broucke, "Progressive damage in stitched composites : Static tensile tests and tension-tension fatigue," in *Proceedings of the 17th International Conference on Composite Materials (ICCM-17).*, 2009.

[167] V. Koissin *et al.*, "Structurally stitched NCF preforms : Quasi-static response," *Compos. Sci. Technol.*, vol. 69, no. 15–16, pp. 2701–2710, 2009.

[168] A. Yudhanto, G. Lubineau, I. A. Ventura, N. Watanabe, Y. Iwahori, and H. Hoshi, "Damage characteristics in 3D stitched composites with various stitch parameters under in-plane tension," *Compos. Part A Appl. Sci. Manuf.*, vol. 71, pp. 17–31, 2015.

[169] J. Treiber, D. D. R. Cartié, and I. K. Partridge, "Effects of mesostructure on the in-plane properties of tufted carbon fabric composites.," *CompTest*. Cranfield University, pp. 2–4, 2011.

[170] K. P. Plain and L. Tong, "The effect of stitch incline angle on mode I fracture toughness – Experimental and modelling," *Compos. Struct.*, vol. 92, no. 7, pp. 1620–1630, 2010.

[171] G. Pappas, S. Joncas, V. Michaud, and J. Botsis, "The influence of through-thickness reinforcement geometry and pattern on delamination of fiber-reinforced composites : Part I – Experimental results," *Compos. Struct.*, vol. 184, pp. 924–934, 2018.

[172] M. Troulis, I. K. Partridge, and D. D. R. Cartie, "SCIENCE AND Delamination of Z-pinned carbon fibre reinforced laminates," vol. 66, pp. 855–861, 2006.

[173] J. Bigaud, "Analyse du comportement mécanique de structures composites renforcées par coutures," Université de Technologie de Compiègne, 2016.

[174] M. C. De Verdiere, A. A. Skordos, M. May, and A. C. Walton, "Influence of loading rate on the delamination response of untufted and tufted carbon epoxy non crimp fabric

composites : Mode I," *Eng. Fract. Mech.*, vol. 96, pp. 11–25, 2012.

[175] P. Deconinck, J. Capelle, V. Bouchart, P. Chevrier, and F. Ravailler, "Delamination propagation analysis in tufted carbon fibre-reinforced plastic composites subjected to high-velocity impact," *J. Reinf. Plast. Compos.*, vol. 33, no. 14, pp. 1353–1363, 2014.

[176] M. C. De Verdiere, A. K. Pickett, A. A. Skordos, and V. Witzel, "Effect of tufting on the response of non crimp fabric composites," in *ECCOMAS Thematic Conference on Mechanical Response ofComposites*, 2007.

[177] B. Najafloo, A. M. Rezadoust, M. Latifi, and R. Plastics, "Effect of through-the-thickness areal density and yarn fineness on the mechanical performance of three-dimensional ... Effect of through-the-thickness areal density and yarn fineness," *J. Reinf. Plast. Compos.*, vol. 35, no. 20, pp. 1447–1459, 2016.

[178] B. Lascoup, Z. Aboura, K. Khellil, and M. Benzeggagh, "On the mechanical effect of stitch addition in sandwich panel," *Compos. Sci. Technol.*, vol. 66, no. 10, pp. 1385–1398, 2006.

[179] B. Lascoup, Z. Aboura, K. Khellil, and M. Benzeggagh, "Impact response of three-dimensional stitched sandwich composite," *Compos. Struct.*, vol. 92, no. 2, pp. 347–353, 2010.

[180] S. Samlal, V. Paulson, and R. Santhanakrishnan, "Effect of Stitching Angle on Impact Characteristics of Sandwich Panels," *Int J Innov Res Sci Eng Technol*, vol. 4, no. 12, pp. 30–34, 2015.

[181] A. Henao *et al.*, "Enhanced Impact Energy Absorption Characteristics of Sandwich Composites through Tufting," *Mech. Adv. Mater. Struct.*, vol. 22, pp. 016-1023, 2014.

[182] F. Xia and X. Wu, "Study on impact properties of through-thickness stitched foam sandwich composites," *Compos. Struct.*, vol. 92, no. 2, pp. 412–421, 2010.

[183] C. Mittelstedt and M. Beerhorst, "Closed-form buckling analysis of compressively loaded composite plates braced by omega-stringers," *Compos. Struct.*, vol. 88, no. 3, pp. 424–435, 2009.

[184] Y. Feng, Y. He, H. Zhang, X. Tan, T. An, and J. Zheng, “Effect of fatigue loading on impact damage and buckling / post-buckling behaviors of stiffened composite panels under axial compression,” *Compos. Struct.*, vol. 164, pp. 248–262, 2016.

[185] W. Wang, S. Guo, N. Chang, and W. Yang, “Optimum buckling design of composite stiffened panels using ant colony algorithm,” *Compos. Struct.*, vol. 92, no. 3, pp. 712–719, 2010.

[186] J. . Kratz, H. . Clegg, G. . Dell ’ Anno, and I. . K. . Partridge, “Improving the damage tolerance of composite joints with tufting,” in *Proceedings of the 20th International Conference on Composite Materials ( ICCM20)*, 2015.

[187] H. M. Clegg and J. Kratz, “Evaluation of the effects of Tufting on the performance of composite T-joints,” in *Proceedings of the 17th International Conference on Composite Materials (ICCM-17).*, 2016, no. February 2018, pp. 1–7.

[188] P. B. Stickler and M. Ramulu, “Investigation of mechanical behavior of transverse stitched T-joints with PR520 resin in flexure and tension,” *Compos. Struct.*, vol. 52, pp. 307–314, 2001.

[189] P. B. Stickler, M. Ramulu, and P. S. Johnson, “Experimental and numerical analysis of transverse stitched T-joints in bending,” *Compos. Struct.*, vol. 50, pp. 17–27, 2000.

[190] P. Taylor, and M. Ramulu, “Experimental study of composite T- joints under tensile and shear loading,” *Advanced Composite Materials*, vol. 15, no 2, pp. 193-210, 2006.

[191] A. R. Mills and J. Jones, “Investigation , manufacture , and testing of damage-resistant airframe structures using low-cost carbon fibre composite materials,” in *Proceedings of the Institution of Mechanical Engineers, Part G: Journal of Aerospace Engineering*, 2009, vol. 224, no. 4, pp. 489–497.

[192] M. Préau, J. Treiber, and I. Partridge, “Comportement et endommagement d’ un raidisseur Ω carbone/époxy renforcé par tufting,” in *17èmes Journées Nationales sur les Composites (JNC17)*, 2011, pp. 1–5.

[193] L. S. Liu, P. Wang, X. Legrand, and D. Soulat, “Investigation of mechanical properties of tufted composites : Influence of tuft length through the thickness reinforcement,”

*Compos. Struct.*, vol. 172, pp. 221–228, Jul. 2017.

[194] M. R. Abusrea and K. Arakawa, "Enhanced tensile strength CFRP adhesive joint constructed from carbon fiber-reinforced plastic and dry carbon fiber laminates," in *Proceedings of the 17th International Conference on Composite Materials ( ICCM17)*, 2016.

[195] ASTM D7136, "Standard test method for measuring the damage resistance of a fiber-reinforced polymer matrix composite to a drop-weight impact event," *ASTM International: West Conshohocken*. ASTM International, West, Conshohocken, PA, 2005.

[196] N. Mccormick and J. Lord, "Digital Image Correlation," *Mater. Today*, vol. 13, no. 12, pp. 52–54, 2010.

[197] "Measurement Principles of (DIC)," *DANTEC Dynamics*, 2018. [Online]. Available: https://www.dantecdynamics.com/measurement-principles-of-dic. [Accessed: 12-May-2018].

[198] K. Genovese, L. Casaletto, J. A. Rayas, V. Flores, and A. Martinez, "Stereo-Digital Image Correlation ( DIC ) measurements with a single camera using a biprism," *Opt. Lasers Eng.*, vol. 51, no. 3, pp. 278–285, 2013.

[199] N. Mccormick, J. Lord, "Digital Image Correlation (DIC)." *Materials Today*, vol. 13, no. 12, pp. 52-53, 2010.

[200] M. Huang, L. Jiang, P. K. Liaw, C. R. Brooks, R. Seeley, and D. L. Klarstrom, "Using acoustic emission in fatigue and fracture materials research," *JOM*, vol. 50, no. 11, pp. 1–14, 1998.

[201] J. Kaiser, "Erkenntnisse und Folgerungen aus der Messung von Geräuschen bei Zugbeanspruchung von metallischen Werkstoffen," *steel Res. Int.*, vol. 24, no. 1–2, pp. 43–45, 1953.

[202] A. Laksimi, S. Benmedakhene, and L. Bounouas, "Monitoring acoustic emission during tensile loading of thermoplastic composites materials," in *Proceedings of the 12th International Conference on Composite Materials ( ICCM12)*, 1999.

[203] J. Kakakasery *et al.*, “Cure cycle effect on impact resistance under elevated temperatures in carbon prepreg laminates investigated using acoustic emission,” *Compos. Part B*, vol. 75, pp. 298–306, 2015.

[204] R. Boominathan, V. Arumugam, C. Santulli, A. A. Plato, R. A. Sankar, and B. T. N. Sridhar, “Composites : Part B Acoustic emission characterization of the temperature effect on falling weight impact damage in carbon / epoxy laminates,” *Compos. Part B*, vol. 56, pp. 591–598, 2014.

[205] J. J. Andrew, V. Arumugam, K. Saravanakumar, H. N. Dhakal, and C. Santulli, “Compression after impact strength of repaired GFRP composite laminates under repeated impact loading,” *Compos. Struct.*, vol. 133, pp. 911–920, 2015.

[206] D. Scida, Z. Aboura, and M. L. Benzeggagh, “The effect of ageing on the damage events in woven-fibre composite materials under different loading conditions,” *Compos. Sci. Technol.*, vol. 62, no. 4, pp. 551–557, 2002.

[207] P. J. De Groot, P. A. M. Wijnen, and R. B. F. Janssen, “Real-time frequency determination of acoustic emission for different fracture mechanisms in carbon/epoxy composites,” *Compos. Sci. Technol.*, vol. 55, no. 4, pp. 405–412, 1995.

[208] S. Barr and M. L. Benzeggagh, “On the use of acoustic emission to investigate damage mechanisms in glass-fibre-reinforced polypropylene,” *Compos. Sci. Technol.*, vol. 52, no. 3, pp. 369–376, 1994.

[209] S. Pawlak, “A comparison study of the pulse-echo and through-transmission ultrasonics in glass / epoxy composites,” *J. Achiev. Mater. Manuf. Eng.*, vol. 22, no. 2, pp. 51–54, 2007.

[210] “C-Scan mapping.” [Online]. Available: https://www.olympus-ims.com/en/ndt-tutorials/instrumententation/cscan/. [Accessed: 15-Jul-2018].

[211] A. Fahr, “Ultrasonic C-scan inspection of composite materials,” *Eng. Qatar Univ.*, vol. 5, pp. 201–222, 1992.

[212] L. Liu, B. Zhang, D. Wang, and Z. Wu, “Effects of cure cycles on void content and mechanical properties of composite laminates,” *Compos. Struct.*, vol. 73, no. 3, pp. 303–

309, 2006.

[213] Y. O. Kas and C. Kaynak, “Ultrasonic ( C-scan ) and microscopic evaluation of resin transfer molded epoxy composite plates,” *Polym. Test.*, vol. 24, no. 1, pp. 114–120, 2017.

[214] K. Imieli, M. Castaings, R. Wojtyra, J. Haras, E. Le Clezio, and B. Hosten, “Air-coupled ultrasonic C-scan technique in impact response testing of carbon fibre and hybrid : glass , carbon and Kevlar / epoxy composites,” *J. Mater. Process. Technol.*, vol. 157, pp. 513–522, 2004.

[215] R. Suvarna, V. Arumugam, D. J. Bull, A. R. Chambers, and C. Santulli, “Effect of temperature on low velocity impact damage and post-impact flexural strength of CFRP assessed using ultrasonic C-scan and micro-focus computed tomography,” *Compos. Part B*, vol. 66, pp. 58–64, 2014.

[216] D. D. R. Cartie and P. E. Irving, “Effect of resin and fibre properties on impact and compression after impact performance of CFRP,” *Compos. part A Appl. Sci. Manuf.*, vol. 33, no. 4, pp. 483–493, 2002.

[217] M. Barus *et al.*, “Bonded repair issues for composites: An investigation approach based on infrared thermography,” *NDT E Int.*, vol. 85, pp. 27–33, 2017.

[218] S. A. Grammatikos, E. Z. Kordatos, T. E. Matikas, and A. S. Paipetis, “On the fatigue response of a bonded repaired aerospace composite using thermography,” *Compos. Struct.*, vol. 188, pp. 461–469, 2018.

[219] M. Barus *et al.*, “NDT-based design of joint material for the detection of bonding defects by infrared thermography,” *NDT E Int.*, vol. 93, pp. 157–163, 2018.

[220] R. V Prakash and M. Maharana, “Damage Detection using Infrared Thermography in a Carbon-Flax Fiber Hybrid Composite,” in *Procedia Structural Integrity*, 2017, vol. 7, pp. 283–290.

[221] Y. Li, Z. wei Yang, J. tang Zhu, A. bo Ming, W. Zhang, and J. yu Zhang, “Investigation on the damage evolution in the impacted composite material based on active infrared thermography,” *NDT E Int.*, vol. 83, pp. 114–122, 2016.

[222] S. Boccardi, G. M. Carlomagno, C. Meola, G. Simeoli, and P. Russo, “Infrared thermography to evaluate thermoplastic composites under bending load,” *Compos. Struct.*, vol. 134, pp. 900–904, 2015.

[223] C. Meola *et al.*, “Impact damaging of composites through online monitoring and non-destructive evaluation with infrared thermography,” *NDT E Int.*, vol. 85, pp. 34–42, 2017.

[224] C. Meola, S. Boccardi, G. M. Carlomagno, N. D. Boffa, E. Monaco, and F. Ricci, “Nondestructive evaluation of carbon fibre reinforced composites with infrared thermography and ultrasonics,” *Compos. Struct.*, vol. 134, pp. 845–853, 2015.

[225] T. Lisle, M. L. Pastor, C. Bouvet, and P. Margueres, “Damage of woven composite under translaminar cracking tests using infrared thermography,” *Compos. Struct.*, vol. 161, pp. 275–286, 2017.

[226] T. Lisle, C. Bouvet, N. Hongkarnjanakul, M. L. Pastor, S. Rivallant, and P. Margueres, “Measure of fracture toughness of compressive fiber failure in composite structures using infrared thermography,” *Compos. Sci. Technol.*, vol. 112, pp. 22–33, 2015.

[227] ASTM D2344/ D2344M, “Standard Test Method for Short-Beam Strength of Polymer Matrix Composite Materials and Their Laminates.” ASTM International, West, Conshohocken, PA, 2013.

[228] ASTM 6641/ D6641M-09, “Standard Test Method for Compressive Properties of Polymer Matrix Composite Materials Using a Combined Loading Compression (CLC) Test Fixture.” ASTM International, West, Conshohocken, PA, 2009.

[229] ASTM D7137, “Standard Test Method for Compressive Residual Strength Properties of Damaged Polymer Matrix Composite Plates.” ASTM International, West, Conshohocken, PA, 2012.

[230] T. D. Mcquigg, “Compression after impact experiments and analysis on honeycomb core sandwich panels with thin facesheets,” Virginia Tech, 2011.

[231] B. Vieille, V. M. Casado, and C. Bouvet, “Influence of matrix toughness and ductility on the compression-after-impact behavior of woven-ply thermoplastic- and

thermosetting-composites: A comparative study," *Compos. Struct.*, vol. 110, no. 1, pp. 207–218, 2014.

[232] A. T. Rhead, S. Hua, and R. Butler, "Damage resistance and damage tolerance of hybrid carbon-glass laminates," *Compos. Part A Appl. Sci. Manuf.*, vol. 76, pp. 224–232, 2015.

[233] Y. Song, "Évaluation de l'apport simultané des coutures sur la perméabilité des préformes cousues et sur les performances mécaniques des structures composites cousues," Université de Technologie de Compiègne, 2015.

[234] N. Alif, L. A. Carlsson, and L. Boogh, "The effect of weave pattern and crack propagation direction on mode I delamination resistance of woven glass and carbon," *Compos. Part B*, vol. 29, no. 5, pp. 603–611, 1998.

[235] A. F. Gill, P. Robinson, and S. Pinho, "Effect of variation in fibre volume fraction on modes I and II delamination behaviour of 5HS woven composites manufactured by RTM," *Compos. Sci. Technol.*, vol. 69, no. 14, pp. 2368–2375, 2009.

[236] R. Balaji and M. Sasikumar, "Development of strain and damage monitoring system for polymer composites with embedded nickel alloys," *Measurement*, vol. 111, pp. 307–315, 2017.

[237] C. L. Wilson, K. Lonkar, S. Roy, F. Kopsaftopoulos, and F.-K. Chang, "7.20 Structural Health Monitoring of Composites," 2018.

[238] G. Rajan and B. G. Prusty, *Structural Health Monitoring of Composite Structures Using Fiber Optic Methods*. CRC Press, 2016.

[239] R. Di Sante, "Fibre Optic Sensors for Structural Health Monitoring of Aircraft Composite Structures: Recent Advances and Applications," *Sensors*, vol. 15, pp. 18666–18713, 2015.

[240] K. Lau and L. Zhou, "The mechanical behaviour of composite-wrapped concrete cylinders subjected to uniaxial compression load," *Compos. Struct.*, vol. 52, pp. 189–198, 2001.

[241] D. Balageas, "Introduction to structural health monitoring," in *Structural Health*

*Monitoring*, Wiley Online Library, 2010.

[242] M. Rothmaier, M. P. Luong, and F. Clemens, "Textile Pressure Sensor Made of Flexible Plastic Optical Fibers," *Sensors*, vol. 8, pp. 4318–4329, 2008.

[243] S. Masmoudi, A. El, and S. Turki, "Use of piezoelectric as acoustic emission sensor for in situ monitoring of composite structures," vol. 80, pp. 307–320, 2015.

[244] Y. J. Yan and L. H. Yam, "Online detection of crack damage in composite plates using embedded piezoelectric actuators / sensors and wavelet analysis," *Compos. Struct.*, vol. 58, pp. 29–38, 2002.

[245] G. Park, C. R. Farrar, A. C. Rutherford, and A. N. Robertson, "Piezoelectric active sensor self-diagnostics using electrical admittance measurements," *J. Vib. Acoust.*, vol. 128, no. 4, pp. 469–476, 2006.

[246] C. I. Merzbacher, A. D. Kersey, and E. J. Friebele, "Fiber optic sensors in concrete structures: a review," *Smart Mater. Struct.*, vol. 5, no. 2, p. 196, 1996.

[247] B. R. Loyola, V. La Saponara, and K. J. Loh, "In situ strain monitoring of fiber-reinforced polymers using embedded piezoresistive nanocomposites," *J. Mater. Sci.*, vol. 45, pp. 6786–6798, 2010.

[248] Z. Qiu, X. Yao, J. Yuan, and C. Soutis, "Experimental research on strain monitoring in composite plates using embedded SMA wires," *Smart Mater. Struct.*, vol. 15, no. 4, p. 1047, 2006.

[249] G. Yuan, Y. Bai, Z. Jia, D. Hui, and K. Lau, "Enhancement of interfacial bonding strength of SMA smart composites by using mechanical indented method," *Compos. Part B*, vol. 106, pp. 99–106, 2016.

[250] A. Todoroki, K. Omagari, Y. Shimamura, and H. Kobayashi, "Matrix crack detection of CFRP using electrical resistance change with integrated surface probes," *Compos. Sci. Technol.*, vol. 66, pp. 1539–1545, 2006.

[251] K. Schulte and C. Baron, "Load and Failure Analyses of CFRP Laminates by Means of Electrical Resistivity Measurements," *Compos. Sci. Technol.*, vol. 36, pp. 63–76, 1989.

[252] O. Ceysson, M. Salvia, and L. Vincent, “Damage mechanisms characterization of carbon fiber/epoxy composite laminates by both electrical resistance measurements and acoustic emission analysis,” *Scr. Mater.*, vol. 34, no. 8, 1996.

[253] J. C. Abry, S. Bochard, A. Chateauminois, M. Salvia, and G. Giraud, “In situ detection of damage in CFRP laminates by electrical resistance measurements,” *Compos. Sci. Technol.*, vol. 59, pp. 925–935, 1999.

[254] K. Ogi and Y. Takao, “Characterization of piezoresistance behavior in a CFRP unidirectional laminate,” *Compos. Sci. Technol.*, vol. 65, pp. 231–239, 2005.

[255] R. B. Ladani, S. Wu, A. J. Kinloch, K. Ghorbani, A. P. Mouritz, and C. H. Wang, “Enhancing fatigue resistance and damage characterisation in adhesively-bonded composite joints by carbon nanofibres,” *Compos. Sci. Technol.*, vol. 149, pp. 116–126, 2017.

[256] V. K. Vadlamani, V. Chalivendra, A. Shukla, and S. Yang, “In situ sensing of non-linear deformation and damage in epoxy particulate composites,” *Smart Mater. Struct.*, vol. 21, 2012.

[257] L. Böger, M. H. G. Wichmann, L. O. Meyer, and K. Schulte, “Load and health monitoring in glass fibre reinforced composites with an electrically conductive nanocomposite epoxy matrix,” *Compos. Sci. Technol.*, vol. 68, pp. 1886–1894, 2008.

[258] H. Zhang, Y. Liu, M. Kuwata, E. Bilotti, and T. Peijs, “Improved fracture toughness and integrated damage sensing capability by spray coated CNTs on carbon fibre prepreg,” *Compos. Part A*, vol. 70, pp. 102–110, 2015.

[259] P. Ma, B. Hao, Q. Ma, S. Yang, and M. Edith, “Comparative study on monitoring structural damage in fiber- reinforced polymers using glass fibers with carbon nanotubes and graphene coating,” *Compos. Sci. Technol.*, vol. 129, pp. 38–45, 2016.

[260] A. Erklig, N. F. Dogan, and M. Bulut, “Charpy Impact Response of Glass Fiber Reinforced Composite with Nano Graphene Enhanced Epoxy,” *Period. Eng. Nat. Sci.*, vol. 5, no. 3, pp. 341–346, 2017.

[261] K. Hamdi, Z. Aboura, W. Harizi, and K. Khellil, “Improvement of the electrical

conductivity of carbon fiber reinforced polymer by incorporation of nanofillers and the resulting thermal and mechanical behavior," *J. Compos. Mater.*, pp. 1–9, 2017.

[262] ASTM C635 / C635M - 17, "Standard Specification for Manufacture, Performance, and Testing of Metal Suspension Systems for Acoustical Tile and Lay-in Panel Ceilings." ASTM International, West, Conshohocken, PA, 2017.

[263] N. Angelidis, C. Y. Wei, and P. E. Irving, "The electrical resistance response of continuous carbon fibre composite laminates to mechanical strain," *Compos. Part A Appl. Sci. Manuf.*, vol. 35, no. 10, pp. 1135–1147, 2004.

[264] G. Allegri, M. Yasaee, I. K. Partridge, and S. R. Hallett, "A novel model of delamination bridging via Z-pins in composite laminates," *Int. J. Solids Struct.*, vol. 51, no. 19–20, pp. 3314–3332, 2014.

[265] A. Y. Zhang, A. P. Mouritz, Y. W. Mai, H. Y. Liu, A. P. Mouritz, and Y. W. Mai, "Experimental study and computer simulation on degradation of z-pin reinforcement under cyclic fatigue," *Compos. Part A Appl. Sci. Manuf.*, vol. 39, no. 2, pp. 406–414, 2008.

[266] B. N. Cox, "Constitutive Model for a Fiber Tow Bridging a Delamination Crack," *Mech. Compos. Mater. Struct.*, vol. 6, no. 2, pp. 117–138, 1999.

[267] M. Blacklock, M. W. Joosten, K. Pingkarawat, and A. P. Mouritz, "Prediction of mode I delamination resistance of z-pinned laminates using the embedded finite element technique," *Compos. Part A Appl. Sci. Manuf.*, vol. 91, pp. 283–291, 2016.

[268] F. Bianchi, "Numerical Modelling of Through-Thickness Reinforced Structural Joints," Cranfield University, 2012.

[269] B. N. Cox, "Snubbing Effects in the Pullout of a Fibrous Rod from a Laminate," *Mech. Adv. Mater. Struct.*, vol. 12, no. 2, pp. 85–98, Mar. 2005.

[270] V. Dantuluri, S. Maiti, P. H. Geubelle, R. Patel, and H. Kilic, "Cohesive modeling of delamination in Z -pin reinforced composite laminates," *Compos. Sci. Technol.*, vol. 67, pp. 616–631, 2007.

[271] G. D. Anno, J. W. G. Treiber, and I. K. Partridge, “Robotics and Computer-Integrated Manufacturing Manufacturing of composite parts reinforced through-thickness by tufting,” *Robot. Comput. Integr. Manuf.*, vol. 37, pp. 262–272, 2016.

[272] F. Pegorin, K. Pingkarawat, S. Daynes, and A. P. Mouritz, “Influence of z-pin length on the delamination fracture toughness and fatigue resistance of pinned composites,” *Compos. Part B Eng.*, vol. 78, pp. 298–307, 2015.

[273] C. Osmiani, G. Mohamed, J. W. G. Treiber, G. Allegri, and I. K. Partridge, “Exploring the influence of micro-structure on the mechanical properties and crack bridging mechanisms of fibrous tufts,” *Compos. Part A Appl. Sci. Manuf.*, vol. 91, pp. 409–419, Dec. 2016.

[274] G. Pappas, S. Joncas, V. Michaud, and J. Botsis, “The influence of through-thickness reinforcement geometry and pattern on delamination of fiber-reinforced composites : Part II – Modeling,” *Compos. Struct.*, vol. 181, pp. 379–390, Dec. 2017.

[275] M. Yasaee, L. Bigg, G. Mohamed, and S. R. Hallett, “Influence of Z-pin embedded length on the interlaminar traction response of multi-directional composite laminates,” *J. Mater. Des.*, vol. 115, pp. 26–36, 2017.

[276] A. Turon, P. P. Camanho, J. Costa, and J. Renart, “Accurate simulation of delamination growth under mixed-mode loading using cohesive elements : Definition of interlaminar strengths and elastic stiffness,” *Compos. Struct.*, vol. 92, no. 8, pp. 1857–1864, 2010.

[277] A. Turon, C. G. Dávila, P. P. Camanho, and J. Costa, “An engineering solution for mesh size effects in the simulation of delamination using cohesive zone models,” *Eng. Fract. Mech.*, vol. 74, no. 10, pp. 1665–1682, 2007.

[278] L. Peng, “Modélisation numérique d’assemblages collés : application à la réparation de structures en composites,” Université de Bourgogne, 2013.

[279] K. Ha, H. Baek, and K. Park, “Convergence of fracture process zone size in cohesive zone modeling,” *Appl. Math. Model.*, vol. 39, pp. 5828–5836, 2015.

[280] C. Y. Hui, A. Jagota, S. J. Bennison, and J. D. Londono, “Crack blunting and the strength of soft elastic solids,” *Proc. R. Soc. A Math. Phys. Eng. Sci.*, vol. 459, pp. 1489–1516,

2003.

[281] M. L. Benzeggagh and M. Kenane, “Measurement of mixed mode delamination fracture toughness of unidirectional glass/epoxy composites with mixed mode bending apparatus.,” *Compos. Sci. Technol.*, vol. 56, pp. 439–449, 1996.

# APPENDIX A - FINITE ELEMENT MODELING

## Introduction

The present work proposes a numerical simulation by the finite element method (FEM) to minimize the counter effects caused by the tufting insertion and improve the mechanical behavior of the composites structures. The proposed technique considers optimizing the structure response from the tufting parameters and thread properties using a trial-and-error approach.

There is a lack of studies in the literature concerning numerical models applied to through-thickness reinforcements, especially to the tufting method. The toughening mechanisms have been reported for the Z-pins reinforcements in micro-mechanical models [264]–[266] and subsequently applied to mesoscale models [267]–[270] to simulate the bridging effects of the reinforcements. The mesoscale models employed discrete non-linear springs, cohesive elements or combining the two approaches to reproduce the bridging behavior. However, the force-separation behavior of composites reinforced by tufting differs entirely from the z-pinned composites because tufts can cause failure by breaking in the delamination plane or pulling partially out [193] while for the z-pins the damages are in the majority due to pull-out in the two pure failure modes I and II [271], [272].

Osmiani et al. [273] developed an FE model based on experimental data obtained by mode I loading tests, which predicts the delamination propagation and the crack bridging behavior of the tufts. They used a cohesive zone model (CZM) to simulate delamination. The beam shaped for 8-node reduced integration of solid elements and bonded in the middle plane of the thickness by cohesive elements, to simulate the threads rupture, modeled the tufts. Also, the model has been considered the fracture along the interface tuft/composite observed in the experimental data that is probably due to the pull out of the tuft threads. Pappas et al. [274] also reported a numerical model from the experimental investigation of the mode I loading to tufted composites. They implemented a CZM to create delamination in the interface and 1D connector elements for discrete tufts to produce the bridging response. Unidirectional connectors have the properties based on the separation force obtained by uniaxial pulling tests of the threads. The authors varied the tufting pattern and geometry (with loop and loop-less tufts) to evaluate the experimental response and utilize them in the model.

The present work studies the mechanical response of the composite omega stiffeners reinforced through-thickness by tufts under pull-off loading. This approach is different from the mentioned researches which based on single tuft pull-out and DCB tests to their models [273], [274]. The model uses the experimental results acquired during pull-off tests of the omega stiffeners to adjust their parameters, such as the cohesive elements and especially the mechanical properties of the tuft threads. The primary goals consist of validating the numerical model with the experimental data and investigate different models by changing the tufting parameters (e.g., angle, position, and density) to achieve the optimal parameters. This method can avoid time and material cost for the manufacturing of several samples with different tufting parameters to analyze their results and select the most performing.

The results obtained in this thesis for the specimens from the batch I of omega stiffeners were utilized to perform the FE model by the commercial software Abaqus 2016. The experimental results showed multiple layers delamination, mainly concentrated in the stiffener radius as already reported in Chapter 4. Therefore, the layers of cohesive elements were introduced between each composite ply to simulate the interlaminar cracks. The crack development was bridged by transversal circular beam elements embedded in the composites, from the top surface of the flange stiffener to the bottom of the skin, according to the tufting pattern. This method used for modeling the tufts allowed changing the tufting parameters with ease when compared to the others works [273], [274] and applying multiple cohesive layers without the need to modify each surface contact to create the tuft bridging.

**Finite element modeling**

The finite element modeling utilized the commercial software Abaqus 2016 to perform the analyses. The model size was reduced in comparison to the experimental dimensions of the specimens based on a symmetrical part concerning the y and x-axis to decrease the simulation time. Skin and stiffener parts employed linear hexahedral elements C3D8 for the model. The stiffener part consisted of 8 pieces that concern the number of carbon fabric plies used in the manufacturing of the structure. The cohesive layers modeled with COH3D8 cohesive elements were placed between each layer of the stiffener as well as in the contact stiffener/skin. Table A. 1 lists the elastic properties used for the composites.

The delamination growth between the layers was simulated using a cohesive zone model. Traction-separation law described the exponential softening law was employed to characterize

the delamination. The initial interface stiffness (K) must be adjusted to avoid the reduction in the global stiffness of the structure, as explained by previous authors [275]–[277]. Turon et al. [277] proposed an equation (8) to determine the mentioned parameter. This method is applied as a lower bound approach necessary to have an initial K that does not affect the global composite stiffness.

$$K = \alpha \frac{E_3}{t} \tag{8}$$

Where α is a parameter larger than 1 and shows excellent results when superior to 100, resulting on a stiffness loss less than 2% in the structure, $E_3$ is the out-of-plane Young's Modulus of the laminated composite and t, the thickness of the cohesive layer. This equation aids obtaining the lower value necessary, but additional adjustments to the experimental data are essential to achieving optimized value.

The nominal stress response to the damage initiation purely normal to the interface ($\sigma_I$) and in the first ($\sigma_{II}$) and second shear direction ($\sigma_{III}$) were also adjusted to accomplish the accurate relation with the experimental results and, especially to reach the model convergence. As reported by Turon et al. [277] and validate by Peng [278], the equation (9) allows obtaining the optimal ratio $\sigma_I/\sigma_{II}$. The authors described that the results do not change with the absolute variation of the nominal stress, in the two directions, if their ratio continues the same.

$$\frac{K_{II}}{K_I} = \frac{G_{IC}}{G_{IIC}} \left(\frac{\sigma_{II}}{\sigma_I}\right)^2 \tag{9}$$

where $K_I$ and $K_{II}$ are the interface stiffness, and $G_{IC}$ and $G_{IIC}$ are the critical fracture energy in the mode conditions I and II respectively.

The nominal stress is directly related to the cohesive zone length ($l_{cz}$) as shown in equation (10). Furthermore, $l_{cz}$ is directly proportional to the mesh size ($l_e$), and as already reported [278], the region must contain at least three elements to converge and consequently reach good results.

$$l_{cz} = M E_3 \frac{G_c}{\sigma^2} \tag{10}$$

Where $E_3$ is the out-of-plane Young's Modulus, $G_c$ is the critical fracture energy of the interface, σ is the nominal stress to the damage initiation and M a dimensionless parameter that can vary between 0.21 and 1 [279]. Based on the study by Hui et al.[280], the parameter M was maintained at 0.21, which will result in a smaller $l_{cz}$.

Equation (11) presents the relation between the cohesive zone length and mesh size ($l_e$). Then, the nominal stresses were obtained by trial and error until achieving reasonable results with optimized values of time simulation and mesh size:

$$l_e = \frac{l_{ch}}{N_e} \quad \textbf{(11)}$$

where $N_e$ is the minimum number of elements in the $l_{cz}$.

The present work utilized the energy-based damage evolution criterion proposed by Benzeggagh and Kenane (BK) [281], as described in equation (12).

$$G_c = G_{IC} + (G_{IIC} - G_{IC})\left(\frac{G_S}{G_T}\right)^{\eta} \quad \textbf{(12)}$$

Where $G_S=G_{II}+G_{III}$, $G_T=G_I+G_{II}+G_{III}$, and η is a BK material parameter. The properties used as input for the analysis by BK criterion (exhibited in Table A. 1) were obtained from previous tests in the laboratory: $G_{IC}$ on Double Cantilever Beam (DCB) tests, $G_{IIC}$ on End Notched Flexure (ENF) and $G_{II}/G_T$ ratio (15,30,45,60,75,90%) on Mixed Mode Bending (MMB).

The modeling of tuft threads utilized two-node beam elements (B31). The tufted reinforcement as a straight circular beam is a simplification in comparison to the experimental analysis in the literature. The tufted thread exhibits irregular profile and variable cross-section along its length due to the preform compaction during the molding process. The elastic and failure stress properties of the tufts were adjusted from the experimental data of the omega structures subjected to pull-off tests (Table A. 1). The ductile damage initiation and damage evolution caused by displacement described the damage behavior of the tuft threads.

The embedding process of the beam elements considered the tufts location in the specimens of the Batch I. They were inserted entirely throughout the solid and cohesive elements of the skin and flange regions. Figure A. 1 shows the scheme of the beam elements inserted into the model.

The elements were added parallel to the out-of-plane axis throughout the thickness and spaced 5 mm in the x and y-axis from each other. The beam diameter of 0.5 mm based on microscopy analysis.

**Table A. 1– Mechanical properties of the elements utilized for modeling.**

| Composites | | Cohesive | | Tuft Threads | |
|---|---|---|---|---|---|
| $E_{11} = E_{22}$ | 55 GPa | $\sigma_I$ | 30 MPa | $E_{11}$ | 70 GPa |
| $E_{33}$ | 8 GPa | $\sigma_{II} = \sigma_{III}$ | 60 MPa | $\nu_{12}$ | 0.30 |
| $G_{12}$ | 5.20 GPa | $K_I = K_{II} = K_{III}$ | $1x10^8$ N/mm$^3$ | $\varepsilon_{max}$ | 0.1 |
| $G_{23} = G_{13}$ | 2.60 GPa | $G_{IC}$ | 0.425 N/mm | $\sigma_{max}$ | 150 MPa |
| $\nu_{12}$ | 0.03 | $G_{IIC} = G_{IIIC}$ | 1.700 N/mm | | |
| $\nu_{23} = \nu_{13}$ | 0.30 | $\eta$ | 1.5 | | |

The model was constrained (fully built-in) from the rigid cylinder on the skin surface and, loaded vertically by displacement control from the other rigid cylinder on the bottom of the stiffener (Figure A. 2). The meshed finite element model is presented in Figure A. 3.

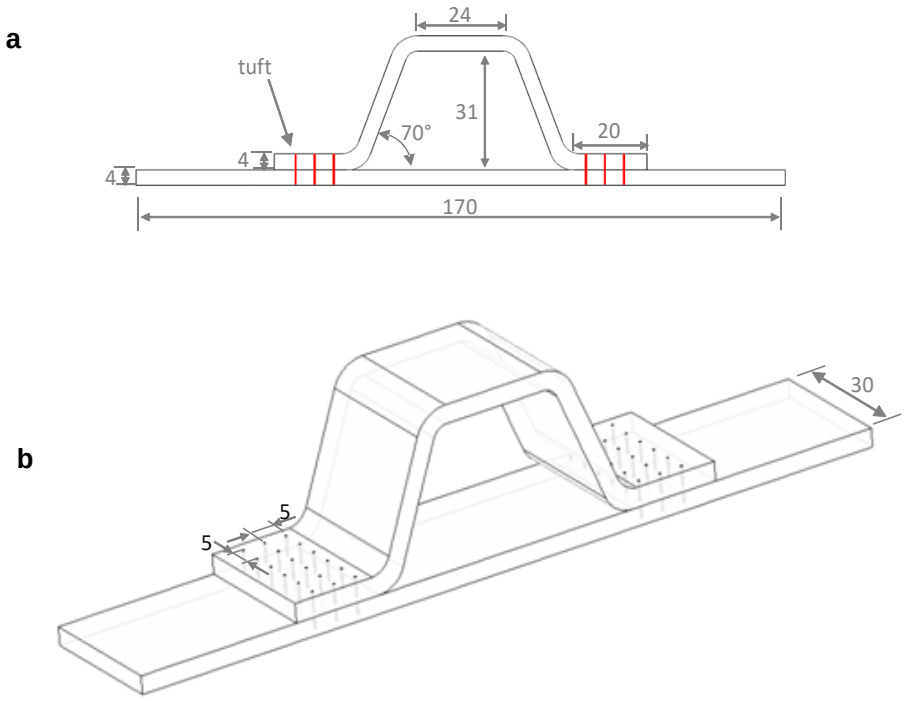


**Figure A. 1- Schematic illustration of the position of the tufts and the dimensions utilized for the model (except length and width due to the reduction of the model).**

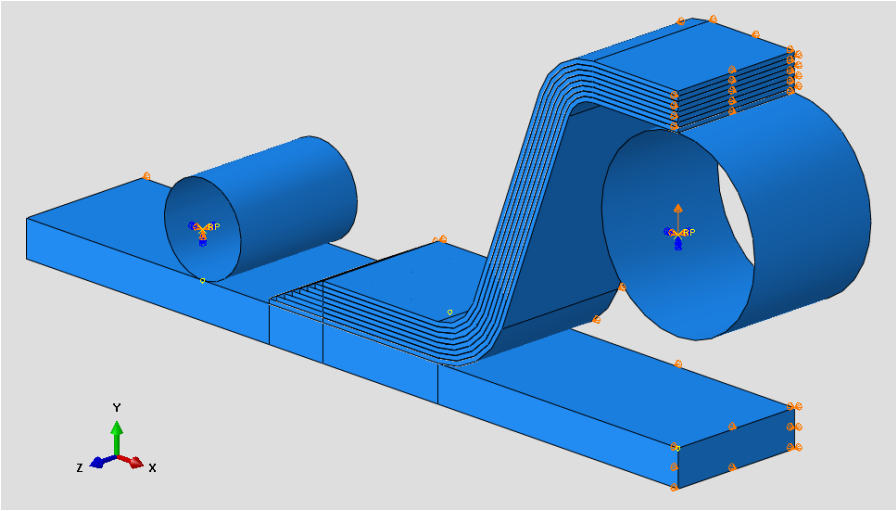


**Figure A. 2 - The distribution of constraints and load used in the model.**

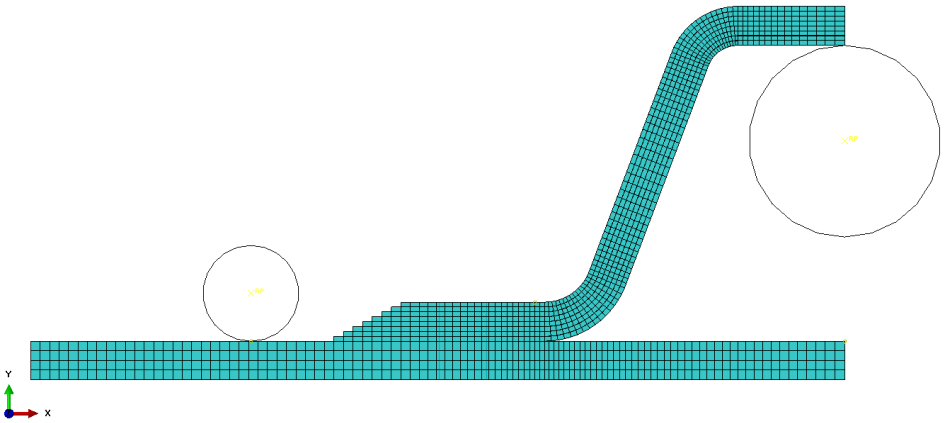


**Figure A. 3- Model ready for the simulation.**

## Results and discussions

Figure A. 4 shows the force versus displacement curve of the typical result obtained under the pull-off tests in comparison to the finite element model response. The curve presented for the model is the result of the various preliminary analysis that consisted of varying especially the properties of the cohesive elements. The investigations concerned the interface stiffness, nominal stress and mesh size of the mentioned elements. Unfortunately, the divergence after crack initiation precluded the simulation up to considerable displacements. Further investigations must solve this issue to improve the model. Despite this, a qualitative analysis was performed and exhibited the capability of the beam elements for bridging the cracks initiated on the stiffener radius as already seen in the experimental study (Figure A. 5).

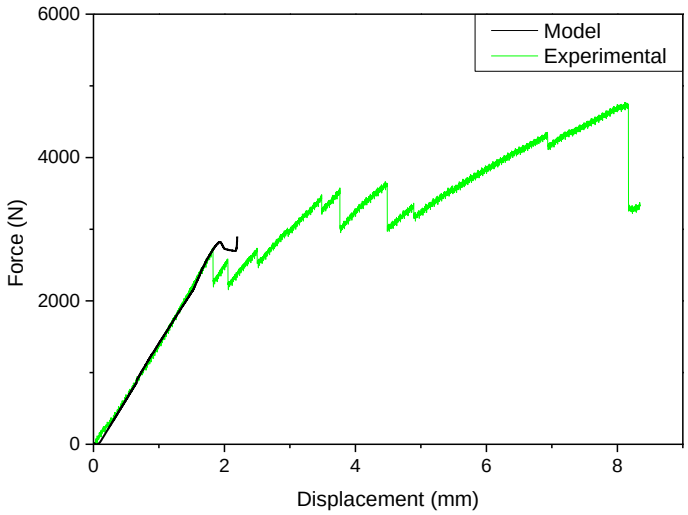


**Figure A. 4 - Numerical and experimental force-displacement curves for an omega stiffener reinforced by tufting.**

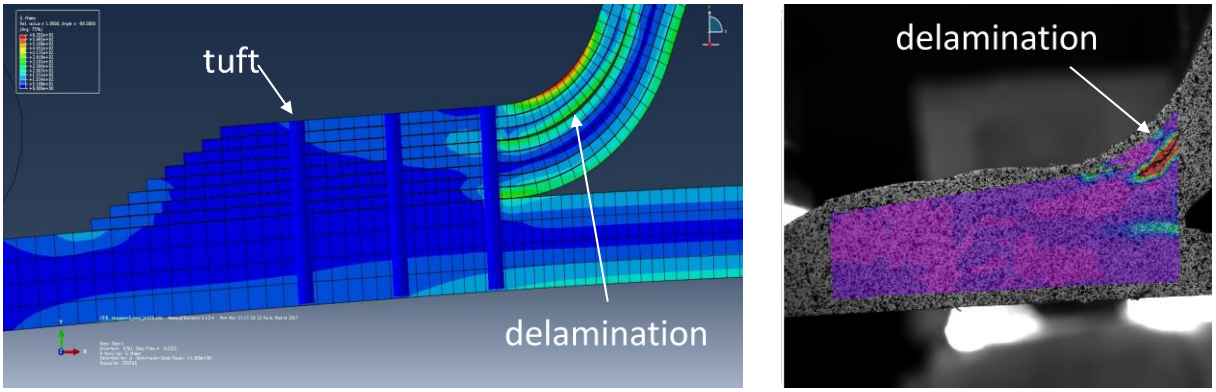


**Figure A. 5 – Crack arresting by tufts represented for finite element model and DIC strain map under pull-off test.**

Some analyses were also carried out by changing the damage evolution type from BK to displacement with the independent mixed mode behavior. These analyses that counted to lower interface stiffness, $1x10^3$ against $1x10^8$ for the simulation mentioned above, allowed to the damage initiation and evolution between plies. Figure A. 6 shows the Von Mises stress distribution on the zone skin/cohesive element and beams (tufts). The stress concentration is diminished in the region behind the beam thanks to the bridging effect of the tufts. This will generate the interlaminar crack branching subsequently to the crack arresting (seen in Figure A. 5) as exemplified on the picture by delamination in a tufted omega stiffener from the top view. The image presents the format of delamination front similar to the stress distribution around the tufts in the model. The loading evolution leads to delamination propagation and therefore, to the rupture of tuft threads as represented for the model in Figure A. 7. The failure

occurs in the first tuft row from the internal radius that consists in the critical region of the omega stiffened specimen.

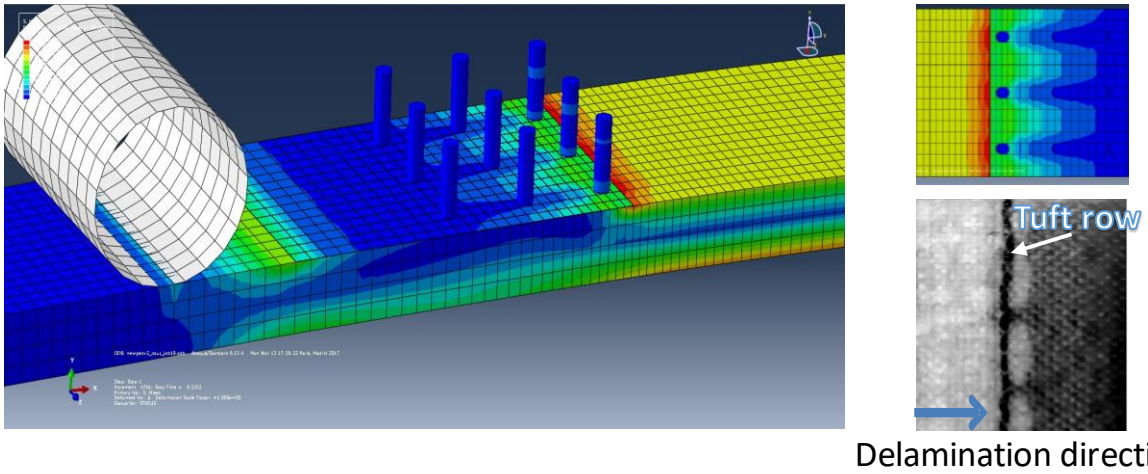


**Figure A. 6 – Von Mises stress distribution through the skin part, cohesive element layer and, the beam elements (tufts). The picture of delamination in a tufted omega stiffener exemplifies the crack branching behavior.**

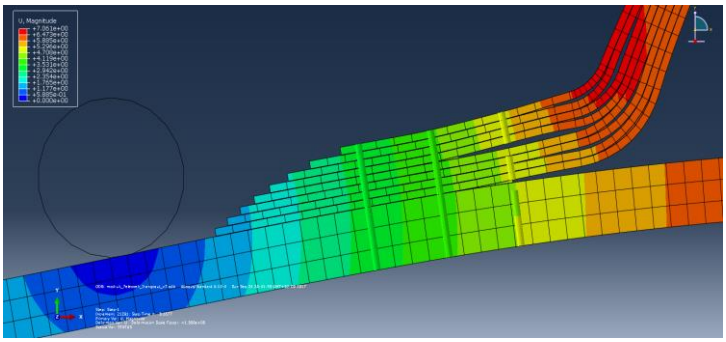

**Figure A. 7 – Interlaminar crack propagation and tuft rupture.**

## Conclusions

The approach employed for modeling the tufts embedded into the composites seems promising to obtain a model capable of evaluating the tufting parameters in the mechanical properties of the composites. Cohesive elements have been presented in several works as a delicate matter because their dependence to various settings and the considerable effort employed to adjust the model. For this reason, significant attention should be given to this subject to improve the model and amplify its reliability. Furthermore, micromechanical tests may be carried out in tufted composites to avoid the complexity of a stiffener composite and subsequently validate the approach by a simpler model. The health monitoring for the tuft threads can aid adjusting their

properties in the model once that, the techniques employed in this thesis (DIC, AE, and, in-situ microscopy) had significant issues to detect significant damages in the tufts.